REFERENCE ONLY

UNIVERSITY OF LONDON THESIS

Degree PhD Year 2006 Name of Author CIM S T

FUNDAMENTAL ASPECTS OF HELICAL WIRE REINFORCEMENT FOR FLEXIBLE PIPE PRESSURE ARMOUR

SOON YAU LIM

Department of Mechanical Engineering
University College London

A thesis submitted to the University of London for the degree of
Doctor of Philosophy (Ph.D.)

January 2006

ProQuest LLC
789 East Eisenhower Parkway
P.O. Box 1346
Ann Arbor, MI 48106-1346

Abstract

This thesis describes work undertaken to enhance the current understanding of the fundamental mechanics of flexible pipe structures. In particular, this work relates to flexible pipes that are used as flowlines and risers to convey oil and gas in offshore environments. These are subjected to various loadings such as axial, torsional and bending forces, and variations in external and internal pressure.

The structure of these pipes is complex, comprising several concentric layers of various materials and includes steel armouring, which also resists the internal pressure due to the fluid. It is the behaviour of the armouring (which in some designs is interlocked) that forms the basis of this thesis. In order to understand the mechanics of this 'pressure armour', the work presented here reduces the layer to its most basic form - that of a helical spring. This rationale has permitted several loading modes to be characterized, including axial loading, internal pressure loading and the combination of axial-internal pressure loading.

Analytical solutions were developed for the modes of loading considered, followed by numerical solutions and finally experimental investigation. The results provide a better understanding of armour behaviour and hence can assist in the design of pressure armour. Unexpected, non-conventional responses were seen in helices that were subjected to combined axial and internal pressure loads. Surface contact between adjacent coils in a helix was also studied, given that this is a feature of interlocked pressure armour designs, and when combined with applied loads, this can give rise to failure mechanisms such as fretting fatigue. Attempts were made to understand some of the significant factors in this aspect. Studies were also undertaken to improve the design of pressure armour profiles for use in high pressure environments based on a patented design, the Omega cross-section, which has an interlocking feature.

Acknowledgements

I would first like to express my gratitude to Prof. Joel Witz for his support and guidance in the early part of this work and to Ray Burke for his guidance in demonstrating the use of ABAQUS finite element modelling software and initial insights into fretting fatigue issues.

The successful completion of the thesis would not have been possible without the immense contribution from Dr Adam Wojcik. I am particularly indebted for his positive criticism of the work and enthusiasm throughout the remaining course of the research.

Additionally, I would like to thank Dr Kevin Drake and Hugh Martindale for invaluable discussions on rod mechanics. Thanks are also extended to the staff in the workshop and laboratory who provided technical assistance. A special mention must be extended to Raymond for valuable feedback on the thesis, and Sharon and Jenny for meticulous proofreading.

The financial support from Overseas Research Students (ORS) Awards Scheme, UCL Graduate School and the Department of Mechanical Engineering, UCL is gratefully acknowledged.

Finally, I would like to thank my family, in particular my parents for their love, sacrifices and encouragement, for without their support, this work would not have been possible. This thesis is dedicated to all of you at home.

Contents

List of Figures

List of Tables

Nomenclature

A	area of wire cross-section
a	contact half-width
a_{crack}	crack half-length
a_i	base vector
a_r	long side of rectangular cross-section
a_s	length of side of square cross-section
$\mathbf{b}$	binormal vector
b	short side of rectangular cross-section
c	helical spring index
c_h	number of turns in the helix
c_{sz}	stick zone half-width
D	diameter of helical spring
d	diameter of helical wire
dv	variation in axial strain of wire
d_c	distance of load to centroid of cross-section
d_f	relative surface displacement
d_w	width of helical wire
d_{wcs}	width of profile
E	Young's modulus
e	offset of centre of stick zone from centre of contact
e_{ijk}	alternating symbol
F_A	axial load
F_L	lateral load
$F_{friction}$	frictional force
F_p	equivalent force due to internal pressure
f	angle between section principal axes and rod centreline normal
G	modulus of rigidity of helical wire
G_b	binormal resultant internal moment
G_n	normal resultant internal moment
H	tangential resultant internal moment
h	length of cylinder

h_w	height of wire cross-section
I_b	moment of inertia of wire about binormal axis
I_n	moment of inertia of wire about normal axis
I_x	moment of inertia of ring cross-section with respect to x-axis
J	polar moment of inertia of wire section
K	normal resultant external moment
K_C	stress intensity factor
K_b	binormal resultant external moment
k	spring stiffness
k_{r1}	correction factor for large spring index
k_{r2}	correction factor for small spring index
$k_{11,\ 12,\ 21,\ 22}$	stiffness coefficients
l	length of wire
l_{as}	length of spring
M	applied moment
M_C	twisting moment about the centreline of wire
M_t	twisting couple per unit length
N	normal resultant internal force
N_b	binormal resultant internal force
n	principal normal vector
n	number of pitch in helical spring
P	normal force
P_{cyl}	internal pressure of helical wire with equivalent area of a cylinder
P_X	internal pressure on helical wire
p	pitch length
p_0	peak contact pressure
Q	contact force per unit length
Q_L	helical line load in the axial direction of pipe
Q_f	shear force
q	shear traction
R	radius of helical spring
R_c	contact radius
R_r	radius of ring
r	position vector

r	radius of helical wire
S	arc length along centreline in initial configuration
S_R	stress ratio
s	current arc length
T	tangential resultant internal force
T_r	torque
$\mathbf{t}$	tangent vector
t	time
t_p	parametric variable
X	normal resultant external force
X_R	total line load in radial direction
X_c	radial line load
x	horizontal displacement point of the contact surface
Y	binormal resultant external force
Y_K	geometric factor
Z	tangential resultant external force

Greek Symbols

α	helix angle
β	lay angle
ΔR	change in helical spring radius
Δp	change in pitch length
δ	deflection of helical coil
δ_{ij}	Kronecker delta function
δ_{total}	total deflection of spring due to both internal pressure and axial load
δU	variation in internal strain energy
δV	variation in external potential forces
$\delta\varepsilon_{aw}$	element volume of wire
ε_{as}	spring axial strain
ε_{aw}	wire strain
ε_r	radial strain
γ	angle between contact force and surface of the reference cylinder

κ_b	curvature in the binormal direction
κ_{ij}	curvature matrix elements
κ_n	curvature in normal direction
λ	angle between contact force and resultant force
$d\lambda$	arc angle of element
μ	coefficient of friction
ν	Poisson's ratio
ϕ	twisting angle of helix
φ	angle of twist of cross-section
σ	stress due to radial strain
σ_b	bulk stress
σ_c	contact stress
σ_p	contact stress at thin width of protrusion
τ	tortuosity
θ	tangential resultant external moment

Subscripts

1, 2 denote initial and final values respectively

c denotes parameter derived by Phillips and Costello (1973)

Superscript

' refers to parameter with the effect of twisting of cross-section

1 Introduction

1.1 Background

This thesis describes work carried out in understanding the mechanical behaviour of the armour reinforcement used within the structure of flexible pipes. Such pipes are employed to convey oil and gas from the wells to offshore production systems, such as the oil rigs in the offshore industry. These pipes have to withstand dynamic loads due to sea currents, as well as to operate in high pressure and high temperature settings to extract the oil safely and efficiently to the production systems. In the 1970s, fixed jacket platforms were the prevalent production systems, operating in depths of 200 – 400 metres. They were later followed by tension leg platforms (TLP), SPARS, semi-submersibles and floating production system and offloading (FPSO), which operated in depths of well over 2000 metres. For example, GSF Explorer FPSO operated by ExxonMobil was positioned in the Gulf of Mexico at 2200 metres and Deepwater Expedition FPSO operated by Petrobras, is currently (2005) offshore of Brazil drilling in the region of 2600 metres.

Initially, rigid steel pipes were used for the connection between the wells and the fixed platforms. However, these were replaced with flexible pipes when introduced in the 1970s (Feret and Bournazel, 1987; Tan, 1992). Now, flexible pipes are used extensively in offshore applications as flowlines and risers for hydrocarbon production. Flowlines are used for intrafield connections of wells, wellheads and loading terminals to the processing platform while risers are mainly used for conveying the hydrocarbon products from wells and delivering injection fluids into wells from the sea surface facilities. Thus these are dynamic pressure vessels in dynamic service (Berge et al, 1992). For applications using long lengths of these pipes, it is of great advantage that the flexible pipe has a compliant structure compared to their rigid steel pipe equivalents. Production of long lengths of flexible pipes is easier, and installation and retrieval of such pipes are much simpler compared to rigid pipes. By using long lengths of a flexible pipe, fewer connections and end fittings are needed.

Flexible pipe systems have evolved into highly complex composite structures, containing many concentric layers and a range of materials including metals and polymers. Some of these layers are designed specifically to contain fluids, withstand internal pressure, protect and armour the flexible pipe and/or withstand axial loads. The design codes that govern their construction have been determined largely by the years of experience gained since their introduction. Only recently have serious attempts been made to understand the underlying mechanics of the structures in order to improve and optimize their design.

The use of flexible pipes is advantageous compared to rigid steel pipes as described earlier. However, with the decreasing availability of oil reserves from shallow water regions, there is a definite trend towards drilling and production of oil and gas in deeper regions, and thus higher pressures are experienced by the flexible pipe structure. The increasing use of FPSO units for exploration and production confirms this trend. As the shallow regions are being exhausted, it makes economic sense to move into deeper regions, where there are thought to be massive oil reserves. Hence, there is a need to further improve the performance of subsea systems such as flexible pipes to accommodate the higher operating pressures and temperatures experienced in deep-water applications. In order to do this, the mechanics of flexible pipe systems needs to be better understood. There is a deficiency in the present knowledge and in the approaches taken by various workers in optimizing designs and understanding their behaviour. For example, insufficient consideration has been given to the effect of the internal pressure (due to the hydrocarbon) on the mechanics of flexible pipes.

This thesis attempts to further understand the fundamental mechanics of flexible pipe design, in particular the pressure armour layer of the pipe. This is a layer of steel reinforcement that helps to withstand load and protect a pipe. Additionally, the present knowledge of flexible pipes considers the global deformation of the structure under load, for example as described in Oliveira et al (1985) and Goto et al (1987), whilst this work aims to deal with deficiencies in the limited understanding of the localized behaviour of individual layers. This knowledge will provide the basis for the optimization of the design of flexible pipe structures for higher pressure applications. A brief review of flexible pipe structure and design

is given in section 1.2 below and will aid in defining the scope of work presented here.

1.2 Flexible Pipe Structures and Configuration

1.2.1 Construction Layers and Material

The construction of a flexible pipe includes two generic components; *helical metal wires* to withstand axial, torsional and bending loads and *polymer cylindrical tubes* for containment of fluid (Berge et al, 1992; Patel et al, 1993).

There are two classes of flexible pipe: -

- Unbonded flexible pipe
- Bonded flexible pipe

Unbonded flexible pipes are structures where each layer forms an independent cylindrical layer of polymer or wire. Each layer performs a particular function and the layers deform independently in response to the loading conditions applied (American Petroleum Institute (API) document 17B, 1998). Bonded flexible pipes are structures where the layers of steel, fabric and polymer are bonded together to form a composite structure, which allows flexibility when deformed under shear and tension. The bonding process involves the use of adhesives or by application of heat and pressure (Berge et al, 1992). Examples of these flexible pipes are shown in figures 1.1 and 1.2 respectively.

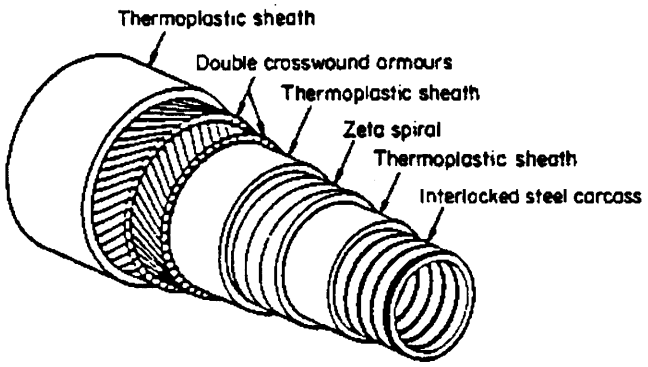

Figure 1.1 Unbonded flexible pipe (Berge et al 1992)

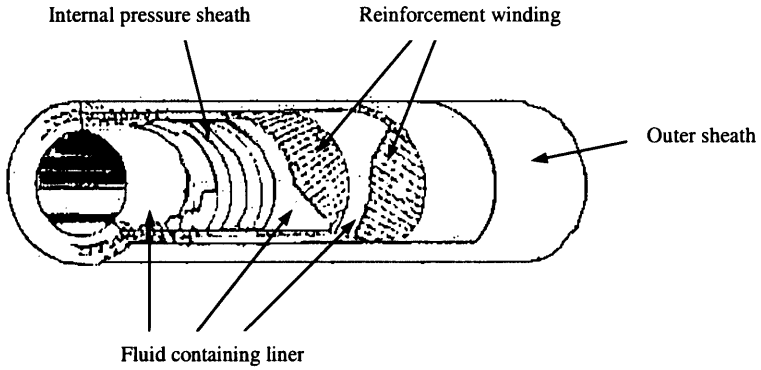

Figure 1.2 Bonded flexible pipe (adapted from API document 17B 1998)

The work in this thesis concentrates on the unbonded pipe configuration given that this allows the optimization of the design of the pressure armour layer, independent to the function of other layers. From here on, any illustration or description refers to the unbonded pipe configuration unless specifically quoted otherwise. Referring to figure 1.1, a typical unbonded flexible pipe consists of the following layers, starting from the innermost layer: -

- Internal carcass – Interlocking metallic layer which is used to prevent collapse of the structure due to external pressure load.
- Inner sheath – This is a polymer sealing layer for containment of fluid such as crude oil and gas.
- Pressure armour – Consists of overlapped and/or interlocked, wound helical metallic wire or wires, and acts to prevent internal pressure of the fluid from expanding the polymer.

- Intermediate sheath – Polymer layer to reduce friction and wear between the pressure armour layer and the tensile armour layer.
- Tensile armour – Usually cross-wound to obtain torsional balance of the whole pipe structure and to provide axial strength of the pipe.
- Outer sheath – Polymer sheath acting as robust marine coating which prevents chemical degradation of the pipe.

The polymer sheath layers are extruded onto the metallic layers, and are primarily used for fluid containment or separation of the armour layers. Therefore, the key requirements for the polymer material are long term resistance to chemicals such as crude oil, to include a low permeability, low absorption and high resistance to swelling, as well as being able to withstand long term static and dynamic strains. Such details are given in API document 17B (1998). Additionally, the polymer is required to have good wear and abrasion resistance, to function well as a marine coating. Typically, high density polyethylene (HDPE), polyamide 11 (PA11) or polyvinylidene fluoride (PVDF) are suitable for internal and intermediate sheaths depending on operating temperature, fluid compatibility and fatigue characteristics. However, for the outer sheath, polyamide 11 (PA11) is preferred to HDPE for higher temperature applications because of better abrasion resistance.

For the metallic layers, stainless steel and low carbon steel are usually used. The choice of metal for an internal carcass is based on the fluid components that are being conveyed. As the severity of the fluid environment grows, stainless steel alloys are usually used to resist corrosion. Carbon steels are used for the armour layers since high structural strength and fatigue resistance is required.

1.2.2 Riser Configurations

Another important parameter which has to be considered when designing a flexible pipe system is the riser configurations. A good riser configuration provides compliancy to the vessel motions, and also allows the riser to sustain the extreme loading conditions to which it is subjected to when in-service (Patel et al, 1993; API document 17B, 1998). For example, large tensile loads near both the

riser-vessel and riser-seabed points can cause an undesirable response of the flexible pipe to the various loading conditions. There are several designs of riser configuration for optimum operation of a flexible pipe for different loading conditions. These configurations are depicted in figure 1.3 and are described briefly as follows: -

- Simple catenary – The simplest and least expensive of the various configurations, where the riser is suspended freely between the surface vessel and the seabed. This configuration is only suitable for shallow waters. In deeper regions, the tension of the pipe increases via the additional weight of the pipe. This can cause tensile failure at the vessel connection because most of the weight is supported at that point.

- Steep-S – The configuration consists of two different sections with the introduction of subsea buoys in between. The buoys effectively support the lower section of the pipe, hence reducing the high loads experienced at the vessel connection point. This configuration is suitable for moderate depths (200 metres) but can experience possible torsional instability.

- Lazy-S – This is a natural progression from the Steep-S configuration. The upper section is similar to the Steep-S while the lower section is in the form of a simple catenary. The buoys are tethered using a large weight and chains. This is used in deeper waters where the Steep-S and simple catenary configuration are not suitable due to tension or buoy stability problems.

- Steep wave – The buoyancy is distributed rather than concentrated at points as is the case for the various S configurations. This configuration is suitable for heavy flexible pipes in shallow waters where axial tension needs to be reduced.

- Lazy wave – Similar to Lazy – S configuration but with distributed buoys instead. A large vessel offset from the wellhead can be accommodated and this configuration is suitable for large water depths.

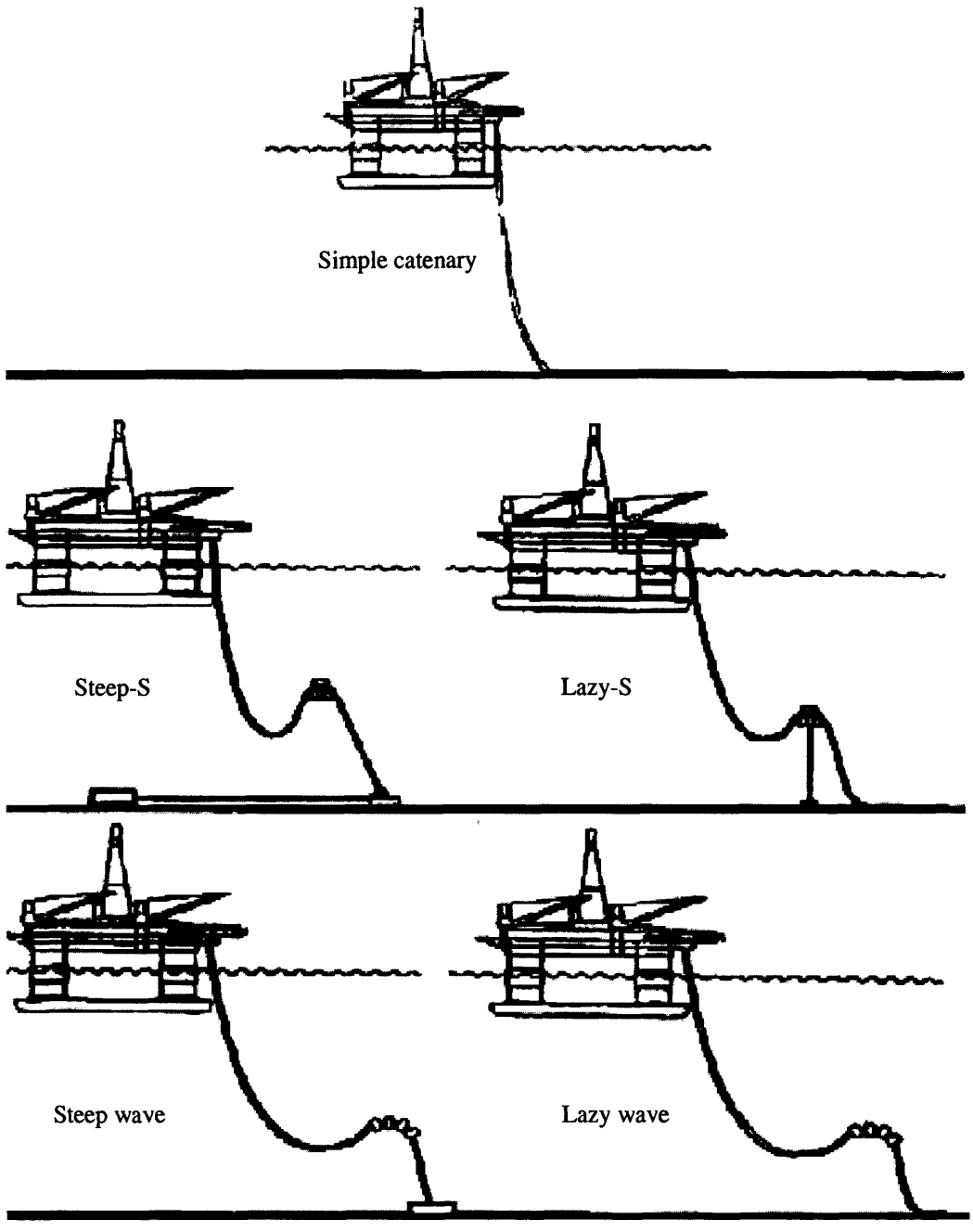

Figure 1.3 Riser Configurations (API document 17B 1998)

1.3 Pressure Armour Profiles and Issues

As discussed earlier, there is a growing demand to employ flexible pipes in high pressure environments, which is the case when exploration depths of 2000 metres or more are reached as cited in the examples given previously. The conventional structural configuration of flexible pipes is capable of reliably supporting pressures resulting from only a shallow water environment. Hence, to accommodate the higher pressure ratings experienced in deep water, the size of the pressure armour layer of the pipe has to be increased. Sometimes, an additional backup pressure armour layer is used instead to achieve higher pressure ratings. Consequently, the flexible pipe experiences an increase in weight, posing difficulty in transportation, installation and operation and also a significant increase in the costs involved.

Flexible pipe manufacturers have been looking at alternatives to current pressure armour material as a means to achieve higher pressure ratings and reduce weight of these flexible pipes. One alternative material under consideration is *carbon fibre* which has higher strength compared to steel and is relatively light in weight. However, carbon fibres are expensive when employed in long lengths of pipe.

One other possible method of overcoming the high in-service pressure loading is by optimizing the design of the cross section of the pressure armour layer. The pressure armour layer is primarily designed to withstand internal pressure loading. This work will also consider the ability of this layer to resist axial loading. Currently, there is no data on the axial loading capability of the pressure armour layer. The pressure armour layer is also an important component in contributing to the overall weight of the flexible pipe.

There are several cross sectional profiles currently available for use as pressure armour wires. Examples of commonly used profiles are shown in figure 1.4.

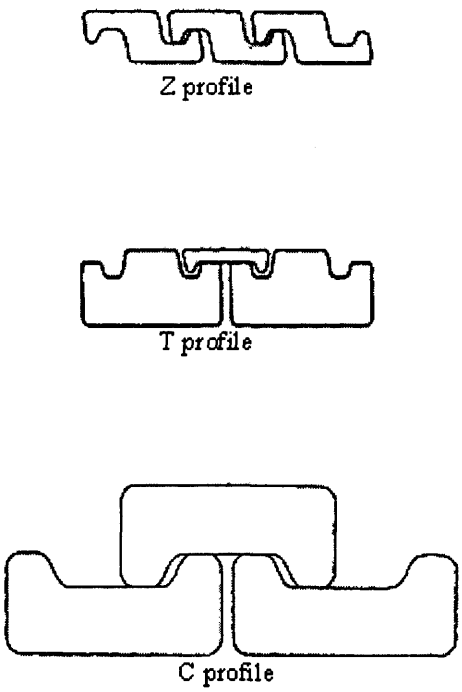

Figure 1.4 Pressure armour cross sections (API document 17B 1998)

Interlocks of subsequent turns of the pressure armour wires maintain the structural integrity of the layer when an internal pressure loading is applied. The profiled wires can also allow axial movement and flexural rotation without generating excessive gaps. Large gaps in between the profiled wires are detrimental because they allow the polymer layer underneath the pressure armour to creep through and compromise the fluid containment ability. These profiled wires can reliably support the pressure loading experienced in shallow waters.

Very little, however, is known about the behaviour of the interlocked sections of the pressure armour layer when subjected to internal pressure and axial loads. For example, contact between the tips of Z profiled wires can affect the way in which the pressure armour responds to internal pressure loading and axial loading (Chen et al, 1995). There has been relatively little work done on contact forces on pressure armour profiles despite its importance in resisting loads in flexible pipes.

There are also potential issues involving the frictional effects of the pressure armour layer when the internal pressure loads are being applied. Together with the

oscillatory movements experienced by profiled wires under service conditions, this could generate fretting fatigue on the contacting surfaces of the pressure armour wires (API document 17B, 1998; Burke and Witz, 1999). Fretting fatigue is a contact failure mode, which can lead to crack formation, when tangential and normal forces are applied to contacting surfaces. While fretting is a common problem in mechanical components such as bearings, relatively little work has been done in observing this in pressure armour wires (Burke and Witz, 1999).

With a non-symmetrical profiled wire such as the Z profiled wire, the stress distribution across the cross-section of the wire is not uniform under internal pressure loading mode. This could be due to rotation of the section being generated by moments as a result of the internal pressure load acting on a non-symmetrical cross-section. Stress gradients across the profiled wires can cause the cross-section to be inefficient in terms of material utilisation. To date, twisting moments of these non-symmetrical profiled wires due to internal pressure load has not been fully observed. In this work, the T and C profiled wires are not considered as they are symmetric sections.

An alternative pressure armour wire profile, the Omega profiled wire has been developed within the Department of Mechanical Engineering at UCL (GB Patent No. 2336886, 1999) to eliminate the need to scale up the conventional flexible pipe structure for high pressure load applications. An example of this profile is shown in figure 1.5.

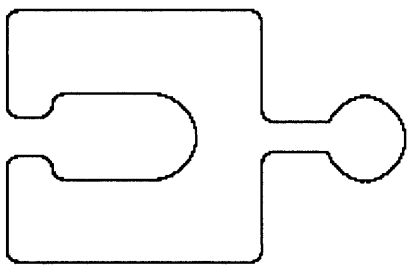

Figure 1.5 Omega profiled pressure armour cross section

Potential advantages of the Omega profile are as follows: -

- Ability to resist axial tension load when compared to conventional profiled wires, hence possibly eliminating the need to use the tensile steel layer to withstand axial loads.
- Ability to operate in higher pressure environments due to the more uniform cross section of the wire, which increases the efficiency of the material utilisation for the same cross-sectional area.
- Interlocking feature of Omega profiled wire allows small uniform displacement of gaps when load is applied, and therefore no excessive creep of the polymer sealing layer occurs.

The Omega profiled wire has been designed in such a way as to have a protrusion at one end and a socket at the other end of its cross-section. This allows the profiled wire to interlock with the subsequent turn of its helical configuration by having the protrusion locked into the socket of its adjacent coil. The need to interlock the sections of the helical coil will inevitably require new or modified production methods but the benefit appears to be attractive. An example of the interlocking of Omega profiled sections is shown in figure 1.6.

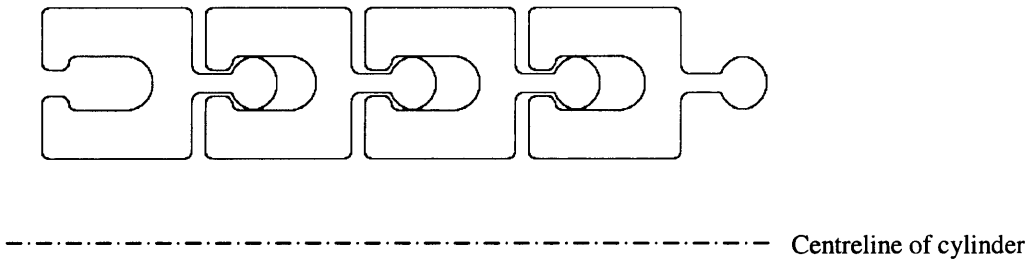

Figure 1.6 Interlocking Omega Profiled pressure armour sections

The Omega profiled wire is an exciting development but there are many issues that need to be addressed if it is to be realized in practice. For example, the mechanics of the Omega profiled wire's response to axial deformation with respect to internal pressure loading and axial tension loading should be

investigated. The way in which the cross-section of the wire twists with respect to the loading modes is important in order to understand the stress distribution and also the contact stresses arising from these loads.

As the Omega profiled wire interlocks with each subsequent turn, there is a coupling force generated along the length of this pressure armour layer. The effect of this coupling force on the performance of the flexible pipe to withstand higher in-service pressures is unknown. Also, frictional forces that arise from the contact of the turns of the Omega profiled when loads are applied have not been accounted for and this may well be an important issue to the load carrying capacity of the flexible pipe and fretting fatigue susceptibility.

Another point of interest is whether the Omega profiled wire, which has an axis of symmetry in the cross-section, improves the material utilization by having a more uniform stress distribution for the same cross-sectional area as of a conventional profiled wire. Clearly the structures utilised in flexible pipes are complex but most of the modern work to date has attempted to tackle this complexity by dealing with the structure as a global entity rather than examining the individual behaviour of the constituent components. Whilst this approach is a valid one, it can fail to provide localized information regarding aspects of behaviour and failure, or potential degradation in these structures.

As can be seen in section 1.4, this work attempts to address some of the issues highlighted above by examining the behaviour of pressure armour components away from the overall flexible pipe structure. The insight into the behaviour of pressure armour that this work provides has also been used to lay down the foundations of an understanding of the mechanics of an Omega type interlocked pressure armour.

1.4 Aims of Work

Much of the current understanding of the behaviour of helically reinforced flexible pipes has been obtained through experience of in-service installations.

The historical development of flexible pipes and their reinforcement has occurred through piecemeal improvements in design and materials, rather than through an understanding of the fundamental mechanics behind their operation. The work described herein aims to redress at least some of this imbalance through the generation of analytical and finite element based models. It is hoped that such models will enable engineers to better understand the mechanics and interactions that occur within the pressure armour layer, such that structural design can be enhanced and design codes developed to raise the reliability and safety of flexible pipeline systems. Furthermore, with the invention of more complex pressure armour designs, such as the Omega profiled wire cited earlier, it is important to understand the fundamental constraints operating so that potential issues and problems with these new designs can be addressed before they are placed in service.

The approach used in this work starts by simplifying the notional construction of pressure armour reinforcements such that the underlying mechanics can be investigated. A further fundamental simplification has been the assumption to treat the pressure armour reinforcement as a helical spring. This is justified not just on the grounds of geometric similarity but also on the desire and need to validate the models developed.

In this thesis, the mechanics of helical springs are first investigated for circular cross-sections from an analytical viewpoint. This is then extended to the study of more complex cross-sections to eventually arrive at a model which is able to analyze interlocked designs (such as the Omega profile). The behaviour was investigated under various loading conditions, including tensile, internal pressure and the combination of the two. Other scenarios such as bending and torsion were not part of this study, although where deemed relevant, then they are briefly considered.

To be ultimately useful, the analytical solutions presented here should also be able to account for some frictional effects. However, this is limited to a discussion of the role of friction in interlocked profiles, given the complexity of the problem. For now, it is sufficient to assume that many of the simplifications made here have

been done in order to expedite the overall analysis, and to ease the design of the experimental apparatus used to make the observations necessary to assist in model validation. With relevance to the latter, a novel approach was made towards observing the practical behaviour of helical springs by the design and construction of a spring lathe which was successfully used to cut helical springs of different profiles. The spring lathe was also used to cut an interlocked Omega profile type spring. This would have been extremely costly to produce by any other means, and provided a useful insight into the Omega wire concept.

While it is straightforward to carry out tensile testing of a spring, it is a challenging task to apply pure internal pressure loads on a helical spring structure. This loading scenario is critical to developing and understanding at how pressure armour behaves in practice. It was thus necessary to devise a means of applying internal pressure loads to the experimental helical springs. A purpose-built pulley rig was thus developed to apply radial loads, and to simulate as authentically as possible, the changes in response originating from the application of an internal fluid pressure.

The spring lathe and pulley rig are fully described in chapter 5. In addition to performing analytical and experimental investigation, a third aspect of this work has been the numerical modelling of various loading scenarios relevant to pressure armour profiles. ABAQUS was selected as the finite element modelling software and attempts were made to mesh and model a wide variety of coil configurations. In general, strong correlation between analytical and finite element modelling was observed, which is not surprising given that the origin of the latter is within the former. Although similar trends were observed in the practical experiments, close correlation was more difficult to achieve.

Overall, by applying the helical spring simplification, it has been possible to generate a staged route to the development of a useful flexible pipe pressure armour reinforcement model. This is discussed in more detail in chapters 3 - 6, which also reveal how, at each stage in the development of the model, constraints or extra degrees of freedom were introduced in order to move further towards the goal of a global model capable of handling complex profiled wires and multi-axis

loading scenarios. A final aspect of this work has been to utilize the information gleaned from the analytical, numerical and experimental studies to provide feedback into the design of future pressure armour profiles. There are many design criteria that are relevant to pressure armour, but one of the most significant, other than load carrying capacity, is the ability to withstand long term degradation and failure of the attendant components of the armour. Fatigue is a significant factor, but for this study, it was decided to concentrate on a more insidious form of damage, namely that due to fretting fatigue.

As was mentioned earlier, fretting fatigue occurs when mating surfaces rub together, hence a significant part of this study was devoted to understanding where these relative movements could occur. Treatment of the pressure armour as a helical spring allowed several modes of movement to be studied, including axial, radial, and intercoil sliding. By combining the predicted movements with an understanding of the stresses that could be developed, a prediction of the likely impact upon the fretting behaviour could be made. This in turn was used as a basis for suggested design modifications and/or criteria that could improve component lifetimes. In this way, it has been possible to feed back the results of the analysis of the mechanics of helical wire reinforcement into a set of design recommendations and to also discuss how the design of the fully interlocked systems, such as the Omega profiled wire, could be optimized.

A summary of the aims of this work is described as follows: -

- To develop analytical solution of a helical wire subjected to combination of axial and pressure loads, by reducing pressure armour to a helical spring analogue.

- To extend the analytical solution to include the behaviour of non-symmetric helical wire cross-sections.

- To verify of the analytical solutions developed using finite element analysis.

- To cut and test helical springs of various cross-sectional shapes under axial and radial loads, to aid in model verification and physical observation.

- To understand the behaviour of interlocked helical wire profiles, such as the Omega profiled wire.

- To develop design codes of flexible pipe pressure armour based on observations from the analysis carried out, with an emphasis on reducing susceptibility to fretting fatigue damage.

1.5 Overview of Chapters

The arrangement of chapters in this thesis has been largely determined by the need to present three forms of analysis in a coherent manner. These take the form of an analytical, numerical and experimental study into the mechanics of helical wire reinforcement. Chapters 3 – 6 contain this information whereas chapter 7 builds on the implications generated and attempts to influence the future design of flexible pipe structures through best practice recommendations. The background of flexible pipe design in general, and the aims of work are described in the present chapter. A detailed overview of the rest of the thesis is provided below.

Chapter 2 centres around a literature review of the work relating to the mechanics of helical wires. This includes the review of the early work done with regards to cables and wire ropes (the mechanics of helical wire for a pressure armour layer is similar to the analytical solutions for wire ropes, albeit more complex because of the cross-section of the wire involved). Also presented therein is the state of the art of flexible pipe design in general, together with a discussion of the possible failure of such pipes, in particular, through fretting fatigue.

Chapter 3 describes the theory of conventional spring behaviour, limited to circular cross-section wire. From the basis of wire rope theory, where Love's equilibrium equations are presented, an analytical solution for a single helical wire constituent, subjected to various loading conditions, is described. Finite element

models are used to confirm the analytical solutions obtained. A key feature in this chapter is the spring stiffness results obtained from analytical and finite element analysis for combined axial tension and internal pressure load on the helical wire, which interestingly has revealed a variable stiffness behaviour.

Similarly, the analytical solution of a helical wire for different cross-sectional shapes, based on Love's equilibrium equation, is presented in chapter 4. The effects of the axial, internal pressure and combination of both loads on the different cross-sectional shapes are also discussed. Additionally, for non-symmetrical sections such as L and Z, the twisting effect of the cross-section due to internal pressure load is discussed.

Chapter 5 details the experimental work, where a spring lathe was developed to cut polystyrene springs for subsequent testing. A pulley rig was also built for application of internal pressure to the springs. Results were compared to the analytical solutions developed in chapter 4 and are discussed.

Chapter 6 investigates the loading behaviour and also clarifies the difference between conventional spring based layers and interlocked layers, both in mechanical terms and with a view to the failure mechanics (particularly fretting fatigue). As the surfaces of interlocked profiles such as Z and the Omega cross-section are in contact with its adjacent turns, frictional effects critical to some particular loading modes can become an issue and are addressed here. Results of an Omega cross-section polystyrene test to destruction are also discussed here. The mechanics of a helical wire are influenced by the condition at the termination ends, for example, whether it is fixed from movement or free to rotate or move axially. To this end, chapter 6 also discusses the influence of pipe end fittings to the behaviour of the helical wire constituent on the flexible pipe.

Design codes for pressure armour profile are described in chapter 7 using the observations made through theoretical, numerical and experimental aspects of the behaviour of helical wires. As detailed in chapter 6, the pipe end condition, which is important in the design consideration of pressure armour is also discussed in chapter 7.

Finally, the overall conclusions and recommendations for high pressure applications are presented in chapter 8. Discussions on the shortcomings of the analytical model and identification of future work to advance and improve the solutions to replicate in-service scenarios are also presented.

2 Literature Review

2.1 Introduction

This chapter outlines the fundamental development of the theories pertaining to the mechanics of helical wires of flexible pipe pressure armour. As flexible pipes were only introduced in the late 1970s, much of the analytical solutions were based on the behaviour of wire ropes and cables, both which have helical strands wound onto a central core. Although quite similar in nature, there are some apparent differences in the orientation of the helical components as well as some of the loading modes experienced by the pressure armour. Notwithstanding the latter, the review presented here details the development of the mechanics of wire ropes and demonstrates to how these approaches are made applicable to the analysis of flexible pipes mechanics. Several theoretical approaches have been taken previously for the study of the mechanics of wire ropes and cables, namely:-

- Equilibrium of forces
- Slender rod theory
- Castigliano's energy method
- Orthotropic sheet theory

A discussion of these methods used by past researchers is presented here together with the assumptions made and the type of cables investigated. Where possible, comparison of the various methods is made.

Much of the work done on flexible pipe designs concentrated on the global deformation of the composite structure. The review presented here includes various analytical solutions produced for interlayer interaction and the global deformation of the pipe subjected to axial, torsional and bending loads. None of the literature to date has focused on the pressure armour layer and the complex interaction that such a layer has between the contacting surfaces (adjacent coils). Some designs have the coils partially (or even fully) interlocked and therefore

constraint by friction is a consideration that needs to be addressed, but has largely been ignored by previous workers. Hence relevant aspects of fretting fatigue are also described.

2.2 Mechanics of Helical Wires and Flexible Pipes

The analytical behaviour that describes the behaviour of a wire rope under axial loading was first introduced by Hruska (1951). In this instance, the wire rope consisted of concentric helical wires wrapped around a central core. The forces considered were purely tensile, without any consideration of torsion or bending loads on the wire rope. Also, small deformations were considered, therefore the helix angle (defined in section 3.22) was assumed to be constant. The analytical solution was solved by summing up the contribution from the different layers, via resolving the forces experienced in each individual helical wire, together with the contribution experienced via the rope's core.

Further to this, Hruska (1952, 1953) also considered the effects of radial and tangential forces that arose when the helical wire components pressed on to the central core due to applied axial loads. As the wire rope being considered consisted of helical wires with a large helical angle, such a radial contact load could be significant because the radial deformation was expected to be larger. It should be noted that the wire rope configuration considered by Hruska (1952, 1953) is not necessarily similar to a pressure armour configuration, where the helical angle is usually very small. The small helix angle generates a smaller radial loading scenario. Nevertheless, for a pressure armour, the main contribution to the radial loading is the force that arises from the internal pressure load. The tangential force arose due to the applied axial load and the resulting tension in the helical wire. Tangential loads considered by Hruska (1952, 1953) caused the wire rope to rotate along the centreline of the core, thus producing a moment on the cable. It was pointed out by Hruska (1953) that if both ends of the cables were fixed, then the driving moments are negated by the reaction moments produced at the ends. However, when one or both ends are not fixed, then the cable is free to rotate.

Machida and Durelli (1973) extended Hruska's work to investigate the response of a cable made up of circular cross section wires, subjected to axial (tensile) and torsional (twisting) loads, and also under a combination of both loads. The cable investigated was limited to the case of six concentric helical wires wrapped around a central core. From geometrical considerations, analytical solutions for axial force and bending moments were established using the assumption that no frictional forces arose from contact of wire with the core and that the deformation was small, i.e. the initial helix angle and the final helix angle remained the same. In the combined effects of torsion and tension, the analytical solution was similar to one under the effect of torsion alone (again when deformation of the wire was small). Based on this, it was concluded that if the rope deformation was small, the torsional rigidity of the strand would not be affected by the effects of an axial load component. It is worth noting that the experimental work done by Machida and Durelli (1973) showed that cables with fixed ends were stiffer than ones with free ends.

The behaviour of a helical wire can be regarded as that of an elastic rod of narrow cross-sectional area with respect to its length, assuming that plasticity is ignored. The theory of elastic slender rods was first postulated by Kirchoff in the 19^{th} century and later considered by Love (1934). A set of equilibrium equations describing the forces and moments of a slender rod was established. Love's equilibrium equation can be used to solve for the forces and moments in helical rods, assuming that the rod is inextensible. This assumption however, leads to the conclusion that the cable is of infinite stiffness in some loading modes, for example pressure loading. This will prevent the equilibrium equation from being solved in these cases. In this work, the assumption of inextensibility is removed for the pressure loading cases so that the equilibrium equations can be solved.

Love's equilibrium equation (slender rod theory by Love (1934)) was extended by Phillips and Costello (1973) to the application of wire ropes which were helically wound. They considered a cable consisting of a single layer, made up of several concentrically wound helical wires. Each wire was considered as a slender rod, subjected to an axial load and a twisting moment (via the application of a torsion force). The assumptions made in solving the general non-linear equations were

that frictional forces between wires were ignored and the radial forces exerted by the core of the cable (if any was used) on the wire were neglected. This meant that the radial deformation was solely within the outer wires. The investigation by Phillips and Costello (1973) also included contact stresses between the wires when they were pressed together due to the applied loads.

Blanco and Costello (1974) illustrated the effect of having a cylindrical constraint on a helical wire. The work again assumed that there was no wire strain and because of the constraints imposed, no radial strain was present as well. The results showed that the system comprising the helical wire had a higher stiffness compared to one which was not radially constrained.

Costello and Phillips (1976) extended their previous studies to determine the effective tensile modulus of twisted wire system. Basically, the same initial and final configuration as in Phillips and Costello (1973) was used and the same assumptions were made. However, the assumption that the wire was inextensible was removed. The effects of cable axial force due to the cable strain and rotation for two cases were determined. The first case was for conditions of the cable end free to rotate and the second for one with no end rotation. A few notable conclusions were made. The stiffness of a cable with fixed ends was deemed to be higher than one which ends are free to rotate and the stiffness of cables with fixed ends were not influenced by axial load applied. Also, increasing the load applied increased the stiffness of cable with free ends unless the wires were almost straight initially. This investigation showed that cable end conditions were important in determining the cable's stiffness.

Further analysis using Love's equilibrium equations was carried out by Velinsky et al (1984) on complex cable cross-sections. The cable considered was '6 x 19 Seale', which is a cable with a large number of helical wires, each having large helical angle. The work performed by Velinsky et al (1984) showed that the equilibrium equations were useful in solving multi-layered cables consisting of a large number of helical wires. LeClair and Costello (1986) considered frictional forces between the helical wire layer and the core. The bending behaviour of the cable, consisting of numerous helical wires wrapped around the core was

investigated and their work concluded that slippage of the helical wires took place as the cable was being bent.

An analytical solution for the axial – torsional and bending response of a helical wire was presented by Ramsey (1988). This theory was similar to the one obtained by Phillips and Costello (1973) based on Love's slender rod theory. However, the current analysis included a set of generalized strain equations which characterized the helical wire response under various loading conditions. One critical difference in this approach was that it illustrated the difference between twist and tortuosity of a wire. In the work by Costello and his co-workers (Phillips and Costello, 1973; Costello and Phillip, 1976; LeClair and Costello, 1986), the rod cross-sectional rotation was not taken into account due to misrepresentation of the twist – tortuosity term in Love's equilibrium equation. The difference between twist and tortuosity is further explained in section 3.2.3. In view of this, the solution by Ramsey (1988) clearly provided a means to determine the orientation of the wire cross-section. This is particularly useful if the wire cross-section is non-circular, given that if the wires used were circular in nature, the misrepresentation by Costello and his co-workers would not have been obvious because the rotation could not be clearly observed. Since the work presented in this thesis covers various wire cross-sectional profiles, the rotation of the cross-section is evidently important in the response of the helical wire subjected to various loading conditions.

Further advanced models were developed by Ramsey (1990) to investigate interwire friction in multilayered cables. When the cable undergoes uniform extension or twisting, the only extra component in Love's equation that is attributed to the frictional force is a moment generated between the sliding wires. In this instance, it was argued that the frictional moment only acts to resist the change in helix angle of the wires. This may not be particularly true if the cable changes its radial dimension. Ramsey (1991) extended this work to study the effects of clamped ends of the helical wires in multilayered cable. Here, the interwire frictional components were ignored for simplicity of analysis. Boundary conditions were applied at the ends of the cable in the slender elastic rod theory to analyze the effect on the fixed ends. It was found that the effect on the stresses of

the wires was small but caused slippage of the wires near the fixed ends, and may have contributed to wear. The effect of end terminations on the behaviour of helical wire structures is further discussed in chapter 6. It will be clear from chapter 6 that the constraint imposed by end terminations is significant in determining the lifetime of helical reinforcement and hence its design.

An energy method first introduced by Castigliano was used by Knapp (1979) to obtain the axial and torsional response of helical armoured cable. The effects of core radius variation were considered. Core radius variation could be due to pressure from other layers of the cable. The non-linear equations produced by Knapp (1979) were linearized to achieve a closed-form solution, albeit limited to small cable deformation. Another important consideration in the analysis was that it could be extended to non-circular cross section wires by approximating an equivalent wire radius.

The effects of coupling between axial, torsional and flexural forces for helically armoured cables under static loading conditions were studied by Lanteigne (1985). The analytical solution provided could be used to solve for cases of unbalanced load where some of the constituent wires in the cable had failed and these loads transferred directly to other wires in the cable. It was found that the effect of coupling forces between the axial–flexural and torsional–flexural did not produce a significant difference when compared to the behaviour of the wires under each independent load alone. However, for the cases of unbalanced loads, these coupling forces should be taken into account.

Another approach that was used to model cables was due to Raoof and Hobbs (1988). The analysis treated the individual layers of helical wires as a series of cylindrical sheets (in essence, a collection of thin walled tubes) using orthotropic sheet theory to determine the overall response. This method is more applicable to *large strands*, that is having large number of wires in a layer. The underlying assumption is that the wires in each layer are just touching each other when no axial load is applied. An attempt was also made to analyze the effects of friction and interwire contact. Similarly, Raoof (1991) extended the analysis for the combined axial – torsional loading of large strand cables.

Blouin and Cardou (1989) used a similar method to that of Raoof and Hobbs (1988) in treating the helical wires as a cylindrical layer. However, the cylinder was treated as a (local transverse isotropic) material under symmetrical loads in the axial direction. This method is attractive only if a large number of wires are present in each layer of the cable so that the total area of the wires approximates the area of a cylindrical layer.

Jolicoeur and Cardou (1991) presented a comparison of results of different models of twisted wire under *axisymmetric* loading (thus bending was excluded). Axisymmetric loads that were considered were those due to axial forces and twisting moments. This led to the assumption that the wires had the same elongation and twist per unit length across the length of the cables. The models compared were from different approaches such as the simple equilibrium of forces by Hruska (1951) and energy methods by Knapp (1979). These models were linear and ignored the torsional and bending stiffness of the wires, which is often not the case in the actual response of a flexible pipe where the geometry of the structure is complex. Nevertheless, many of these linear analyses are still used today to study the behaviour of flexible pipes subjected to axisymmetric loads despite the limitation due to its structural complexity. The solution based on Love's equilibrium equation by Phillips and Costello (1973) was also considered in Jolicoeur and Cardou's study.

The type of cables that were considered by Jolicoeur and Cardou (1991) contained several helical wire layers, typically of large helix angle. Although all the models presented in Jolicoeur and Cardou (1991) gave good correlation with the experimental data, Knapp's model gave closer results to experimental data because the cable's core radial variation was included.

In spite of the different starting points in the approaches used, the first three theories mentioned earlier in the introduction of this chapter produced quite similar results as pointed out by Feld (1992). The orthotropic sheet theory is less relevant in the study of pressure armour layers as it assumes that the helical wires

behave in a similar manner to that of a cylindrical layer, and that the localized twisting and bending stiffness of a helical wire cannot be properly observed.

The modelling of global deformation of flexible pipe structure has only surfaced in the last two decades. Early investigation into the axial and torsional effects on the flexible pipe was carried out by Oliveira et al (1985). The global deformation of a flexible pipe constructed from different layers of polymer sheath and helical steel armours were considered. Simple axial, torsional and bending stiffnesses were derived from geometric considerations and the equilibrium of forces. Reasonable agreement was obtained when the analytical result was compared with the experimental data for a representative flexible pipe.

Goto et al (1987) presented similar solutions to that of Oliveira et al (1985) for axial, torsional, bending and crushing strength of flexible pipes. Crushing strength is the elastic deformation of the pipe when opposing pair of concentrated loads act in plane of the pipe's diameter. Feret and Bournazel (1987) extended this to evaluate the stresses and contact pressure of the different layers of flexible pipes due to axisymmetric loads. The flexible pipes were assumed to have small deformation after loads were applied, all layers remained in contact after loads were applied and that the polymer sealing layers transmitted the loads fully to the helical steel wires. Feret and Bournazel (1987) concluded that the analytical solution would be a good approximation of the behaviour of the pipe. However this would not have been the case if gaps between layers occurred after loads were applied.

McNamara and Harte (1989) presented a general computational solution of a flexible pipe structure based on the work done by previous workers (Lanteigne, 1985; Goto et al, 1987). The polymer layers were treated as orthotropic sheets while the solution for the pressure armour layer was obtained from Lanteigne (1985). The analysis also involved determining the pressure differential between layers when the internal pressure or external pressure was a known quantity.

In an extension to his previous work on the modelling of helical wire under tension and torsion, Knapp (1988) produced a computer program for the structural

model of undersea power cables. Analytical solutions from Knapp (1979) were used and the same underlying assumptions were made. The computer program can be used as a preliminary design tool for structural analysis of cables.

Witz and Tan (1992) presented the results of axial torsional structural behaviour of flexible pipes, umbilicals and marine cables. For helical wire, similar initial and final configuration of the wires to the conditions of Phillips and Costello (1973) were used. For any given number of helical wires wound together, the same expressions for axial force and bending moments were obtained. The non-linear governing equations which described the interaction of the multilayered structures were solved using the Newton-Raphson numerical method. A comparison of the experimental and theoretical results of tensile tests carried out on the marine cable and umbilical was made. A good correlation was obtained for the marine cable and the umbilical tested. The results of the axial loading and the longitudinal deformation of the flexible pipe exhibited high linearity although the analytical model was non-linear.

The effects of tension, torque and wall pressure on the different layers of the flexible pipe section were considered by McIver (1995). Analytical solutions for tension and torque were established, and the analysis took into account the temperature changes (due to service conditions) in the wire section. McIver (1995) investigated the different layers across the pipe section and tested the validity of the widely used assumption that each layer in a complex flexible pipe structure could be designed in isolation without compromising its overall pipe structural integrity. In the conclusion of his work, models that used the above simplifying assumption could be used to provide reasonably good results. However, for wear and fatigue analysis, McIver (1995) recommended that the different layers should be taken into account, as contact forces invariably emerged between layers.

McIver (1995) also pointed out the difference between tortuosity and twist of a wire. Tortuosity measures the changing direction of the binormal vector rather than measuring the wire twist. The principal normal and binormal vectors are constantly changing throughout the orientation of the wire for twisting (the normal, binormal and tangent vector directions on a wire are shown in the next

chapter). Succinctly, the normal vector measures the direction of curvature of the wire while the tangent measures the rate of change of the arc length. The binormal vector is mutually perpendicular to the normal and tangent vector. This is further explained in section 3.2.3.

The use of finite element analysis to study the cross section of a flexible pipe in general has only surfaced in the last ten years. A simple analytical model which describes the global axial deformation of flexible pipes was derived by Chen et al (1995). Frictional forces between layers were neglected and a small displacement of the pipe was assumed. Also, the internal carcass and pressure armour reinforcement were modelled as thin tubes (even though the two structures were actually helical in shape) because the helix angle was very small. Results were in agreement to experiments carried out on a typical flexible pipe. However, for detailed stress distribution of the pressure armour layer, finite element modelling was employed, as the analytical solution could not predict the localized stresses in flexible pipe layers. An axisymmetric model of the pressure armour cross-section subjected to internal pressure was presented to show good agreement between the circumferential stress of the global analytical model and the numerical results obtained from finite element modelling. Thus, it was pointed out by Chen et al (1995) that finite element analysis proved to be a good method for studying localized stresses of the pressure armour reinforcement to better understand its fatigue and wear behaviour. Much of the remaining literature on such analysis is invariably confined to the pipeline components and remains out of public domain and proprietary.

A case study on a commercial flexible pipe was performed by Witz (1996). Analytical results in the structural analysis of flexible pipes were obtained from different investigators and were compared to experimental data collected for a representative commercial pipeline cross-section. Witz (1996) mentioned that the structural analysis of a flexible pipe was not straightforward and often analyses were simplified by considering axisymmetric loading of the pipe structure only. For such axisymmetric load, uniform extension and twist were assumed. Results from the different models showed that the axial stiffness of the pipe was smaller than the one predicted from Hruska (1951) which assumed a rigid core.

Ramos et al (2000) compared analytical solution of a flexible pipe with finite element based models using the same underlying assumptions as of Witz (1996). The agreement between the analytical and finite element models was reasonable given the fact that some of the assumptions imposed in solving the analytical solution could not be directly applied to the finite element models. For instance, when modelling the analytical solution, every layer of the pipe was assumed to have the same twist and elongation. However, this restriction is applied only at the extremities of a finite element model.

A new model that could estimate the stresses and displacement in each of the flexible pipe layers and the overall flexible pipe structure under axisymmetric loads was presented by Custodio and Vaz (2002). This model took into account material non-linearity and gaps formations after loads were applied.

It should be noted that these investigations into flexible pipes take into account the global deformation only and not those due to the independent layers, while this present work attempts to present the deformation and stress distribution solution on the pressure armour reinforcement layer alone.

2.3 Fretting Fatigue

As was mentioned in the introduction to this work (chapter 1), one of the possible causes of failure in pressure armour is likely to be initiation and propagation of fatigue cracks. An understanding of the possible mechanisms of failure is critical to any design process. In the case of a pressure armour, the possibility of contact between layers, and between coils means that *fretting fatigue* is a strong candidate for the principal failure mechanism, and hence this work concentrates on this aspect.

Fretting occurs when components are subjected to oscillating forces, for example, mechanical vibrations, giving rise to relative slip over the contacting surfaces on the components. The pressure armour reinforcement of a flexible pipe is therefore a likely candidate for this type of fatigue as the pressure loads experienced by the

pressure armour reinforcement cause the contact surfaces to rub against each other, together with a substantial contact load in the normal direction.

Johnson (1985) explained the stresses and deformations involved in contacting bodies for various types of contacts. There are several types of relative movement between two bodies; these include sliding, rolling and spin. The design of the pressure armour used in flexible pipe construction will obviously affect the expected form of contact that occurs. In the case of the Omega profiled wires, for example, sliding occurs between the contacting surfaces due to movements in the axial direction of the pipe.

Another important factor for occurrence of fretting fatigue is the normal force acting on the contacting surfaces. Johnson (1985) noted that the effect of normal loads on elastic bodies was first investigated by Hertz in 1882. Hertzian contact on elastic bodies was introduced where the stress distribution of the contact area was generally assumed to be elliptical based on his observations on contact of lenses. The Hertzian theory of elastic contact can be used to calculate local stresses on contacting bodies where each body is treated as an elastic half-space. This implies that the stress distribution on the contacting bodies is not affected by the general stress distribution of the bodies which is due to their shape and the way they are supported. For this to be applicable, the contact size must be much smaller compared to the dimension of the bodies. Also, the strain produced on the contacting surfaces must be small.

Mindlin (1949) investigated the distribution of tangential load over the contact surface when the bodies in contact are subjected to small displacements. Smith and Liu (1953) investigated the stresses on elastic bodies due to tangential and normal loads. Analytical solutions presented by Smith and Liu (1953) can be used for problems involving sliding friction force or normal loads acting when cylindrical rollers are pressed against each other. It was noted by Smith and Liu (1953) that the rollers generally failed in two principal modes. Failure could either start out as a localized inelastic deformation followed by fracture or fracture due to repetition of loads on the localized crack.

The expressions for stresses beneath a circular region of contact subjected to tangential and normal loads were then derived by Hamilton and Goodman (1966). It was found that the most likely region of failure is the front edge of the contact circle. A novel study of normal loading effects in fretting on different metal alloys was presented by Goss and Hoeppner (1974). From the experimental work carried out, it was concluded that fretting damage due to normal loads imposed different life behaviour for different metal alloys which could be explained in terms of the material's microscopic variation in toughness.

More specifically, fretting fatigue experiments were carried out on carbon steel by Endo and Goto (1976). Small fatigue cracks were found to initiate very early in the life of the material and grow to be propagating cracks. Tangential loads and repeated stress were found to affect the initiation of the crack propagation. However, very little is discussed on the crack initiation stage of fretting. Hills et al (1988) proposed that a critical contact size must be reached before fretting fatigue cracks were observed to nucleate.

The crack propagation behaviour of a stainless steel under contact pressure in fretting was studied in detail by Sato and Fujii (1986). In their work, experimental investigations were carried using a stainless steel fretting pad on a flat stainless steel plate and the crack propagation rate for a number of contact pressures was measured for different crack lengths. It was explained by Sato and Fujii (1986) that in fretting fatigue, the shorter cracks propagated very rapidly in comparison to plain fatigue. The crack propagation rate then decreased with crack growth when it reached a crack length of 1 millimetre. From this point onwards, the crack propagation rate increased monotonically with crack growth which was associated with plain fatigue. It was also concluded that at very high contact pressures, the crack propagation rate in fretting fatigue decreased because of crack closure.

Contact conditions in fretting changes with the displacement amplitude. Vingsbo and Soderberg (1988) identified three different regimes in fretting by variation of tangential loads and measurement of displacement in their experimental work. A series of fretting maps was produced for a few materials and this was useful to identify whether fretting was likely to occur given the contact regimes

experienced. Nowell and Hills (1990) further reinforced that the crack initiation criteria had to be associated with the displacement amplitude and contact width as suggested by Hill et al (1988).

Waterhouse (1992) presented a review of the development of fretting fatigue mechanisms from the experimental and analytical studies of previous researchers (Mindlin, 1949; Endo and Goto, 1976; Sato and Fujii, 1986; Nowell and Hills; 1990). It was mentioned that their major development had been the measurement of the crack growth rates due to fretting fatigue. Additionally, the mechanical factors such as normal load, slip amplitude and the physical factors such as the material properties and surface finish were discussed in greater detail in order to predict the likelihood of fretting fatigue. Waterhouse (1992) emphasized the importance of tackling fretting at the design stage, whether through better design of the components or by applying the appropriate surface treatments when the problem could not be overcome by changes in design to avoid contacting interfaces.

The effect of slip amplitude to the fretting fatigue behaviour of several alloy steels was investigated by Gao et al (1991). Experiments were carried out on flat contacting surfaces of the alloy steels under axial tension. It was concluded that in the range of gross slip, the fretting fatigue decreases as slip amplitude increases. Conversely, in the stick-slip regime, where slip amplitude was in the region of micrometres, the fretting increases as slip amplitude increases. Further to this, Nakazawa et al (1994) investigated the combined effects of the slip amplitude and the contact pressure on high strength steels. The relationship of the fretting fatigue life due to the contact pressure on the fretting specimens for a range of slip amplitudes was established. In their work, the minimum life of the specimens was taken in terms of localized stress concentration at the fretted area.

More recently, Nakazawa et al (2003) studied the effect of the contact pressure on the fretting fatigue behaviour of austenitic stainless steel. The experiments performed by Nakazawa et al (2003) considered the effect of the contact pressure using a bridge-type flat fretting pad on flat specimens of the same material. Bridge-type pads have contacting pads which are flat, therefore forming complete

contact with the surface of the specimen (a complete contact is resulted when the size of the contact is independent of the normal load applied). This result was compared to another set of fretting fatigue test using the same type of specimens and conditions, however this time, together with the introduction of plain fatigue for a number of cycles prior to the fretting tests.

In was concluded by Nakazawa et al (2003) that an increase in contact pressure decreased the fretting fatigue life rapidly. This observation was attributed to the concavity form at the fretted area during the high contact pressure tests due to contact with the fretting pad. Introduction of plain fatigue to the specimen before a fretting fatigue test at high contact pressures resulted in an increase in the fretting life since the concavity formed was thought to be suppressed by the cyclic strain hardening of the material. Conversely, no apparent effect on fretting was observed for low contact pressure when the specimen was subjected to plain fatigue initially.

Much of the above work has been applied to controlled laboratory conditions and in order to transfer the knowledge obtained in practical applications, such as the offshore case of flexible pipe pressure armour, a link needs to be generated between the lab based fretting behaviour, the forces and contact zones that are likely to be generated in pressure armour systems. Whilst much of the present work has been aimed at understanding the way in which pressure armour behaves (and hence interacts with itself), problems remain with transferring fretting data over to real life scenarios. Chief among these is actually determining the levels of loads and the actual contact area involved. Work undertaken by Liu et al (2001) highlighted this problem, and presented a novel numerical method simulation technique to analyze the contact loads in sliding wear. They also confirmed that the pre-test surface finish of the specimens (which has implications for machining and manufacturing processes) had a significant effect on the contact behaviour.

From the review of the literature, it is difficult enough to characterize the fretting fatigue failure mechanism, on contacting surfaces, in terms of the displacement amplitude, tangential or normal loads, let alone factor in the different behaviour of various materials and the size of contact area. For different components and

materials, the fretting characteristics are totally different. Szolwinski and Farris (1996) provided a good review into the work on the mechanics of fretting. Their work noted that the models so far had their shortfalls and none could suggest a specific method in predicting the life because of the complexity involved. In addition, an analytical model which could predict fretting fatigue crack nucleation was presented by Szolwinski and Farris (1996).

Fellows et al (1997) characterized the initiation of fretting using shear stress amplitude. It was claimed that a critical shear stress amplitude must be exceeded before fretting occurred. However, it was acknowledged that it was very difficult to quantify initiation life of a fretting crack from experimental methods.

A review of the experimental methods used to carry out fretting fatigue tests was presented by Lindley (1997). In his study, the preferred type of specimen and contact pad geometries for fretting experiments was identified. Well defined stress fields were necessary to study the effect of fretting. Therefore fretting pads which were cylindrical in nature, in contact with flat plate specimen were desired compared to flat fretting pads because of the difficulty in defining stick-slip zones in such geometries and also the stress singularity that would be present at the flat fretting pad corner. Comparisons of the fatigue strength of various engineering alloys were presented by Lindley (1997) for cases of specimens with and without fretting. Additionally, Lindley (1997) compared the fretting strength data for a range of contact pressures and contact width. The various analytical approaches for quantifying the crack growth were also examined.

Fretting fatigue should not be confused with plain fatigue as discussed in Moobola et al (1998). Surface displacement of the contacting bodies encourages initiation of a crack in fretting fatigue while in plain fatigue, cracks can initiate from small defects or imperfections on the surface of the material. In fretting fatigue, unlike plain fatigue, as the crack moves away from the contact, the tip experiences a decreasing stress field (unless there are superimposed tensile loads), hence the crack growth rate may slow down and then be impeded. Conversely, for the particular case of pressure armour, there are often combined loading scenarios where normal loads and cyclical movement can be augmented with static tensile

or dynamic loading of components. Hence there is a possibility that cracks initiated purely by fretting mechanisms could rapidly enter tensile stress fields and/or propagate by conventional fatigue mechanism. Therefore, fatigue is comprised of two distinct phases, initiation and propagation. Fretting fatigue has an important effect on the initiation of the crack but has very little influence on the propagation stage of the crack (Moobola et al, 1998).

Since fretting can lead to premature failure of mechanical components, methods to mitigate the effect of fretting should be employed. Waterhouse (1992) suggested surface treatments should be encouraged in situations where contact of components cannot be avoided. The effect of *palliatives* to the fretting fatigue mechanism was investigated by Zhou and Vincent (1999). Generally, palliatives fall into one of these three categories: -

1) reducing the relative slip
2) raising the strength by changing the base material
3) lower the coefficient of friction between the contacting surfaces

However, these palliative methods can interact with each other, for example lubricants, which could allow relative slip but at the same time lower the coefficient of friction of the contacting surfaces. Zhou and Vincent (1999) investigated the influence of various lubricant types on fretting. The result indicated that the palliative effect of lubricants on fretting should be characterized using slip amplitude regimes.

The investigation into the effects of fretting fatigue so far has been limited to mechanical components such as bearings and gears. The possibility of fretting fatigue occurring in pressure armour reinforcements has only been mentioned recently. Saevik and Berge (1995) carried out experimental tests on flexible pipes with multiple layers of tensile armours. The pipes were subjected to axial, internal pressure and bending loads. The fatigue failure of the tensile armours was found to be due to fretting mechanisms. An analytical model to characterize this fretting failure of the tensile armours was established by Saevik and Berge (1995). Additionally, Saevik and Berge (1995) identified the likely sites of fretting failure on the tensile armours based on their experimental work and analytical model.

Burke and Witz (1999) addressed the issue of fretting fatigue of flexible pipe pressure armour due to high pressure loading. Generally, the structural performance of the pressure armour is determined by considering the wires of the pressure armour as a continuous helix. In high pressure dynamic service, fretting fatigue in pressure armour was thought to be influenced by factors such as normal and tangential loads and also the coefficient of friction of the contacting surfaces (Burke and Witz, 1999). They explained that since the contact was non-conformal (that is the contacting surfaces have different profiles), the contact condition was similar to that of a cylinder-on-flat plate for a 'Z' profiled wire. Contact points where stress concentrations existed because of geometric discontinuity was thought to be the critical points of potential fretting fatigue. It was proposed that the fretting crack would initiate at the 'cylinder' part of the contact as opposed to conventional studies where the stress distribution was thought to concentrate on the surface of the flat plate (Burke and Witz, 1999). This is because the pressure armour layer effectively experienced the same dynamic stress across the profile. Another important point to note was that the manufacturing and assembly process leaves the component with residual stresses that may affect the fretting response as well.

In summary to this section, chapter 7 provides a further insight into the particular aspects of fretting fatigue relevant to the case of pressure armour and discusses issues of design that can possibly improve the service lifetimes.

3 Helical Spring Theory and Analysis

3.1 Introduction

This chapter concentrates on the development of analytical solutions that help describe the behaviour of the pressure armour layer of the type found within riser structures. It begins with the fundamental consideration of helical armour layers, making the assumption that they behave, to the first approximation as helically wound tension/compression springs. This approximation is fair, given that many designs of pressure armour are simple helices, and those that are overlapping or even interlocked helices are likely to (at least initially) behave as helical springs. The possibility that this approach can in turn be used to explain the response of the pressure armour layer to different loading conditions is attractive as it offers a simplified route to understanding the fundamentals of the behaviour of the pressure armour layer whilst providing good opportunities for experimental verification.

This chapter describes the development of the analytical solution for the simple case of circular cross-section helical springs based on three different approaches, basic theory provided by Wahl (1963), the energy approach by Knapp (1979) and the other from slender rod theory by Love (1934) and this approach has been extended further for wire rope and cable analyses. It will be shown later that the slender rod theory provides the option to investigate more complex cross-sectional shapes under the different loading conditions. Where possible, the results of these methods are compared with each other and also with the finite element analysis in chapters 3 and 4. The approach here has been to review the existing literature, present an understanding of the major factors in helical spring mechanics and then attempt to modify some of the analysis to fulfil some of the needs of this work.

The early investigation into the mechanics of springs was carried out by Thomson and Tait (1889). The curvature and tortuosity of a helix was defined and this study formed the basis of the work of Love (1934) and Wittrick (1966). Subsequently, aspects of spring theory have been developed for specific components such as

wire ropes as is evident in the works of Phillips and Costello (1973), Phillips and Costello (1979), Lin and Pisano (1988) and Costello (1990).

The equilibrium equation used by Love (1934) for solving the forces and moments in slender rods has been used by Phillips and Costello (1973) to derive the contact forces in wire ropes which has multiple wires wound together in a helical manner. If the number of wires are reduced to just a single wire, the contact force no longer exists and the analytical solution reduces to the force and moment equation acting on a simple helical spring based on the works of Blanco and Costello (1974) and Tan (2002). The mechanics of a simple spring based on slender rod theory will be further discussed in section 3.2.3. The following sections introduce the theory of helical spring mechanics for circular cross-section spring starting with Wahl (1963).

3.2 Mechanics of Helical Springs – Circular Cross-section

3.2.1 Basic Helical Spring Equations

Wahl (1963) defined a spring as an elastic body which deflects under an applied load and recovers its original shape when the load is removed. The basic equations of the helical spring provide the parameters for the author's study of the mechanics of the pressure armour reinforcement. For example, the deflection and stiffness equations will provide the necessary understanding on how much the pressure armour reinforcement displaces under an applied load and also how this displacement is affected by the stiffness of the helical structure.

Timoshenko (1955, 1956) produced a simple derivation for the shear stress and in turn the deflection of circular cross-section helical spring. Shear stress of the coil cross–section here is caused by a twisting couple on the coil. These equations were comprehensively presented in Reiner (1960) and Wahl (1963). The shear stress of helical spring loaded in the axial direction of the spring was assumed to behave similarly to a straight bar in pure torsion. This implied that the axial load

applied onto the spring is resisted by a transverse shear force together with torque acting on the cross section of the spring. Each element of the pitch, which is one complete turn of a helix, is thus subjected to a torque about the centreline of the spring, T_r, shown in figure 3.1, which is given by

$$Torque, T_r = F_A R \tag{3.1}$$

where F_A = axial load

R = radius of helical spring

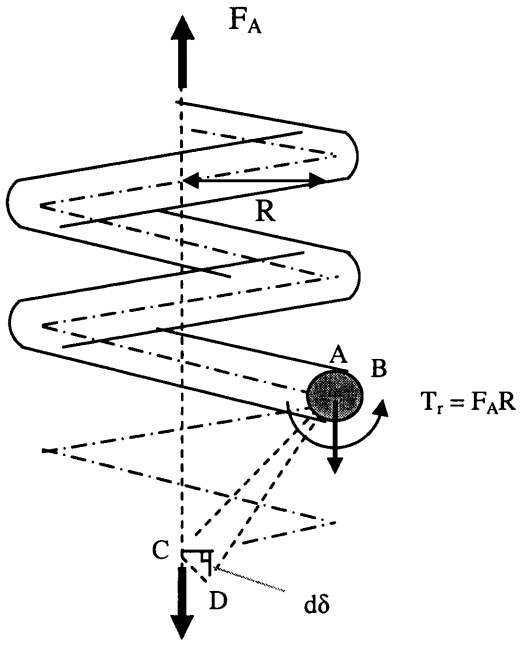

Figure 3.1 Helical spring under axial load

The extension of the spring is mainly due to the twisting effect of the helical spring under the torque, T_r as described by Reiner (1960). Although the shear stress can be an important parameter in determining the deflection of a spring, usually only the effects of torsion of the spring are taken into account when defining the deflection equation as explained by Timoshenko (1955). This was essentially done to simplify the analysis and also done in part due to the fact that if

the helical spring in consideration is of large spring index (defined in equation 3.2), the maximum shearing stress will be one caused by torsion.

The helical spring index, c is defined as

$$c = \frac{D}{d} = \frac{R}{r} \tag{3.2}$$

where d = diameter of helical wire

r = radius of helical wire

Now, consider point B, which is fixed and point C at the end of the spring as shown in figure 3.1. When an axial load is applied, all the elements below point A of the spring would have rotated, fixed relative to point A. Thus, point C would now have moved to point D. The complete deflection of the spring is obtained by summing up the extension, dδ (which was deduced by similarity of triangles), due to the twisting of the elements along the length of the spring. Hence, the deflection, δ of a helical spring considering the effects of torsion only, is presented by Wahl (1963) based on Timoshenko's derivation as

$$\delta = \frac{4F_A R^3 n}{Gr^4} \tag{3.3}$$

where G = modulus of rigidity of helical wire

n = number of pitch in helical spring

From here on, the analytical solutions presented here will be expressed in terms of the radius of helical spring since the subsequent analyses is derived in terms of the helical spring radius. Ancker and Goodier (1958) derived another expression for the deflection, δ of a helical spring taking into account the curvature effects of the beam.

This corrected deflection equation by Ancker and Goodier (1958) is given in terms of the helical spring radius, as: -

$$\delta = \frac{4\psi F_A R^3 n}{Gr^4} \tag{3.4}$$

$$where\ \psi = 1 - \frac{3}{16}\left(\frac{r}{R}\right)^2 + \frac{3+\nu}{2(1+\nu)}\tan^2\alpha$$

ν = Poisson's ratio

α = helix angle

Solution in equation 3.3 by Wahl (1963) differs with equation 3.4 by a factor ψ which involves the material Poisson's ratio, helical spring index parameter and its helical angle. For example, if the spring index is large and equal to 25 while the helical angle is about 10 degrees and given Poisson's ratio of 0.33 for steel, equation 3.4 gives a deflection value which is about 4% larger than Wahl (1963). Deviation in the two solutions gets progressively larger if the helical angle is of large value. Therefore basic spring solution by Wahl (1963) is used when the spring does not undergo large changes in its dimensions, for example its helix angle and spring radius, which meant that the spring was initially closed coil as well. Additionally, this solution only takes into account the stress due to the torsional moment but not the stress due to axial force as it is negligible unless a spring of small spring index was used.

The deflection experienced by a helical spring varies linearly with the applied load. This is true given the system behaves in a linear elastic manner for small displacements and as long as the elastic limit is not exceeded as stated in Hooke's law. Therefore

$$F_A = k\delta \tag{3.5}$$

where k = spring stiffness

δ = deflection of the helical spring

The spring stiffness, k is then a measure of the force required to produce a unit deflection. It should be noted that Hooke's law is only an approximation. Even if the elastic limit of the spring is not exceeded, a spring stretched to the state of being uncoiled or straightened has a larger spring constant than that is predicted using Hooke's law.

Based on the solution by Wahl (1963), it can be shown that from equations 3.3 and 3.5,

$$k = \frac{F_A}{\delta}$$

$$= \frac{Gr^4}{4R^3 n} \tag{3.6}$$

and from the solution based on Ancker and Goodier (1958) in equation 3.4, the spring stiffness gives

$$k = \frac{Gr^4}{4\psi R^3 n} \tag{3.7}$$

Although Ancker and Goodier (1958) took the curvature effect into consideration and provided a more accurate result, the solution from Wahl (1963) is still widely used for calculation because it is less laborious compared to the former (the helical angle of the spring needs to be known and is not easily measured) and still gives a very good approximation of the load-deflection of the spring.

The load-deflection solution by Wahl (1963) is valid for fairly large helical spring deflections, but ignores changes in its spring diameter and helical angle, therefore is only valid for closed coil springs. The limitation of this solution is discussed in the results section of this chapter. The following section provides the axial load and twisting moment of a helical spring solution from the principle energy method, which is useful for analyses involving small strains. In addition, these solutions are particularly practical for wire ropes and cables analyses as well. It is

important to note that the axial loading solution from the energy approach is defined in terms of the spring helical angle and wire strain, which can readily be plotted on a load-deflection curve for comparison with basic spring theory.

3.2.2 Helical Spring Theory Based on Energy Method

The energy method principle first introduced by Castigliano, states that the system is in equilibrium when the potential energy has a stationary value for small displacements. Although the method has been used extensively to solve beam deflection equations, this approach can be used to obtain a load-deflection solution for helical springs. The method was first used to solve for the axial and torsional loads for cables rather than helical springs by Knapp (1979) and investigated for combined axial and bending loads by Lanteigne (1985). Cables in question here refer to those with helical wire constituents wrapping around a central core.

Similarly, when the central core of the cable is removed and the solution is treated for a single wire, the expression reduces to the form which can be used to solve for helical springs. This work here illustrates the derivation of the energy method for the case of a helical spring which was first presented for a cable in Knapp (1979) and Lanteigne (1985). Certain modifications which were applicable to the helical spring and more latterly pressure armour were included and are defined in this section.

The geometry of the helical spring is shown in figure 3.2. A reference spring cylinder is used to define the helical spring radius. The pitch of spring is denoted as p while R is the helical spring radius.

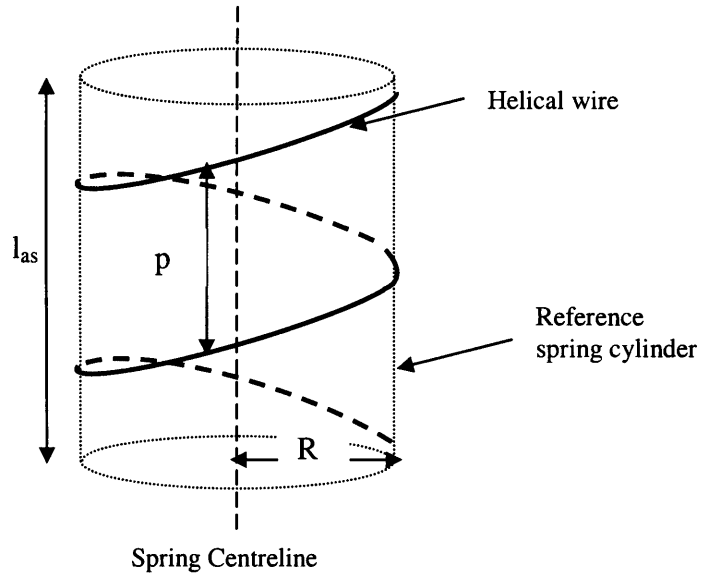

Figure 3.2 Helical spring geometry

Axial strain of a spring, ε_{as} is given by

$$\varepsilon_{as} = \frac{\delta}{l_{as}} \tag{3.8}$$

where δ = deflection of spring

l_{as} = length of spring

p = pitch length

R = radius of helical spring

When a helical spring is deformed axially, either in tension or compression, the helical spring changes its dimension in terms of its length, helix radius and thus its helical angle. Also, if the helical spring is not fixed at the ends, coiling or uncoiling of the spring occurs.

For pure radial deformation (twisting moment of wire not taken into consideration), this radial strain is defined as

$$\varepsilon_r = \frac{R_1 - R}{R}$$

$$= \frac{\Delta R}{R} \tag{3.9}$$

where ε_r = radial strain

R_1 = final radius of helical spring

ΔR = change in helical spring radius

From geometric considerations, the relationship between change in radius, length of spring, length of wire and its twisting angle can be derived and is shown in the figure 3.3. This illustration depicts the deformation parameters of the helical wire for one pitch length. The helix angle, α is defined as the angle the helical wire makes with the axis perpendicular to the helical spring centreline. The helix angle, α and the lay angle, β of a helical spring is complementary. Therefore,

$$\alpha + \beta = \frac{\pi}{2} \tag{3.10}$$

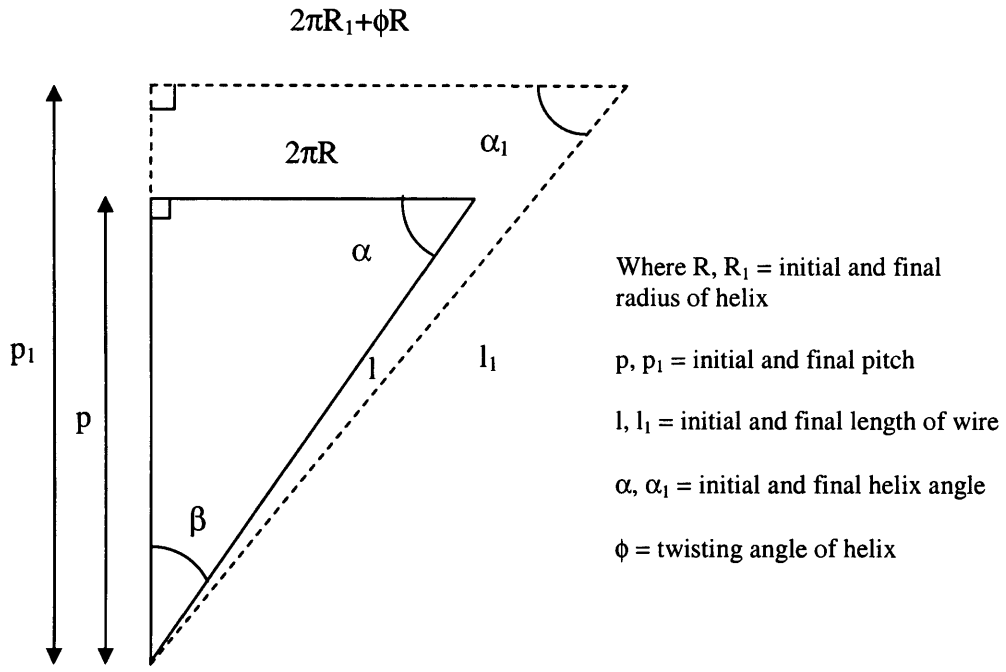

Figure 3.3 Geometrical relationship of initial and final helical wire configuration

The twisting angle of helix, ϕ is the helical spring rotation when deformed under load. An illustration of the twisting angle of spring is shown in figure 3.4 below.

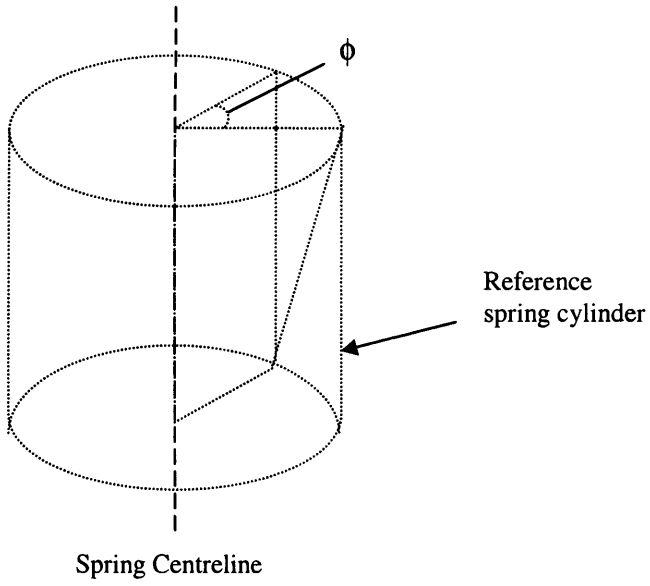

Figure 3.4 Twisting angle of helical spring

From figure 3.3, the spring axial strain, ε_{as} is given as

$$\varepsilon_{as} = \frac{p_1 - p}{p}$$

$$p_1 = p(\varepsilon_{as} + 1) \tag{3.11}$$

The axial strain of wire, ε_{aw} is given as

$$\varepsilon_{aw} = \frac{l_1 - l}{l}$$

$$l_1 = l(\varepsilon_{aw} + 1) \tag{3.12}$$

and the relationship of the initial and final helix angles in terms of its spring geometry is given respectively in equation 3.13 and 3.14.

$$\sin\alpha = \frac{p}{l} \tag{3.13}$$

$$\sin\alpha_1 = \frac{p_1}{l_1} \tag{3.14}$$

It follows that from equation 3.11 – 3.14, the deformed helix angle can be expressed in terms of the strain components and is given by

$$\sin\alpha_1 = \sin\alpha \frac{(\varepsilon_{as} + 1)}{(\varepsilon_{aw} + 1)} \tag{3.15}$$

Equation 3.15 is rearranged to give

$$(\varepsilon_{aw} + 1)\sin\alpha_1 = \sin\alpha(\varepsilon_{as} + 1) \tag{3.16}$$

The helix angle can also be expressed in terms of the change in helical spring radius and twisting angle. From figure 3.3, this is given by

$$\tan\alpha_1 = \frac{p_1}{2\pi R_1 + \phi R}$$

$$= \frac{p(\varepsilon_{as}+1)}{2\pi R_1 + \phi R}$$

$$= \frac{\tan\alpha(\varepsilon_{as}+1)}{\frac{R_1}{R} + \frac{\phi}{2\pi}} \tag{3.17}$$

From the wire axial strain in equation 3.12 and using relationships in 3.13 and 3.14, it can be shown that

$$\varepsilon_{aw} + 1 = \frac{\sin\alpha}{p} l_1 \tag{3.18}$$

which leads to

$$(\varepsilon_{aw}+1)^2 = \sin^2\alpha\left[\left(1+\frac{\Delta p}{p}\right)^2 + \left(\frac{1}{\tan\alpha}(1+\varepsilon_r) + \frac{R\phi}{p}\right)^2\right] \tag{3.19}$$

where Δp = change in pitch length

Equation 3.19 now takes into account the effects of radial deformation of helical spring. In the work of Lanteigne (1985), the radial deformation of helical constituent wires of the cable is ignored since the wires are assumed to touch the core and are not allowed to compress the core when a tension load is applied. It is also worth mentioning that the deformed helical spring geometry in figure 3.3 differs slightly from the one in Knapp (1979), hence it is important to show the full derivation of equation 3.19 which can be found in Appendix A. Now, the strain equation can be linearized, ignoring second order strain quantities.

Therefore,

$$\varepsilon_{aw} = \sin^2\alpha\left(\frac{\Delta p}{p}\right) + R_1 \sin\alpha\cos\alpha\left(\frac{\phi}{p}\right) \tag{3.20}$$

Equilibrium is achieved when the sum of its internal strain energy and the potential energy of applied external forces are equal to zero. This is due to the theory of stationary potential energy given by Knapp (1979) as

$$\delta U + \delta V = 0 \tag{3.21}$$

where δU = variation in internal strain energy

δV = variation in external potential forces

Accordingly, for a linear elastic material, the variation in the internal strain energy is given by Lanteigne (1985) as

$$\delta U = E\iiint_{dv} \varepsilon_{aw}\,\delta\varepsilon_{aw}\,dv \tag{3.22}$$

where $\delta\varepsilon_{aw}$ = element volume of wire

dv = variation in axial strain of wire

E = Young's modulus

The solution is solved for the axial loading mode since this is the only loading scenario that is needed. Full integration is shown in Appendix A. Succinctly,

$$\delta U = AE\left[\sin^3\alpha(\Delta p) + R_1\sin^2\alpha\cos\alpha(\phi)\right]\delta\left(\frac{\Delta p}{p}\right) \tag{3.23}$$

The variation in internal strain energy is created by a variation in the potential of external forces, giving rise to the form shown below as presented in Lanteigne (1985).

$$\delta V = F_A \delta(\Delta p) + M\delta(\phi) \tag{3.24}$$

where F_A = external force

M = applied moment

In matrix form, equations 3.23 and 3.24 lead to the following:-

$$\begin{bmatrix} F_A \\ M \end{bmatrix} = \begin{bmatrix} k_{11} & k_{12} \\ k_{21} & k_{22} \end{bmatrix} \begin{bmatrix} \dfrac{\Delta p}{p} \\ \dfrac{\phi}{p} \end{bmatrix} \tag{3.25}$$

where k_{11}, k_{12}, k_{21}, k_{22} = stiffness coefficients

The stiffness coefficients are of 2x2 matrix. To obtain the axial loading solution, the stiffness coefficients k_{11} and k_{12} can be determined from equation 3.23 and 3.25.

$$k_{11} = AE\sin^3\alpha$$

$$k_{22} = AER_1\sin^2\alpha\cos\alpha \tag{3.26}$$

Therefore from stiffness coefficients determined above, the applied axial load on a helical spring is given as the from below based on the author's geometric deformation of a helical spring illustrated in figure 3.3.

$$F_A = AE\sin^3\alpha\left(\frac{\Delta p}{p}\right) + AER_1\sin^2\alpha\cos\alpha\left(\frac{\phi}{p}\right) \tag{3.27}$$

The solution above is expressed in terms of its deflection and twist angle per unit length of the helical spring. For small deformation, the twist angle term can be

ignored for simplicity of calculation. Also, taking into account the fact that a pressure armour is constrained at its ends, this will prevent twisting of the helical structure.

If all the deformation terms are taken into account, the applied axial force on the spring from equation 3.27 using the relationship from equation 3.20 reduces to

$$F_A = AE\sin\alpha\left[\left(\sin^2\alpha\left(\frac{\Delta p}{p}\right)+R_1\sin\alpha\cos\alpha\left(\frac{\phi}{p}\right)\right)\right]$$

$$= AE\varepsilon_{aw}\sin\alpha \tag{3.28}$$

From here, it can be observed that the solution from the energy method reduces to the same form as that of Hruska (1953) and Machida and Durelli (1973) for the case of pure axial loading, when the cables concerned are assumed to have a rigid core. The rigid core assumption means that the radial deformation of a helical spring does not need to be taken into consideration, implying that the deformation of the helical spring is assumed to be small and is thus given in Machida and Durelli (1973) by

$$F_A = AE\sin\alpha\left[\left(\sin^2\alpha\left(\frac{\Delta p}{p}\right)+R\sin\alpha\cos\alpha\left(\frac{\phi}{p}\right)\right)\right] \tag{3.29}$$

The basic spring theory presented by Wahl (1963) and the energy method provide the necessary means to measure the deflection of a spring under axial force. However, it does not account for the localized behaviour of the cross-section of the spring. This is important in view that a pressure armour reinforcement cross-section can twist along its rod centreline and therefore affect its overall behaviour under load. In view of this, the axial force and twisting moment equations of a helical spring derived from the slender rod theory is presented in the next section. Although the slender rod theory is more complicated compared to the basic spring theory, the analytical solution can be adapted to account for the behaviour of the cross-section of the helical wire.

3.2.3 Helical Spring Based on Slender Rod Theory – Circular cross-section

The slender rod theory was presented in Love (1934) which considered the forces and moments on a thin rod. A thin rod is defined as one whose cross-sectional dimension is small compared to its length. This theory can be used to solve for rods in a helical configuration. Particularly, the curved rod in the deformed and undeformed state possesses both curvature and tortuosity and is related to the equilibrium equation of a helical spring by the applied forces and moments in three principal directions that hold the rod in its final configuration. The rod cross-section is constrained to remain plane before and after deformation and normal to its centreline. Also, the analysis here is for small helical wire strain, although large deflections of the spring are permitted. The equilibrium equation will be presented below starting with the description of a rod in terms of a space curve and assumption that the centroid of the cross-section of the rod coincides with its wire centreline.

The points along the centreline of a rod can be described using a position vector as shown in figure 3.5. This is identified as

$$\boldsymbol{r} = \boldsymbol{r}(S,t) \tag{3.30}$$

where **r** = position vector

S = arc length along centreline in initial configuration

t = time

The initial state is taken when t = 0 and is taken as the undeformed reference state.

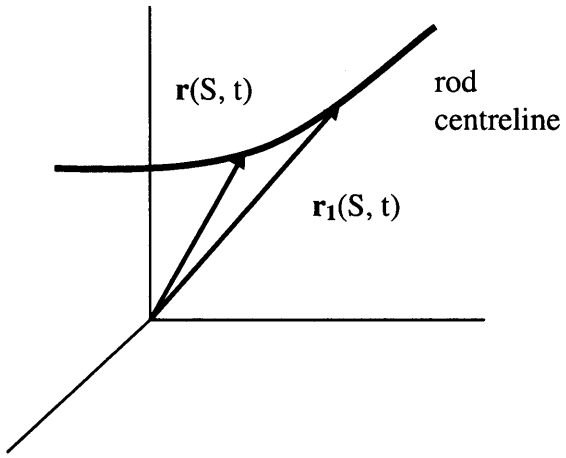

Figure 3.5 Position vector of a rod centreline

Right-handed orthogonal base vectors can be used to describe the deformed state as one that moves along the curve, in which

$$a_i = a_i(S,t) \tag{3.31}$$

where a_i = base vector in the orthonormal set in which a_3 coincides with the tangent of the centreline. Therefore

$$a_3 = \frac{\partial r}{\partial s} \tag{3.32}$$

where s = current arc length which will vary as load is applied

Vectors that are mutually perpendicular to each other are known as orthogonal vectors. Orthonormal refers to unit vectors that are orthogonal. In this instance, there are three vectors direction that are mutually perpendicular, namely the normal, binormal and tangent vector. Figure 3.6 illustrates the direction of these vectors on a helical strip.

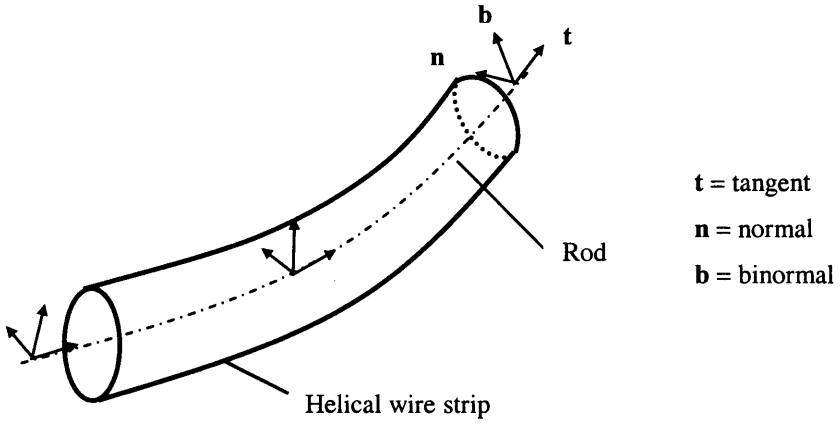

Figure 3.6 Relationship between the normal, binormal and tangent vector directions

Referring to the figure above, the normal vector gives the direction in which the centreline of the helical rod is turning. The tangent vector acts along a line which touches the centreline at a single point as the curve is turning. The binormal vector completes the right handed orthonormal triplet.

In terms of the arc length of the wire from figure 3.3,

$$ds = dS\left(\varepsilon_{aw} + 1\right)$$

$$\frac{ds}{dS} = \varepsilon_{aw} + 1 \tag{3.33}$$

Vectors $\mathbf{a_1}$ and $\mathbf{a_2}$ then correspond to the rotation of the cross-section. It is deduced later that the direction 1 and 2 corresponds to the normal and binormal direction of the cross-section of the rod.

If the vectors are orthonormal, they satisfy the condition that

$$\boldsymbol{a}_i \cdot \boldsymbol{a}_j = \delta_{ij} \tag{3.34}$$

where δ_{ij} = Kronecker delta function, in which a set of nine quantities occur and can take suffixes of value between 1 and 3

Differentiation of the base vectors with respect to S gives

$$\frac{\partial \boldsymbol{a}_i}{\partial S} = \kappa_{ij}\boldsymbol{a}_j \tag{3.35}$$

where κ_{ij} = curvature matrix elements which defines curvature and tortuosity of rod

From Ramsey (1988), it can be deduced that κ_{ij} is a skew symmetric matrix when equation 3.34 is differentiated with respect to S and then substituted into expression 3.35. A skew symmetric matrix is a square matrix where the transpose equals the minus of the matrix. For example, if the value of matrix element, κ_{21} is the negative value of element κ_{21} and transpose of all other corresponding elements behave in the same way, then the matrix is said to be skew symmetric. Depending on the relevant values of i and j, κ_{ij} gives rise to the curvature or tortuosity of the curved rod.

Tortuosity must not be confused with twist of the cross-section. This will be explained when Love's equilibrium equation is described in the following paragraphs. This confusion rendered mistakes in the solution produced by Costello et al and was pointed out by Ramsey (1988) and McIver (1995). However, since all the cited references so far have dealt only with circular cross-section wires, it does not make a difference to the results obtained as the curvature and tortuosity remain the same. For non circular cross-section wires such as those used in pressure armour reinforcements, this aspect is important and will be described in chapter 4.

The initial value of κ_{ij} in the undeformed initial configuration is denoted by K_{ij}. Since it is a skew symmetric matrix as described in Ramsey (1988), it can be shown that

$$e_{ijk}\omega_k = \kappa_{ij} - K_{ij} \tag{3.36}$$

where e_{ijk} = alternating symbol in which i, j, and k can take the values 1,2 or 3

ω_k = bending or twisting strain

Therefore, $\kappa_{ij} - K_{ij}$ measures the bending or twist of the rod.

In a curved rod, points along the centreline of the rod can also be described using the widely used Serret – Frenet set of equations which have been presented in Ramsey (1988) and McIver (1995). This is given by

$$\frac{d}{ds}\begin{bmatrix} \boldsymbol{t} \\ \boldsymbol{n} \\ \boldsymbol{b} \end{bmatrix} = \begin{pmatrix} 0 & \kappa & 0 \\ -\kappa & 0 & \tau \\ 0 & -\tau & 0 \end{pmatrix} \begin{bmatrix} \boldsymbol{t} \\ \boldsymbol{n} \\ \boldsymbol{b} \end{bmatrix} \tag{3.37}$$

where d/ds represents the change in parameter with respect to current arc length

t = tangent

n = principal normal

b = binormal

κ and τ are the generalized curvatures and tortuosity respectively

When the base vectors defined earlier is used in equation 3.37 to coincide with the three orthogonal vectors, in the initial configuration, it can be shown that

$$K_{ij} = \begin{pmatrix} 0 & \tau_0 & -\kappa_{b0} \\ -\tau_0 & 0 & 0 \\ \kappa_{b0} & 0 & 0 \end{pmatrix} \tag{3.38}$$

where κ_{b0} = initial curvature in binormal direction

τ_0 = initial tortuosity

Equation 3.36 is substituted into equation 3.38 to give

$$\kappa_{ij} = \begin{pmatrix} 0 & (\tau_0 + \omega_3) & -(\kappa_{b0} + \omega_2) \\ -(\tau_0 + \omega_3) & 0 & \omega_1 \\ (\kappa_{b0} + \omega_2) & -\omega_1 & 0 \end{pmatrix} \tag{3.39}$$

where ω_1 = bending strain in normal direction

ω_2 = bending strain in binormal direction

ω_3 = twisting strain of cross-section

The initial and final curvature and tortuosity of a helical wire can now be defined based on the configuration given in figure 3.7 below.

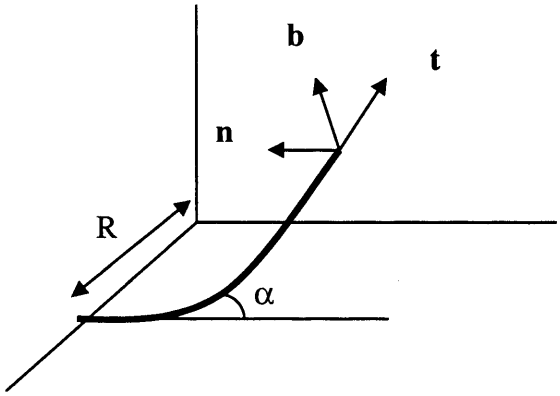

Figure 3.7 Helical wire orientation

Initial configuration of a helical wire as presented in Phillips and Costello (1973) give

$$\kappa_{n0} = 0 \tag{3.40}$$

$$\kappa_{b0} = \frac{\cos^2 \alpha}{R} \tag{3.41}$$

$$\tau_0 = \frac{\sin \alpha \cos \alpha}{R} \tag{3.42}$$

where κ_{n0} = initial curvature in normal direction

κ_{b0} = initial curvature in binormal direction

τ_0 = initial tortuosity

R = initial radius of helical spring

α = initial helix angle

After loads are applied to the structure, it is assumed that the helical wire remains a helix in shape. The deformation causes the helical wire to take a final configuration as

$$\kappa_{n1} = 0 \tag{3.43}$$

$$\kappa_{b1} = \frac{\cos^2 \alpha_1}{R_1} \tag{3.44}$$

$$\tau_1 = \frac{\sin \alpha_1 \cos \alpha_1}{R_1} \tag{3.45}$$

where κ_{n1} = final curvature in normal direction

κ_{b1} = final curvature in binormal direction

τ_1 = final tortuosity

R_1 = final radius of helix

α_1 = final helix angle

The equilibrium equation of slender rod is given by Love (1934) as components of forces and moments on the wire cross-section. This method was used extensively by Phillips and Costello (1973) in their work for wire ropes, which as described in the literature review, consists of multiple helical wires wound together. The solution obtained by Phillips and Costello (1973) is reduced to that of a single wire to get analytical solution required for a helical spring. As the analysis involves only a singular wire, contact forces which arises due to multiple wires considered in previous work is no longer valid.

Slender rod equation by Love (1934) gives

$$\frac{dN}{ds} - N_b \tau + T \kappa_b + X = 0 \tag{3.46}$$

$$\frac{dN_b}{ds} - T \kappa_n + N \tau + Y = 0 \tag{3.47}$$

$$\frac{dN_b}{ds} - T \kappa_n + N \tau + Y = 0 \tag{3.48}$$

$$\frac{dG_n}{ds} - G_b\tau + H\kappa_b - N_b + K_n = 0 \tag{3.49}$$

$$\frac{dG_b}{ds} - H\kappa_n + G_n\tau + N + K_b = 0 \tag{3.50}$$

$$\frac{dH}{ds} - G_n\kappa_b + G_b\kappa_n + \Theta = 0 \tag{3.51}$$

where s = arc length

X, Y, Z = components of external force

K_n, K_b, θ = components of external moments

N, N_b, T = resultant internal forces

G_n, G_b, H = resultant internal moments

Earlier, it was shown that the tangent to the centreline, **t** is coincident with vector $\mathbf{a}_3$ and from expressions 3.33, 3.35 and 3.37, it follows that from substitution,

$$\frac{d\boldsymbol{t}}{ds} = \kappa\boldsymbol{n} = \left(1 - \varepsilon_{aw}\right)\kappa_{3j}\boldsymbol{a}_j \tag{3.52}$$

When the bending and twisting strains are taken to be small, the equations can be linearized, that is to ignore product of strains. This is done to simplify the corresponding analysis since small wire strain was considered. Further to this, when equation 3.52 is used in conjunction with expression 3.39, it can be shown by Ramsey (1988),

$$\kappa\boldsymbol{n} = \left(\kappa_{b0} - \kappa_{b0}\varepsilon_{aw} + \omega_2\right)\boldsymbol{a}_1 - \omega_1\boldsymbol{a}_2 \tag{3.53}$$

Describing equation 3.53 in terms of the curvature and the principal normal gives

$$\kappa = \left(\kappa_{b0} - \kappa_{b0}\varepsilon_{aw} + \omega_2\right) \tag{3.54}$$

$$\boldsymbol{n} = \boldsymbol{a}_1 - \frac{1}{\kappa_{b0}}\omega_1\boldsymbol{a}_2 \tag{3.55}$$

Similarly, now to derive the expression for the twisting strain, equations 3.33, 3.35, 3.37 are used together with 3.55. This gives

$$-\kappa \boldsymbol{t} + \tau \boldsymbol{b} = \frac{d\boldsymbol{n}}{ds} = (1 - \varepsilon_{aw})\kappa_{1j}\boldsymbol{a}_j - \frac{1}{\kappa_{b0}}\frac{d\omega_1}{dS}\boldsymbol{a}_2 - \frac{1}{\kappa_{b0}}\omega_1\kappa_{2j}\boldsymbol{a}_j \tag{3.56}$$

When 3.37 and 3.54 are used, it follows that

$$\tau \boldsymbol{b} = \frac{1}{\kappa_{b0}}\tau_0\omega_1\boldsymbol{a}_1 + \left(\tau_0 - \tau_0\varepsilon_{aw} + \omega_3 - \frac{1}{\kappa_{b0}}\frac{d\omega_1}{dS}\right)\boldsymbol{a}_2 \tag{3.57}$$

Finally, ignoring all products of the different strains due to assumption of small strains, the twisting strain, ω_3 as described in Ramsey (1988) is of the form shown below.

$$\tau = \left(\tau_0 - \tau_0\varepsilon_{aw} + \omega_3 - \frac{1}{\kappa_{b0}}\frac{d\omega_1}{dS}\right) \tag{3.58}$$

This completes the necessary derivations to define the constitutive equations of a curved rod with respect to a helical spring of the relevant cross-sectional shapes. In structural analysis, constitutive equations relate the stresses to the strain of the material. Now, the equilibrium equation can be solved once the constitutive equations have been defined. So far, a helical spring of circular cross-section has been considered and the relevant second moment of area of a circle and polar moment of inertia are thus used. The bending moment and twisting moment of the wire cross-section is related to its respective stiffnesses by

$$T = AE\varepsilon_{aw} \tag{3.59}$$

$$G_n = EI_n\omega_1 \tag{3.60}$$

$$G_b = EI_b\omega_2 \tag{3.61}$$

$$H = GJ\omega_3 \tag{3.62}$$

where AE = axial stiffness

EI_n = normal bending stiffness

EI_b = binormal bending stiffness

GJ = torsional rigidity

These constitutive expressions which relate to the axial, bending and twisting strains presented by Ramsey (1988) are rather different to the expressions presented by Costello et al. As pointed out by Ramsey (1988), this is due to the fact that Costello et al has mistakenly identified the tortuosity in Love's equilibrium equation as the twist of the rod cross-section. These set of constitutive expression are presented below to illustrate the differences.

$$G_{nc} = EI_n\left(\kappa_{n1} - \kappa_{n0}\right) \tag{3.63}$$

$$G_{bc} = EI_b\left(\kappa_{b1} - \kappa_{b0}\right) \tag{3.64}$$

$$H_c = GJ\left(\tau_1 - \tau_0\right) \tag{3.65}$$

where G_{nc}, G_{bc}, H_c are the internal moments derived by Phillips and Costello (1973)

From 3.63 – 3.65, it can be observed that the internal moments are expressed in terms of the change in curvature and tortuosity rather than the correct form which related to the bending and twisting strains. To understand the implication of the above equations, a simple illustration is required. If a straight rod is twisted, then the twist of the centreline is equal to zero as there is no initial twist. Therefore, $\tau_0 = 0$. When equation 3.65 is used, it is clear that the twisting moment does not take into account any rotation of rod cross-section. This is fine given that a circular cross-section helical spring is used, as the curvatures will remain the same. However, it poses a different problem if a non-circular cross-section helical wire is used given that the curvature will change accordingly when the profile is rotated. This problem is investigated separately and is discussed in chapter 4. Therefore, the constitutive expressions used by Costello et al suppresses the rotational factor which was presented in Ramsey (1988), which was shown to be important if non-circular cross-section helical wire is used.

Now, assuming that there are no external moments acting, which means that the helical spring is not bent, and with the tensile force along the wire cross-section constant, the equations 3.46 – 3.51 reduce to

$$-N_b\tau_1 + T\kappa_{b1} + X = 0 \tag{3.66}$$

$$-G_b\tau_1 + H\kappa_{b1} - N_b = 0 \tag{3.67}$$

To find the applied axial force and twisting moments of the spring structure, the components of internal forces on the wire are added and resolved in the direction of centreline of the spring. This is given by

$$F_A = T\sin\alpha_1 + N_b\cos\alpha_1 \tag{3.68}$$

$$M = H\sin\alpha_1 + G_b\cos\alpha_1 + TR_1\cos\alpha_1 - N_bR_1\sin\alpha_1 \tag{3.69}$$

It can be seen that the axial load spring solution here in equation 3.68 differs from the energy method in equation 3.29 because of the fact that the energy method does not consider the binormal shear force. In the energy method analysis, as the applied force is acting at the end of the helical spring, the shear forces are inevitably ignored. For small deformations, the applied axial load equation for both slender rod theory and energy method gives good agreement. However, for larger deformations, the energy method is no longer applicable unlike the solution from slender rod theory. Also, because the equations were linearized in the energy method, the deformed parameters were not taken into consideration in defining the axial load.

3.3 Combined Load Analysis of a Helical Spring

Whilst the above can be used to understand and model the behaviour of springs under axial loads, such as purely tensile or compressive, the equations are inadequate for dealing with springs under the complex loading scenarios which might occur in the case of pressure armour reinforcements. To understand this aspect further, an attempt has been made here to simplify matters and consider

helical springs under three different loading conditions, namely axial loading (which was described in section 3.2), internal pressure, and the combined effect of an internal pressure and axial loading.

These three loading scenarios were chosen because together, they approximate to the conditions thought to occur within pressure armour reinforcements under service, with the internal pressure load being applied by the fluid contained within the pipe and the axial load being created by the effects at pipe termination and weight of suspended pipe, as described in chapter 1. The following section attempts to investigate the effect of an internal pressure load on a helical structure.

3.31 Helical Wire under Internal Pressure

From the previous section, the axial loading of a helical structure was defined in equation 3.68 by resolving the internal forces in the axial direction. In the case of internal pressure, the loading acts in the lateral direction, which is perpendicular to the axial direction. This is illustrated in figure 3.8.

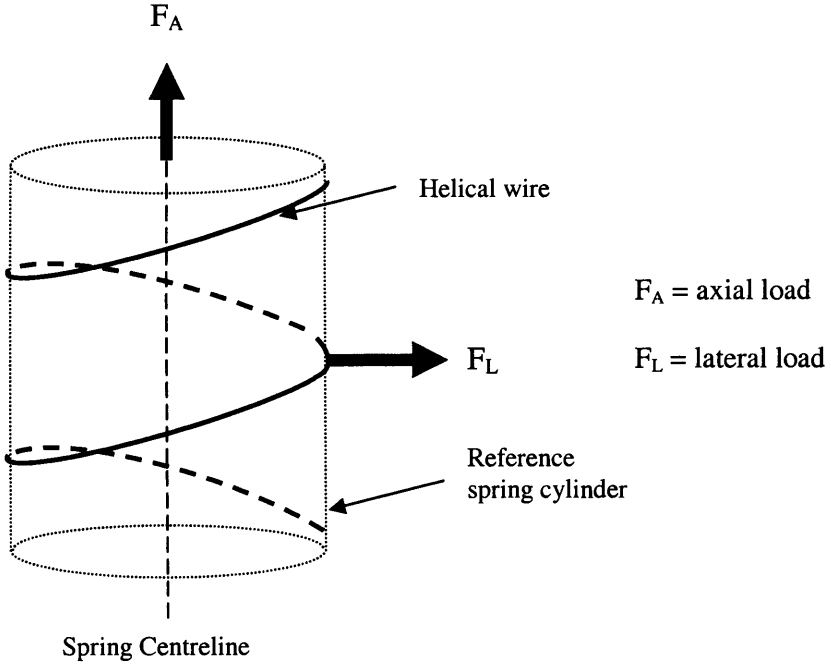

Figure 3.8 Direction of loads on the helical wire

The lateral load, F_L has been defined here to assist in obtaining the internal pressure solution. It shows the way in which the helical spring deforms in the radial direction. Therefore, from equations 3.66 and 3.68 using the slender rod theory, it can be shown that

$$F_L = T\cos\alpha_1 - N_b \sin\alpha_1 \tag{3.70}$$

Rearranging expression 3.66 gives the tension of the rod, T in terms of the binormal shear force, N_b and the radial line load, X of the helical spring,

$$T = \frac{N_b\tau_1 - X}{\kappa_{b1}} \tag{3.71}$$

When equation 3.71 is substituted into 3.70, the lateral load can be defined in terms of the radial line load component.

$$F_L = \frac{N_b\tau_1 - X}{\kappa_{b1}}\cos\alpha_1 - N_b \sin\alpha_1$$

$$= -\frac{XR_1}{\cos\alpha_1} \tag{3.72}$$

The above defines the lateral force, F_L in terms of the internal line which acts towards the centreline of the helical spring. Dividing the internal line load by the width of the cross-section of the rod gives

$$P_X d_w = -X \tag{3.73}$$

where P_X = internal pressure on helical wire

d_w = width of helical wire

The above expression describes the internal pressure on a helical spring wire. If the wire is of circular cross-section, the width is just the diameter of the helical spring wire. This internal pressure solution will be the one used fundamentally for future analytical solution.

Additionally, this solution is compared to the one presented by Oliveira (1985). The helical wire was treated such that it was closely wound and as such, covers the area of a cylinder. This meant that the solution was usually used to measure the internal pressure of the helical structure as if it were made up of a cylindrical tube. A modification of this solution is clearly necessary in order to provide a comparison with the solution using slender rod approach. To illustrate this, a cylinder whose area is equivalent to the area covered by the helical strip is sectioned into half and the internal pressure is treated as an axisymmetric load. This is shown in figure 3.9.

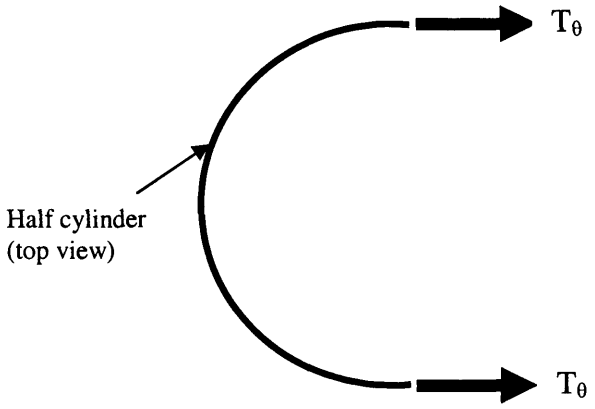

Figure 3.9 Forces on cut cylinder

From Oliveira (1985), the internal pressure is given by

$$P_{cyl} = \frac{2T_\theta}{hD} \tag{3.74}$$

where P_{cyl} = internal pressure of helical wire with equivalent area of a cylinder

h = length of cylinder

D = diameter of cylinder (diameter of helix centreline)

$T_\theta = T \cos \alpha$

The solution above is used when the helical wire is closely wound. Also, it was noted that T_θ corresponded with F_L in equation 3.70. However, similarly, as in the case of the energy method, this solution by Oliveira (1985) considered only the

tension in the wire and not the binormal shear force as developed in equation 3.70 from slender rod theory. Now, if the helical spring in question has a certain pitch length and helical angle with a width of d_w, the internal pressure on wire, P_x is modified from equation 3.74 and is given here as

$$P_X = \frac{2T_\theta}{d_w D}$$

$$= \frac{T\cos\alpha}{Rd_w} \tag{3.75}$$

Comparing the solution by Oliveira (1985) with analytical solution, it could be observed that the former take into account the initial dimension of the helical spring only and not the changes in dimension as the helical spring wire deforms. Hence, the solution in equation 3.73 is used for subsequent analysis.

The following section describes the analytical solution for the helical spring under combined axial and internal pressure load, based on slender rod approach.

3.32 Helical Wire under Combined Axial and Internal Pressure Loading

The solution for a helical spring wire under the combination of axial load and internal pressure is presented here. Referring to figure 3.8 in the previous section, it can be observed that the components of the two different loads act perpendicular to each other. Since there are two variable forces in question, the solution here is to make one load constant while varying the other. This gives a clearer relationship on how the helical spring is behaving under application of an axial load for a certain internal pressure load and vice-versa. Rearranging the axial load solution in equation 3.68, the tension of the wire gives

$$T = \frac{F_A - N_b\cos\alpha_1}{\sin\alpha_1} \tag{3.76}$$

Furthermore, when equation 3.76 is substituted into expression 3.66, the response of helical spring to the internal line load and axial load can be obtained for condition $F_A \neq 0$ and $X \neq 0$. The full derivation is shown in Appendix A.

$$-X = \frac{F_A \cos \alpha_1 - N_b}{R_1 \tan \alpha_1} \tag{3.77}$$

Conversely, if the axial load response is expressed in terms of the shear force in the binormal direction, the response of the helical spring to internal line load and applied axial load in terms of the tension of the wire for $F_A \neq 0$, $X \neq 0$ gives

$$-X = \frac{T - F_A \sin \alpha_1}{R_1} \tag{3.78}$$

Using the internal pressure load equation in 3.73 and considering a fixed axial tension force in equation 3.77,

$$P_X = \frac{F_A \cos \alpha_1 - N_b}{dR_1 \tan \alpha_1} \tag{3.79}$$

where P_X = internal pressure of strip

N_b = shear force in binormal direction

α_1 = final helix angle

R_1 = final radius of helical spring

d = diameter of helical wire

Similarly, from equation 3.78, the internal pressure load on the helical wire, P_X for a fixed axial load in terms of the tension in the wire is given by

$$P_X = \frac{T - F_A \cos \alpha_1}{dR_1} \tag{3.80}$$

where T = tension of helical wire

The relationship of the deformation of the spring subjected to an axial load for a fixed internal line loading rearranging from 3.77 for $X \neq 0$, $F_A \neq 0$ is then given by

$$F_A = \frac{N_b - XR_1 \tan \alpha_1}{\cos \alpha_1} \tag{3.81}$$

Therefore, together with equation 3.73 for relationship between the internal pressure and internal line load, for an axial load on spring with fixed internal pressure, where $P_X \neq 0$ and $F_A \neq 0$,

$$F_A = \frac{P_X dR_1 \tan \alpha_1 + N_b}{\cos \alpha_1} \tag{3.82}$$

Finally, the total deflection of spring due to both internal pressure and axial load, δ_{total} is given here as

$$\delta_{total} = \delta_{PX} + \delta_A \tag{3.83}$$

This is a valid assumption since the total deflection of the spring is taken as the sum of each individual deflection due to axial load and internal pressure loading respectively. In other words, the deflections caused by the loads are independent of each other. If the axial load is kept constant, the total deflection of a spring due to a varying internal pressure can be measured. Conversely, the deflection of a spring due to varying axial load with constant internal pressure loading can also be measured.

The analytical solutions presented above are used to solve for helical springs of circular cross-section under various loading conditions. Verification of these solutions is made using numerical modelling and will be described in the following section.

3.4 Finite Element Analysis of Helical Wire

In order to verify the analytical solutions obtained, finite element analysis was used. It offered several advantages to solve complex non-linear equations as presented in the previous sections. First and foremost, finite element analysis is a numerical method and is particularly useful for structural analysis. Succinctly, in this instance, finite element analysis can easily work out the stress distribution of a beam when loads are applied by breaking down the beam to smaller elements and the behaviour of these smaller elements determined from simple mathematical analysis. A computer is used to perform the calculation on these elements and reveal the stress distribution of the whole structure. This served as a means to verify the analytical solution determined from the basis of the helical spring mechanics, starting from a simple circular wire to more complex cross-sectional wire profile (as described in chapter 4).

Secondly, as can be observed from the analytical solutions presented earlier, the determination of the deformation of the helical spring requires an iterative process in order to obtain an approximation of the spring dimensions after loads are applied. This was conventionally performed using a purpose written FORTRAN (Feld, 1992) or C^{++} program. Finite element analysis was used in this work to obtain the strain of the helical spring wire after loads are applied. This was also estimated iteratively using a spreadsheet based analysis. In this way, the finite element analysis was used as a verification tool.

3.4.1 Helical Spring Modelling Software

ABAQUS finite element software was used to model and perform the analysis on helical springs. This software was chosen because it offered excellent convergence for solving non-linear problems and modelling of the full helical spring structure using solid elements.

3.4.2 Modelling Procedure and Parameters

There are several routes to the modelling of the helical spring in ABAQUS and the reasons for the chosen method of modelling are described here. In finite element modelling, not only the accuracy of the results is important, but also the time and computational costs involved in achieving these results. While a complex helical spring wire of numerous coils can be modelled using 3-dimensional solid elements (that is to model the spring as a whole structure), it is time consuming and uses a lot of computer resources for the solution to reach convergence. Hence, a helical spring structure was modelled here mainly using 3-dimensional beam elements.

Beam elements are one dimensional representation of the actual solid three dimensional models where the deformation of the spring can be considered entirely along the length of the beam axis rather than its cross-section. This type of modelling is appropriate for a structure which is slender, that is the dimension along the beam axis is much larger than the dimension of its cross-section. There are six degrees of freedom at each node of the beam, which can describe the rotation and moments at the nodes of the beam. Since only the global deformation of the spring under applied load is needed, the use of beam elements offered a clear advantage in terms of simplicity of modelling and computational resources without the sacrificing the accuracy of the results obtained.

The full 3-dimensional solid element modelling was used only when the strain parameter of helical wire was required. The beam element did not provide the stress distribution across its cross-sectional area of the wire, hence did not provide the strain results required for the internal pressure loading analytical solution. Only for this particular parameter, the helical spring was modelled using 3-dimensional solid elements and this did not affect the verification process and analysis undertaken via beam element modelling.

Although a helical spring is made up of numerous coils, it is possible to model one coil of the spring as each coil experiences the same deformation as long as it is not

affected by the conditions of the spring ends. It was not possible to model a helical coil using beam elements directly in the ABAQUS/CAE program. ABAQUS/CAE is the pre-processor module where the modelling of the structure is performed. Additionally, it can also be used for monitoring the analysis and viewing of the results.

The helical spring coil elements were created by the author through coordinate generation of the parametric equation of a helix using a purpose written C^{++} program and the results fed back into ABAQUS/CAE via an input file. The parametric equation of a helix was given by Kreyszig (1999) as

$$x(t_p) = (R\cos t, R\sin t, c_h t_p) \qquad (c \neq 0) \tag{3.84}$$

Where R = radius of helical spring

t_p = parametric variable where 1 pitch of the helix corresponded to2π

c_h = number of turns in the helix

The C^{++} program written for the coil model is shown in Appendix B. The elements were modelled for 10 degree turns (the implication of the element size used is described later in the mesh density discussion). Each model consisted of a helical spring with a helix radius of 152.4 mm (6") and a corresponding pitch length of 125.66 mm. The coil radius was chosen to replicate as closely as possible the helical wire reinforcement structure of a flexible pipe. Additionally, for pressure armour layers, the wires are closely wound, therefore they have a small helix angle. The output of the program successfully generated a finite element modelling based coil with the desired small helical angle as shown in figure 3.10.

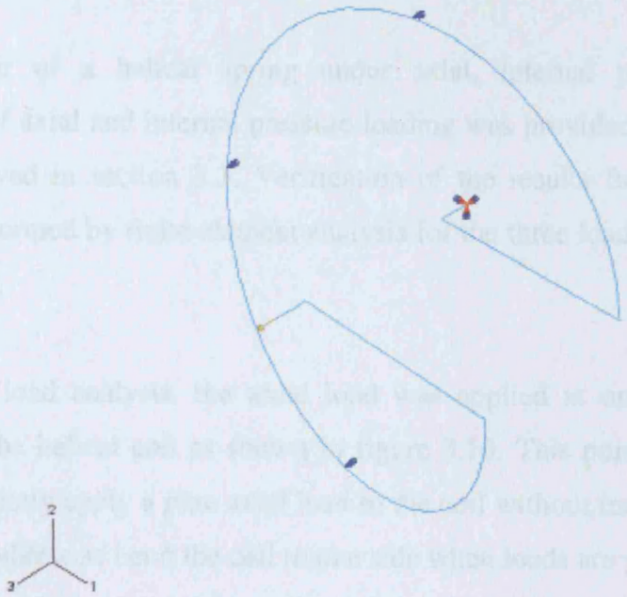

Figure 3.10 Example of helical coil modelled into ABAQUS

The radius of the circular cross-section coil wire was modelled as 3 mm to replicate typical pressure armour layer thickness. The material employed for the helical spring was steel with a Young's modulus of 207 GPa and Poisson's ratio of 0.33. The coil was fixed from moving at one of its ends as shown in figure 3.10. Additional boundary conditions were imposed on the helical coil where necessary depending on the loads applied to the coil.

ABAQUS/Standard, which is the analysis module, was used to perform the load analysis on the helical coil constructed of beam and solid elements. ABAQUS/Standard is a general-purpose analysis module which provided the necessary capability to solve the static stress or displacement response to a structure under applied load. The general static stress analysis step was chosen and the analysis was carried out to include the effects of geometric non-linearity, which can occur due to helical coil undergoing large deformations after loads are applied. The load analysis on the coil in the finite element model is described in the next section.

3.4.3 Finite Element Loading Analysis

The behaviour of a helical spring under axial, internal pressure, and the combination of axial and internal pressure loading was provided by the analytical solutions derived in section 3.3. Verification of the results from the analytical work was performed by finite element analysis for the three loading modes, and is described here.

For the axial load analysis, the axial load was applied at one end but at the centreline of the helical coil as shown in figure 3.10. This point was essentially chosen to correctly apply a pure axial load to the coil without inducing a moment, which would otherwise bend the coil to one side when loads are gradually applied. For the axial tension case, the incremental loads were taken to coincide with the values of the axial load calculated in the analytical solution. The corresponding deflection obtained by the finite element analysis was compared with the deflections which had been defined in the analytical work. The percentage difference in result for each load was measured. Similarly, this was done in the axial compression models. The change in geometry of the helical coil was noted. The deflection and change in spring radius was measured from the distance between the respective nodes in the model.

A pressure load could not be applied directly to a beam element model because in theory there were no surfaces for the force to be applied to. A distributed load was applied instead and divided by the width of the wire to obtain the pressure load. This distributed load was coincident with the internal line loading parameter, X, derived earlier. The distributed load was applied along the length of the wire, which represented the force on the helical wire which was constantly changing its orientation due to its helical configuration. Hence, it was necessary to define the beam orientation appropriately so that the correct loading was experienced along each element. Figure 3.11 depicts the line loading on each element for a helical coil model. The small boxes indicate the line force on the element. Additionally, a set of constraints were placed on the end of the coil pitch as shown to prevent the coil from opening up due to the applied load.

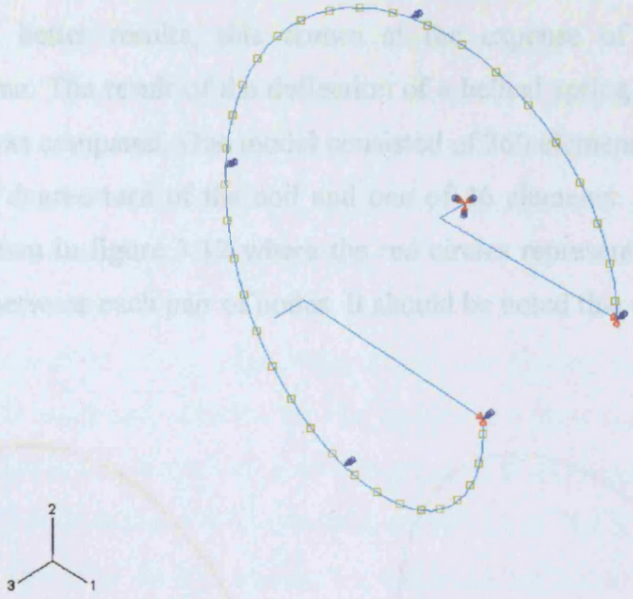

Figure 3.11 Line load and constraints on helical coil model

For the case of combined loading, it had been decided to use the model similar to that of the internal pressure loading analysis. This meant that the constraints were still in place on the coil pitch end to prevent the coil from opening up. Such a constraint had some restriction on the axial movement of the coil. The implication of this will be further discussed in section 3.5. The helical coil was subjected to a series of axial loads for a given internal pressure load. The process was then repeated for a series of chosen increments of internal pressure. Additionally, the whole analysis was repeated for variable internal pressure loading, together with a fixed axial load on the coil.

3.4.4 Helical Coil Mesh

As described earlier, the helical coil was modelled using an element size corresponding to a 10 degree turn (as measured from the centre). Therefore the mesh of one coil consisted of 36 elements. The number of elements in a mesh is known as the mesh density. This mesh density was chosen because it was sufficiently accurate for the analysis considering the number of load analyses that

had to be performed. While an increase in the mesh density of the coil can potentially give better results, this comes at the expense of computational resources and time. The result of the deflection of a helical spring using different mesh densities was compared. One model consisted of 360 elements, which is one element of each degree turn of the coil and one of 36 elements. The nodes and elements are shown in figure 3.12 where the red circles represent nodes and the elements are in between each pair of nodes. It should be noted that each element is a straight beam.

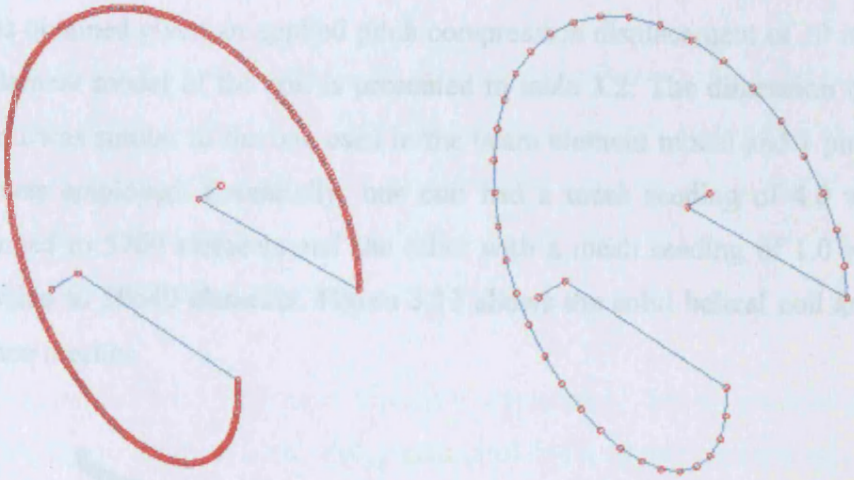

Figure 3.12 Nodes and elements on helical coil of different mesh densities

An axial load of 2.22 N was applied to each of the coils. This was chosen as it corresponded to a 5 mm deflection as calculated using the analytical solution derived earlier. Comparison of results is shown in table 3.1.

Mesh density (no. of elements)	360	36
Deflection (mm)	4.992	4.955
% difference to 5 mm	0.16	0.9

Table 3.1 Comparison of deflection to helical spring for applied axial load

The coil with higher mesh density showed a closer result to the predicted deflection value. Nonetheless, both sets of results showed good accuracy (within 1%). For this work, therefore, it was sufficient to use the helical coil model with the lower number of elements since it did not affect the outcome of the result significantly and considerable time and computer resources was saved given the number of analyses that had to be performed.

Similarly, for estimation of the wire strain value, which was necessary for the verification of the analytical solution for the internal pressure scenario, the wire strain was obtained given an applied pitch compression displacement of 10 mm to a solid element model of the coil is presented in table 3.2. The dimension of the helical coil was similar to the one used in the beam element model and 1 pitch of the coil was employed. Essentially, one coil had a mesh seeding of 4.0 which corresponded to 5760 elements and the other with a mesh seeding of 1.0 which corresponded to 38640 elements. Figure 3.13 shows the solid helical coil and its section face meshes.

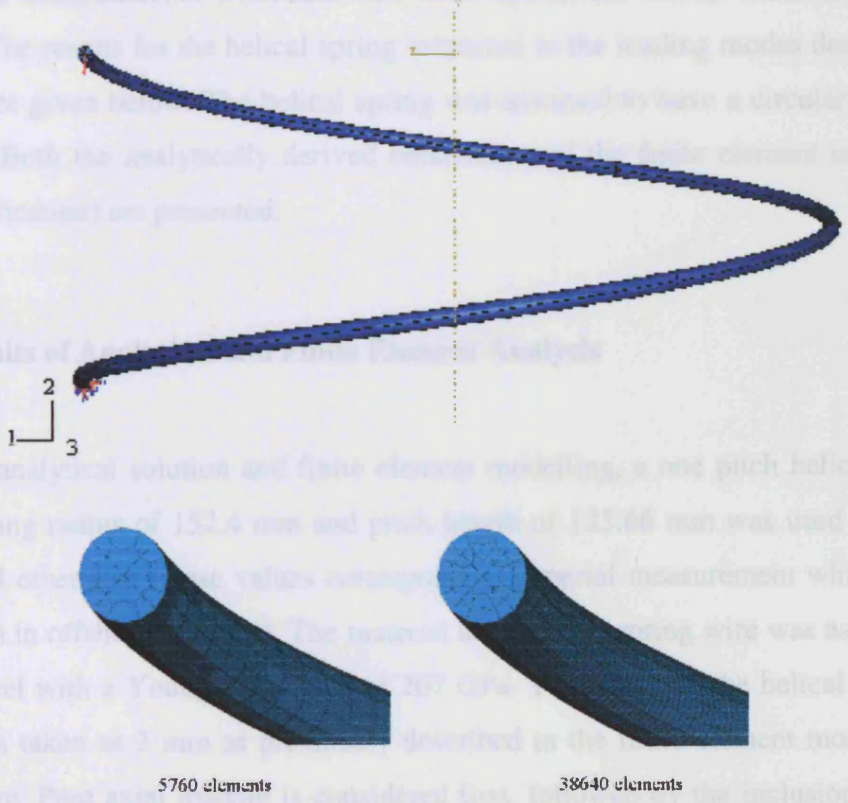

Figure 3.13 Helical coil and section face meshes using solid elements

The wire strain, measured at the centreline of the helical wire was calculated for an axial compression of 10 mm and is given in the table below.

Mesh density (no. of elements)	5760	38640
Wire strain	-4.68675×10^{-6}	-4.9624×10^{-6}
Run time (minutes)	5	30

Table 3.2 Comparison of wire strain of helical spring for 10 mm axial compression

The calculated run time was typical for analysis performed using a Pentium IV based machine with 1 GB of Ram. The percentage difference in result was 5.6%. Given that the helical coil with lower mesh density gave close agreement to the one with high mesh density, it was decided to use the former for subsequent analysis to reduce cost of computational analysis.

Once the computational overheads had been optimized, formal modelling was begun. The results for the helical spring subjected to the loading modes described earlier are given below. The helical spring was assumed to have a circular cross-section. Both the analytically derived behaviour and the finite element analysis (for verification) are presented.

3.5 Results of Analytical and Finite Element Analysis

For the analytical solution and finite element modelling, a one pitch helical coil with spring radius of 152.4 mm and pitch length of 125.66 mm was used unless specified otherwise (these values correspond to imperial measurement which are the norm in offshore industry). The material used for the spring wire was assumed to be steel with a Young's modulus of 207 GPa. The radius of the helical spring wire was taken as 3 mm as previously described in the finite element modelling procedure. Pure axial loading is considered first, followed by the inclusion of an internal pressure load.

3.5.1 Results for Axial Loading

A comparison of the axial load – deflection curves from the three different theories used in this work are shown in figure 3.14. The helical spring was subjected to a tensile load. The three theories showed a highly linear trend in the deformation range as depicted in figure 3.14. As larger deformations were considered, the energy method solution deviated from the solution of Wahl's basic spring equation and the analytical solution based on Love's equilibrium equation for slender rods. This confirmed that the energy method analysis was applicable only to small wire strains and applied loads. In figure 3.15, it could be seen that the theory was accurate for spring axial strain of up to 0.01 for the given spring length. For the spring dimension considered, the solution using energy method differs by about 20% from the basic spring theory after 0.01 spring strain. It should be noted that the wire strain relates to the actual strain in the length of the wire from which a spring is made and spring strain relates to the change in the deflection of the spring as a complete system.

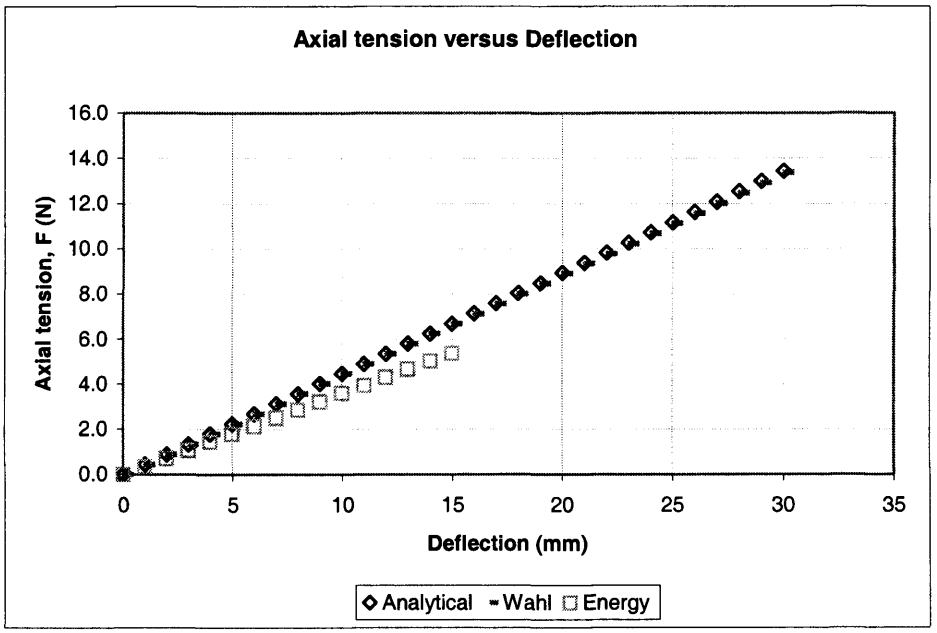

Figure 3.14 Comparison of the axial load versus deflection response

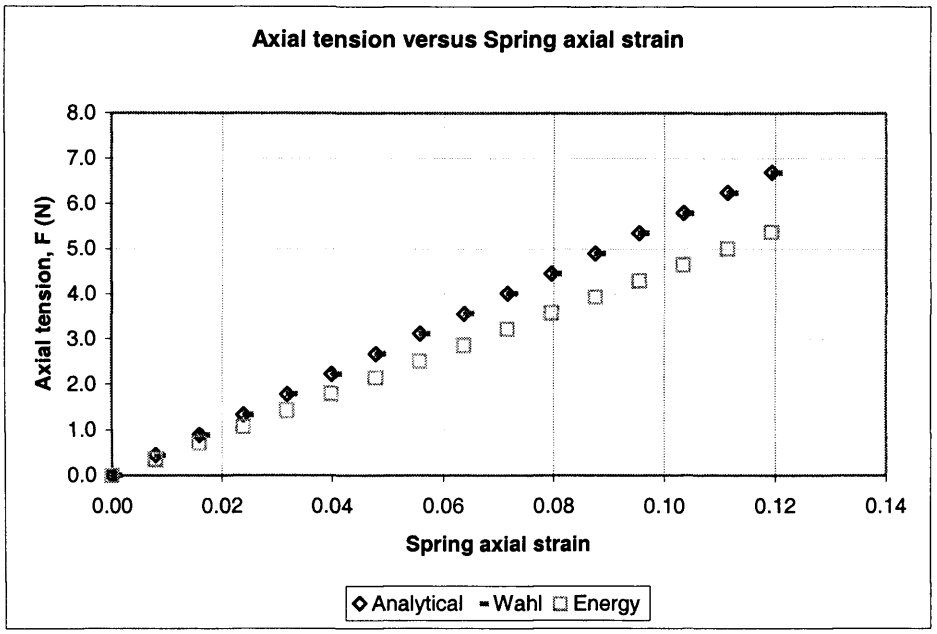

Figure 3.15 Comparison of axial load versus spring axial strain

For large deflections of the spring, which is of several spring lengths, the solution by slender rod theory accounted for the changes in the diameter of the spring and the helical angle of the spring. The response of the spring became non-linear. This somewhat unusual result is counter to the commonly accepted view that springs are linear systems. However on closer inspection it is of course unreasonable to expect a spring system to behave in this manner at deflections where the spring geometry becomes substantially deformed. Indeed Wahl (1963) recognized this limitation and suggested that modifications to the basic spring theory were required. For this work, it is sufficient to note that the deflections likely to be experienced in pressure armour layers are small enough to be very remote from the non-linear region of behaviour. Therefore, the basic solution by Wahl (1963) can only be use if the change in dimension of the helical spring is not large. Figure 3.16(a) – (c) shows the change in dimensions of a helical spring coil subjected to axial tension load using the slender rod theory for large deformation.

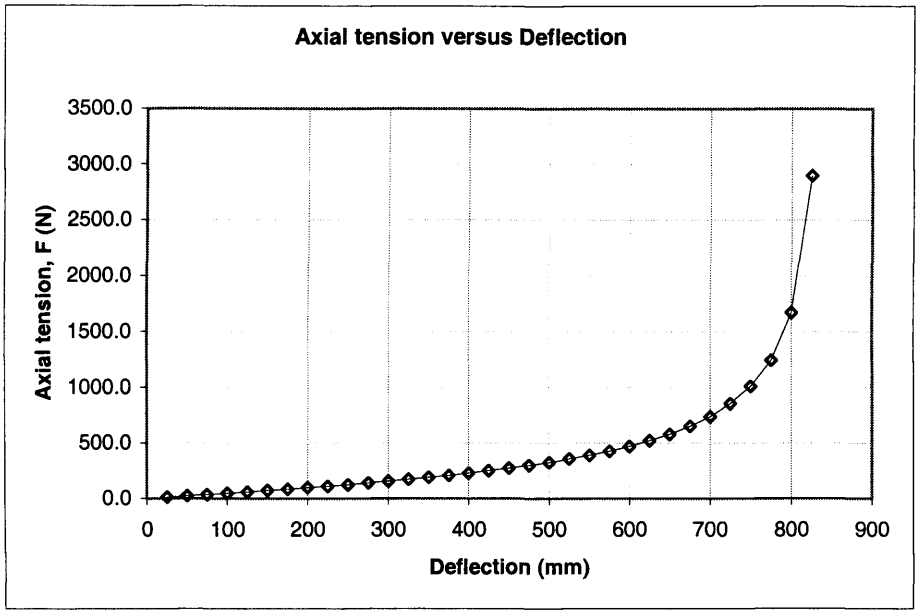

Figure 3.16a Axial load versus deflection for large deformation

The deflection of the spring revealed the non linear behaviour as large axial loads were applied (figure 3.16(a)). The spring became progressively stiffer. A similar non-linearity is revealed for the spring radius under axial load, and is shown in figure 3.16(b). However, what is interesting is that a non linear behaviour is also detected at small deflections (which corresponded to large spring radii). This may well have implications for understanding the behaviour of a pressure armour, especially those which is multilayered, where one layer impinges upon another and where the contact forces can lead to damage.

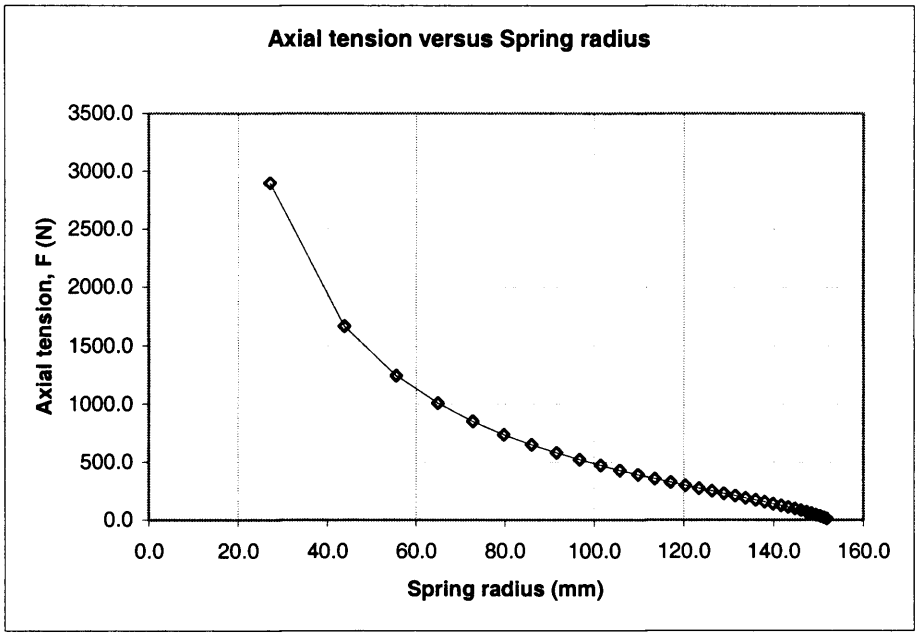

Figure 3.16b Axial load versus spring radius for large deformation

It can be seen from figure 3.16(c) that the spring deflection begins to deviate from linear behaviour (with respect to applied load) when the helical angle exceeds 45 degrees. This non-linearity is therefore not apparent since most helical spring analyses are usually subjected to applied load, which do not change spring radii or helical angles by large amounts. Hence, it was decided that for the forthcoming analyses, the helical spring would be treated to behave in a linear manner. From a simplistic viewpoint, a spring no longer behaves like a true helical spring due to the fact that the wire under large deflections behaves like a bent beam being straightened out. This explained the increasing stiffness observed in figure 3.16(a). The remaining responses of the spring radius and spring deflection with helix angle are given in Appendix C.

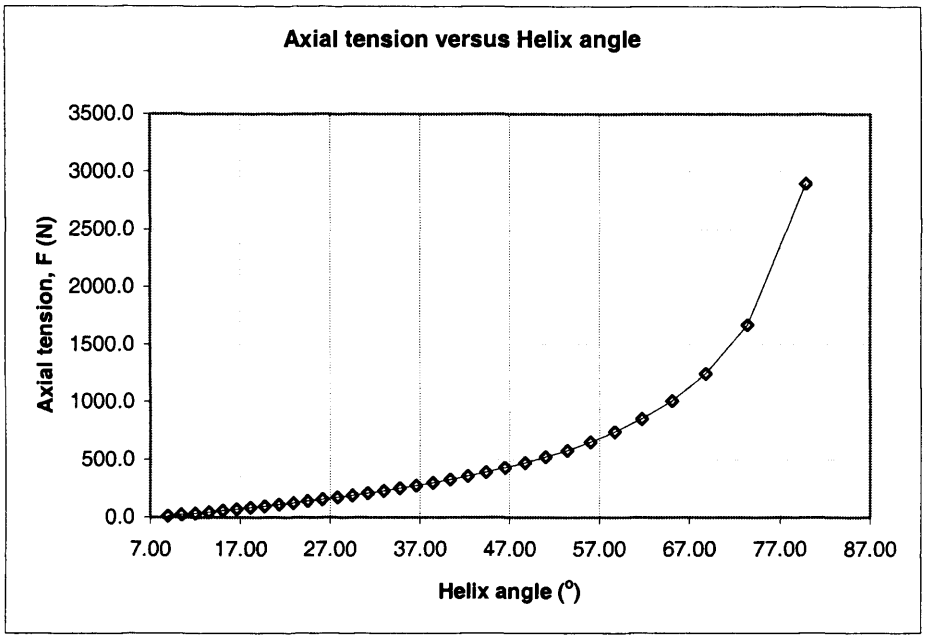

Figure 3.16c Axial load versus helix angle for large deformation

The basic spring theory presented by Wahl (1963) is useful, but only valid for certain cases of spring design. Firstly, the springs are assumed to have a small helix angle and changes in the spring radius after a load is applied, is ignored. This means that the conventional spring theory predicts a linear axial load – deflection as expected. However, when large changes in the dimensions of the spring occurred, this theory was no longer useful. The energy approach is useful to investigate the deformation of a cable or wire rope wrapped helically by a number of smaller wires. Usefully, if the number of wires were reduced to that of a single helical wire constituent, the solution is similar to that of a basic helical spring. This method however is restricted to small spring strain (i.e. a small deformation of the structure). In spite of this, the energy approach can still be used since the pressure armour of a flexible pipe has relatively small movements in the axial direction of the pipe. Nonetheless, an analytical solution was sought to include the deformation of a helical spring under internal pressure loading. This was akin to the pressure armour layer of a flexible pipe being subjected to internal pressure loading. It was decided to continue using the slender rod theory given that it had been shown to account for large changes in the dimensions of the

helical wire whilst at the same time account for the changes in dimension of the spring as it was deformed. This suggested it might be better at dealing with internal pressure loads. It also provided a means to solve for an internal pressure loading on a helical spring, and a means to measure the combined effect of the axial and internal pressure loading on a helical wire constituent. Advantageously, the analytical solution based on the slender rod theory was able to account for various cross-sectional shapes other than a circular section. This was important considering the fact the pressure armour layers usually consist of non-circular profiles. These analytical solutions and the discussion of the results are presented in chapter 4.

While these approaches are appropriate to use with pressure armour configurations, the analytical solution provided by the author nevertheless considered the implications of large dimensional changes of the helix to the overall change in behaviour of the spring. The reason for this is that the work here has revealed that non-linearities in spring behaviour do exist, and in order to ascertain the origin of these, it was important to understand whether large deflections were implicated. This will be further discussed later. Another important point to note is that good correlation between basic spring theory by Wahl (1963) and solution based on slender rod theory was obtained. This confirmed that helical wire reinforcements are essentially analogous to a spring. An interlocked profile helical wire is just a constraint experienced due to the deformation of a helical spring which justified the assumption of pressure armour being similar to a helical spring in terms of its free movement.

The analytical solution presented here is for a spring with ends fixed from rotation while the finite element result is for a spring free to rotate. This was done to simplify calculation of the results from the analytical solution. An example of the finite element analysis result obtained is shown in figure 3.17. For an applied axial load, the corresponding deflection and spring radius was measured from the distance of the appropriate nodes on the coil. The procedure was repeated for each load step to obtain enough data points for graph plotting.

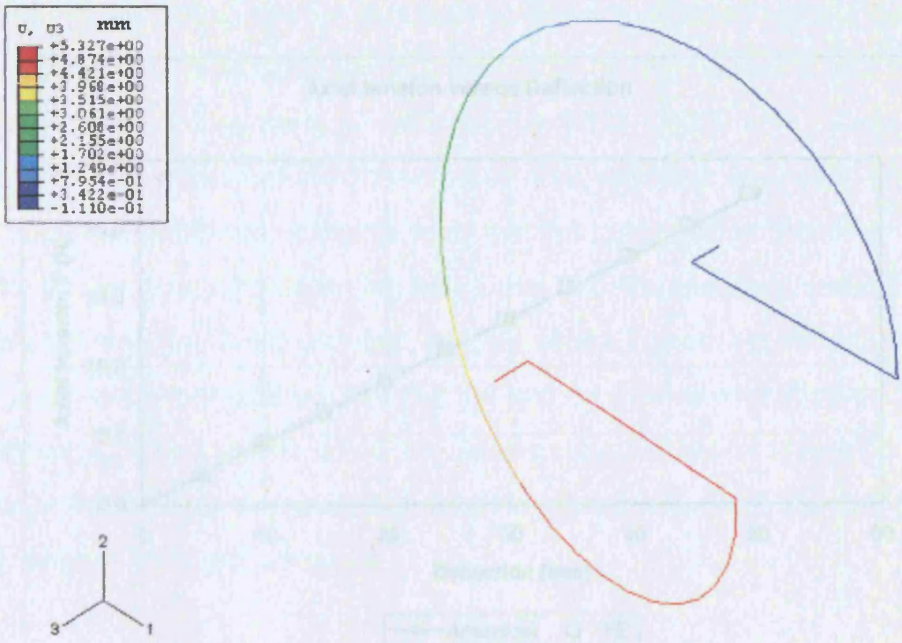

Figure 3.17 Finite element analysis for deflection of helical spring under 2.22N axial load

The following graphs depict the finite element analysis results obtained in the 'small deflection region' characteristics of pressure amour. Figure 3.18(a) – (c) shows the response of a helical coil subjected to axial tension load and the corresponding finite element analysis results.

In figure 3.18(a), it could be seen that the solution is highly linear in both the analytical and finite element result. Additionally, it should be noted that the finite element analysis gave a very close approximation to the analytical solution even though the spring coil was allowed to rotate (the ends were not constrained). This showed that in practice the helical spring does not rotate much for the given applied loads. Figure 3.18(b) confirmed this observation from the plot of twisting moment against deflection. This twisting moment is induced when a helical spring is fixed at the ends against rotation. In other words, the twisting moment acts to prevent the helical spring from coiling or uncoiling.

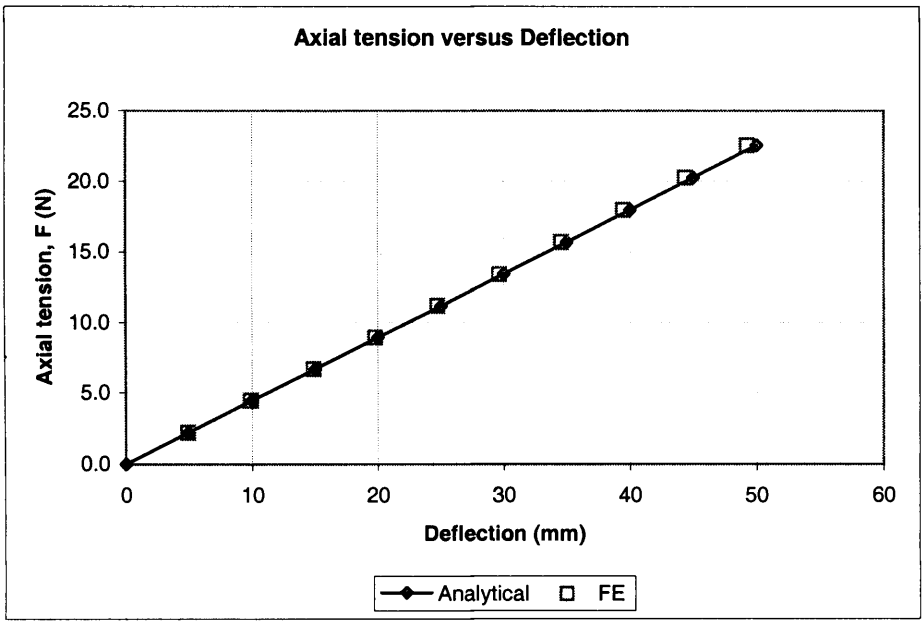

Figure 3.18a Axial load versus deflection for analytical and finite element

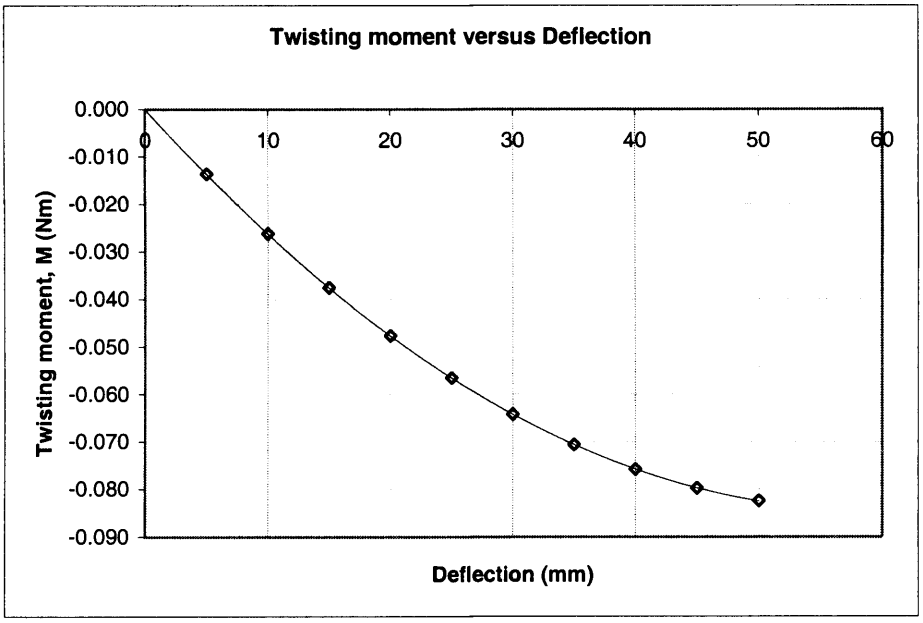

Figure 3.18b Twisting moment versus deflection for analytical solution

Figure 3.18(c) shows the change in spring radius due to axial tension load. It can be seen that the radius does not vary linearly with respect to the applied loads. The spring radius contracts when the deflection of the spring increases. The fact that the relationship is non-linear is confirmed by Wahl (1963), who noted that the spring radius is a function of power of three, with respect to an applied axial load and hence the deflection. It can be seen that the spring radius behaviour via the finite element route differed by less than 1 mm from the analytical route. It can be concluded that the finite element analysis showed good agreement with the analytical solution despite the fact that the analytical solution predicted a slightly stiffer spring. This could be due to the fact the helical spring in consideration was fixed at the ends in the analytical solution, which prevented the spring from contracting in the radial direction.

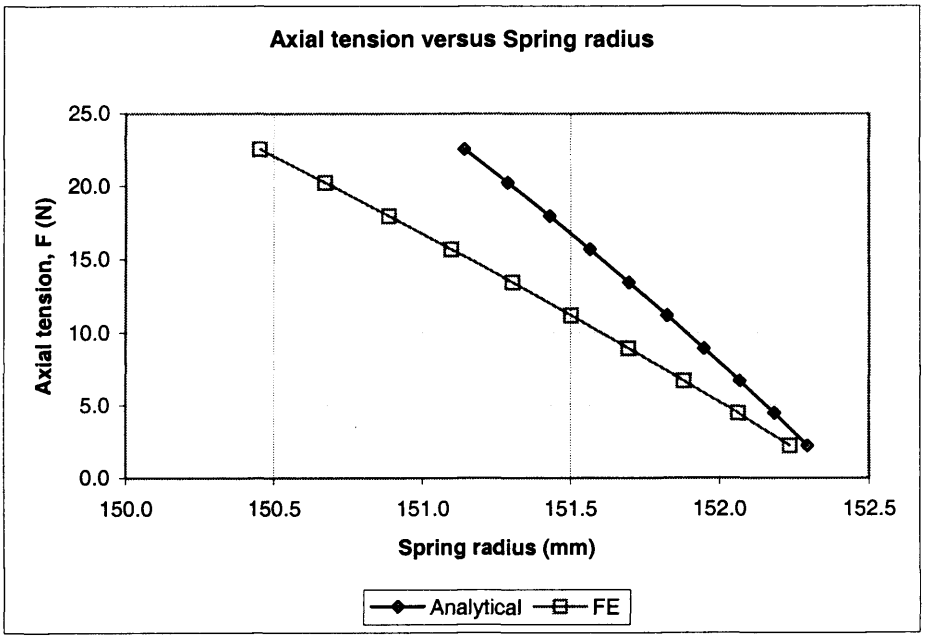

Figure 3.18c Axial load versus spring radius for analytical and finite element

The change in helical angle with applied load was plotted for the analytical solution and is shown in figure 3.18(d). As small deformations were encountered, an approximate linear response of the change in helical angle with respect to axial load was observed.

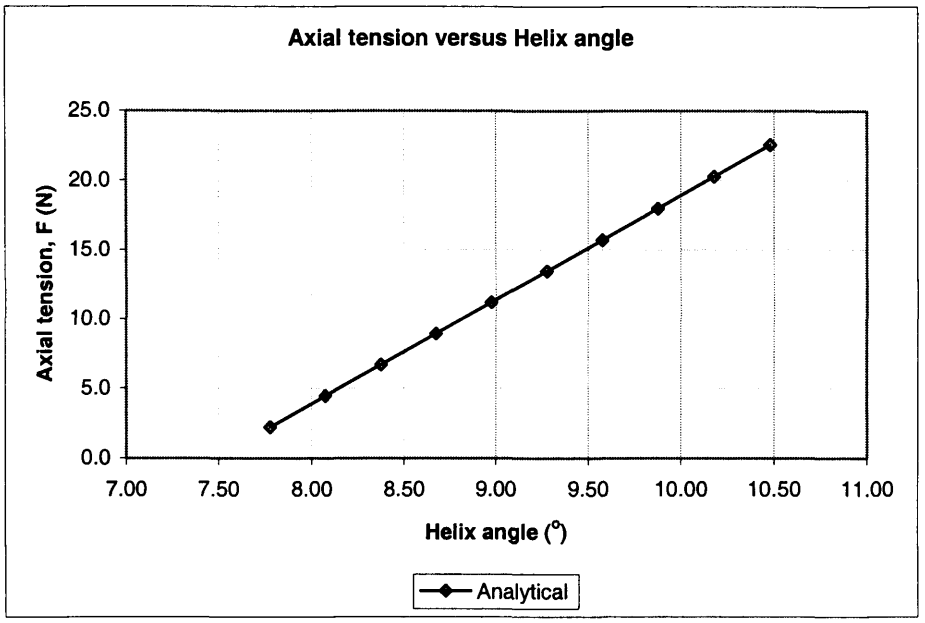

Figure 3.18d Axial load versus helix angle for analytical solution

It can be seen that the helix angle varied linearly with the applied axial tension load for the small helical angle in consideration. The change in helical angle with respect to axial load could not be measured in the finite element model, although it can still be estimated (given that the deflection and radius of the helical spring were measured in the finite element model) using the geometric analysis shown in figure 3.3.

Similarly, in the axial compression loading mode, the deflection varied linearly to the compressive force. The deflection curves are positive in the direction of decreasing length and should not be confused with the axial tension cases. The graphs of the change in spring radius, deflection and spring helical angle under compressive loads are shown in Appendix C for completeness. Finite element analysis showed good agreement with the responses of the analytical solution.

3.5.2 Results for Internal Pressure Loading

The internal pressure solution from slender rod theory was compared with the equilibrium of forces solution obtained by Oliveira (1985) and the responses

shown in figure 3.19. A helical spring of similar dimensions to the one subjected to axial loading (in the previous analysis) was used. In order to solve the slender rod analytical solution, the wire strain had to be estimated and this was done through the use of spreadsheet iteration method described earlier and verified using finite element analysis. The wire strain was calculated for different values of spring deflection and the internal pressure loads corresponding to these spring deflections were calculated. An important point to note is that a helical spring decreases in length and expands in radius when subjected to axial compressive force. In such a case, the strain of the wire is assumed to be negative. However, in the internal pressure loading mode, although the helical spring decreases in length and the radius expands, the tension in the wire is positive because the wall of the spring is undergoing a tension force in the radial direction because the internal pressure is trying to enlarge the spring in that direction. This is akin to a pressure vessel being subjected to internal pressure and hence expanding its radius because of tension forces in the hoop direction. Therefore, in contrast to an axial compressive load, which generates a negative wire strain, the wire strain of the helical spring when subjected to an internal pressure load is positive.

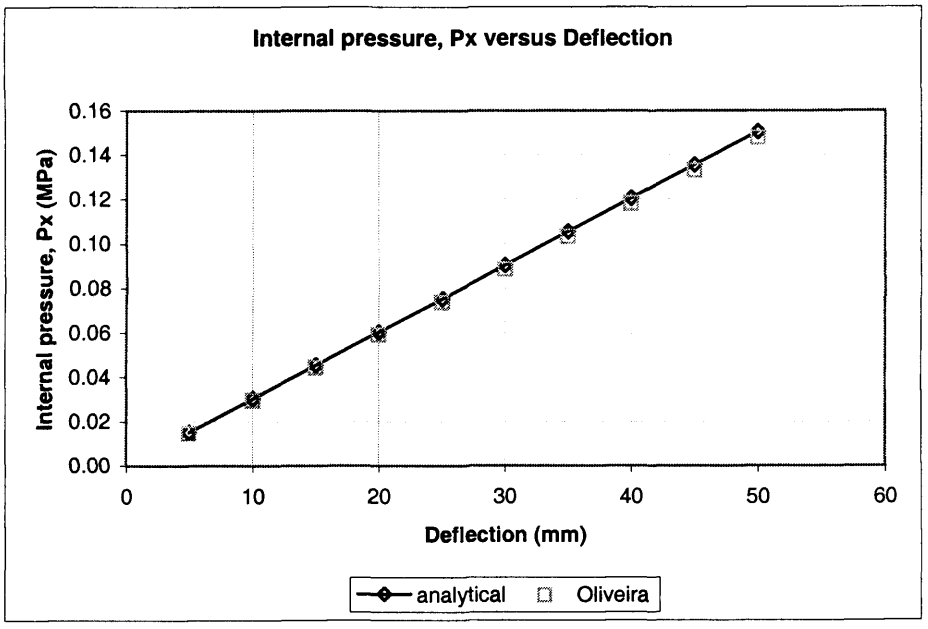

Figure 3.19 Comparison of internal pressure versus deflection for analytical and Oliveira model

It can be seen that the internal pressure solution from both analytical and the modified Oliveira (1985) equation showed good agreement although the latter did not take into account changes in the dimensions of helical spring. However, for larger deformations, a noticeable deviation of the solution occurs as the internal pressure gets larger.

Figures 3.20 and 3.21 show the example wire strain obtained from the finite element analysis and the corresponding radial deflection generated by the applied line loading (pressure) respectively.

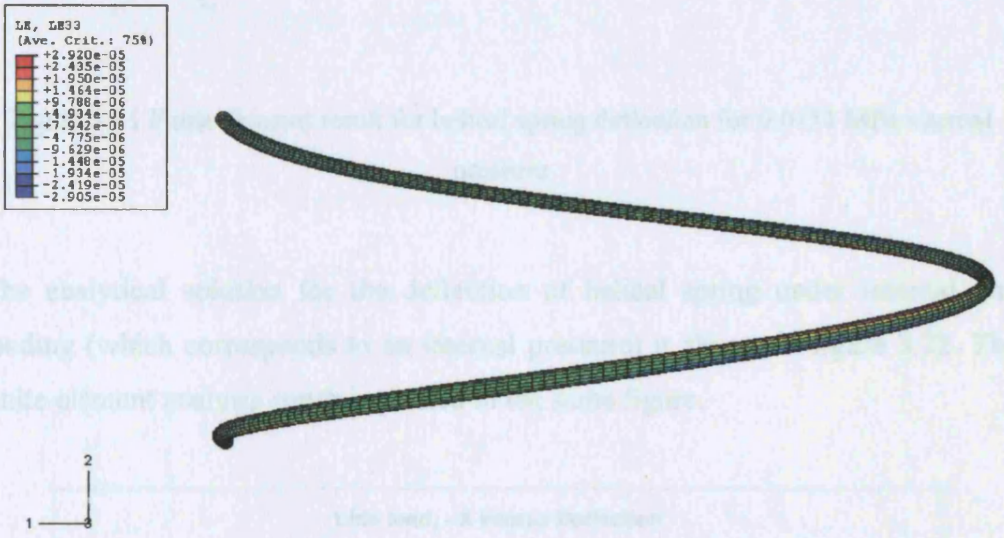

Figure 3.20 Result of finite element for helical spring wire strain for 5 mm compression

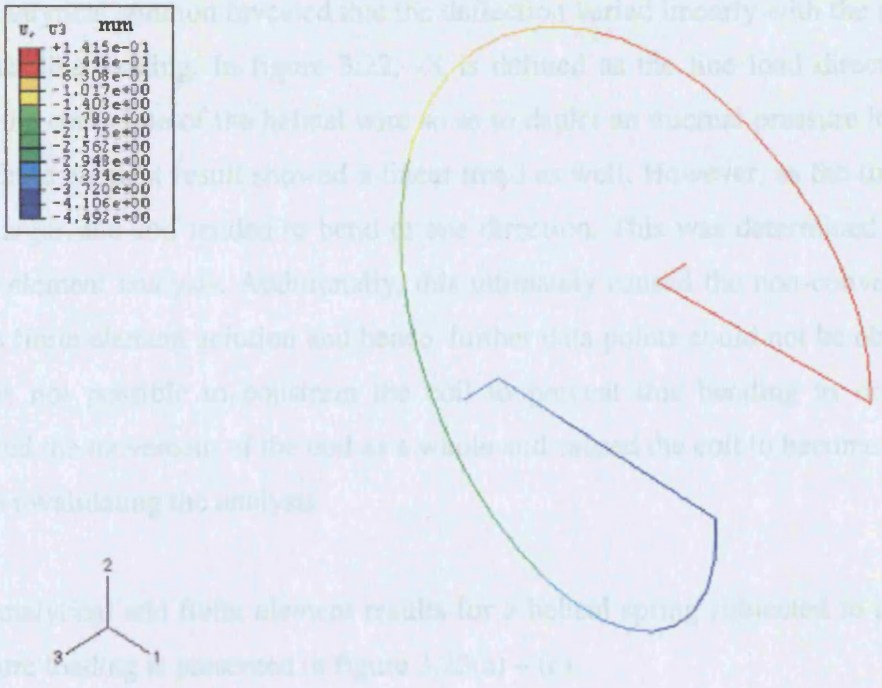

Figure 3.21 Finite element result for helical spring deflection for 0.0151 MPa internal pressure

The analytical solution for the deflection of helical spring under internal line loading (which corresponds to an internal pressure) is shown in figure 3.22. The finite element analysis result is plotted in the same figure.

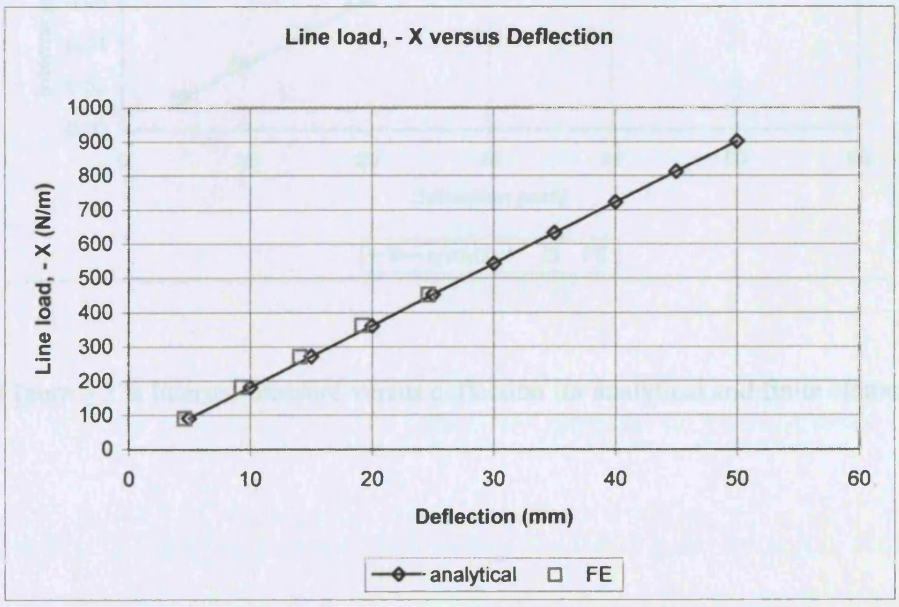

Figure 3.22 Internal line load versus deflection for analytical and finite element

The analytical solution revealed that the deflection varied linearly with the applied internal line loading. In figure 3.22, -X is defined as the line load directed out from the centreline of the helical wire so as to depict an internal pressure loading. The finite element result showed a linear trend as well. However, as the line load gets larger, the coil tended to bend in one direction. This was determined during finite element analysis. Additionally, this ultimately caused the non-convergence of the finite element solution and hence, further data points could not be obtained. It was not possible to constrain the coil to prevent this bending as doing so affected the movement of the coil as a whole and caused the coil to become stiffer, hence invalidating the analysis.

The analytical and finite element results for a helical spring subjected to internal pressure loading is presented in figure 3.23(a) – (c).

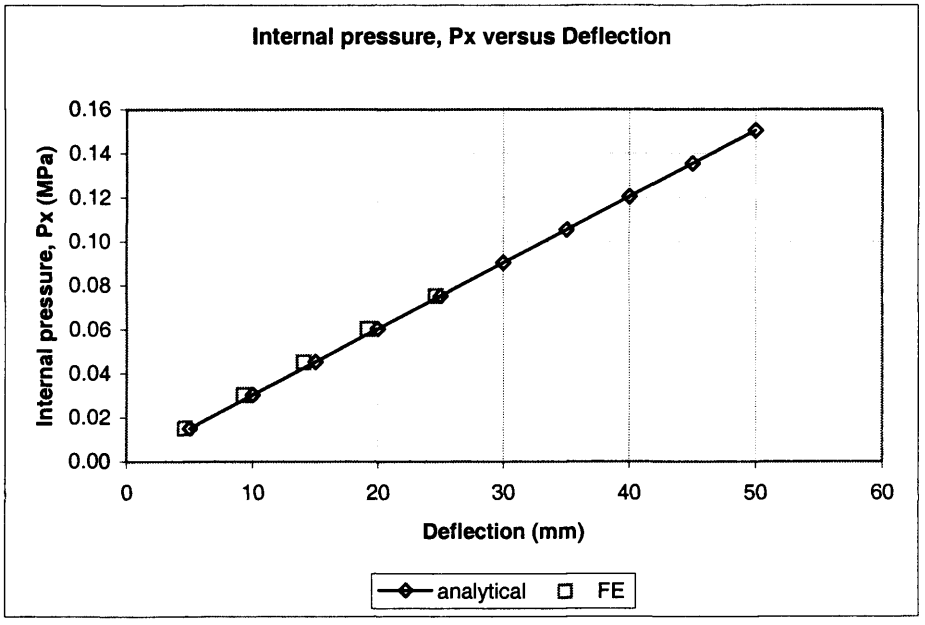

Figure 3.23a Internal pressure versus deflection for analytical and finite element

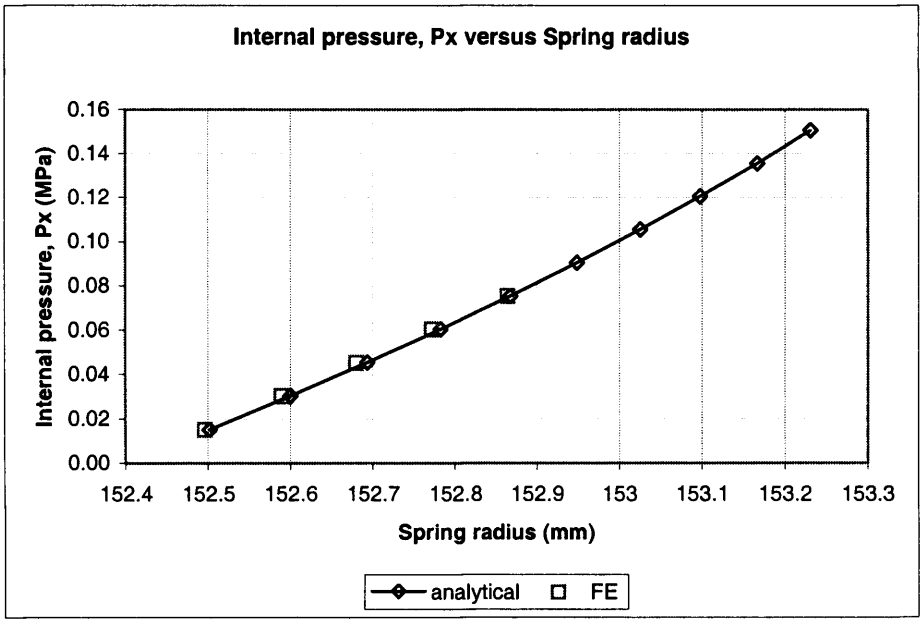

Figure 3.23b Internal pressure versus spring radius for analytical and finite element

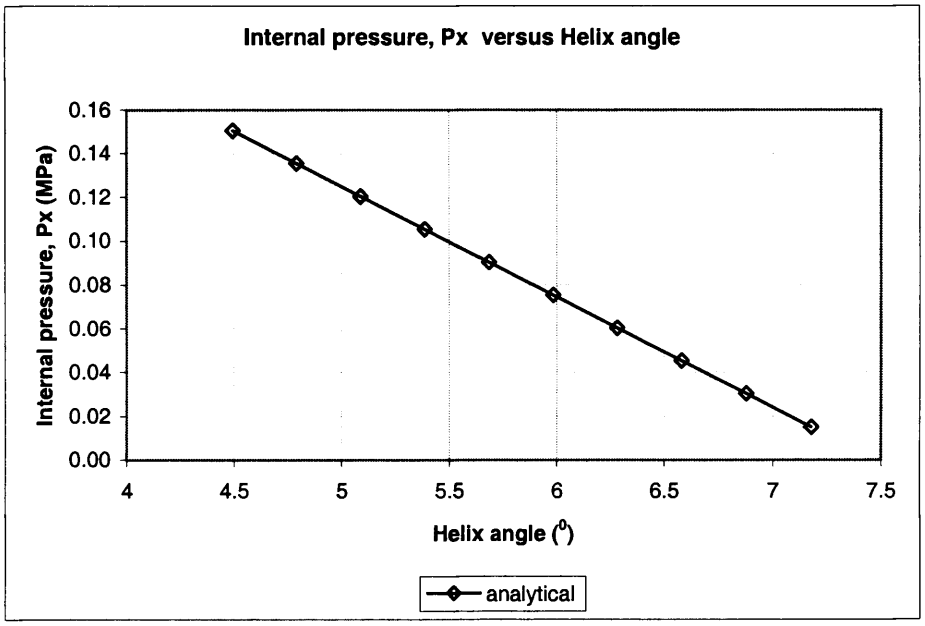

Figure 3.23c Internal pressure versus helix angle for analytical solution

The level of the internal pressure loading was chosen in order to deflect the helical spring by the same amount as would be the case for an axial compressive load and the behaviour is shown in figure 3.23(a). A linear trend is observed. Figure

3.23(b) reveals that the internal pressure does not vary the spring radius linearly. This was expected given the earlier comment that the spring radius is a function of the power of three in relation to the deflection. Figure 3.23(c) shows the variation of the helix angle to the internal pressure loading. As internal pressure increases, the helix angle decreases and the sign change is in contrast to the response that is obtained when the spring is subjected to axial load.

3.5.3 Results for Combined Axial and Internal Pressure Loading

The finite element analysis of a helical spring subjected to combined loading modes is shown in figure 3.24 for internal line load of 91 N/m (this corresponds to an internal pressure of 0.015 MPa, chosen to ensure resultant deflections are comparable to the previous section) as the axial load is varied.

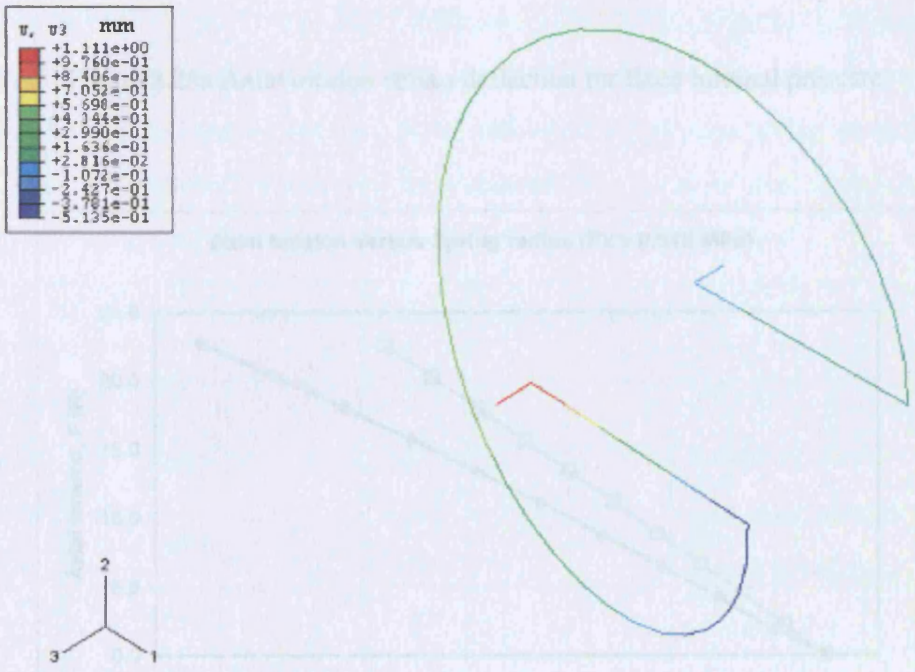

Figure 3.24 Sample finite element analysis result for combined 2.22N and 0.0151MPa

Figures 3.25(a) and (b) show the result of the helical spring subjected to combined axial tension and internal pressure. The 0.015 MPa internal pressure causes a spring contraction of 5 mm.

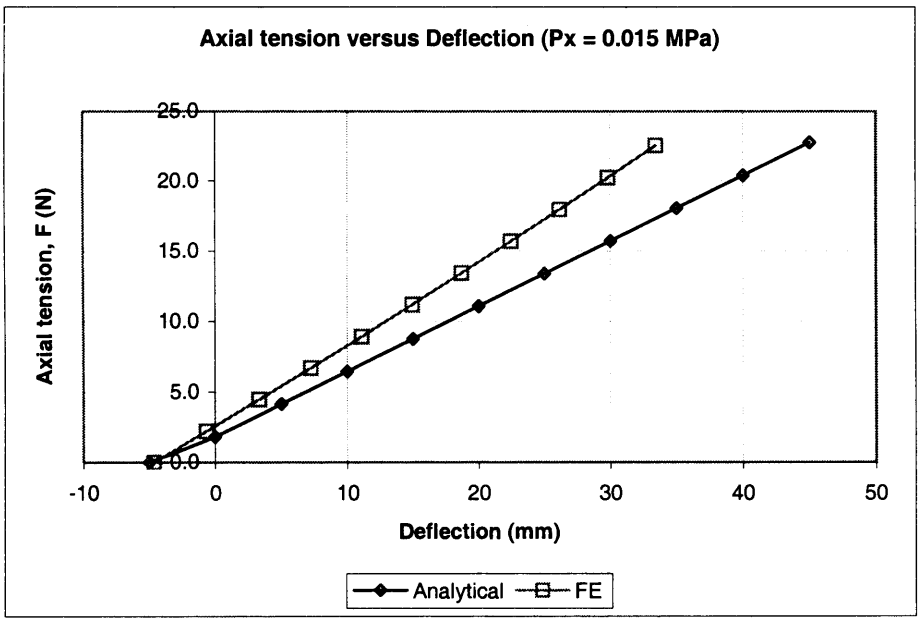

Figure 3.25a Axial tension versus deflection for fixed internal pressure

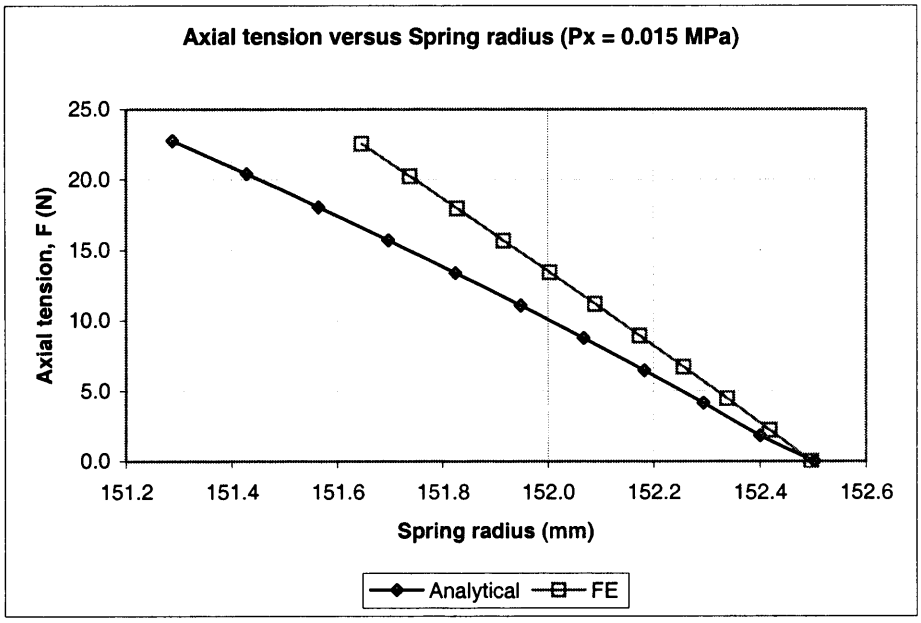

Figure 3.25b Axial tension versus spring radius for fixed internal pressure

It can be seen from the responses in figure 3.25(a) and (b), that the finite element analysis predicted a spring with a somewhat larger spring stiffness than the analytical solution. This is probably due to the fact that the axial loading is partly constrained by the boundary condition imposed when applying an internal pressure load. The coil ends had to be fixed to prevent the helix from uncoiling itself due to the applied internal pressure. Hence, the axial movement of the helical spring was restricted and the deflection of the spring affected. Nevertheless, this did not change the overall response shown by the helical spring. The deflection measured from the finite element model for large loading gave differences of more than 10%. In addition to the effect of end constraints, the deviation may be partly due to the fact that the differences seen in the purely axial and purely pressure loaded models, are now combined, and may do so unfavourably.

Following on from this, the subsequent models were used to verify the combination of a varying axial load for different internal pressure loadings (fixed at step values of 0.015 MPa, 0.030 MPa and 0.045 MPa). Figures 3.26(a) and (b) show the response of the helical spring under these loads. This analysis was done to check that the response of the spring and in particular, the spring constant, did not alter as the pressure load was incremented. The pressure was raised in steps, and the corresponding tension versus deflection response obtained.

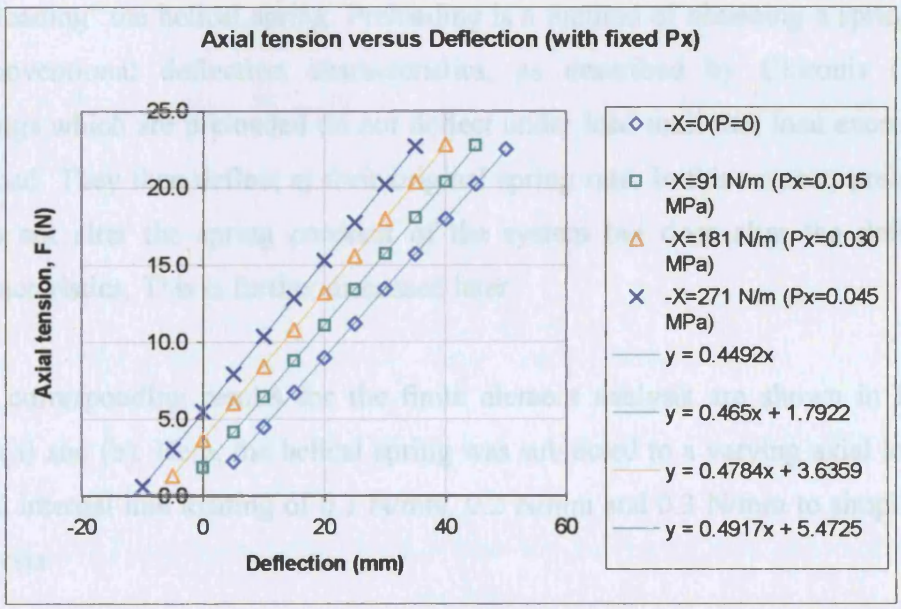

Figure 3.26a Axial tension versus deflection for fixed internal pressure step values

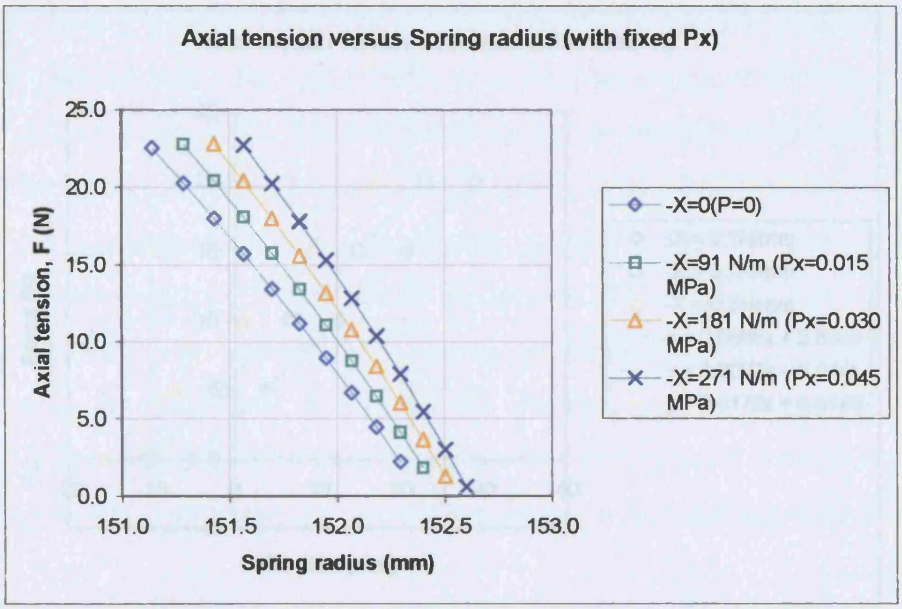

Figure 3.26b Axial tension versus spring radius for fixed internal pressure step values

It can be seen from figure 3.26(a) that when in combination with an internal pressure load, the axial load required to cause the same amount of deflection as for a helical spring under purely axial loading increases with each internal pressure load step. This basically shifts the curves to the left side of the original zero internal pressure curve. Effectively, the internal pressure becomes a way of 'preloading' the helical spring. Preloading is a method of obtaining a spring with unconventional deflection characteristics, as described by Chironis (1961). Springs which are preloaded do not deflect under load until that load exceeds the preload. They then deflect at their original spring rate. In this respect, preloading does not alter the spring constant of the system but does alter the deflection characteristics. This is further discussed later.

The corresponding results for the finite element analysis are shown in figures 3.27(a) and (b). Here, the helical spring was subjected to a varying axial load for fixed internal line loading of 0.1 N/mm, 0.2 N/mm and 0.3 N/mm to simplify the analysis.

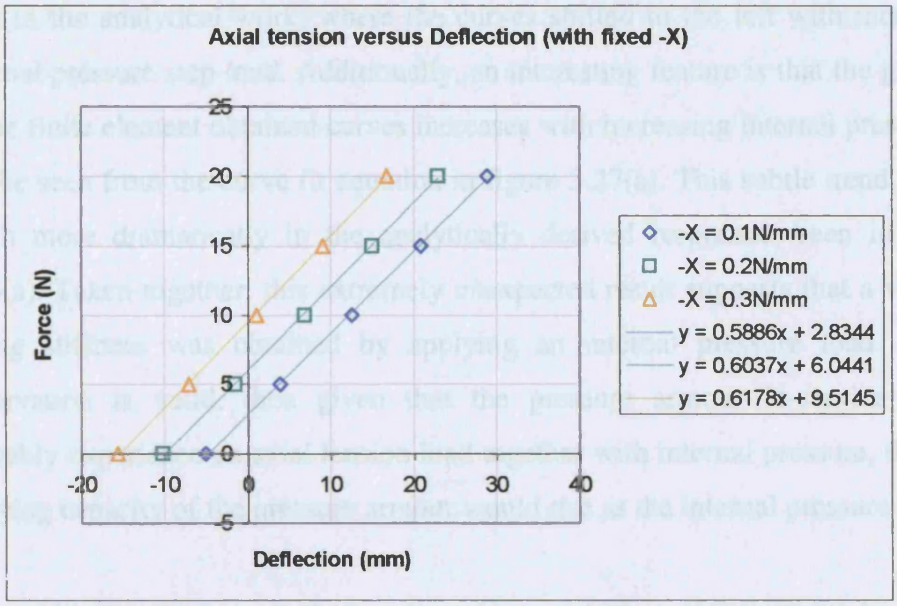

Figure 3.27a Finite element result for axial tension versus deflection for fixed internal line load

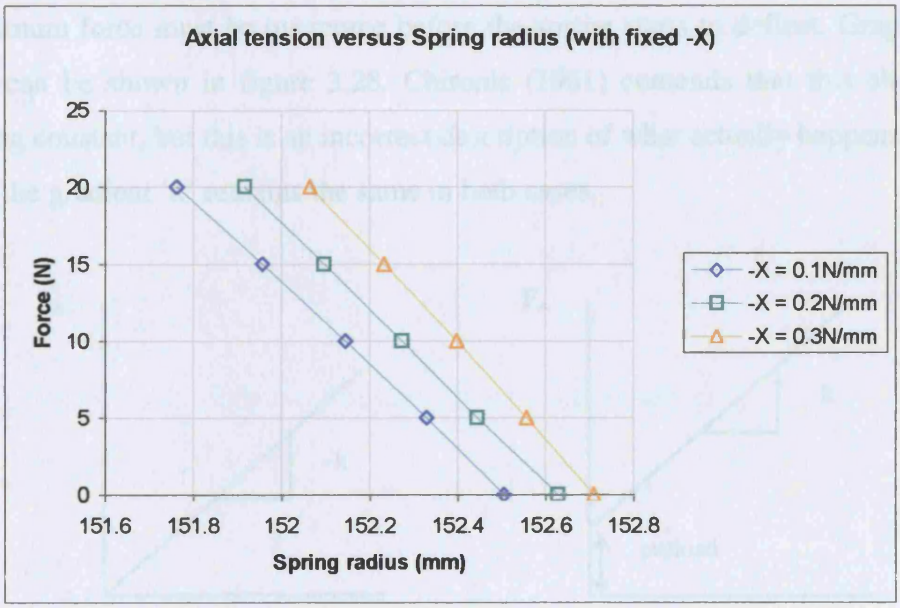

Figure 3.27b Finite element result for axial tension versus spring radius for fixed internal line load

The finite element analysis results in figures 3.27(a) and (b) confirmed the trend seen in the analytical work, where the curves shifted to the left with increasing internal pressure step load. Additionally, an interesting feature is that the gradient of the finite element obtained curves increases with increasing internal pressure as can be seen from the curve fit equation in figure 3.27(a). This subtle trend is seen much more dramatically in the analytically derived responses, seen in figure 3.26(a). Taken together, this extremely unexpected result suggests that a variable spring stiffness was obtained by applying an internal pressure load. If this observation is valid, then given that the pressure armour in-service would probably experience an axial tension load together with internal pressure, the load carrying capacity of the pressure armour would rise as the internal pressure rose.

It should be noted that a helical spring with a variable spring stiffness is entirely different from a spring with preload. Chironis (1961) described two methods of changing the stiffness of a spring system. The first method is to preload the spring. As described earlier, this means that the spring is prevented from moving back to its original free length position. An additional force is required to overcome the load preventing the spring from deflecting to its original length. Hence, a minimum force must be overcome before the spring starts to deflect. Graphically this can be shown in figure 3.28. Chironis (1961) contends that this alters the spring constant, but this is an incorrect description of what actually happens, given that the gradient 'k' remains the same in both cases.

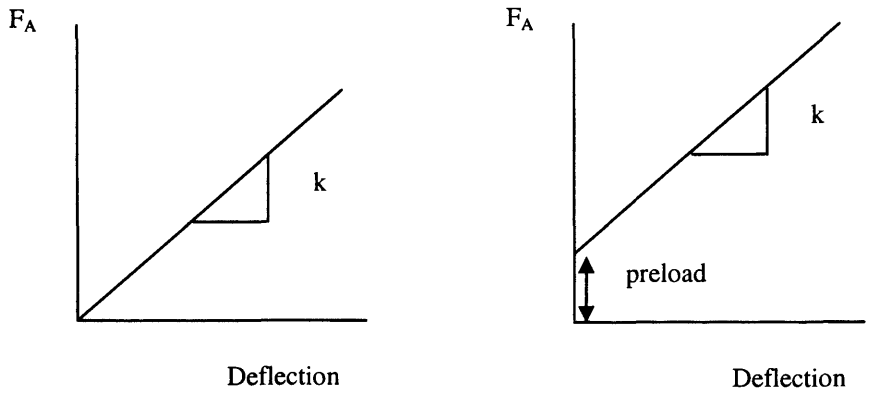

Figure 3.28 Change in curve of axial load versus deflection under preload

The second method, and one which genuinely delivers a system of variable spring rate (although not continuously variable), is to combine springs of different spring rates which will reduce the total spring stiffness of the system. For example, consider two springs, one with spring stiffness k_1 and the second with stiffness of k_2 shown in figure 3.29.

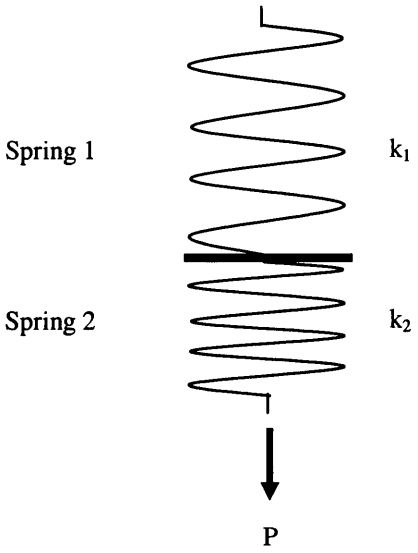

Figure 3.29 Helical springs arranged in series

The total spring stiffness of the system becomes

$$\frac{1}{k_{total}} = \frac{1}{k_1} + \frac{1}{k_2}$$

$$k_{total} = \frac{k_1 k_2}{k_1 + k_2} \tag{3.85}$$

and a typical load – deflection response is shown in figure 3.30.

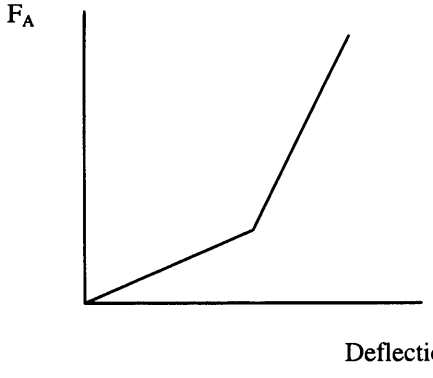

Figure 3.30 Load – deflection response of combined helical springs

Furthermore, both methods can be combined together, to generate further degrees of freedom of the deflection of the system. In practical terms, this procedure is used in applications where variable damping is required such as in the automobile industry.

Returning to the earlier analysis, it is clear form the finite element analysis and analytical responses, that the application of a preload, of the type discussed by Chironis (1961), can be achieved by subjecting a helical spring to an internal pressure. As an aside, this offers some interesting technological advantages over mechanical preloading, in that a pressure derived preload can be varied and removed at will. It should be remembered, however that in preloading, the actual spring stiffness of the helical wire itself does not change but the load-deflection curve is altered to accommodate a new load-deflection characteristic which can be customized to a particular application or purpose. This applies equally to both the mechanically generated preload condition and the pressure generated preload.

As described earlier, a series of springs are required to produce multi-rate stiffness in a spring, but the rates present in the system cannot be altered during operation. In essence, they are predetermined by the springs selected. However, the behaviour seen in figure 3.26(a) indicates that the application of an internal pressure load can alter the absolute spring rate. Given that the pressure load can be removed and applied infinitely, the change in the stiffness can also be varied infinitely. Once an internal pressure load is applied to a spring, the spring stiffness of that spring changes to a new value and remains constant whilst the pressure is maintained. The reason for this behaviour clear but the author believes that the subtle changes in the geometry of the spring when under internal pressure act to alter its subsequent behaviour under load (and by definition, its stiffness).

This can be illustrated by the following argument. Consider two springs of different dimensions as shown in figure 3.31. Each of the springs will have its own spring stiffness due to the difference in overall length and in spring radius. Assume that the chosen spring geometry and load scenario such that helical spring 1 deflects to the length of spring 2 and also contracts in dimension to reach the same spring radius as of helical spring 2. Subsequently, when the springs are

loaded axially, it would be expected that because the spring dimensions are the same, their spring stiffness should be the same, but this ignores the fact that the stress state in the material of spring 1 is different from that of spring 2. It should be noted that the springs originally had different spring constants and that these are unlikely to change during extension (unless large extensions are applied). The fact that the springs retain their original stiffness value despite one being tensioned, was confirmed by the author using slender rod analysis, which showed that the two springs maintained the difference in their spring constants. It can therefore be concluded that the spring constant is determined not just by geometry and dimension but also by the stress state in the spring wire. The spring stiffness of helical spring 1 (which is strained to the size of helical spring 2) is higher compared to helical spring 2 because of the axial tension loading that is present. It is thought that this causes the strain of the helical wire to increase. An increase in the strain leads to an increase in the overall stiffness of the wire and thus the helical spring structure, because the wire is predicted to be longer. This increase in length is extremely small and was measured to be micro strains using the finite element modelling.

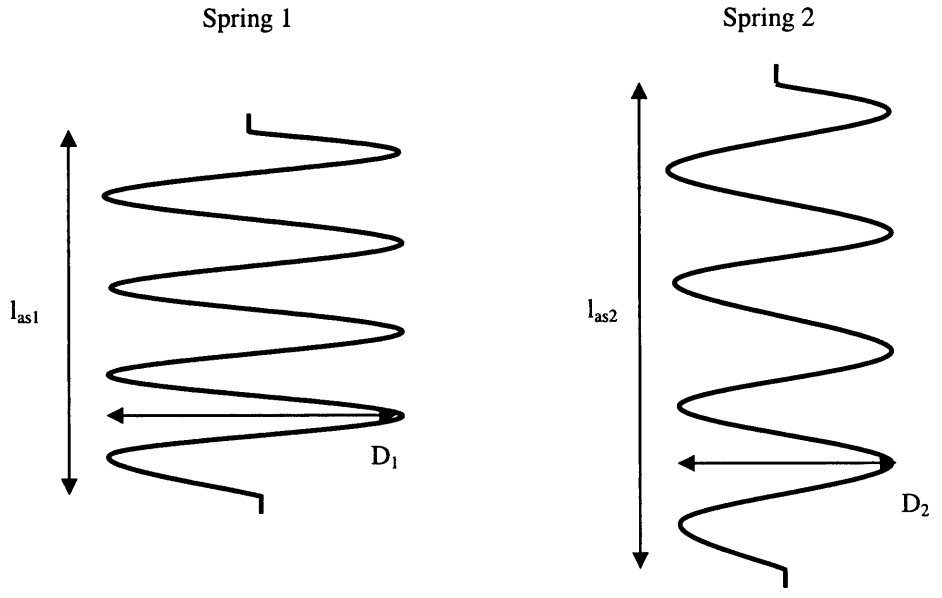

Figure 3.31 Springs of different dimensions

As has been shown, the internal pressure loading will alter the dimensions of the spring and acts as a preload, but the presence of the line tension also ensures that the spring constant is altered too. These two effects can clearly be observed in figure 3.26(a) where the preload is responsible for the change in x-axis intercept and the tension effect alters the gradient of the load – deflection response. The effect of an internal pressure is to raise the spring constant, commensurate with a rise in the tension of the wire. It should be noted that a supplementary effect might also be present given that as the spring radius of the spring gets smaller due to the axially applied load, the internal pressure now acts on a smaller radius and hence increases the tension in the wire further. However, this is probably a second order effect, given that it would suggest a change in the spring constant as the axial load is increased and this was not observed.

Figures 3.32(a) and (b) show the response of the helical spring subjected to axial *compression* load with fixed internal pressure. For a varying axial *compression* load on a spring under an applied internal pressure, the linear relationship in figure 3.32(a) shows that a larger compressive force is required to produce the same deformation. Thus, it can be observed that the spring stiffness also increases with increasing internal pressure, due to an increase in wire tension.

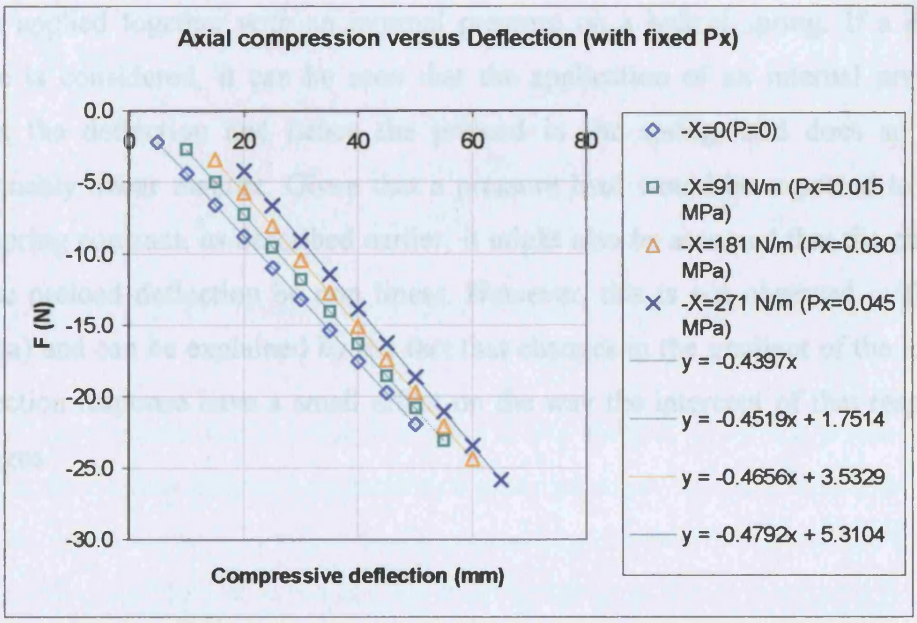

Figure 3.32a Axial compression versus deflection for fixed internal pressure step values

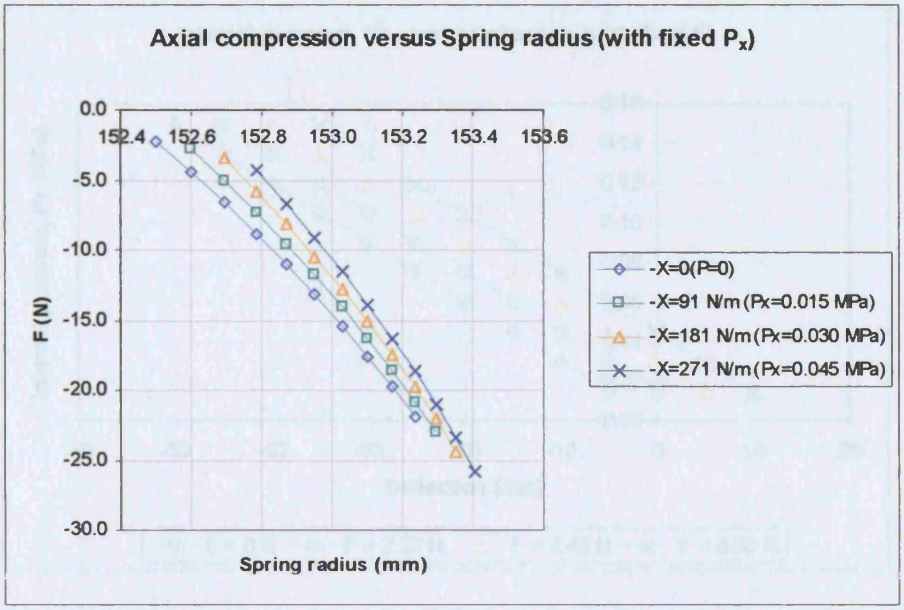

Figure 3.32b Axial compression versus spring radius for fixed internal pressure step values

Figure 3.32(b) shows the corresponding change in spring radius under axial compressive force (with internal pressure load fixed). Result of helical spring subjected to varying internal pressure with the axial tension load fixed at various load steps is presented in figures 3.33(a) and (b). In figure 3.33(a), axial load steps were applied together with an internal pressure on a helical spring. If a single curve is considered, it can be seen that the application of an internal pressure alters the deflection and hence the preload in the spring, and does so in a reasonably linear manner. Given that a pressure load would be expected to alter the spring constant, as described earlier, it might also be assumed that the change in the preload deflection be non linear. However, this is not observed in figure 3.33(a) and can be explained by the fact that changes in the gradient of the load – deflection response have a small effect on the way the intercept of that response changes.

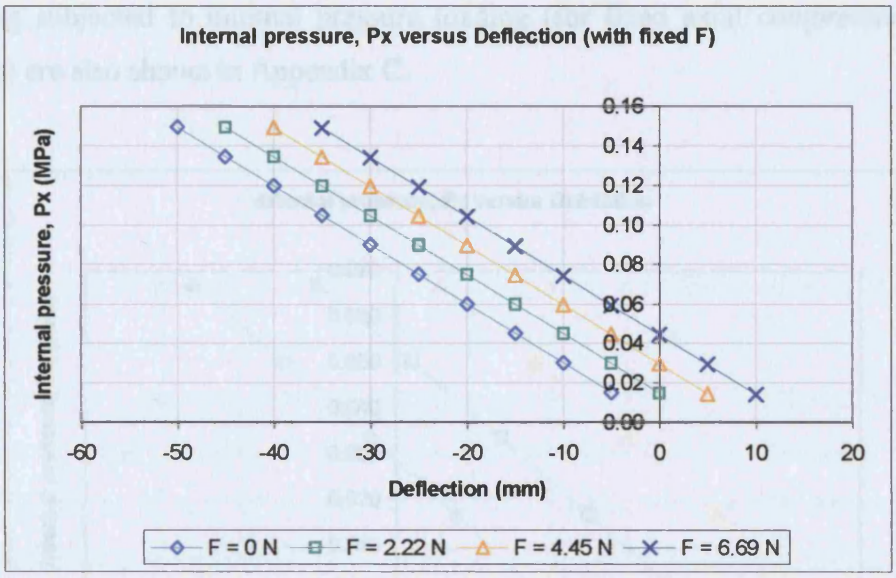

Figure 3.33a Internal pressure versus deflection for fixed axial tension step values

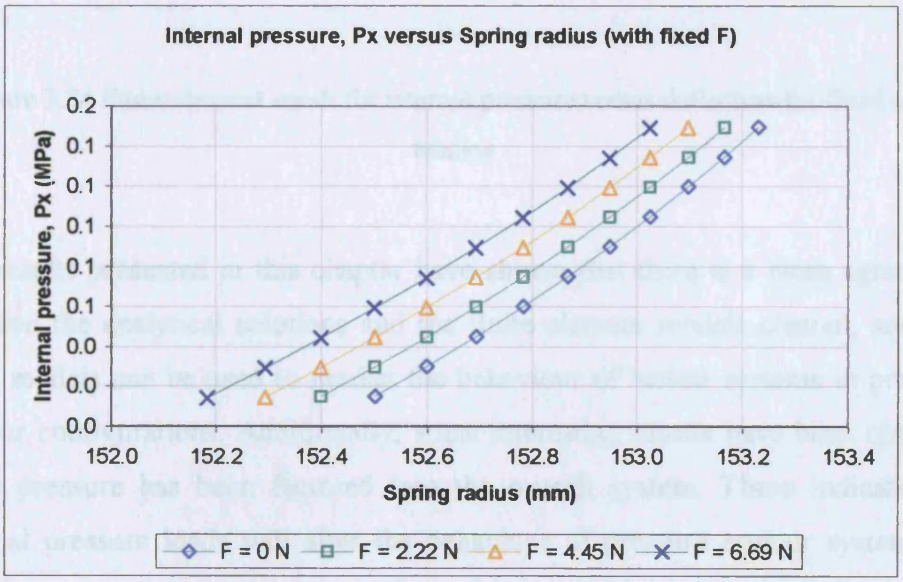

Figure 3.33b Internal pressure versus spring radius for fixed axial tension step values

The finite element analysis result (figure 3.34) showed a similar trend to the analytical solution although numerical model did show a higher stiffness. This was discussed earlier and is due to the constraint placed on the helical spring coil in the radial direction to avoid the coil from opening up due to pressure load. The corresponding response of the change in the spring radius with respect to the internal pressure is shown in Appendix C. Additionally, results for the helical

spring subjected to internal pressure loading (for fixed axial *compressive* load steps) are also shown in Appendix C.

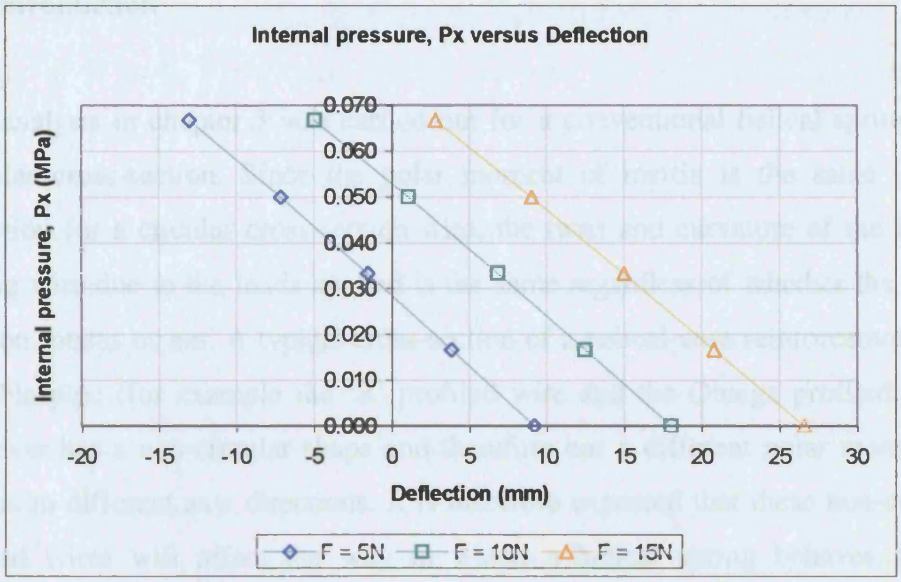

Figure 3.34 Finite element result for internal pressure versus deflection for fixed axial tension

The results presented in this chapter have shown that there is a close agreement between the analytical solutions and the finite element models created, and that these models can be used to predict the behaviour of helical systems in pressure armour configurations. Additionally, some interesting results have been obtained when pressure has been factored into the overall system. These indicate that internal pressure loads will alter the behaviour of pressure armour systems. In particular, the change in spring stiffness with applied pressure suggests that the conditions within a flexible pipe need to be considered more closely in future analyses. Rather interestingly, the ability to alter spring stiffness by the presence of an internal pressure may have applications outside of the flexible pipe area and are the subject of a patent application by the author.

The following chapter extends the theory of helical wire to accommodate non-circular profiles. Behaviour of non-symmetric cross-sections due to the various loading modes was discussed.

4 Analysis of Helical Spring for Various Cross-sectional Shapes

4.1 Introduction

The analysis in chapter 3 was carried out for a conventional helical spring with circular cross-section. Since the polar moment of inertia is the same in any direction for a circular cross-section wire, the twist and curvature of the helical spring wire due to the loads applied is the same regardless of whether the cross-section rotates or not. A typical cross-section of a helical wire reinforcement of a flexible pipe (for example the 'Z' profiled wire and the Omega profiled wire), however has a non-circular shape and therefore has a different polar moment of inertia in different axis directions. It is therefore expected that these non-circular shaped wires will affect the way in which a helical spring behaves due to differences in twisting responses of the wire cross-section. A knowledge of orientation of the cross-section with respect to the spring axis is also required for complete understanding of the mechanical response.

This chapter investigates the effect of different loading modes on the various cross-sectional shapes of relevance to pressure armour. Furthermore, it is important to examine how helical springs with different cross sections, whether they are symmetrical about some axis (such as square or rectangular or asymmetrical sections), twist with applied internal pressure and/or axial loads. This twisting effect of the helical wire will tend to generate a stress gradient across the cross-section of the wire. This in turn implies that the profile that twists is not efficient in resisting pressure loads and that cross-sections with more uniform stress are likely to withstand higher pressures.

The analysis presented here begins with a theory of relatively simple non-circular shape helical springs (square and the rectangular sections), and is based on conventional spring theory as given by Timoshenko (1955) and Wahl (1963). More complex cross-sections such as the L, Z and Omega profiles require a

rigorous analytical model based on Love's equilibrium equation and will be considered later in this chapter.

It must be emphasized here that all the analyses were performed for helical springs with ends fixed from rotation, as was first discussed in chapter 3. Although a simplification, this constraint is similar to that found in the end fittings of pressure armour system, which prevents the helical wire from coiling/uncoiling when loads are applied. Issues of end constraints are revisited in chapter 6. From the assumption, it follows that the number of coils of the helical spring remains the same under load, because the helical wire does not coil/uncoil. Also, it is assumed that the wire cross-section does not rotate with applied axial loading and any rotation is due to pressure only. In the scenarios investigated here, the helical spring cross-section can rotate due to the moment generated on the non-symmetric sections by the internal pressure loading. For symmetric sections, the analysis is straightforward and is discussed in the next section.

4.2 Symmetrical Cross-Sections

4.2.1 Basic Spring Theory

Helical springs with non-circular cross-sections are rarely found in industry and are mainly restricted to square and rectangular cross-section wires. This is due to the fact that a non-uniform stress distribution is present in such a cross-section compared to circular cross-sections when loading is applied as discussed in Wahl (1963). The stress concentrations that are generated can affect the fatigue life. Their main advantage, however, is that they can store more elastic energy compared to circular cross-section springs, of a given overall dimension. This section presents the basic theory of closed-coil helical springs for symmetrical sections of square and rectangular nature. Timoshenko (1955) presented an analytical solution for the helical spring for generalized cross-sections.

As described previously, equation 3.1 in chapter 3 gave the expression of the torque on the helical spring elements due to the axial force, F_A. The total deflection of a spring, δ was obtained by summing the deflection due to all the elements along the length of the spring and is given here as

$$\delta = \frac{2\pi n F_A R^3}{GJ} \tag{4.1}$$

where R = radius of helical spring

G = shear modulus of spring material

J = polar moment of inertia

When the polar moment of inertia of the appropriate cross-section is taken into account, the solutions yield the same form as of Wahl (1963) for square and rectangular cross-sections. Because of the warping of non-circular cross-sections (Timoshenko and Goodier, 1970), the corrected polar moment of inertia due to this effect has to be taken into account and these values can be obtained from Young (1989).

Wahl (1963) discussed the design of these square and rectangular cross-section helical wires in detail for axial loading. The curvature of square cross-section springs has a significant effect on the deflection calculations. Hence the corrected stress due to effects of curvature was taken into account for the deflection derivation (Wahl, 1963).

For square cross-section wire, the deflection, δ, and spring stiffness, k, is given by Wahl (1963) as

$$\delta = \frac{44.72 F_A R^3 n}{G a_s^{\,4}} \tag{4.2}$$

$$k = \frac{Ga_s^4}{44.72R^3n} \tag{4.3}$$

where F_A = axial load

D = diameter of helical spring

R = radius of helical spring

G = shear modulus of spring material

a_s = length of side of square cross-section

The calculation for the deflection of a rectangular helical spring is more complicated than a square cross-section. Correction factors that depend on the dimensions of the rectangular section must be included in order to obtain accurate deflections. This correction factor is given in Wahl (1963), adapted from an earlier solution based on a paper presented in German by Liesecke in 1933.

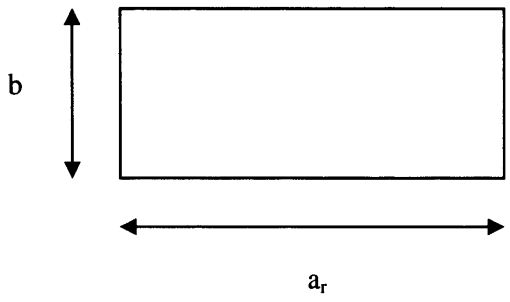

Figure 4.1 Dimensions of a rectangular cross-section

For a large spring index, the deflection is given by

$$\delta = \frac{8F_AR^3n}{k_{r1}a_rb^3G} \tag{4.4}$$

where k_{r1} = correction factor for large spring index which depends on ratio a_r/b

a_r = long side of rectangular cross-section

b = short side of rectangular cross-section

k_{r1} can be estimated from the table below as presented in Wahl (1963).

Ratio a_r/b	1	1.2	1.5	2	2.5	3	5	10	∞
k_{r1}	0.180	0.212	0.250	0.292	0.317	0.335	0.371	0.398	0.424

Table 4.1 Correction factors for rectangular cross-section spring

The deflection for a small spring index is given by

$$\delta = \frac{8k_{r2}F_A R^3 n}{a_r^2 b^2 G} \tag{4.5}$$

where k_{r2} = correction factor for small index spring

The correction factor chart is presented in figure 4.2.

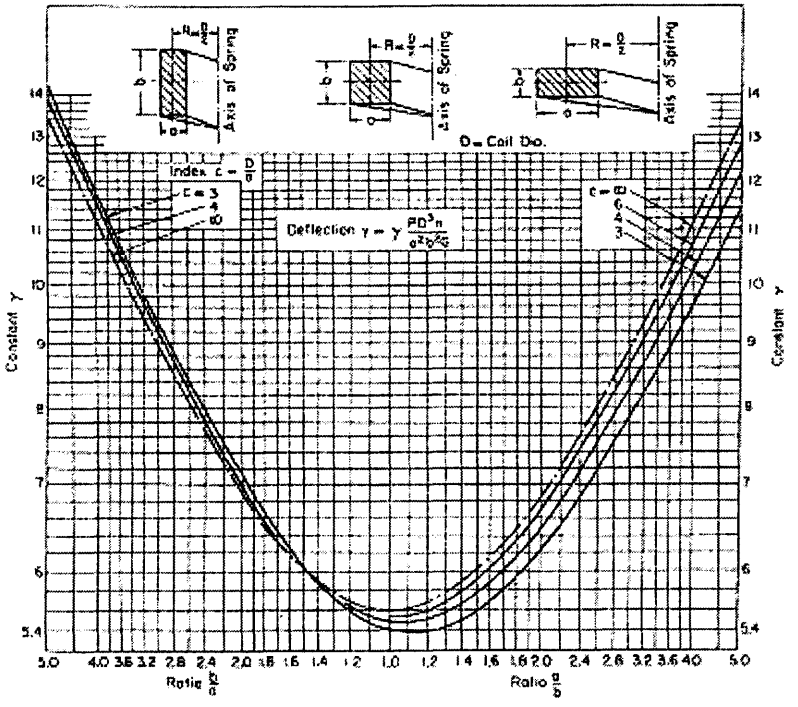

Figure 4.2 Correction factor chart for small spring index (Wahl, 1963)

Spring stiffness, k for rectangular cross-section wires is of the form shown below.

$$k = \frac{Ga_r^2 b^2}{8k_{r2}R^3 n} \tag{4.6}$$

If this equation was to be applied to a typical pressure armour layer configuration, a large spring index ratio is normally encountered and the appropriate deflection expressions would be used. It can be observed that the solution by Wahl (1963) is of the same form as of the analytical solution derived in the general solution by Timoshenko (1955) and can be used readily if the spring index ratio is known.

4.2.2 Slender Rod Theory

The slender rod theory offers many advantages in solving the deformation of a helical wire. Unlike Wahl's approach, the slender rod theory provides a route to solving for springs of various cross-sectional shapes, but it also can account for a combination of axial and internal pressure loading. The previous chapter applied the slender rod approach to circular cross-sections. Here it is applied to sections likely to be encountered in pressure armour. For symmetrical sections, the same underlying solution as presented in section 3.2.3 is valid for use. The only difference here is that the appropriate polar moment of inertia, J was chosen for the respective sections based on the corrected value due to effects of warping. Warping affects the shear strain of the cross-section, but does not affect the overall longitudinal and axial strain of wire because of the assumption that the wire behaves as a slender rod.

The appropriate sectional values for cross-sectional shapes such as square and rectangle can be input into equations 3.59 – 3.62 as before, and are presented again for the reader's ease.

$$T = AE\varepsilon_{aw} \tag{4.7}$$

$$G_n = EI_n\omega_1 \tag{4.8}$$

$$G_b = EI_b\omega_2 \tag{4.9}$$

$$H = GJ\omega_3 \tag{4.10}$$

From equation 3.71, the deflection of a helical spring subjected to axial loading can be described as follows:-

$$F_A = T\sin\alpha_1 + N_b\cos\alpha_1 \tag{4.11}$$

$$M = H\sin\alpha_1 + G_b\cos\alpha_1 + TR_1\cos\alpha_1 - N_bR_1\sin\alpha_1 \tag{4.12}$$

where the deflection is characterized in terms of its helical angle, α

If an internal pressure load is considered, it can be assumed that if it acts on a symmetric cross-sectional shape, no rotation of the section is observed because no moment is generated on the centroid of the cross-section. The internal pressure, as in the case of circular cross-section helical springs, will only cause the helical spring to expand its diameter and shorten its pitch length. Therefore the pressure – line load relationship for a helical spring subjected to internal pressure is as presented in chapter 3 and is given by

$$P_X d_w = -X \tag{4.13}$$

where P_X = internal pressure on helical wire

d_w = width of helical wire

Similarly, for combination of axial and internal pressure, equations 3.80 – 3.82 derived in the previous chapter can be used.

4.3 Non-symmetrical Sections

Non-symmetric cross-sections subjected to an internal pressure load would be expected to rotate. As the analysis here involves only cases where the helix ends are fixed (to simplify the problem), the rotation of the helical wire cross-section is assumed to be purely due to internal pressure load. It is known that the cross-section of a helical spring does rotate with respect to applied axial load. However, since the ends are fixed from coiling/uncoiling, this rotation of the cross-section is assumed to be prevented. Hence, the same expression as given in equation 4.11 can be used for the deflection of helical wire of non-symmetrical shape due to axial loading.

For cross-sections such as L, Z and the Omega, rotation of the cross-sections due to internal pressure loading occurs because a moment is generated on the centroid of the cross-section and not due the helical spring movement. Thus a pressure load will likely alter the helix configuration and this may have important implications on the load carrying capacity (in terms of pressure) of the pressure armour.

The next section analyzes the angle of twist of a non-symmetric helical wire cross-section due to internal pressure.

4.3.1 Angle of Twist of a Cross-Section

Within the literature, some work has been performed on the twisting of pressure armour cross-sections under internal pressure loading. The angle of twist of a helical wire cross-section is conventionally taken as similar to that of the angle of twist of a ring cross-section. This is a common and simplifying assumption given that the helical wire is usually of small helix angle. The helical wire structure can then be modelled in finite element analysis as an axisymmetric problem, for example as was done by Chen et al (1995). They presented a simple analytical model which described the global axial deformation of flexible pipes, with frictional forces between layers neglected and small displacements of the pipe

assumed. Chen et al (1995) modelled the internal carcass and pressure armour reinforcement as thin rings. In reality however, both the internal carcass as and pressure armour structures are actually helical in shape (albeit of small helix angle). Although a helical wire can be described as 'closed-coil', that is having a small helix angle, the axisymmetric ring assumption is too simplified. The ring is akin to a short span of a pressure vessel, thus, is more rigid when compared to a helical spring, which would be connected to its next coil. Therefore it was expected that the axisymmetric modeling would produce some error due to the rigidity of the ring and that the angle of twist of a ring cross-section would be smaller than the actual angle of twist of a helical wire cross-section, when an internal pressure was applied.

Nevertheless, the angle of twist of a ring cross-section is described here first and then compared to a solution developed in this work for the angle of twist of a helical wire cross-section. This is then factored into consideration during axisymmetric modelling of a helical spring structure.

A general solution for the angle of twist of a ring cross-section was presented by Timoshenko (1956). Considering the forces on half of the ring as shown in figure 4.3, the degree of twist was presented for a generalized local system that created a twisting moment.

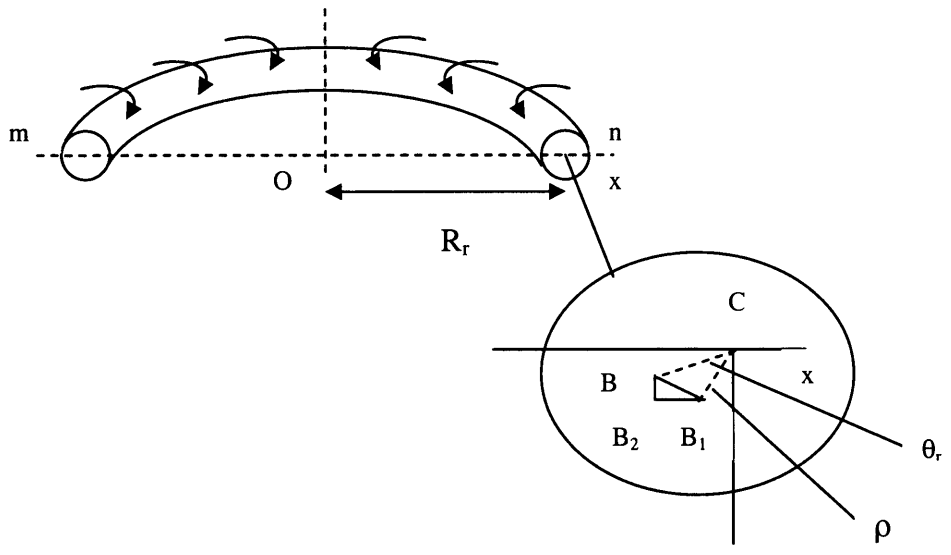

Figure 4.3 Cross-section of half of ring

For condition of equilibrium, there is a twisting moment, M_r acting across the cross-section *mn*, shown in figure 4.3. This gives

$$M_r = M_t R_r \tag{4.14}$$

where M_t = twisting couple per unit length

R_r = radius of ring

The following is summarized from Timoshenko (1956). Point C is defined as the centre of rotation and the angle θ_r, is the twisting angle of the ring cross-section. If the point in the cross–section starts rotating from B to B_1, using similarity of triangles as shown in the figure, then distance B_1B_2 can be measured and is given by

$$B_1B_2 = \theta_r y \tag{4.15}$$

This assumes that the rotation is small and the distance is inscribed by a small arc of the twisting angle θ_r.

Following this, the radial strain, ε can be defined and is given as

$$\varepsilon = \frac{\theta_r y}{R_r} \tag{4.16}$$

The stress, σ due to this radial strain is then given by

$$\sigma = \frac{E\theta_r y}{R_r} \tag{4.17}$$

where E = Young's modulus of the material

From the equilibrium of half of the ring, the sum of the normal forces acting on the cross-section must equal zero and the moment of the forces about the x axis must equal the twisting moment, M_r. Hence

$$\int \frac{E\theta_r y}{R_r} dA = 0 \tag{4.18}$$

$$\int \frac{E\theta_r y^2}{R_r} dA = M_r \tag{4.19}$$

where dA = elemental area of cross-section

Expression 4.18 confirms that the centroid of the cross-section lies at some point on the x-axis. Equation 4.19 defines the twisting angle in terms of the twisting moment. For the purpose of this analysis, it is assumed that the internal moment is generated by an internal pressure loading on the inside of the coil. Integration of equation 4.19 gives rise to

$$\theta_r = \frac{M_t R_r^2}{EI_x} \tag{4.20}$$

where I_x = moment of inertia of ring cross-section with respect to x-axis

If instead of a ring, a helix is now considered, it can be shown that there exists a definite difference in the twisting response. It must be stressed that the rotation of the cross-section of the helix is solely due to the moment generated by the internal pressure, given the constraint conditions imposed as described earlier.

Figure 4.4 shows the twisting moment generated by an internal pressure on a short element of the non-symmetric cross-section helical spring.

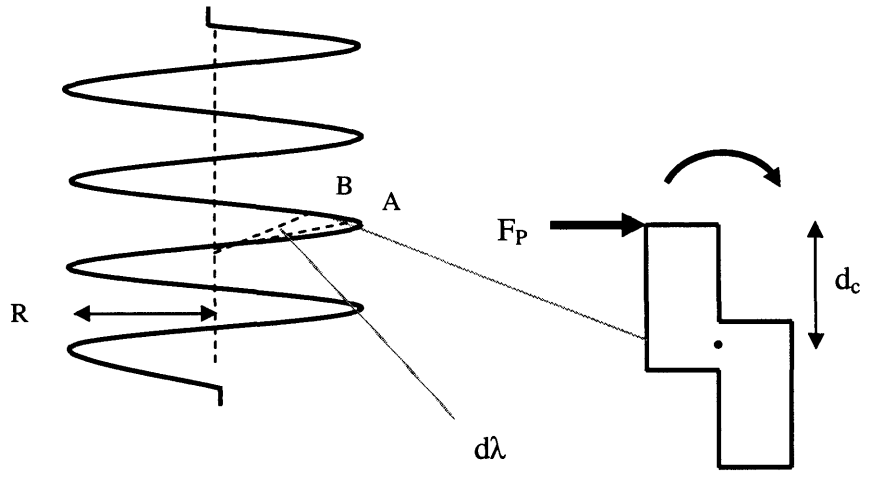

Figure 4.4 Twisting moment on helical spring of non-symmetric cross-section

It is assumed that the helical spring has a small helix angle and its ends are fixed from rotation, therefore, the number of helical coils remains the same. Also, the centroid of the cross-section is taken to coincide with the centreline of the helical wire since the cross-sectional dimension is assumed to be small compared to the dimensions of the helical spring.

The twisting moment, M_C about the centreline of the wire due to internal pressure load is then given by

$$M_C = F_P d_c \tag{4.21}$$

where F_p = Equivalent force due to internal pressure

d_c = distance of load to centroid of cross-section

Now, the small cylindrical element AB is considered. The length of this element is given by $Rd\lambda$, where $d\lambda$ is the angle of arc of the element. The twisting moment of a cylindrical element is commonly known and given in Young (1989) as

$$M_C = GJ\frac{\varphi}{l} \tag{4.22}$$

where G = shear modulus of spring material

J = polar moment of inertia of cross-section

φ = angle of twist of cross-section

l = length of element

Equation 4.21 and 4.22 can be combined to obtain an angle of twist per length of element of the helical wire cross-section element due to internal pressure load. This is given by

$$\frac{d\varphi}{dl} = \frac{F_P d_c}{GJ} \tag{4.23}$$

Integrating expression 4.23 for *n* helical coils, the total angle of twist of the helical wire cross-section can be obtained. The solution gives

$$\varphi = \frac{F_P d_c}{GJ}\int_0^{2\pi n} Rd\lambda$$

$$\varphi = \frac{2\pi RnF_P d_c}{GJ} \tag{4.24}$$

It must be noted that the corrected polar moment of inertia value obtained from Young (1989) should be used for the respective cross-section. Inspection of the equations of the angle of twist of a ring cross-section (equation 4.20) and helical coil (equation 4.24) was performed by substitution of values for an L shape cross-section with dimensions shown in figure 4.7 (see later). In this instance, angle of twist of ring gave 0.01 degrees while angle of twist of closed-coil helical cross-section gave 1.05 degrees based on a 15.24 mm (6") helix radius and coil

deflection of 5 mm. It can be concluded that the values generated by the angle of twist of helical coil will always be larger.

4.3.2 Analytical Solution Based on Slender Rod Theory

The analytical solution presented here by the author considered the change to the equilibrium equation due to twisting of the helical wire cross-section. When twisting of the helical wire cross-section is taken into account, the twist and curvatures of the centreline changes accordingly by an angle φ, therefore changing the constitutive equations in expression 4.8 – 4.10. Figure 4.5 shows the change in curvature of the centreline due to twisting of a helical wire cross-section, where twist in the anticlockwise direction is taken to be positive.

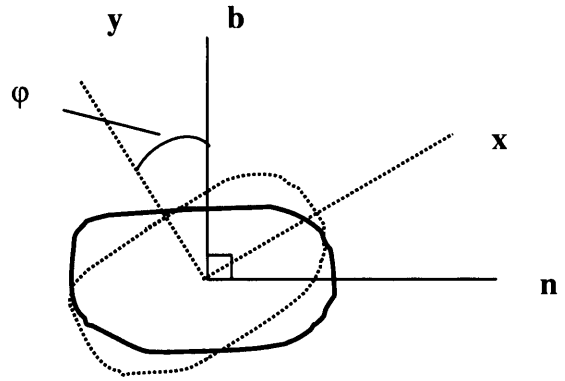

Figure 4.5 Angle of twist and change in curvatures of the centerline of wire

After twist of cross-section occurs through the **xy** plane, the new component of curvatures in the principal normal, κ_{n1}' and binormal, κ_{b1}' of the centreline of the wire are

$$\kappa_{n1}' = \kappa_{b1} \sin\varphi \tag{4.25}$$

$$\kappa_{b1}' = \kappa_{b1} \cos\varphi \tag{4.26}$$

The angle of twist of the cross-section, φ corresponds with the angle π/2 – f defined by Love (1934) as shown in figure 4.6 below. The angle π/2 – f is defined as the angle between the principle plane of the rod and the principal normal of the centreline. In other words, when the rod cross-section is rotated clockwise the angle that the cross-sectional plane makes with the rod centreline normal axis is the angle of twist of the cross-section. The angle f as mentioned in Love (1934) then corresponds to the angle defined by Ramsey (1988) shown in equation 3.58 in the previous chapter and is related to the strain variables in the equations.

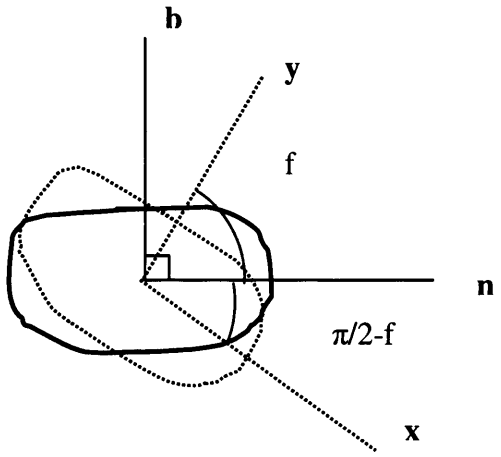

Figure 4.6 Angle between principal plane of cross-section and the centerline of wire

Therefore expressing angle f in terms of the author's defined angle of twist of cross-section,

$$f = \frac{\pi}{2} - \varphi \tag{4.27}$$

As shown previously in chapter 3, the slender rod equation by Love (1934) was given in equation 3.46 – 3.51. When changes in the twist and curvature are taken into account, for an internal pressure load, the set of equilibrium equations reduce to

$$-N_b\tau_1 + T\kappa_{b1}\cos\varphi + X = 0 \tag{4.28}$$

$$-T\kappa_{b1}\sin\varphi + N\tau_1 = 0 \tag{4.29}$$

$$-N\kappa_{b1}\cos\varphi + N_b\kappa_{b1}\sin\varphi = 0 \tag{4.30}$$

$$-G_b\tau_1 + H\kappa_{b1}\cos\varphi - N_b = 0 \tag{4.31}$$

$$-H\kappa_{b1}\sin\varphi + G_n\tau_1 + N = 0 \tag{4.32}$$

where - X = internal line load

N, N_b, T = resultant internal forces

G_n, G_b, H = resultant internal moments

From 4.8 – 4.10, taking the new values of curvatures due to twisting of the cross-section, the internal moments now have the following form respectively (assuming small strain of wire).

$$G_n = EI_n\kappa_{b1}\sin\varphi \tag{4.33}$$

$$G_b = EI_b\kappa_{b1}\cos\varphi \tag{4.34}$$

$$H = GJ\left(\tau_1 - \tau_0 + \frac{df}{ds}\right) \tag{4.35}$$

where f = angle between cross-section principal axes to rod centreline principal normal

s = arc length

Equations 4.30 – 4.32 are found to be redundant, and show the relationship between the normal and binormal shear force, while equation 4.29 expresses the shear force in the normal direction in terms of its wire tension.

Hence, the solution of a non-symmetrical helical spring subjected to internal pressure, P_X (knowing the relationship of internal pressure to the line loading as

given in equation 4.13 and knowing the tension in the wire) is given by solving equations 4.28 and 4.31, thus,

$$P_X = \frac{T\kappa_{b1}\cos\varphi - \left(H\kappa_{b1}\cos\varphi - G_b\tau_1\right)\tau_1}{d_w} \tag{4.36}$$

For the combination of axial and internal pressure load, equations 3.80 - 3.82 derived previously can be used. However, it must be noted that the internal pressure on the helical wire is now taken from equation 4.36. For the cases of a helical spring (ends fixed from twisting) subjected to axial loading with fixed internal pressure load, the respective binormal shear force value for the axial loading is used. This should not be confused with the binormal shear force derived for the internal pressure as shown above.

The results calculated from the analytical solutions are given later in this chapter. Analytical solutions for the helical spring subjected to the various loading modes were verified using finite element modelling and is described below.

4.4 Non-circular Helical Spring Verification using Finite Element Modelling

The finite element modeling procedure as described in section 3.4.2 was used to verify the response of helical coils of various cross-sections, and will not be repeated here. As previously, the helical coil was modelled using beam elements 10 degree turn apart from each other. The material employed was a typical steel with a Young's modulus of 207 GPa and a Poisson's ration of 0.33. A helical spring radius of 152.4 mm (6") was used. Figure 4.7 shows the dimensions of the helical wire cross-section used, which corresponded to the same area as of the circular cross-section wire modelled in chapter 3. This was done to assist the comparison of the load carrying capacity for the different profiles.

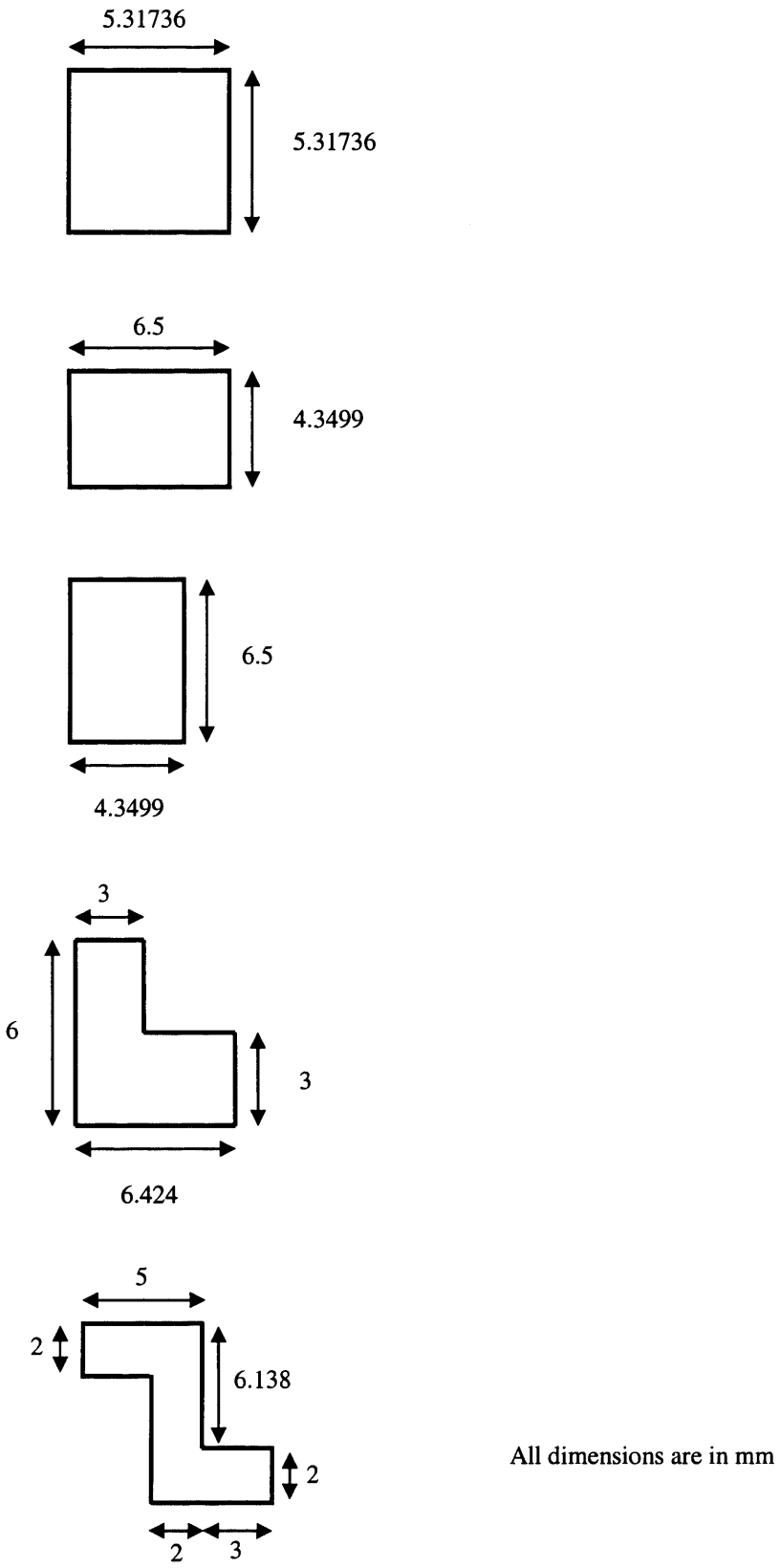

All dimensions are in mm

Figure 4.7 Various helical wire cross-section dimensions

For the verification of angle of twist of the cross-section of a helical spring subjected to internal pressure, a 3-dimensional solid coil was modelled. The dimensions used were similar to those of the beam element models built previously. The non-symmetric cross-sectional dimensions given above were used. Figure 4.8 shows the helical coil of one pitch length modelled using the Z-section profile.

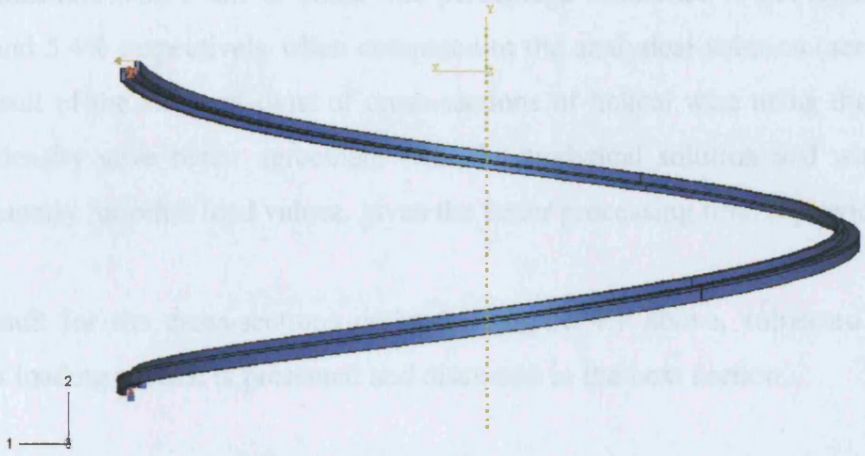

Figure 4.8 Helical coil model for angle of twist of cross-section

The coil was pinned at the centreline of the wire at both ends to prevent the coil from being displaced from its current position. This was done in order to correctly simulate the twisting moment generated by the internal pressure on the surface of the coil, which would twist the cross-section of the helical coil. The force equivalent to this internal pressure was applied at one end of the coil as shown in figure 4.8 as a consequence of the peculiarities of the finite element package used. Coils with mesh densities of 5796 and 10320 elements were used and the comparison of the angles of twist generated is shown in table 4.2.

Mesh density (no. of elements)	5796	10320
Angle of twist, φ (degrees)	5.5	5.3
Run time (mins)	10	25

Table 4.2 Comparison of angle of twist of cross-section of helical spring for 5 mm axial compression due to internal pressure

The calculated run time was typical for analysis performed using a Pentium IV based machine with 1 GB of Ram. The percentage difference in the results was 1.8% and 5.4% respectively when compared to the analytical solution (see later). The result of the angle of twist of cross-sections of helical wire using the lower mesh density gave better agreement with the analytical solution and was used subsequently for other load values, given the faster processing time it provided.

The result for the cross-sections defined in figure 4.7 above, subjected to the various loading modes, is presented and discussed in the next section.

4.5 Results of Analytical Solution and Finite Element Analysis

The analytical results for the helical wire cross-sections shown in figure 4.7 subjected to axial load showed similar trends to that of the circular cross-section wire as described previously.

4.5.1 Results for Axial Loading

For a given axial tension load, the helical spring increases in length while the spring radius decreases. It should be noted that the analytical solutions applied to helical wire with ends fixed from rotation. This meant that a twisting moment was induced as a result of such a constraint. Finite element analysis showed good agreement with the analytical result. Slight discrepancies were obtained for the L and Z-sections, which could be due to the estimation of the section properties obtained from the formula in Young (1989). Individual graphs for the responses

seen for the various cross-sections are shown in Appendix D. Here, only comparison of the result is presented and shown in figure 4.9(a) - 4.9(d).

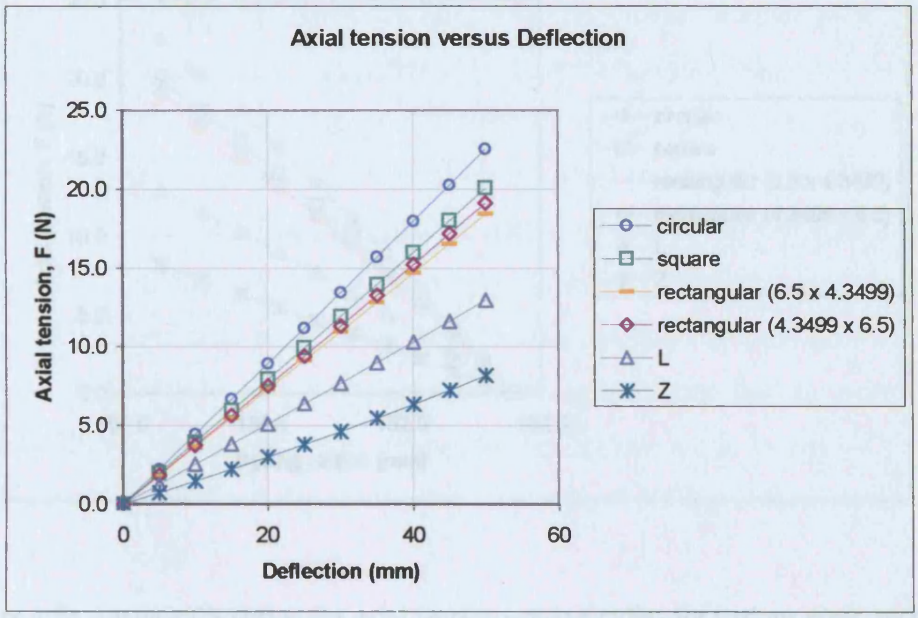

Figure 4.9a Analytical solution for axial tension – deflection for various cross-sections

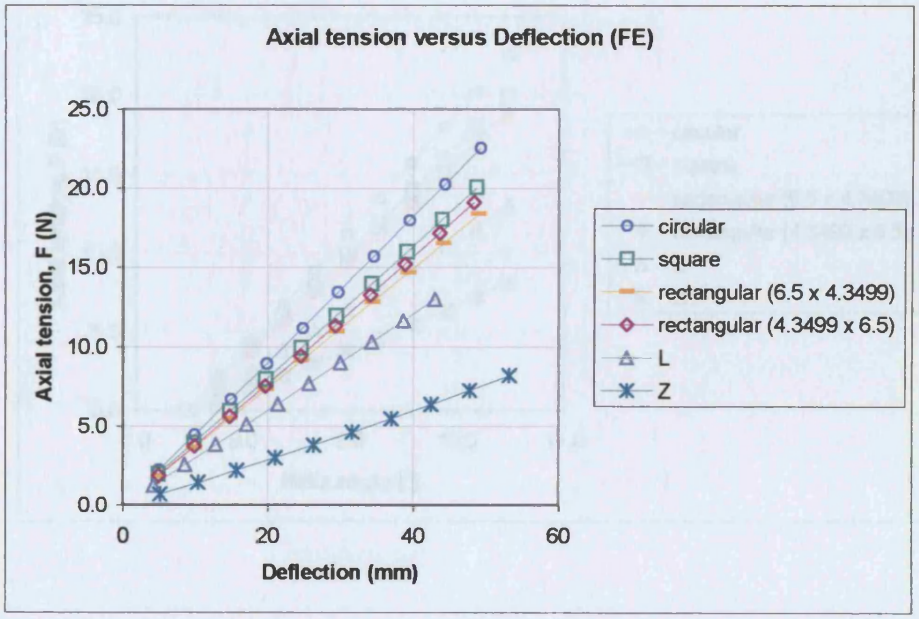

Figure 4.9b Finite element for axial tension – deflection for various cross-sections

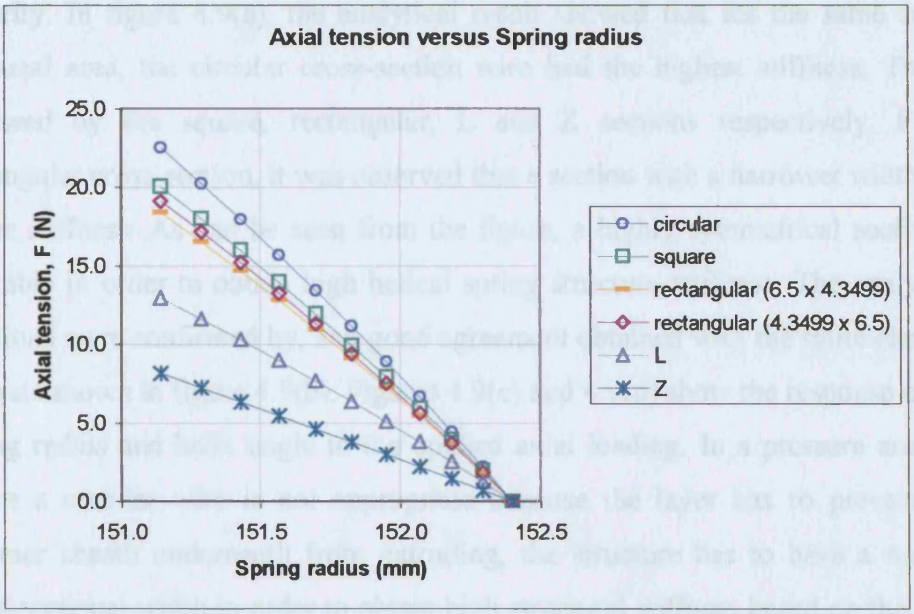

Figure 4.9c Analytical solution for axial tension –spring radius for various cross-sections

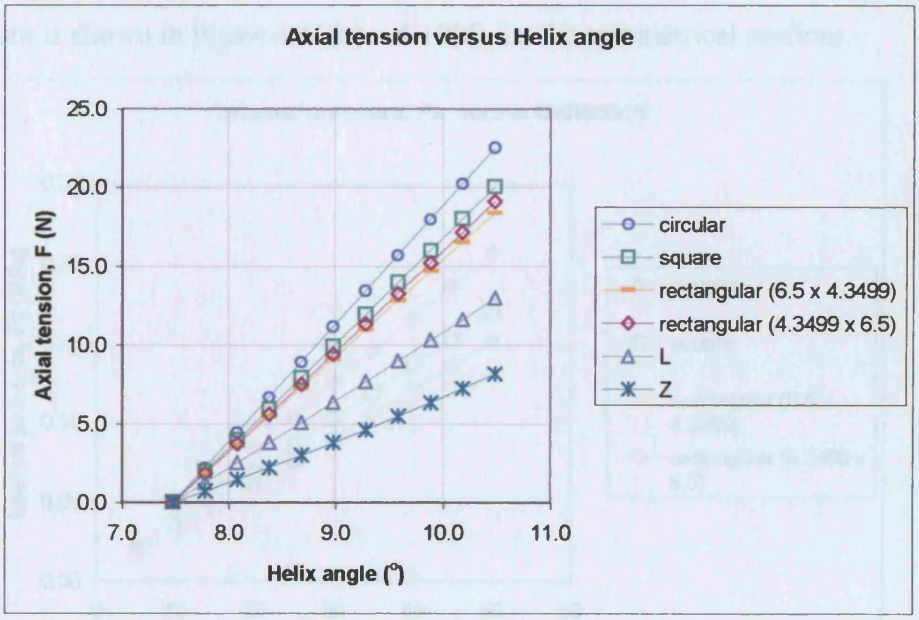

Figure 4.9d Analytical solution for axial tension – helix angle for various cross-sections

For all cross–sections, the axial tension versus deflection curves showed high linearity. In figure 4.9(a), the analytical result showed that for the same cross-sectional area, the circular cross-section wire had the highest stiffness. This is followed by the square, rectangular, L and Z sections respectively. For a rectangular cross-section, it was observed that a section with a narrower width had larger stiffness. As can be seen from the figure, a highly symmetrical section is desirable in order to obtain high helical spring structure stiffness. The analytical solutions were confirmed by, and good agreement obtained with the finite element analysis shown in figure 4.9(b). Figures 4.9(c) and 4.9(d) show the response of the spring radius and helix angle to the applied axial loading. In a pressure armour, where a circular wire is not appropriate because the layer has to prevent the polymer sheath underneath from extruding, the structure has to have a narrow cross-sectional width in order to obtain high structural stiffness based on the axial loading mode result.

4.5.2 Results for Internal Pressure Loading

Similarly, the comparison of results of the helical spring subjected to internal pressure is shown in figure 4.10(a) – 4.10(d) for the symmetrical sections.

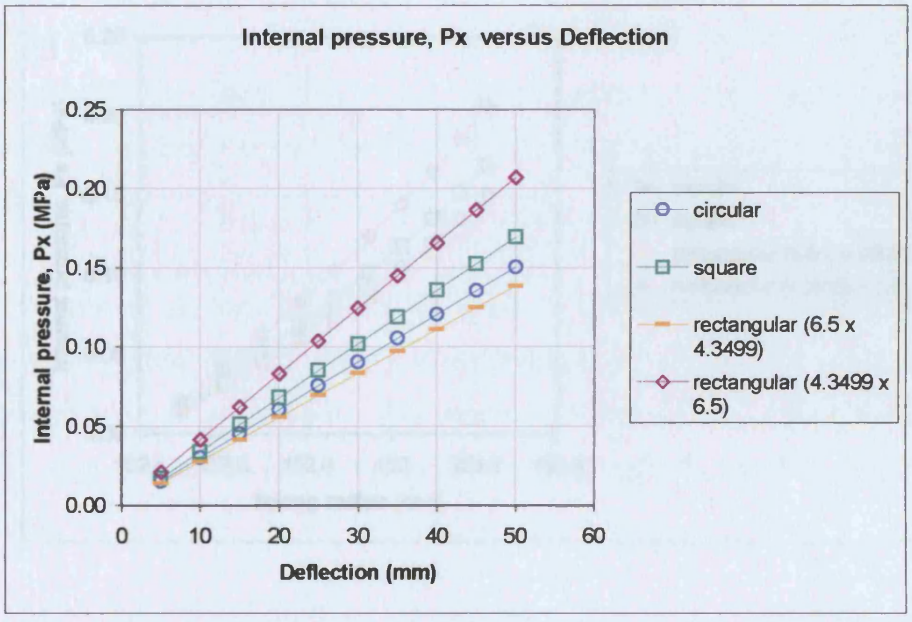

Figure 4.10a Analytical solution for internal pressure – deflection for symmetric cross-sections

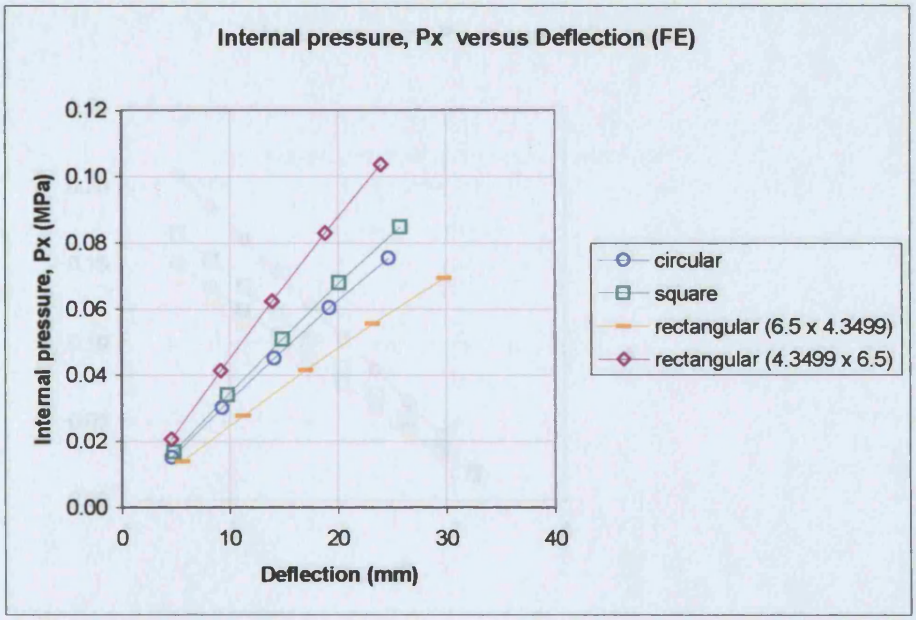

Figure 4.10b Finite element for internal pressure – deflection for symmetric cross-sections

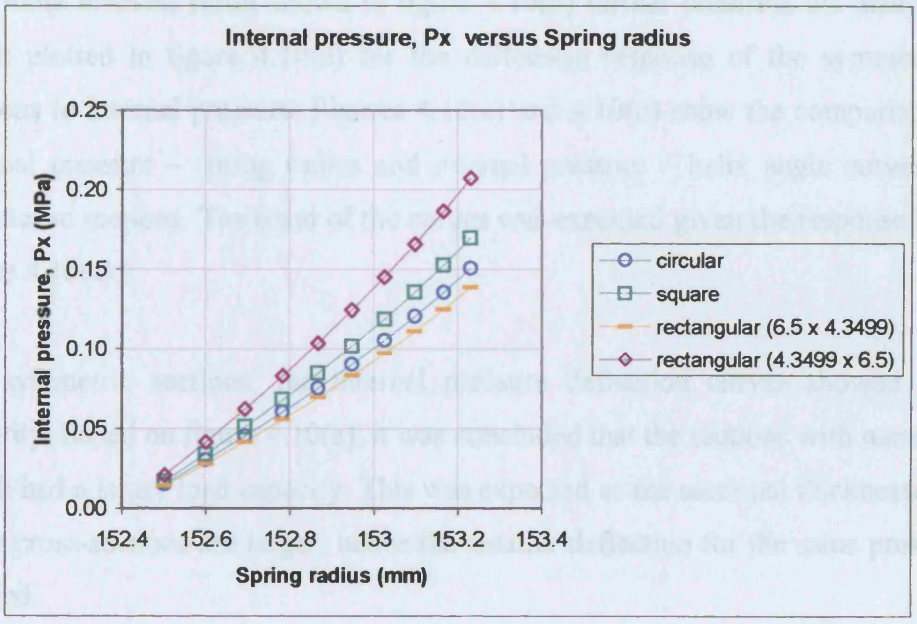

Figure 4.10c Analytical solution for internal pressure – spring radius for symmetric cross-sections

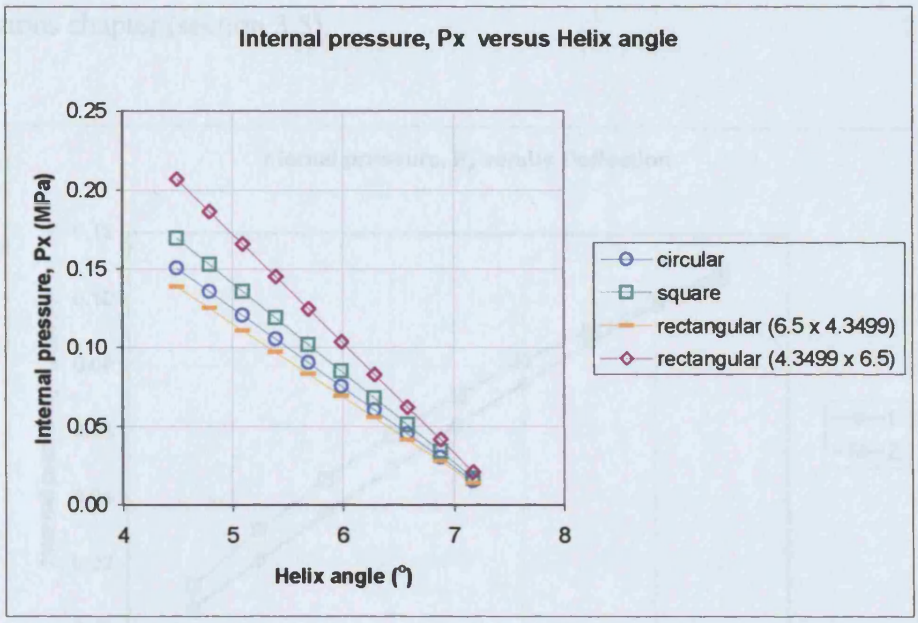

Figure 4.10d Analytical solution for internal pressure – helix angle for symmetric cross-sections

The finite element result shown in figure 4.10(b) further confirms the analytical result plotted in figure 4.10(a) for the deflection response of the symmetrical sections to internal pressure. Figures 4.10(c) and 4.10(d) show the comparison of internal pressure – spring radius and internal pressure – helix angle curves for symmetric sections. The trend of the curves was expected given the response from figure 4.10(a).

For symmetric sections, the internal pressure deflection curves showed high linearity. Based on figure 4.10(a), it was concluded that the sections with narrower width had a larger load capacity. This was expected as the sectional thicknesses of these cross-sections are larger, hence the smaller deflection for the same pressure applied.

The non-symmetrical section results are shown in figure 4.11(a) – 4.11(d). The responses for the helical springs subjected to internal pressure are given in Appendix D. When compared to the respective finite element analysis result, the

analytical responses were found to show similar trends to those discussed in the previous chapter (section 3.5).

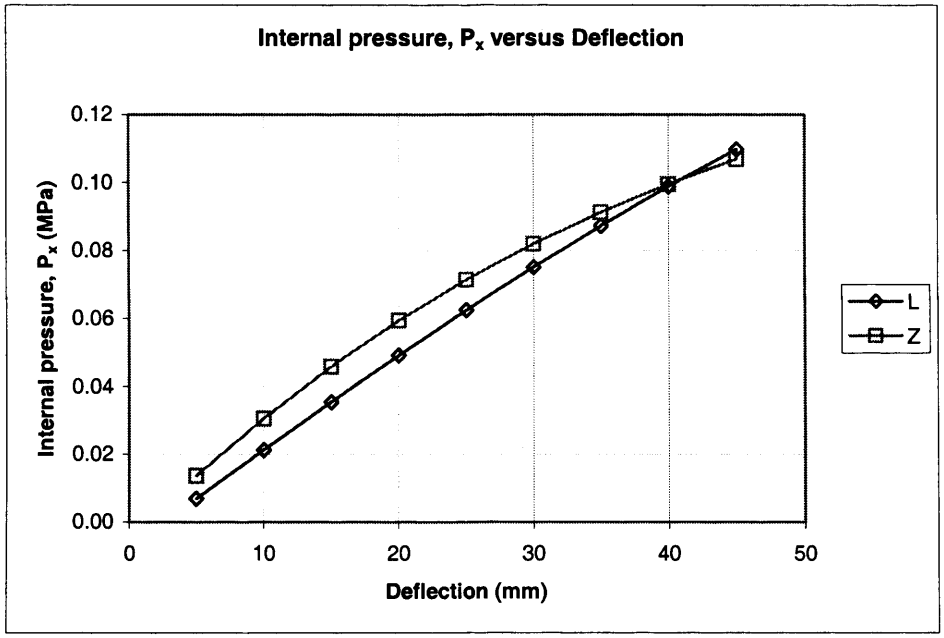

Figure 4.11a Analytical solution for internal pressure – deflection for non-symmetric cross-sections

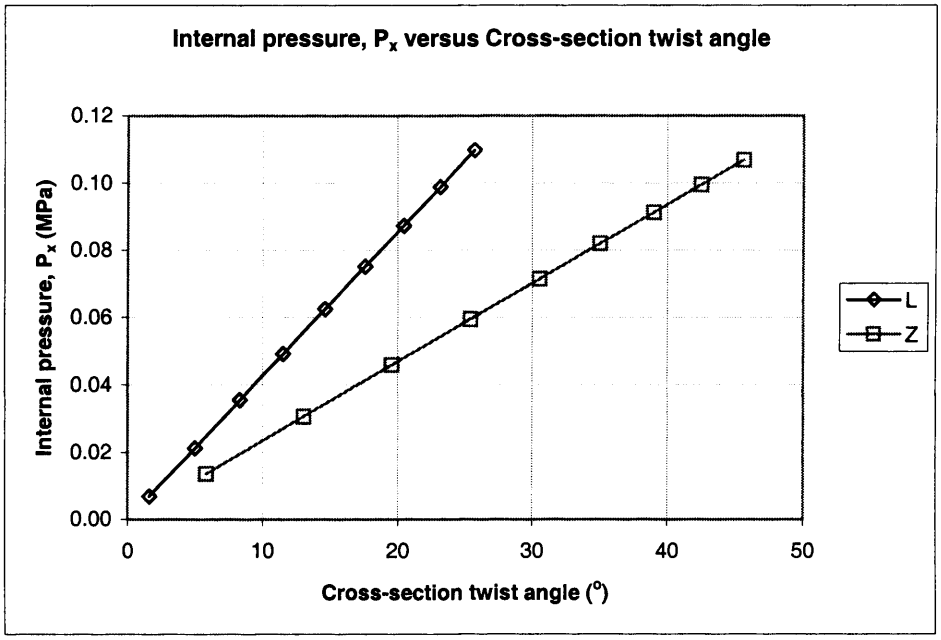

Figure 4.11b Analytical for internal pressure – cross-section twist angle for non-symmetric cross-sections

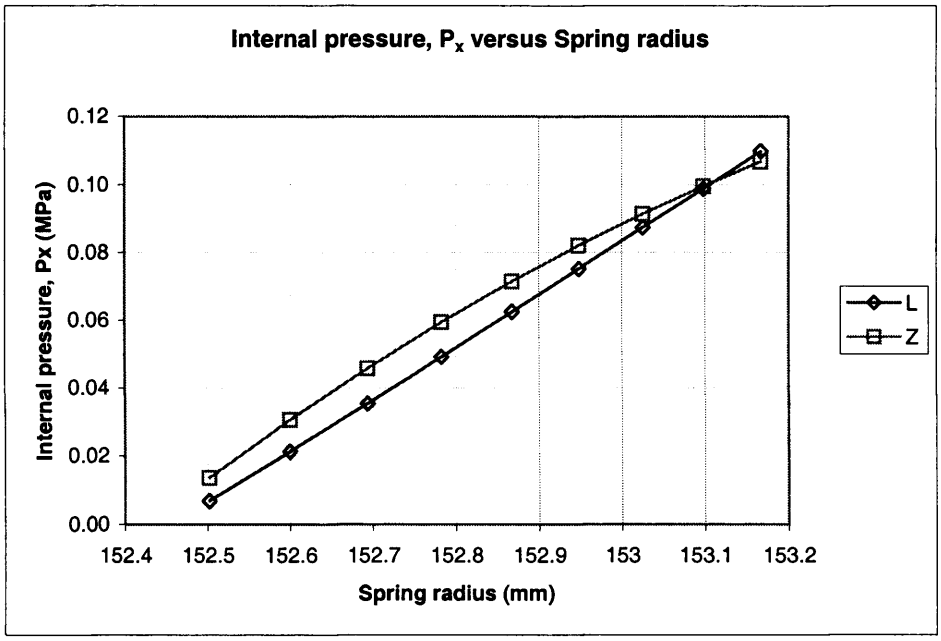

Figure 4.11c Analytical solution for internal pressure – spring radius for non-symmetric cross-sections

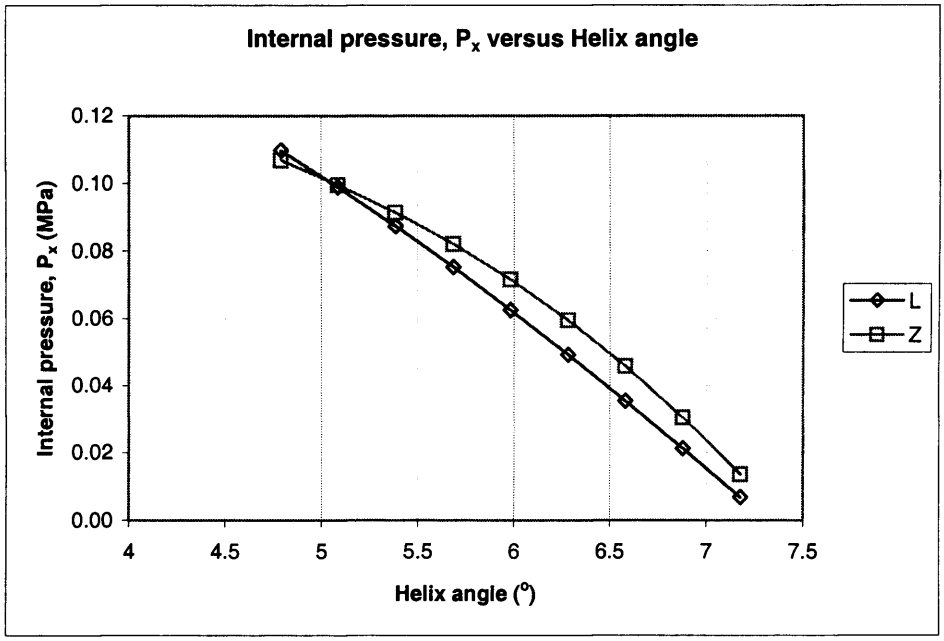

Figure 4.11d Analytical solution for internal pressure – helix angle for non-symmetric cross-sections

The non-symmetric sections had a lower load carrying capacity compared to those of symmetrical cross-sections. Additionally, the internal pressure applied to the L and Z-sections did not vary linearly with the spring deflection compared to the symmetric sections. This can be seen in figure 4.11(a). This is due to the fact that the cross-section twists with an applied internal pressure, causing the surface area exposed to internal pressure to reduce. Hence, as shown in the figure, the spring deflection gets larger with each step change in the load applied. For design considerations, the twisting of cross-section is to be avoided in order that the cross-section can fully maximize its pressure carrying capacity.

Figure 4.11(b) shows the cross-section twist angle for applied internal pressure for L and Z-sections respectively. The polar moment of inertia measures the tendency of a cross-section to twist and a comparison of the L and Z-sections, which are of similar cross-sectional areas, shows that the Z-section has a smaller polar moment of inertia compared to the L-section. Hence, in this case, the Z-section has more tendency to twist as is evident in the graph.

This effect in turn causes the change in spring radius to be smaller for increasing internal pressure as observed in figure 4.11(c), which is an entirely different response compared to that seen for the symmetrical cross-section shapes (figure 4.10(c)). This trend was most prominent in the Z-section, which can be explained by the fact that this cross-section has a larger twist compared to the L-section helical spring. Figure 4.11(d) shows the relationship between the changes in the helix angle to an applied internal pressure. This is non-linear unlike those of the symmetric sections in 4.10(d).

4.5.3 Results for Combined Axial and Internal Pressure Loading

The responses of helical spring when subjected to varying axial load with a fixed internal pressure load (to cause a spring axial contraction of 5 mm) are shown in figures 4.12(a) and (b). These can be compared to those in chapter 3 for circular cross-section systems and is reproduced in the figures 4.12(a) and (b).

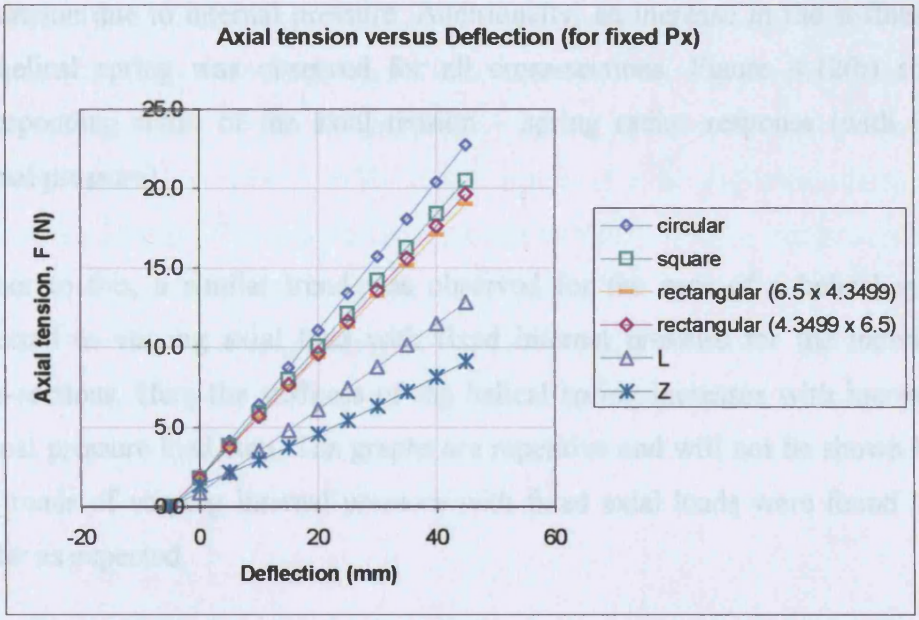

Figure 4.12a Comparison of analytical solution of axial tension – deflection for fixed internal pressure

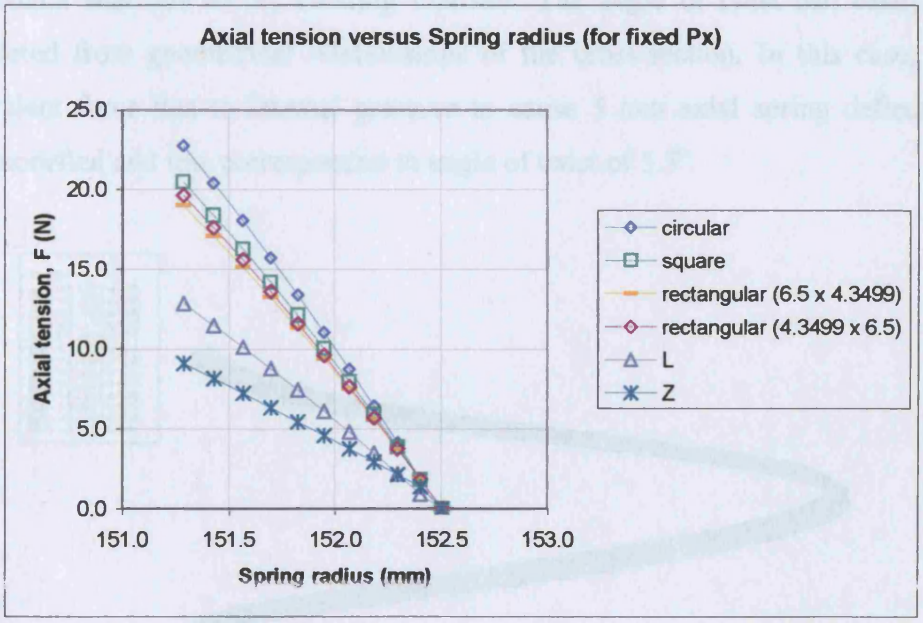

Figure 4.12b Comparison of analytical solution of axial tension – spring radius for fixed internal pressure

Referring to figure 4.12(a), it can be seen that with a fixed internal pressure, the axial load – deflection curves show similar trends to the case of pure axial loading alone, however with an offset to the spring deflection to account for the axial

contraction due to internal pressure. Additionally, an increase in the stiffness of the helical spring was observed for all cross-sections. Figure 4.12(b) shows corresponding result of the axial tension – spring radius response (with fixed internal pressure).

Further to this, a similar trend was observed for the case of a helical spring subjected to varying axial load with fixed internal pressure for the individual cross-sections. Here the stiffness of the helical spring increases with increasing internal pressure load step. The graphs are repetitive and will not be shown here. The trends of varying internal pressure with fixed axial loads were found to be similar as expected.

Figure 4.13 shows an example of the angle of twist (of the cross-section) verification from the finite element analysis models. The results are for displacement of the helical spring cross-section in the direction shown in figure 4.8, which was due to the twisting moment. The angle of twist can easily be calculated from geometrical relationships of the cross-section. In this case, the equivalent force due to internal pressure to cause 5 mm axial spring deflection was modelled and this corresponded to angle of twist of 5.5°.

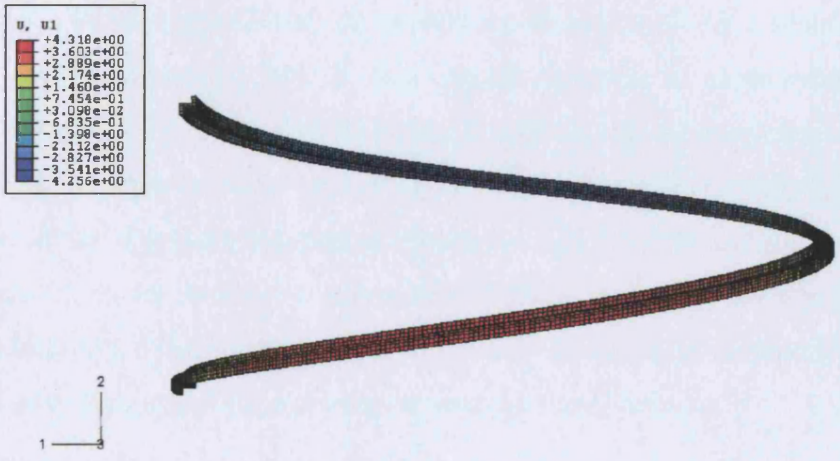

dimensions in mm

Figure 4.13 Example of finite element result for angle of twist of cross-section of helical spring subjected to a twisting moment

In summary, an investigation of how the various cross-sections behaved with respect to a range of loading modes was made and the results presented here. From the discussion above, it should be noted that in particular, an internal pressure load causes a twist in the cross-section of a helical wire with a non-symmetrical profile. The solution obtained can be used to better design a pressure armour layer in order to maximize the pressure loading capacity without having to increase the cross-sectional area. The next chapter further enhances the understanding of the above via an experimental route in order to observe the rotation of the cross-sections under radial loading.

5 Experiments and Results

5.1 Introduction

In chapters 3 and 4, the theory of the mechanics of helical springs was shown to provide the basis for the analytical solutions relevant to pressure armour reinforcements. This work assumed that the complex profiled wire of pressure armour could be usefully reduced to a simple helical spring model of circular cross-sectional shape. Once this was done, the behaviour of various cross-sectional shapes could be investigated by appropriate additions to the model. Such simplifications have been made not only because of the geometric similarity of the pressure armour structure to a helical spring, but also to assist in the verification of the analytical solutions developed via simple experiments carried out on helical spring systems. This chapter describes the experimentation process and the tests carried out to observe the response of helical springs of various cross-sectional shapes to the different loading scenarios. The experimental work provided a useful method to physically observe the deformations of the helical springs. This enabled both the analytical and numerical approaches described earlier to be tested against experimental data. The experimental work was able to highlight some issues in the models developed and permitted subsequent modifications of these. Some of these aspects will be discussed later in this chapter. In order to experimentally test spring designs, it was necessary to source a wide variety of geometries and coil cross sections. Some of these were likely to be fairly complex in shape and it was noted, early on, that the procurement of such springs would be difficult and likely to be costly. In an attempt to solve this problem, it was decided to fabricate springs in-house. This necessitated, as described below, the development of a new method to manufacture helical springs of complex cross-section.

5.2 Spring Lathe and Materials Selection

Although commercially available helical springs come in a large range of sizes and materials, it was decided to fabricate custom helical springs for the

verification work. This decision was made for several reasons. Firstly, in order to measure the forces and the change in dimension generated in the springs under various loading scenarios, large spring dimensions, in particular the spring diameter, wire cross-sections and spring length obviously assisted the process. For example, deflections would be proportionally larger and the measurement sensitivity required would be well within the limits of standard laboratory experimental facilities. However, since most springs, not withstanding their size, are manufactured from ferrous metals, large springs would necessitate the application of large forces in order to generate measurable deformations, hence complicating the experimental setup. Something akin to an automobile suspension coil spring would constitute the size and type of coil in mind for the work proposed. It was obvious that these types of helical springs are difficult and expensive to procure, while large axial forces are required just to carry out simple extension tests. Additionally, a significant portion of this work was dedicated to understanding how coil springs (hence pressure armour layer) behaved when under an internal pressure load. Thus, even if the metallic springs of the required section and geometry were fabricated, the experimental problems associated with pressuring these were likely to be significant. For example, a 25 x 25 mm square cross-section helical spring of nominal pitch length 100 mm and diameter of 300 mm would be expected to show 10 mm deflection only after a pressure of 3.2 bars was applied.

Secondly, although the problems associated with a suspension spring were not insurmountable, such springs would greatly limit the scope of verification work because at the time of writing, nothing other than a circular cross-sectional shaped spring had been found to be available. Specially manufactured helical springs would have been prohibitively expensive. If the verification process was to remain useful and indeed credible, springs comprising complex cross-sections would have to be tested.

As a result of this, an alternative spring material was sought and with it, an alternative and flexible means of helical spring manufacture, which would permit coils of varying and complex cross-sections to be produced. Several materials and methods were considered including: -

1) wood in the form of block sections, bonded together to generate a helix,
2) polymeric resins that could be cast into shape, and
3) expanded polystyrene cut to required cross-sections

The first two ideas were rejected in favour of the one involving expanded polystyrene cut into the required shape. This was because expanded polystyrene offered several advantages as a modelling material. It was inexpensive and fairly easy to shape using conventional methods. Attempts at shaping it using normal woodworking tools revealed that the best method by far was to use a hot wire cutter of the appropriate profile for the helical wire cross-section required.

Initially, the proposed idea was to have blocks of polystyrene cut with the necessary section and cut-off angle, and then adhesively bonded together to form a helical spring. However, it was decided that the block assembly method might introduce errors into the spring system if one considered the bond line as an area of critically enhanced stiffness by virtue of the adhesive used. Therefore a spring fabricated as a continuous, homogeneous form was deemed to be better. To achieve this, a purposed built hot-wire helical spring lathe was designed and fabricated from readily available components on a medium density fibreboard (MDF) carcass. The helical spring lathe was required to perform the following tasks: -

1) machine a cylindrical polystyrene form, approximately 750 mm long and 300 mm in diameter,
2) remove the inside of this cylinder to form a tube of wall thickness of approximately 30 mm,
3) machine a variety of cross-sectional profiles, through the thickness of the polystyrene tube whilst simultaneously traversing the cutting head along the axis of the tube in order to cut a helix.

Whilst requirements (1) and (3) were reasonably straightforward to fulfill in terms of design and construction of the lathe, requirement (2) involved a far more radical lathe design that allowed internal machining to a depth of nearly a metre. The overall design was ultimately simplified by eliminating requirements (1) and (2). To this end, an extensive search of companies that regularly cut and trim expanded polystyrene (mainly for the packaging industry) located several who were willing to fabricate polystyrene tubes to the required dimensions. None of these companies agreed to fulfill requirement (3) bar one, which confirmed that the block assembly method, where the polystyrene was cut into the necessary sections and bonded together, would be used to fabricate such a shape. Hence it was still necessary for the author to construct a lathe capable of 'machining' the various spring designs required for the work.

There were quite a number of profiles to be cut (these will be described later), some of which were fairly complex and would entail interlocking coil sections. This would never have been achievable for metal based specimens unless a major manufacturing facility had been located and employed – and even so, the requirement to interlock adjacent sections would not have been fulfilled simply by a machining process. The spring would have to be coiled and the coils locked together sequentially as part of the coiling process. This would add to the expense and require considerable forces to open and/or close the profile onto its adjacent partner. Polystyrene offered an elegant route to achieving an interlocked profile as it could be wire cut and a single pass could instantly create two sections that were interlocked by default. The design of the apparatus was loosely based on a screw cutting lathe, where a motor rotates the machined item under constant and defined speed and another drive is used to traverse the cutting head along the longitudinal axis of the item, again of a constant and definable speed. Most screw cutting lathes work by deriving the longitudinal drive from the motor that powers the rotational drive, through a series of gears or belts that can be altered to change the pitch of the cut.

It was decided at an early stage to computer control the cutting process in an attempt to simplify the overall design of the lathe. Two motors were used, one to rotate and one to traverse. Stepper motors were chosen in order to give precise

control of speed. A gearbox was mounted to the stepper motor to provide enough torque to rotate and traverse the polystyrene block, and speed control was done via calibration trial runs in order to obtain the optimum speed configuration for various helical pitch cut (the operation of the stepper motors is described later). The gear and belt method, if used, would have posed challenging problems in terms of the speed and torque selection given that it was desired to have numerous cutting speeds (which defines the helical pitch).

The spring lathe consisted of a purpose built frame to rigidly hold the driving and cutting components. Referring to figure 5.1, each of these is described below:-

- 2 stepper motors – to rotate the polystyrene cylinder and to allow the hot wire cutter to traverse along length of cylinder
- stepper motor RS232 serial interface – to allow computer control of the stepper motor
- gearbox – to allow stepper motor to have higher output torque
- rod with disc – to hold the polystyrene cylinder in place
- mechanical holder – a hot wire shaped into desired profile is mounted here and is allowed to move along length of cylinder when a command is given to the stepper motor
- lead screw – the M8 size studding was used and this corresponded to a pitch of 1.25 mm. When the studding completed one rotation, the mechanical holder moved a distance of 1.25mm. The required pitch length of the spring is attained from multiple full rotations of the lead screw.

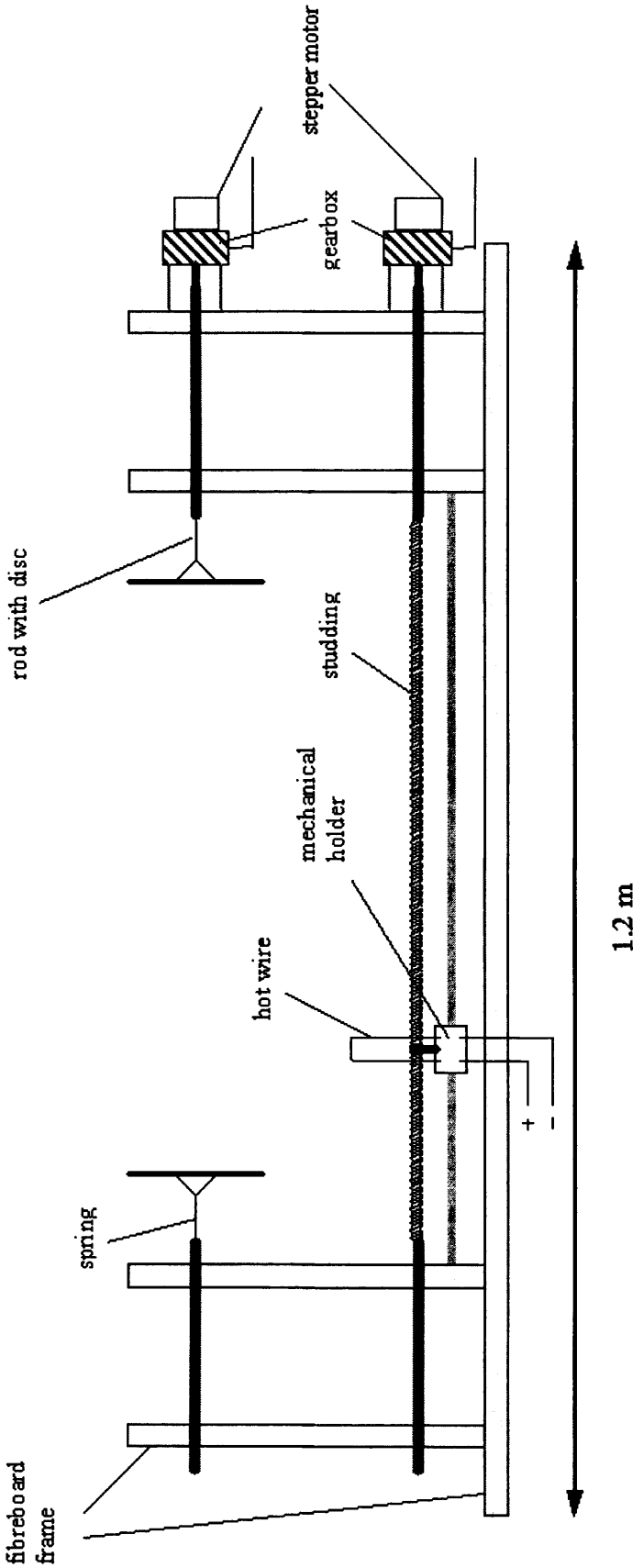

Figure 5.1 Schematic design of helical spring lathe

If it is desired for future work, additions to the spring lathe could be made in order to perform stages 1 and 2, described earlier, by extending the frame and having a long hot wire to cut a central hole in a solid polystyrene cylinder. Details of this design are not discussed here as it did not form part of the experimental work. Figure 5.2 depicts the assembled spring lathe together with the electrical connections.

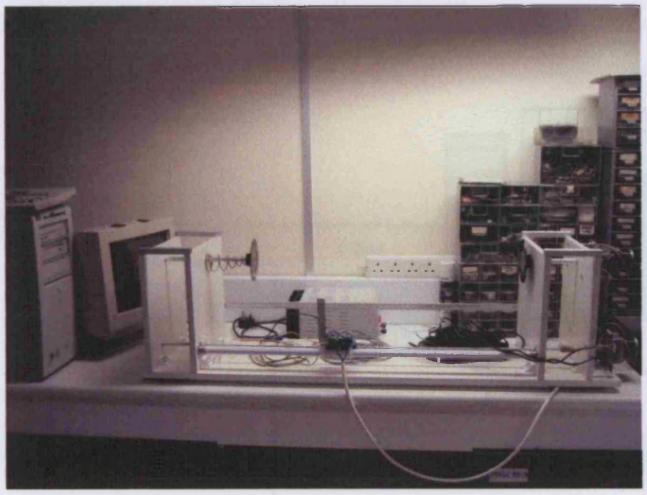

Figure 5.2 Assembled helical spring lathe

Two particular methods were considered for rotational and traverse movements of the cutter to cut a helical spring. Method one involved connecting a series of gears to the rotation and traverse shaft of the lathe. In essence, to obtain the pitch of the coil required, the gears were to be meshed in their respective ratios and mounted to the shafts. A mechanical handle could have been mounted to one end of the shaft and hence the rotational and traverse movements would have been obtained simultaneously when the handle was rotated. For different gear ratios, the gears consisted of different diameters and therefore the many holes would have been drilled into the MDF board with precision. In line with this and also due to the fact that a consistent speed needed to be applied to the handle to obtain a good cut, the second method was chosen. As mentioned earlier, this method involved using two stepper motors mounted at the end of each shaft and the precise movements controlled with consistent speed throughout via a computer. This is further illustrated in the following paragraph.

To control the rotation and traverse movements, the stepper motors were connected to a computer and purposed written stepper motor driver software was used to input the desired speed of the motors. Figure 5.3 shows the schematic diagram of the control circuitry for the stepper motors, the 15 Volts DC power supply and the computer. The stepper motor control board was connected to the host computer by means of an RS232 serial line on COM 1 port.

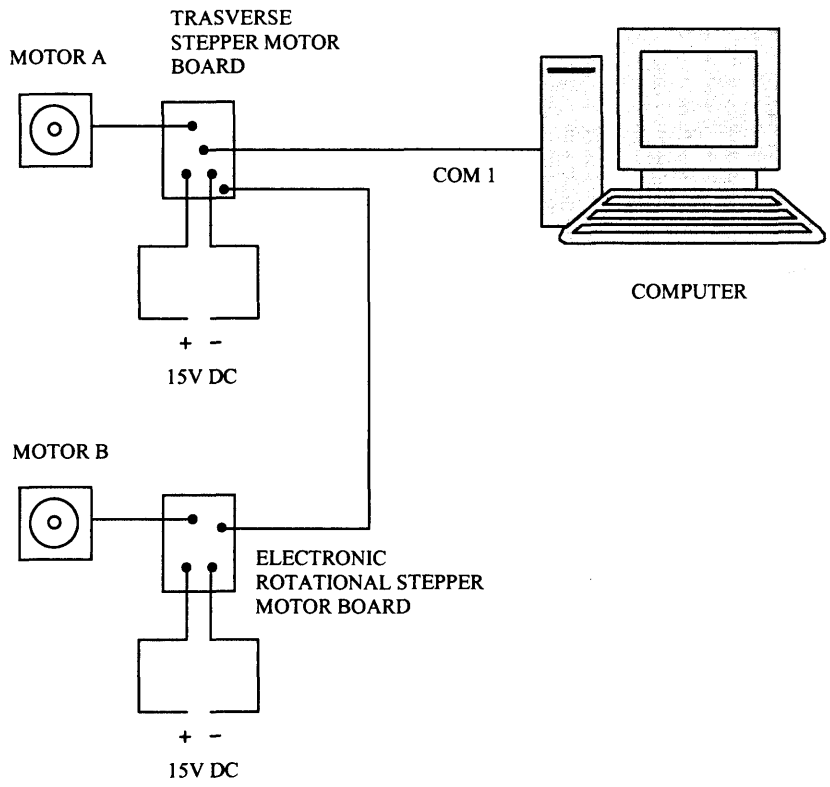

Figure 5.3 Schematic diagram of connections between stepper motor and computer

Shown overleaf in figure 5.4 is an example of the stepper motor driver software provided by the manufacturer of the control board, Milford Instruments Limited UK. There were two sections to this software; the first allowed the stepper motor setup, where the rotational and traverse motors were defined respectively. This included the direction and the relative speed of the motors to each other. The COM port of the serial interface was also defined here. In the second section, the speed and number of rotations of the motors could be defined to obtain the required pitch of the spring coil. The driver software permitted the definition of a

mini program in order to obtain continuous looping of the stepper motor rotation. This was useful as sometimes several continuous runs were necessary in order to cut the required pitch and number of coils.

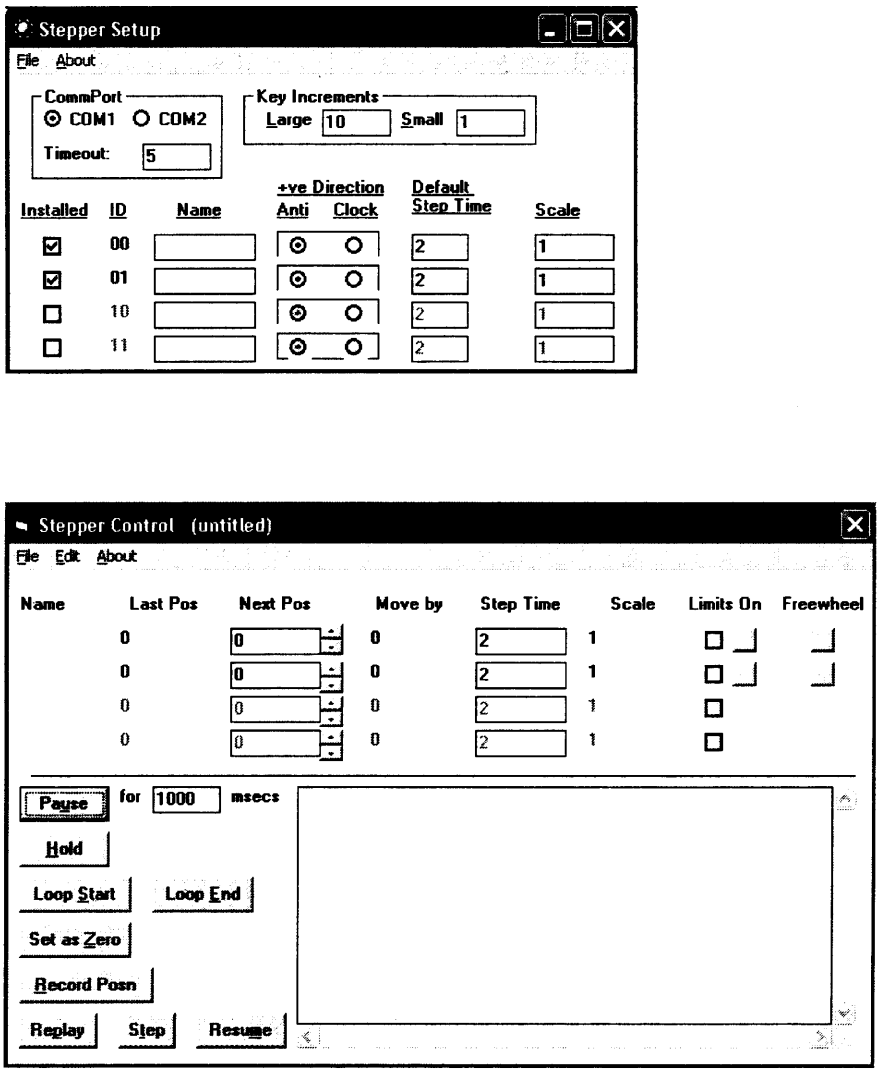

Figure 5.4 Stepper motor driver software

The hot wire cutter was fabricated from *nichrome* wire (based on a nickel chromium formula). When sufficient current was passed through to the cutter, it self heated (due to resistance of the nichrome) to a temperature sufficient to melt the polystyrene. The polystyrene material was very sensitive to the level of heat applied. If the temperature of the wire was too high, for example, the polystyrene burnt away rapidly and this caused uneven cutting or sometimes a variation in thickness throughout the helical spring, while, if the temperature was too low, then frictional effects caused the hot wire to be held up at a particular position, and again gave poor profile consistency along the full helix. This behaviour was also dependent on stepper motor speeds. To prevent such problems from occurring, the hot wire was connected to a current controller. This was a commercial solid state device that permitted output currents to be controlled in the range of 0 – 15 A (DC motor control module type X10335 manufactured by United Automation Ltd.). Current settings were achieved by using a potentiometer and resistor network. The circuit was supplied by a linear power supply at a fixed output voltage with a full load capability of 22 A. Figure 5.5 shows the schematic setup of the hot wire and current controller.

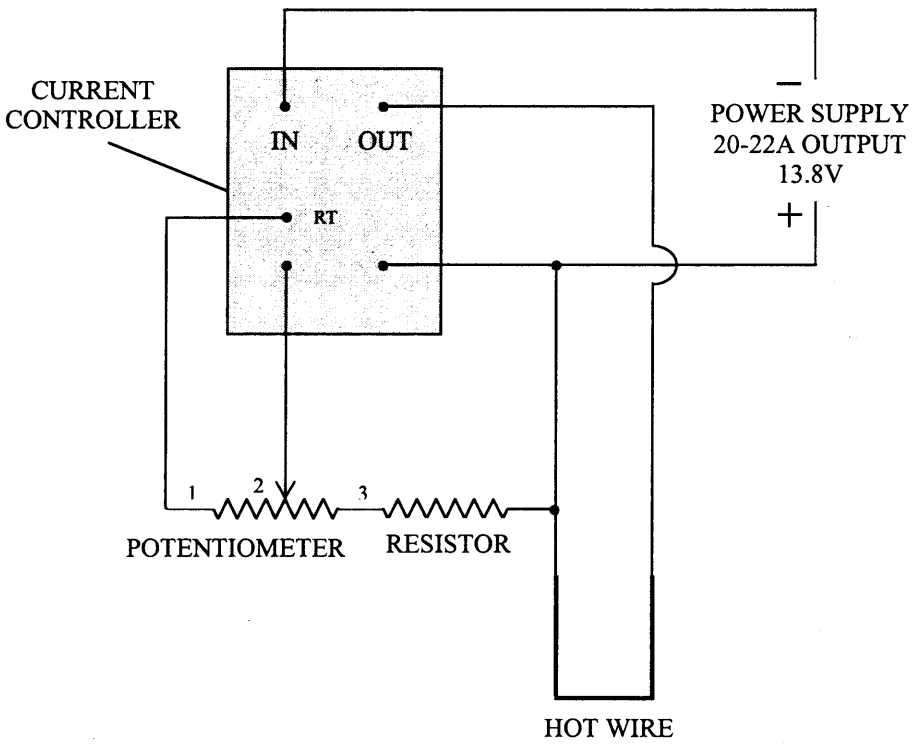

Figure 5.5 Schematic of hot wire and current controller

The interaction between the speed of cutting and the temperature of the wire, and the behaviour of the polystyrene meant that the optimum setting for the cutter current (and hence wire temperature) had to be found by trial and error. However, once this level was ascertained, it varied only marginally between cross-section designs.

5.3 Experimental Procedure and Test Regime

The polystyrene cylinder hollow tube procured had the dimensions shown in figure 5.6. The expanded polystyrene obtained was of the soft grade with density of 16 kg/m^3. This corresponded to shear modulus of 1.93 MPa and Poisson's ratio of 0.086 using standard material data obtained from polystyrene material manufacturers, although data for polystyrene differs greatly between manufacturers and these values may be somewhat inaccurate for the grade chosen here.

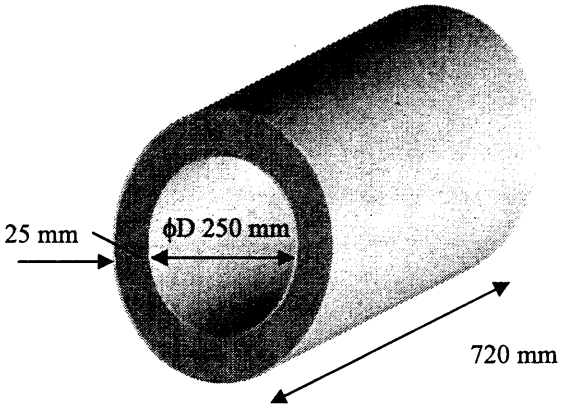

Figure 5.6 Polystyrene tube dimensions

Several polystyrene helical spring cross-sections were cut from these tubes using the spring lathe. These were square, rectangular, L and Z profiles. An attempt was also made to cut the Omega profile. This will be further detailed later. The dimensions of some of the cut profiles are shown in figure 5.7. The dimensions and cross-sectional profiles were chosen using several criteria. For example, in order to verify the expected decrease in spring constant as the cross-sectional depth was reduced (see section 3.5), profiles A, B and C were cut. Additionally in

order to test the hypothesis that asymmetry in cross-section profile would cause a rotation under loading (see section 4.3), profiles D and E were cut. Measurements of the section rotation were made (see later) and the results compared with the analytical solutions for the complex profiled pressure armour cross-sections.

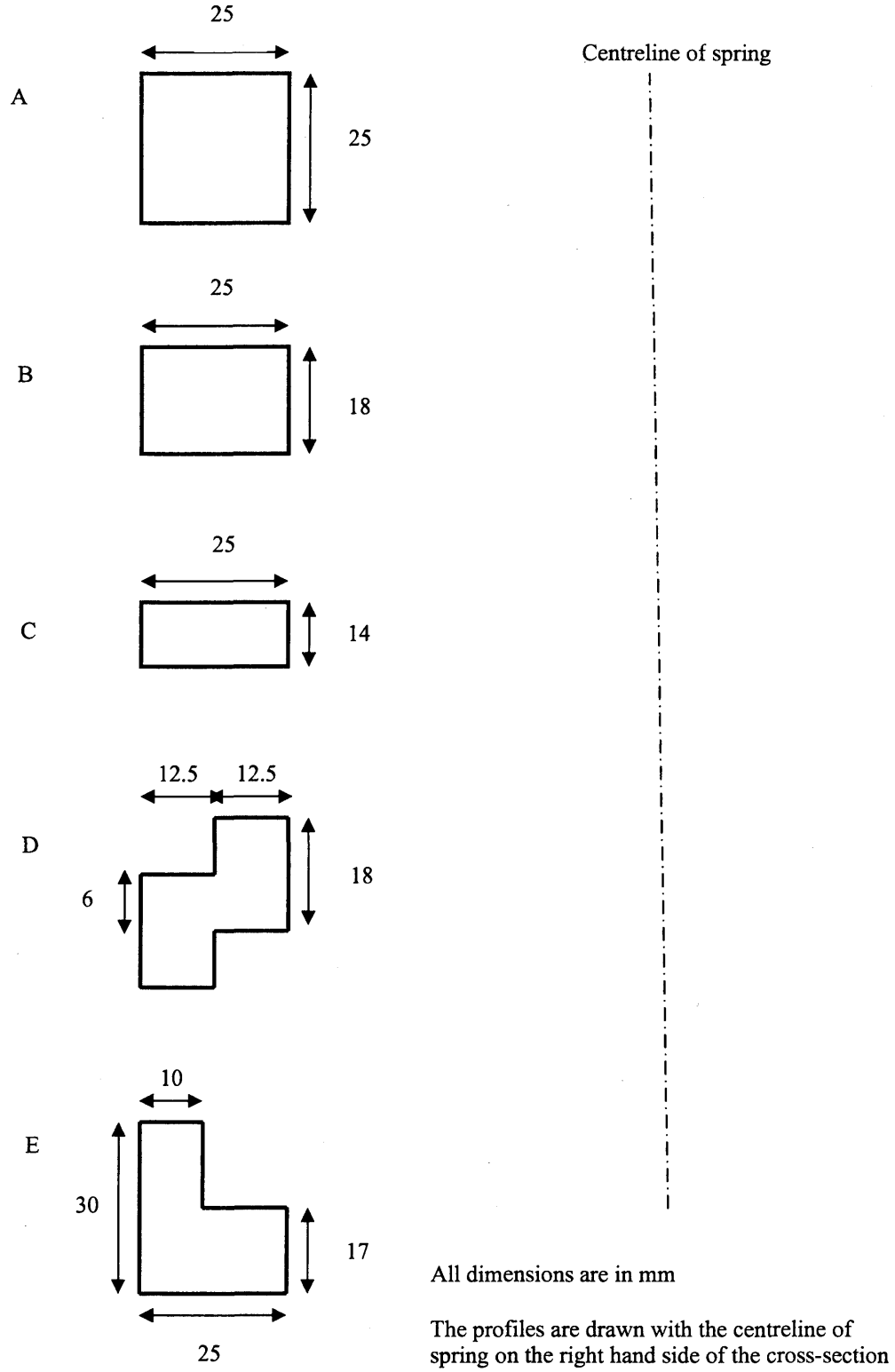

Figure 5.7 Dimensions of some cut helical spring cross-sections

The number of coils present in the spring depended upon the pitch length of the spring that was required. Given the dimensions of the procured polystyrene, the thickness the cross-section was always 25 mm. An example of the cut polystyrene spring of five pitch length is shown in figure 5.8. The photo depicts a square cut profile.

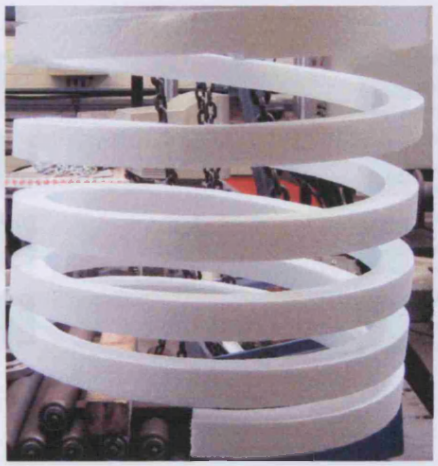

Figure 5.8 Cut polystyrene helical spring

Once the springs were fabricated and enough experience had been gained in using the cutting apparatus, the measurements of the change in diameter, deflection and rotation of the cross-sections were observed for a series of different loading modes. It was hoped that the trends in the deformation behaviour, with respect to the different loading modes, would provide an understanding on how the stiffness of the springs change with internal pressure and axial load, which in turn would assist in the design code of pressure armour layers.

The cut polystyrene springs were subjected to tensile or compressive forces with or without constraints at the spring ends and an internal pressure load via a purpose built test rig which could apply radial forces on the coils of the spring as well as a longitudinal axial load. The three loading modes that were tested on the polystyrene helical spring models were as follows: -

1) pure axial load
2) simulated internal pressure load (lateral loading)
3) combined axial and internal pressure load

These three test scenarios are schematically shown in figure 5.9 and are described in turn below.

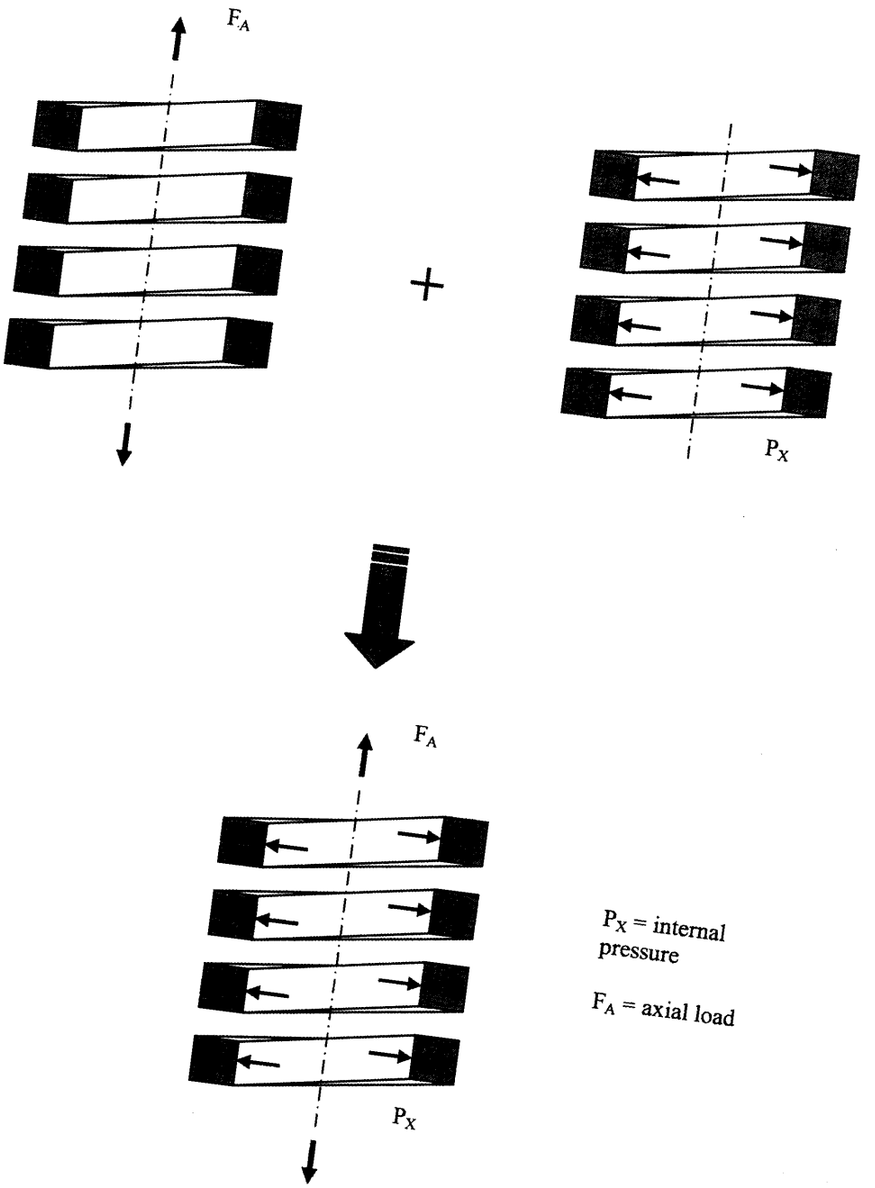

Figure 5.9 Example of square cross-section helical spring with the respective loading modes

1) Experimental methods for pure axial loading mode

For pure tensile loading of a helical spring, although the cut spring was comprised of several coils, only one complete coil was required for the measurements. The spring was fixed at one end with the other end free to rotate. The analytical solution presented in section 4.5 did consider the case of both ends being fixed, however this would have been difficult to achieve experimentally. It was assumed, however, that the polystyrene spring would not rotate much under axial tensile loads. In any case this is a reasonable assumption given the low magnitude of the applied load. Polystyrene has a low Young's modulus, hence only small forces are required in order to get accurate measurements of the change in dimensions of the spring. Axial loading of the spring was performed by placing small weights at the end of the first coil for measurement. Coins in denominations of 1p and 2p were used as weights. A 1p coin weighed 3.5 g whilst 2p coins weighed 7.1 g. The tensile tests were carried out for all the profiles shown in figure 5.7 previously. A coil loaded in this way is shown in figure 5.10. Note that only one coil was needed for loading and measurements although it was possible to use all the coils. This was done to simplify the measurement exercise, not least for the experimental setup of combined axial and radial loading tests.

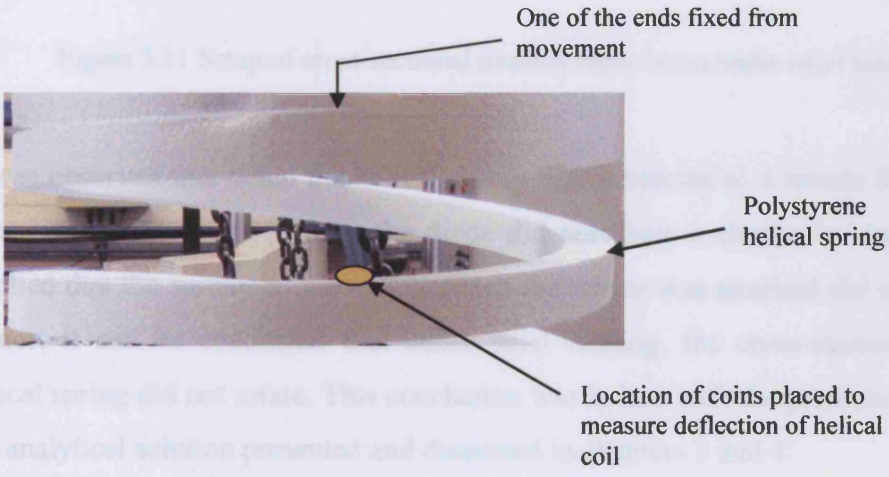

Figure 5.10 Loads on axial loading of spring

Following on from the axial loading tests, an experiment was done to find out whether the helical spring wire cross-section rotated under axial load. The interest in rotation relates to the discussion presented in chapter 4 section 4.3. The setup of this experiment is shown in figure 5.11 below. A small mirror was placed on one of the flat surfaces of the helical spring and aligned to a laser diode mounted on a travelling microscope. When an axial tensile load was applied to the helical spring, any change to the angle of the laser after it reflected back from the mirror was recorded.

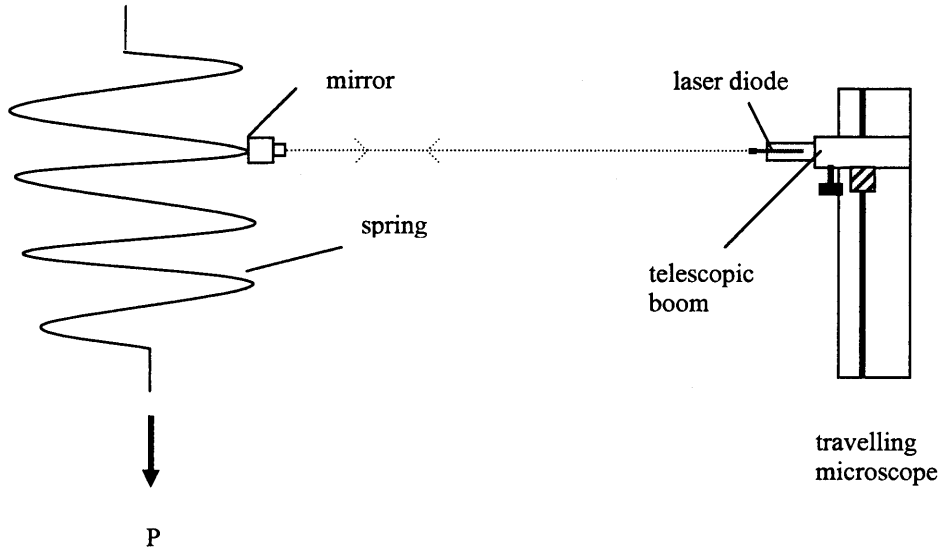

Figure 5.11 Setup of cross-sectional rotation observation under axial load

It was observed that when the helical spring was subjected to a tensile force, the laser light reflecting back from the diode did not show a change in angle. This implied that the surface of the spring where the mirror was attached did not twist. Hence, it can be concluded that under axial loading, the cross-section of the helical spring did not rotate. This conclusion was in line with the predictions from the analytical solution presented and discussed in chapters 3 and 4.

2) Experimental method for internal pressure loading

The simulation of internal pressure loading of a helical spring was more challenging. Several options were considered. An early proposal was to use some

kind of rubber membrane concentric to the spring axis. The pressure load would have been applied using air pumped into the rubber membrane. However this method was not thought to be viable since it was considered that frictional forces would be introduced between the membrane and the coils, and hence free movement of the coils would therefore be prevented and the overall response would be a complicated combination of the response due to internal pressure load and the frictional force. Friction would act to restrain the movement of the spring and generate the impression that it was stiffer than expected and hence mask any real effect caused by an internal pressure load. Free movement of the coils under internal pressure load was a necessary prerequisite for the situation of combined axial and radial loading which is discussed in the next section.

A non-contacting force transfer method was therefore sought and the proposal was to generate magnetic forces between the inside surface of the helical spring and an inner cylindrical tube. This method was considered viable as magnetic discs small enough to fit on the coil profile were relatively cheap and easy to procure. Pairs of magnets were positioned (one magnet on the coil and another on the inner tube) and aligned in such a way that the mutual repulsion would have been strong enough to cause the spring to move radially outwards. The repelling force was measured by a simple calibration test and determined for each coil as long as the distance between the magnet pairs was known. However, once the helical spring coil moved radially it was also likely to move axially (due to applied radial forces), hence the magnet pairs were no longer aligned. This caused the magnetic force to weaken and hence did not reflect the true force applied on the spring.

One other major disadvantage of the magnetic method was the concern that as the magnetic pairs would go out of alignment there would be the possibility that additional and unintentional forces would have been superimposed on those experimentally applied. In other words the magnets would influence the measurements of the deflections. The only way of overcoming this would have been to fabricate the inner cylinder as one whole magnet with the disc magnets being applied to the coils only. In this case, the disc magnets would always be radially aligned with an opposing magnet. Overall, the magnetic method was

abandoned in favour of a simpler and slightly more primitive method utilizing pulleys and suspended masses as described below.

The final method for simulating an internal pressure load comprised a purpose built test rig to apply radial forces to the polystyrene helical spring. It consisted of several pulleys with weights to apply radial forces on the spring coil. The design of the pulley test rig is shown in figure 5.12.

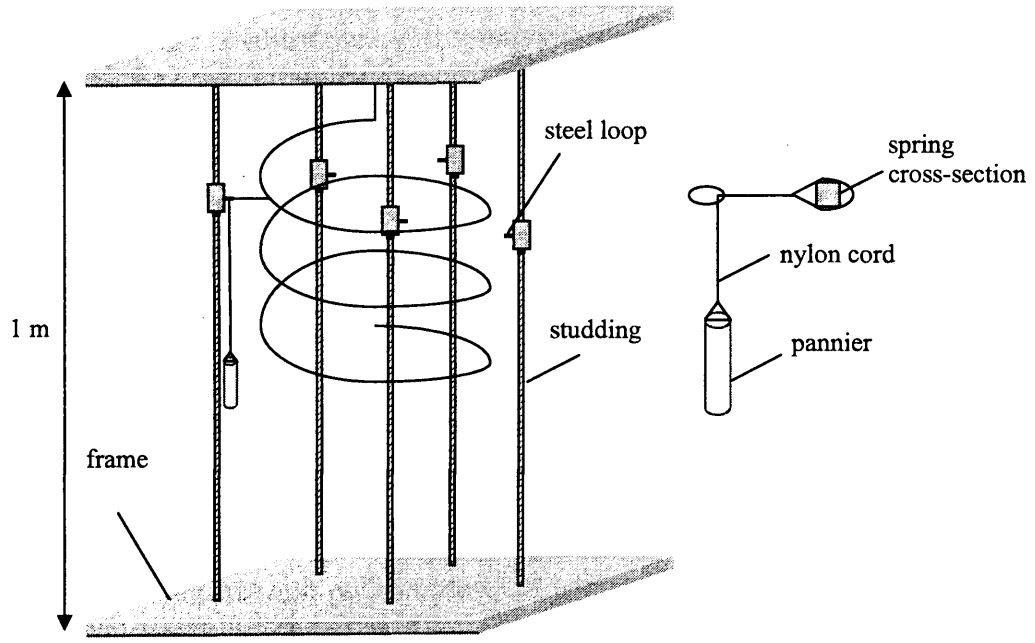

Figure 5.12 Pulley test rig

Studding of about 1 m in length was mounted onto two wooden frames as shown in the figure above. The helical spring to be tested was mounted onto the top wooden frame. Radial loads were applied using weights which were then placed into a pannier and a nylon cord attached between the pannier and the helical coil via a steel loop. Nylon was chosen for its low coefficient of friction between it and steel (used for the 'pulleys'). A pulley took the form of a smooth plated steel loop through which the nylon was passed. The frictional effect was extremely small even with large loads applied. The pulley system was designed to rise up and down along the studding rods by means of an adjusting nut. In order to ensure that the load applied via the pannier and pulley was purely radial (and hence have no

axial component) it was necessary to maintain the angle between pannier, cord and coil at 90 degrees, hence the need for the adjusting nuts. As the coil was loaded (either radially and/or axially) any axial movement in the coil position could be counted by moving the pulley up or down to maintain the 90 degree condition. The 90 degree condition was checked by using a travelling microscope equipped with a horizontal graticule. The adjusting nuts were moved to 'horizontalize' the nylon cord and the travelling microscope was moved up or down so that the image of the line in the graticule was located along the nylon cord. This iterative procedure was repeated every time a mass was added to the pannier in order to adjust the radial 'pressure' load.

Measurements of the change in radius of the coils and of the axial deflection were made as a function of the mass in the pannier. It was important to ensure that the same mass was added to each of the five panniers in order to maintain loading symmetry. A better simulation of the internal pressure load could have been achieved by increasing the number of pulley/pannier combinations, but five was chosen for practical reasons and was considered sufficient. Additionally, it should be noted that the rig only allowed a single coil within the spring to be tested. Again this was chosen for practical reasons (testing more would have required a complex arrangement of pulleys, panniers and studding, offset from each other to avoid interference). The implications of the results are discussed later. Figure 5.13 shows one helical coil being stretched radially using the pulley test rig.

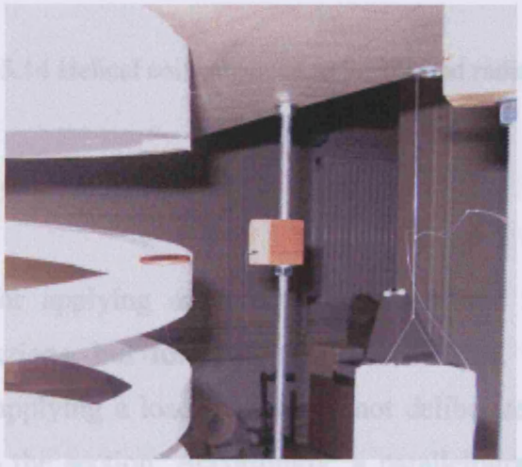

Figure 5.13 Helical coil experiment on pulley test rig

3) Experimental method for combined internal pressure and axial load

For the experiments involving the combined axial tension and internal pressure loading, the whole process described above was repeated but masses were placed on the coil as well as in the pannier. As described previously, coins were found to be an ideal way of uniformly loading the coils axially. Again, all the cords for all the panniers had to be adjusted so that they remain right angles to the studding before any measurements were recorded. Figure 5.14 depicts a helical coil being subjected to tensile and radial forces and it can be seen that the position of the cord between loop and coil is at right angles to studding.

Figure 5.14 Helical coil subjected to tensile and radial forces

4) Supplementary considerations

The arrangement for applying an internal pressure load functioned well for symmetric cross-sections, but for more complex designs, it was necessary to devise a means of applying a load that would not deliberately add an unwanted twisting moment to the section. Accordingly, a parallelogram arrangement was

used as shown in figure 5.15. The parallelogram also permitted free rotation of the cross-section should it have wished to do so.

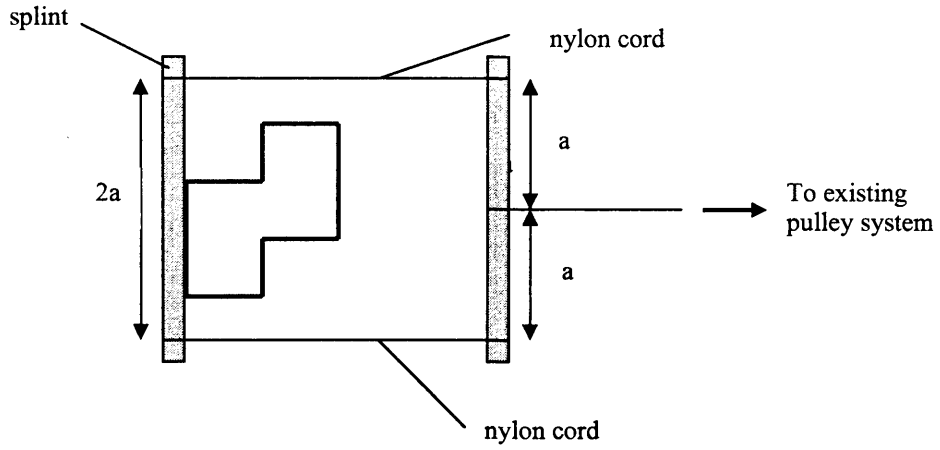

Figure 5.15 Helical spring cross-section attachment for measurement of angle of rotation

The arrangement also permitted the measurement of the angle of twist of a section using a simple protractor based method. This modified pulley system thus allowed the rotation of helical spring cross-sections that were not symmetrical, such as Z and L sections, to be measured when subjected to radial loads.

5.4 Interlocked Profile Cutting

The situation pertaining to the Omega profiled wire was quite complex given that each coil is interlocked within its immediate neighbour. As has been discussed previously, the coupling between the coils is likely to severely restrict the relative movement of the coils with respect to one another. Movement however, must be allowed, or else the pressure armour reinforcement will provide a low degree of flexibility much as would be generated if the reinforcement was a solid tube. Thus the helical spring approach remains justified, albeit within the constraints placed upon the coils by the flexibility and movement allowed within the interlocks.

For the case of the physical model, machining an interlocking cross-section was actually easier than might have been first thought, since the hot wire cutter was

appropriately profiled to cut a line between two coils, without it ever being necessary to reassemble those coils, unlike a true Omega profiled wire reinforcement, which would have to have been manufactured as a wire and then slotted together. Figure 5.16 shows an example of a cut interlocked Omega profile helical spring.

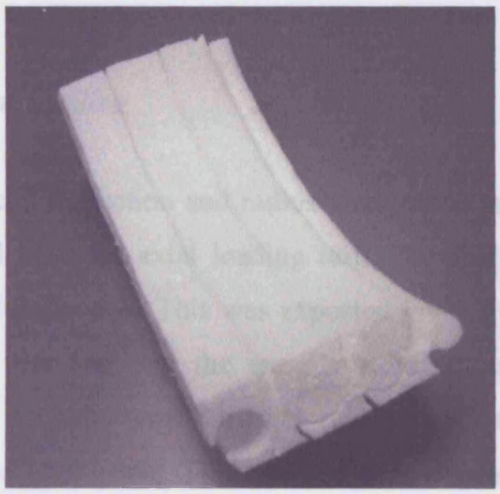

Figure 5.16 Cut Omega profile helical spring

The experimental implications of interlocked profiles, in particular the Omega profile are discussed in chapter 6. Given the relative ease of fabricating interlocked profiles, the polystyrene model described thus offered considerable advantages for the verification of both simple and complex helical geometries. In the next section, the results of some of these cut springs are presented and discussion made on the deformation of the springs.

5.5 Results and Discussion

Figures 5.17 – 5.23 show the experimental results for the range of cross-sectional profiles that were cut. The results are first presented for axial loading cases, followed by radial loading (internal pressure) and the combined axial and radial loading.

5.5.1 Results for Axial Loading

The changes in the coil deflection and radius were noted and plotted against the applied load. For all the pure axial loading tests, the applied axial load varied linearly with the coil deflection. This was expected given the observations in the earlier chapters and the fact that the springs were not operated in the large deflection condition. An axial tensile load caused the coils to extend their length while the coil radius contracted. The coil stiffness depended upon the cross-sectional area of the spring. A larger cross-sectional area generated larger spring stiffness, as was expected from the theory. The reduction in radius due to the applied force was not linear, again as expected from the theory. However, discrepancies occurred in the relative radius magnitudes.

The results for the square cross-section are a representation of most of the profiles and hence will be described here. The responses of the square section subjected to axial loads are shown in figures 5.17(a) - (c). Results for the other cross-sections tested are presented in Appendix E. Although at first look, the discrepancy between the analytical result and the experimental measurements seems large, when consideration is given for the likely inaccuracies in the material data (see section 5.3) and also the necessity to constrain the helix ends (in the analytical model – see section 3.5), then the differences in response are not surprising. End constraint would be expected to raise the stiffness and this indeed is seen in figure 5.17(b).

The experimental results of the axial force – deflections for all cross-sections gave good agreement with the analytical plots (for example, see figure 5.17(a)). Several

reasons were attributed to the small differences obtained. These reasons however were not concerned with the assumptions made in obtaining the analytical solution. First, it was noted that the results were affected by the values of shear modulus and Poisson's ratio. Secondly, the measurements made on the deformation of a coil were to the nearest 0.5 mm. This caused some error in the data measured as some of these deformations were quite small. For example, the coil radius contracted less than 0.5 mm when the coil was deflected by 10 mm axially in the analytical solution. Experimentally, such a small deformation is hard to observe, not least to measure. Hence, where possible, the experiments for the axial tensile loading were carried out twice to obtain a more accurate data spread.

It was also worth noting that the results obtained analytically were for coils with both the ends fixed from rotation. As for the experiments, the coils were only fixed at one end while the other end was free to rotate. The experimental responses mirrored the trends obtained from the finite element responses (see figure 3.18(c) in chapter 3), where the helical coil in the finite element model was also constrained at one end only. This helps to explain the discrepancy seen in figure 5.18(b), where a larger change in the radius was observed experimentally than analytically, as a consequence of the greater degree of freedom.

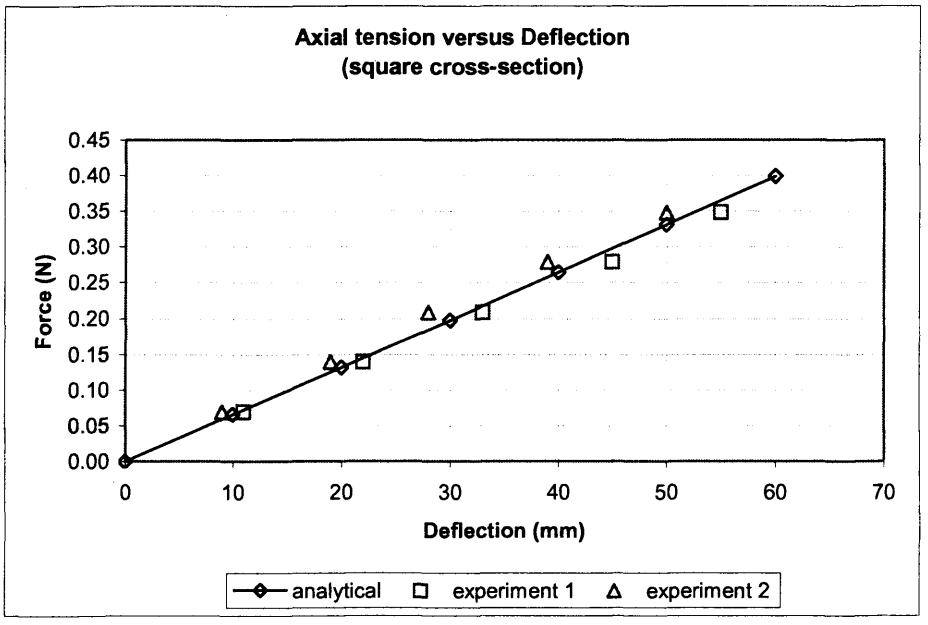

Figure 5.17a Axial load – deflection for square cross-section experimental result

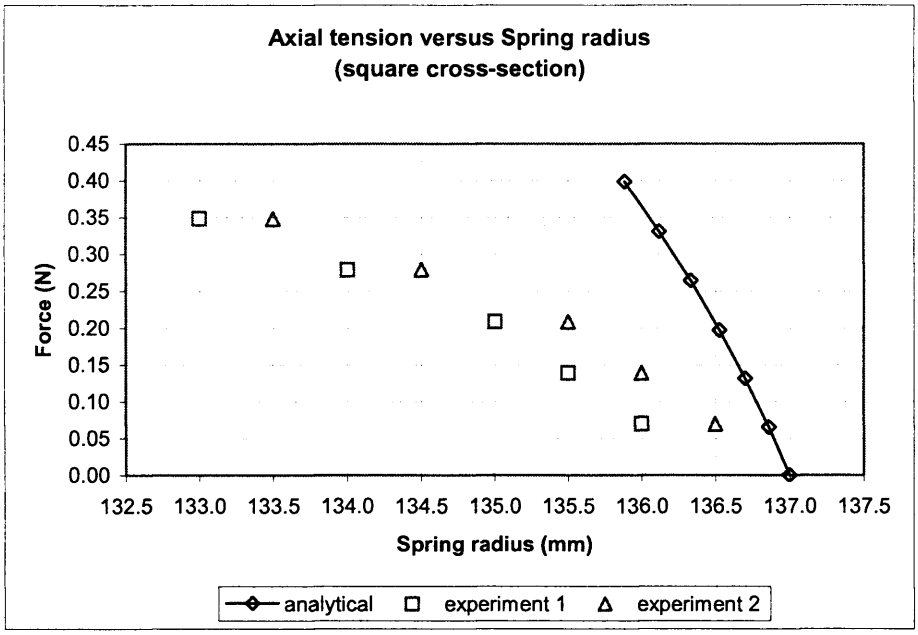

Figure 5.17b Axial load – spring radius for square cross-section experimental result

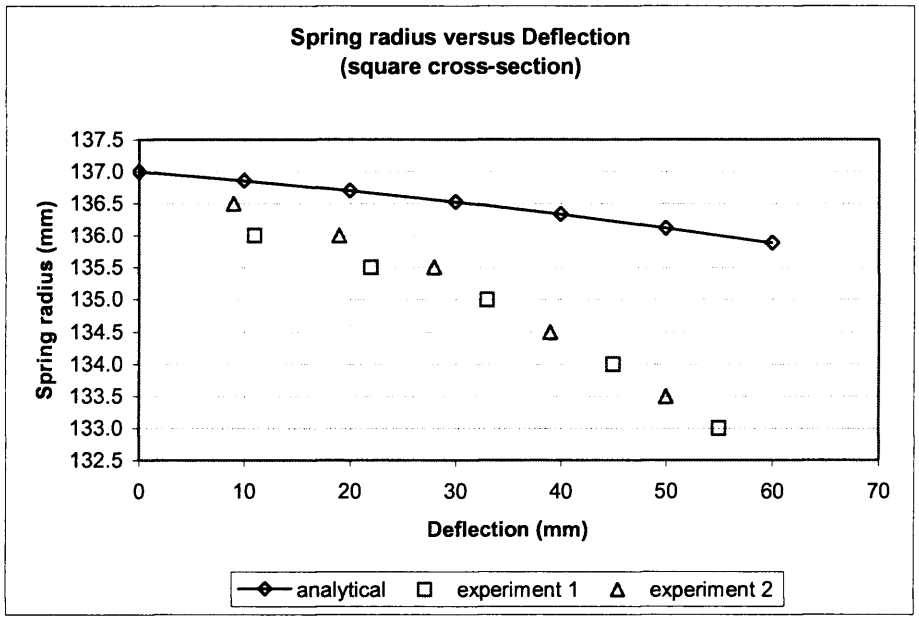

Figure 5.17c Spring radius – deflection for square cross-section experimental result

However, the results are still comparable because the measurements were taken in small deformation region as the polystyrene is not as elastic as a metallic material and large deformations could have caused the coil to plastically deform. Given the discrepancies in the magnitudes of the coil radius obtained, the corresponding response of the change in the overall spring deflection is also affected (see figure 5.17(c)).

5.5.2 Results for Internal Pressure Loading

It was noted that the dimension of the polystyrene cross-sections compared to the helical spring is no longer small, hence there would be some error obtained in the analytical result. However, to minimise this effect, the appropriate wire strain value can be obtained from finite element analysis for the cases of pure radial loading and the cases of combined axial and radial loading modes. This was appropriate since in the previous chapters, the wire strain values obtained from the analytical result corresponded well with the result of finite element analysis. Additionally, the finite element analysis does not work on the assumption of slender rod, hence making it valid for use in this analytical solution.

The results of internal pressure loading for square section are presented in figures 5.18(a) – (b) and results of other sections are shown in Appendix E. It should be noted that the internal pressure was simulated using radial forces applied at five locations at angles equally spaced. There are distinct discrepancies obtained between the analytical results compared to those obtained in the experimental tests. This can be attributed to several problems. One is that the rod from which the spring is fabricated is no longer considered slender and secondly to get close to a distributed line loading, the number of points of applied radial loads appears to be insufficient, and would ideally need to be increased. However, this was not practical given the experimental setup and measurements of the resultant deformation would have been difficult to obtain, as the iterative adjustment of the pulley system would have been required.

In figures 5.18(a) and (b), it can be seen that a radial load applied to the polystyrene expands the spring radius much more than that predicted from the analytical solution. This suggested that the experimental helical spring was of lower stiffness than its analytical model. The reason for this discrepancy is thought to be due to the limited number of points over which the pressure load was applied (as suggested earlier), which causes the coil to expand in a non-uniform manner and to rotate off-centre (one of the ends is not fixed). Measurements of the change in spring radius taken at various diametrical points thus gave larger average values as the coil was eccentric to the spring axis.

Furthermore, as only one coil was loaded, the coil expanded more than it would if more coils were loaded in the tests. The additional loading of adjacent coils would prevent the large radial expansion given that each coil constrains its neighbour. Loading a single coil can be regarded as loading a curved beam whose free end can thus deflect without constraint.

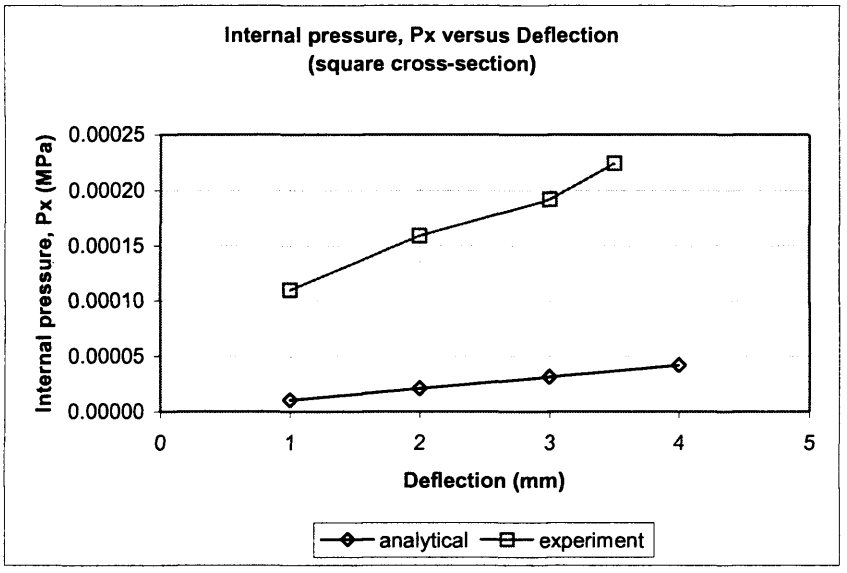

Figure 5.18a Internal pressure – deflection for square cross-section experimental result

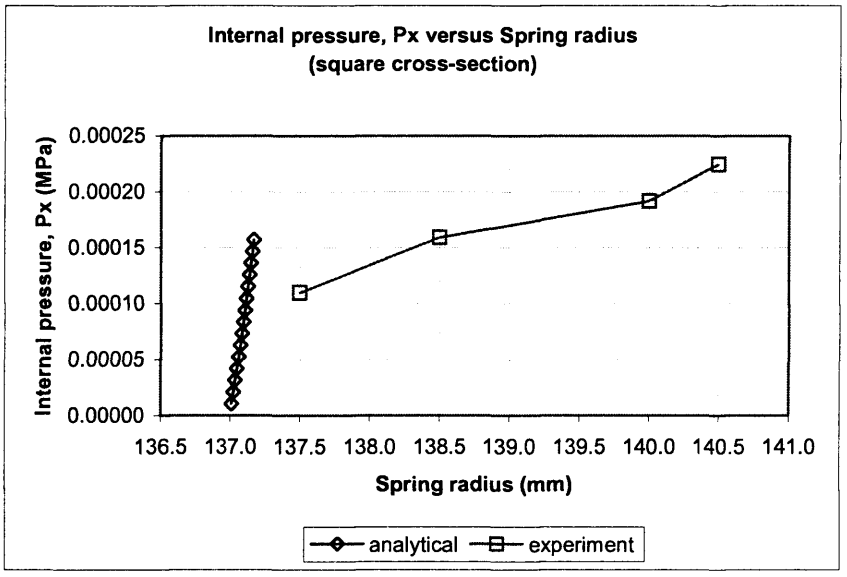

Figure 5.18b Internal pressure – spring radius for square cross-section experimental result

Although the radial load did not fully simulate the internal pressure, the twisting of the cross-section of the helical wire can still be observed for the L and Z

sections and the results are shown in figures 5.19 and 5.20 respectively. This confirmed that that a resultant moment was generated about the centroid of the cross-section by the radial load, resulting in the twist of the wire cross-section. This was not observed in the square and rectangular (i.e. symmetric) sections. The analytically derived response for the angle of twist is not shown in figures 5.19 and 5.20 due to the large discrepancy between these and the magnitudes seen in the experimental work, nevertheless the trends seen are still the same.

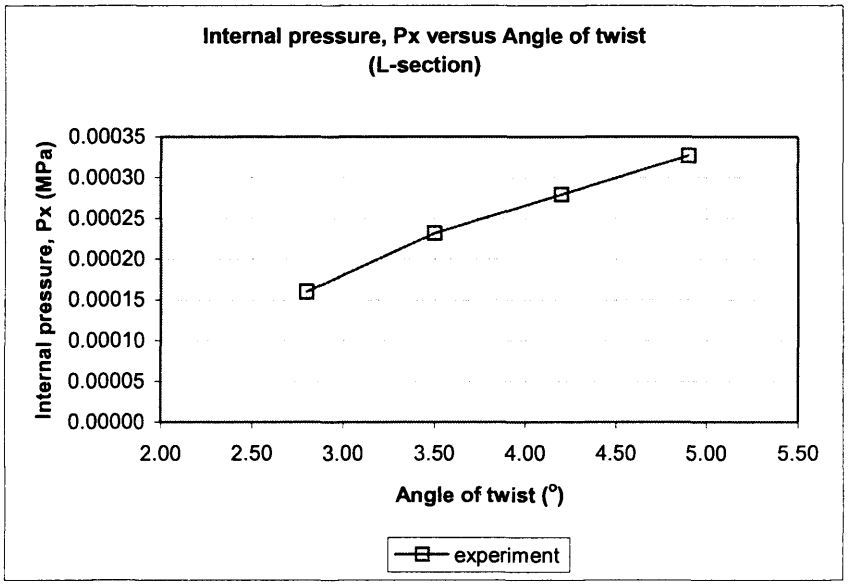

Figure 5.19 Internal pressure – angle of twist for L cross-section experimental result

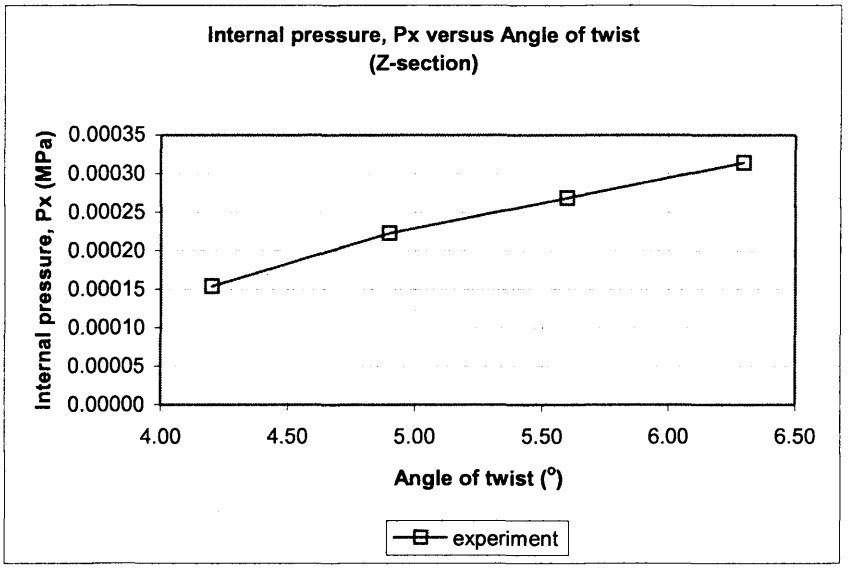

Figure 5.20 Internal pressure – angle of twist for Z cross-section experimental result

5.5.3 Results for Combined Axial and Internal Pressure Loading

The results for the square cross-section helix are presented in figures 5.21(a) and (b) and given that the trends seen in the other sections was similar, these are presented in Appendix E. For the applied tension load with fixed internal pressure load step, it can be seen that the stiffness of each spring increases as the radial load step increases. This is very obvious for the rectangular cross-section helices (shown in figures 5.22 and 5.23) and less obvious for the other sections. This confirms the analytical and numerical findings in this work, that spring stiffness is raised by the application of an internal pressure load. Generally, the pressure and hence the stiffness effect was small as the radial load step only caused small axial deflections. The line loads, X of 2.79, 3.97, 4.79 and 5.61 N/m corresponded to weight of pannier added with 0, 3, 5 and 7 coins respectively in each of the panniers. The results for the spring radius measurements reinforced the above conclusions and were in line with those expected from analytical studies. A representative plot can be seen in figure 5.21(b) with the remaining plots shown in Appendix E.

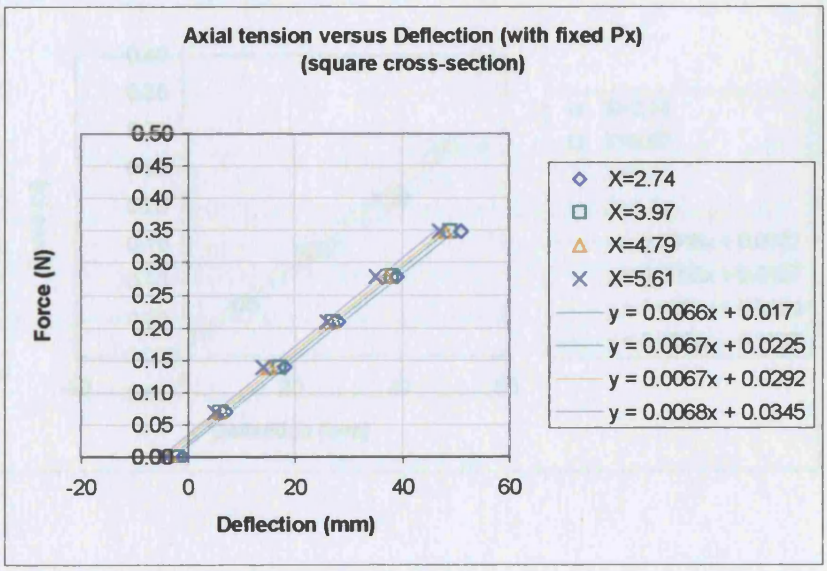

Figure 5.21a Axial tension - deflection for fixed internal pressure step values (experimental result for square section)

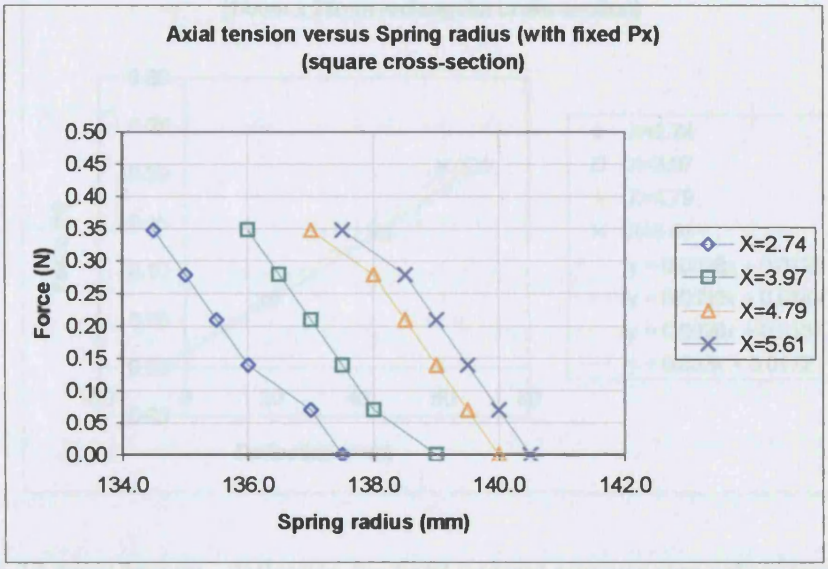

Figure 5.21b Axial tension – spring radius for fixed internal pressure step values (experimental result for square section)

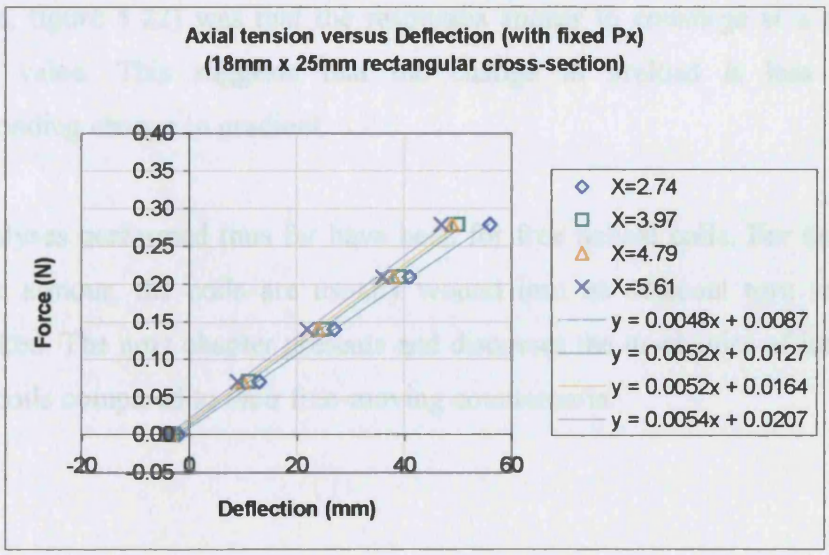

Figure 5.22 Axial tension - deflection for fixed internal pressure step values (experimental result for rectangular section (18mm x 25 mm))

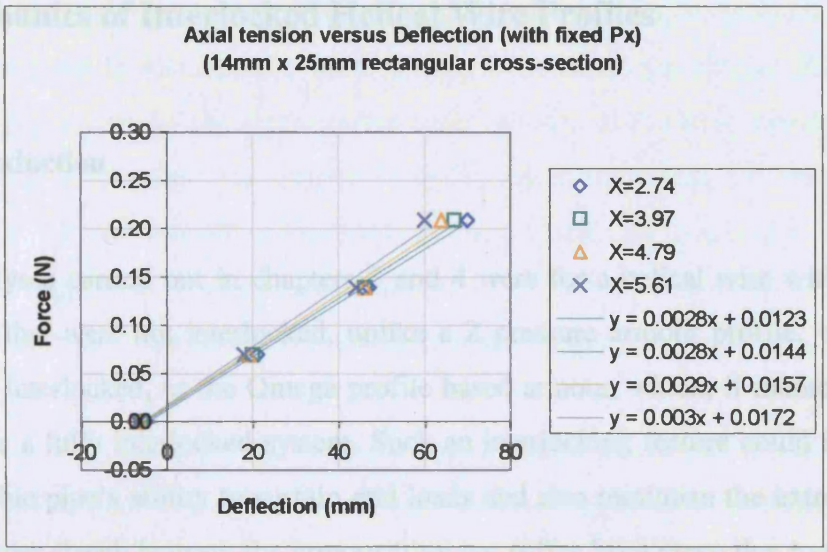

Figure 5.23 Axial tension - deflection for fixed internal pressure step values (experimental result for rectangular section (14mm x 25 mm))

Additionally, the increase in preload that was discussed in section 3.5 (chapter 3) was readily observed for all cross-sections tested (for example, see figure 5.21(a)). An interesting observation which can readily be seen in some of the response (for example, figure 5.22) was that the responses appear to converge at a particular preload value. This suggests that the change in preload is less that the corresponding change in gradient.

The analyses performed thus far have been for free helical coils. For the case of pressure armour, the coils are usually wound into its adjacent turn and hence interlocked. The next chapter presents and discusses the mechanics of interlocked helical coils compared to their free-moving counterparts.

6 Mechanics of Interlocked Helical Wire Profiles

6.1 Introduction

The analyses carried out in chapters 3 and 4 were for a helical wire with cross-sections that were not interlocked, unlike a Z pressure armour profile, which is partially interlocked, or the Omega profile based armour, which, if manufactured would be a fully interlocked system. Such an interlocking feature could improve the flexible pipe's ability to sustain end loads and also minimize the extrusion of the polymer sheath beneath the armour (this can suffer from creep due to the high service temperatures and pressures), and prevent any non-uniform (i.e. localized) extrusion. The interlocked nature will consequently also restrict the degrees of freedom of the helical coil compared to one without the interlock. In reality, the helical coil for a fully interlocked Omega profile layer would most likely be permitted a small movement in the axial direction of the helical structure before being restricted from further movement due to the interlocking feature. The behaviour of the system is therefore complex and may involve several mechanisms.

This chapter describes the mechanics of the interlocked profile, with reference to the Omega profile in particular. The response of interlocked helical coils to axial and pressure loading modes was investigated mainly by analytical methods, and also using some numerical and experimental studies, with these results presented here. Given that the coils were assumed to be interlocked, the structure is akin to a cylindrical tube but with lines of weakness along the tube and hence was expected to have a larger degree of freedom of movement compared to a purely cylindrical tube. The effect of the interlocking feature on the overall response of the helical structure and the implications on its load carrying capacity compared to one which is not interlocked is also discussed here. Additionally, issues with ends of a helical spring were also considered. For a pressure armour, the ends are always fixed to the end fittings, which prevents the coils from rotation when loads are applied.

The analysis of the mechanics of helical springs, presented here, assumes that the pipe is of long length and the relative coil movements are similar along that length. This is most definitely true at the centre portion of the helical structure but towards the ends, there is expected to be some restriction of freedom of movement. The differences in relative movement along that length of the armour may well suggest a variation in the behaviour of the coils in terms of fretting fatigue. This will be discussed in detail in the next chapter.

The next section describes the mechanics of an interlocked profile subjected to axial and pressure loading modes, and highlights any possible mechanisms which could affect the fretting fatigue behaviour (some of these points will be discussed in detail in chapter 7).

6.2 Mechanics of Interlocked Helical Wire

As described in the previous chapters, for a helical wire which is not interlocked, the coil is permitted to change its dimension axially and also radially when subjected to axial loading. This holds true if the helical spring is not fixed at the ends, from rotation. Hence, when an axial load is applied, the helical spring not only changes in length but can also twist.

When a helical wire is interlocked to its adjacent coil, the free movement of the spring will be restricted. Referring to the hypothetical Omega profile given in figure 1.6 in chapter 1, it can be seen that the coil initially behaves like a helical spring until the protrusion part of the profile comes into contact with the walls of its respective socket. When this occurs, a force is generated between the two contacting components. At this stage, the helical spring is then prevented from free movement. The mechanics of the interlocked helical wire when it is fully locked and in contact is of great importance for several reasons. Firstly, the behaviour under axial and pressure loading is expected to be totally different to a conventional non-interlocked profile, and the response to these loads will govern factors such as the flexible pipe's inherent flexibility. Secondly, the fact that the surfaces are now in contact, and that these zones carry substantial loads coupled

with the possibility that relative movement may still occur (before and/or after full locking has been achieved), has implications for fretting fatigue given that a tiny amount of movement can cause fretting to occur on the contacting surfaces. Figure 6.1 shows a schematic of an interlocked helical spring with the Omega profile.

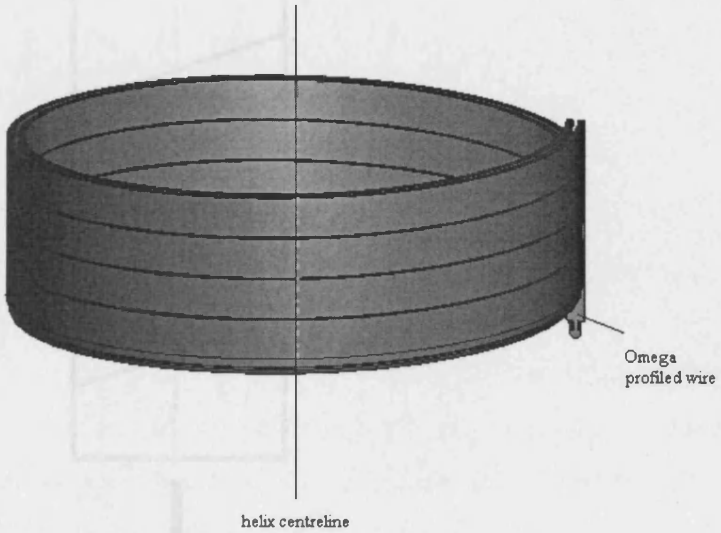

Figure 6.1 Omega profile interlocked wire helical spring

Consider the case where the profile is fully locked and the mating surfaces are in contact. When an axial load, say a tensile force is applied to the ends of the helical wire as shown in figure 6.1, the helical system does not extend in length in the axial direction in the same way a helical spring would. Additionally, conventional helical springs would be expected to rotate about its spring axis when under axial load; however it appears unlikely that an interlocked system would behave in the same manner. In spite of this, minor movements between adjacent coils cannot be ruled out and if they existed, would provide a possible mechanism for fretting fatigue. The possibility of generating small intercoil sliding movements can be understood better by considering figure 6.2. This figure shows a schematic of a series of blocks which are assumed to be interlocked using something akin to an Omega profile.

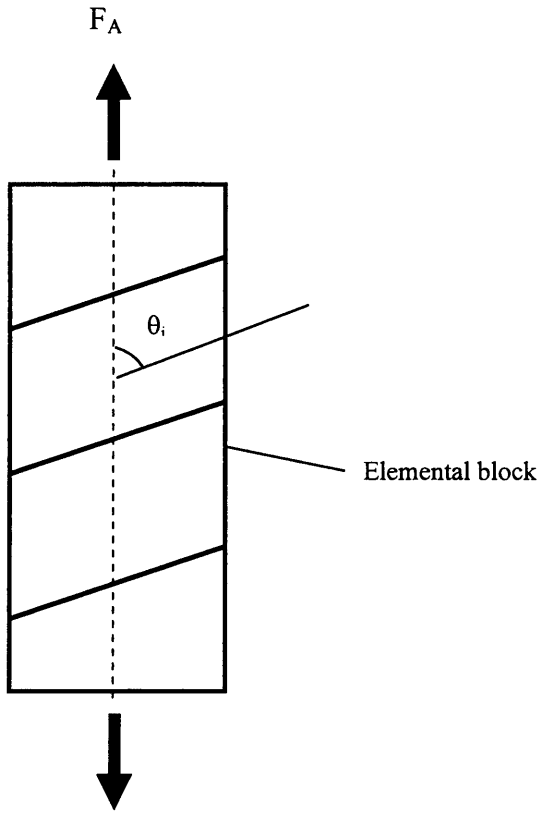

Figure 6.2 Straight elemental interlocked blocks

If the system shown in figure 6.2 is subjected to an axial load, the blocks would be expected to slide away from each other. The smaller the inclination angle, θ_i, to the direction of the axial loading, the greater the tendency of the blocks to slide past each other. This behaviour is due to the fact that the axial load generates a resultant force which tends to move the blocks apart. This is illustrated in figure 6.3.

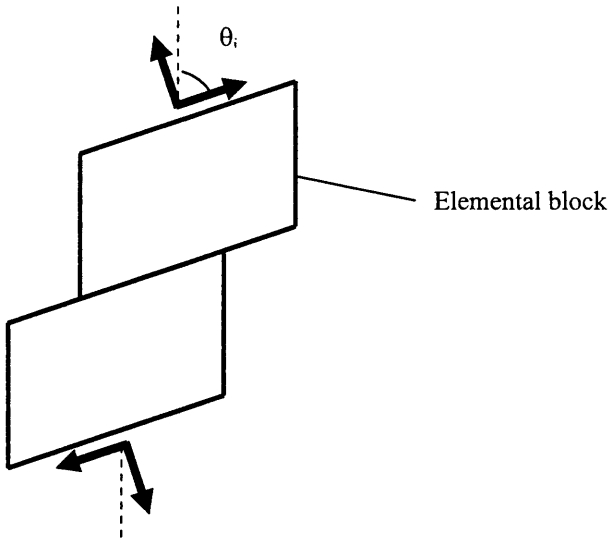

Figure 6.3 Straight elemental interlocked blocks sliding apart under axial load

It is important to note that the sliding motion of the blocks results in a misalignment of the axial load components. If this is permitted to occur (i.e. if the axial loads can shift to accommodate this movement) then the blocks will continue to slide past each other. In practice such a degree of freedom is not present and sliding can only continue if the system rotates such that the axial local axes realign. This is shown in figure 6.4. This structure is similar to the one created in metal single crystals where slippage between the atomic planes occurs (Pascoe, 1978).

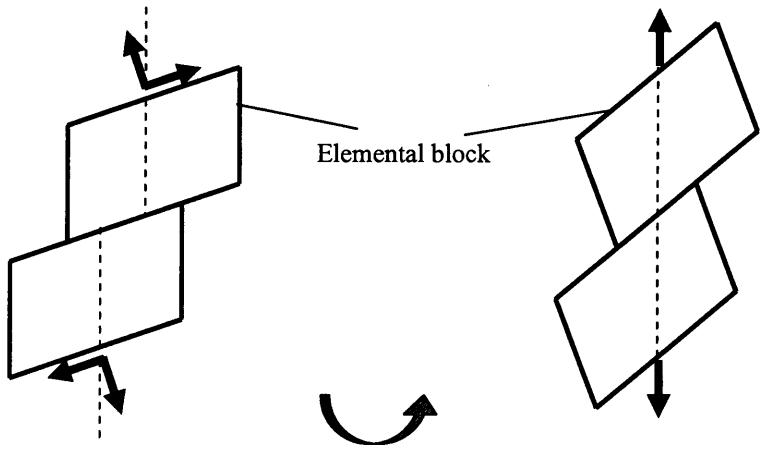

Figure 6.4 Realignment of axial load on interlocked blocks

A physical demonstration of the movement of interlocked blocks was set up using sections cut from cable trunking and adhesively bonded together. This is shown in figure 6.5. An axial tensile load was applied at each end and the blocks tended to slide away from each other as expected.

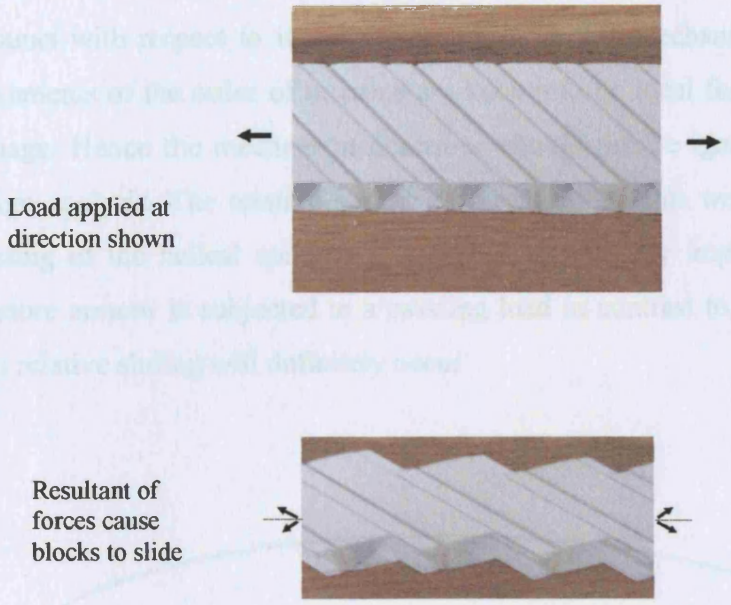

Figure 6.5 Demonstration of interlocked blocks before and after applied axial load

In the course of this work, the initial postulation was that an interlocked helical spring system would behave in the same manner under axial loading. However, this was probably only true in the initial stages after an axial load is applied, given the fact that the helical wire is a curved beam compared to the straight elements considered earlier. This can be illustrated in figure 6.6, which shows a hypothetical single interlocked coil and considers it as a series of interlocked blocks of the type described above.

Initially, it would seem that the interlocked block will also slide relative to its adjacent block under an axial load. From a geometrical consideration, this will be accompanied by a commensurate reduction in coil diameter. However, because the wire is a curved beam, additional force is needed to expand or contract the helical structure as a whole, depending on whether it is subjected to an axial tensile or compression load.

In order to do that, a large force is needed to bend the beam into its required position. Additionally, a large contact force is generated due to the axial loading. This prevents further sliding, if it occurs at all, by generating an increased frictional component which opposes sliding, and rises as the axial load rises. Therefore, the interlocked helical wire would be expected to move only minute amounts with respect to its adjacent coil under this mechanism. Even so, small movements of the order of microns are known to be ideal for generating fretting damage. Hence the mechanism described should not be ignored in any fretting design analysis. The relative sliding of the coil elements will correspond to the twisting of the helical spring about its spring axis. By implication then, if the pressure armour is subjected to a twisting load in contrast to a purely axial load, then relative sliding will definitely occur.

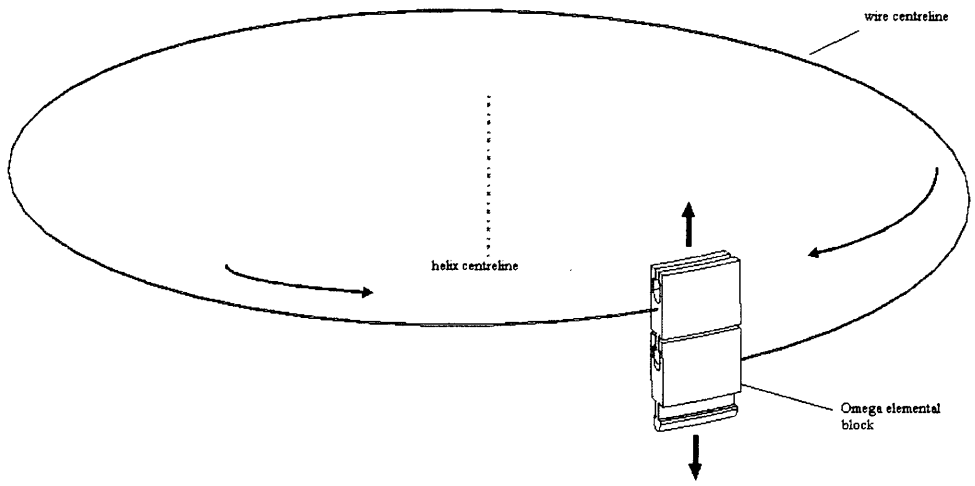

Figure 6.6 Elemental interlocked helical spring under axial load

The presence of constraints in the degrees of freedom of movement of the helical coil as provided by the practical terminations of the flexible pipe suggests that intercoil sliding would theoretically be impossible. However, in practice, these constraints may not be absolute, and in any case, their influence may not be transformed uniformly throughout the helical structure, especially if the frictional forces are substantial.

If the previous discussion is valid, the boundary conditions at the ends of the interlocked helical coils are of great significance to the intercoil movements of an interlocked system (such as the Omega profile). Furthermore, if the nature of the interlocking is such that the coils are permitted a large degree of freedom of movement (i.e. the profiles do not contact fully along all interlock surfaces), then the armour may (at least initially) behave as a simple helical spring until such time as the movement generated, produces a full interlock. This raises the possibility that additional relative movements can occur between adjacent coils, and that these may give rise to fretting fatigue. To illustrate this further, the figure 6.7 shown here is used.

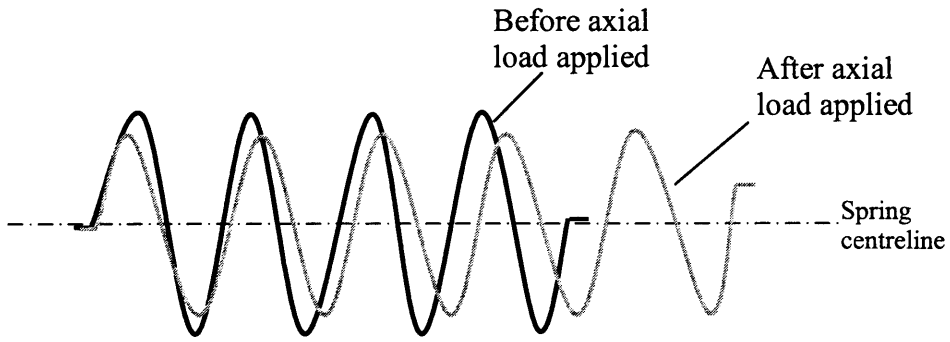

Figure 6.7 Helical coils with ends free to rotate subjected to applied axial load

This shows a simple helical spring with no interlocking between adjacent coils. When an axial load is applied to stretch the helix as shown in the figure, the helix not only increases its length but also experiences a contraction in its diameter. Additionally, the helix is free to rotate about its axis when the axial load is applied and as described in chapter 3, a geometric analysis reveals that this rotation will indeed occur. Hence, in this instance, there is also an increase in the effective number of coils of the helix. This must mean that there is relative movement between adjacent coils. Thus, if an interlocked helical wire is used and the interlock is not perfect, there will then be relative sliding between the contacting surfaces about the spring axis, which in turn could encourage fretting fatigue.

If however, as mentioned earlier, the flexible pipe structure is fixed at the termination ends using end caps, this mode of relative movement is also prevented and the helix only increases in length along its axis and contracts in radius, as axial load is applied. The number of coils remains the same. This is shown in figure 6.8.

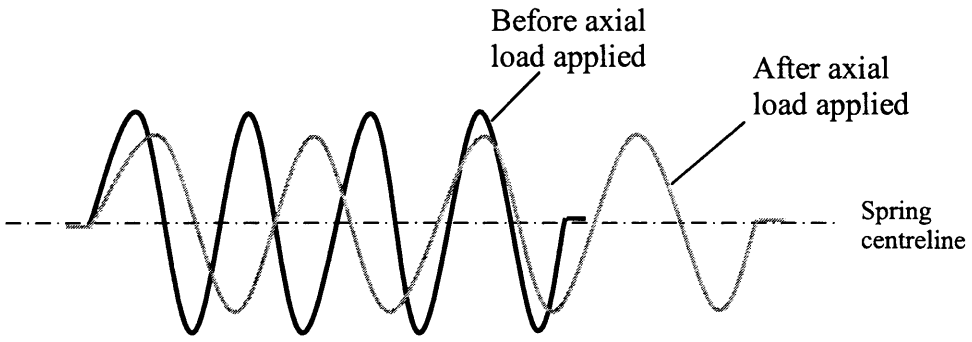

Figure 6.8 Helical coils with ends fixed from rotation subjected to applied axial load

In order to simplify the analysis of an interlocked system, as presented later, it has been assumed that the end rotation is prevented by the constraining influence of terminations. Indeed for the analysis of an interlocked helical wire subjected to an internal pressure, it was necessary that the ends of the helical coil be fixed from rotation, or else the helix will just straighten out when the load is applied. The coils move a similar distance (relative to each other) when an internal pressure is applied, therefore no relative sliding about the spring axis is experienced by the surfaces of the interlocked profile as the number of coils remains the same.

The movements above are assumed to be uniform throughout the length of the pipe. However, in real systems, at coils near to the end terminations of the pipe, which are fixed from movement, there is a constraint imposed which does not allow the coils to move as freely as in the middle portion of the long pipe. End terminations are likely to constrain the end of the helix from radial movement as well as rotation. This implies that relative movement of the coils can occur for short distances near the end terminations. These movements are required in order to reconcile the need to constrain the helix ends, with the need to alter the helix

diameter. The movements, though small could theoretically cause fretting to occur as pointed out by Ramsey (1991). This will be discussed further in the next chapter.

The next section describes the response of the interlocked helical spring, with particular reference to an Omega profiled wire, subjected to axial load, internal pressure and a combination of both.

6.3 Load Analysis of an Interlocked Helical Coil

6.3.1 Axial Loading Analysis

The previous discussion dealt with the possible degrees of freedom of movement of a helical interlocked coil, with a view to understanding the potential for fretting damage. In order to proceed with the analysis of the behaviour of an interlocked helix, the configuration chosen has been of a coil with its ends prevented from rotation and its coils having come into contact along the mating surfaces of the interlocking profiles. For clarity, this is defined as the 'locked' position. When the coils are not locked, the behaviour can be determined from the analysis of the mechanics of a helical spring as presented in chapter 3. However, it should be noted that during the process of reaching the locked condition, the protruding portion of a profile slides along the internal surfaces of the socket of the adjacent coil. There is a possibility that friction impedes the free movement of these sections and hence of the helix as well. The effect of friction on the response of an interlocked system is therefore briefly considered here. Dry Coulomb friction is considered where the frictional force is proportional to the normal force between the two bodies that are sliding and as described in Hills and Nowell (1994). When the surfaces of the interlocked profile is considered, the frictional force, $F_{friction}$ is given here as

$$F_{friction} = \mu X l \tag{6.1}$$

where μ = coefficient of friction between the contacting surfaces

X = line loading (normal force to surface) per unit length

l = length of helical wire in one coil

Since the frictional force acts to oppose the relative motion between two surfaces in contact, the total axial force, F_A of the interlocked helical spring considering the effect of friction is then given here as

$$F_A = T\sin\alpha_1 + N_b\cos\alpha_1 + \mu Xl \tag{6.2}$$

which is a modification of equation 3.68 given in chapter 3.

Moving on to the scenario where the helical coil is now fully locked with its adjacent coil, as discussed above, it is clear that the overall helix length remains the same, and that this implies that the radius remains constant as well. Hence, the helix angle also remains constant from the geometrical relationship defined earlier in chapter 3. Therefore, using the slender rod theory presented in chapter 3, the final curvatures and tortuosity of the interlocked helical coil when subjected to applied axial loading are given respectively by

$$\kappa_{n1} = \kappa_{n0} \tag{6.3}$$

$$\kappa_{b1} = \kappa_{b0} \tag{6.4}$$

$$\tau_1 = \tau_0 \tag{6.5}$$

where κ_{n0}, κ_{n1} = initial and final curvature in normal direction

κ_{b0}, κ_{b1} = initial and final curvature in binormal direction

τ_0, τ_1 = initial and final tortuosity

It must be emphasized that this analysis considers the configuration when the helical coil is fully in contact and therefore fully interlocked. Therefore, the initial curvatures and tortuosity values are different from those defined in section 3.2.3 and can be thought to take the value of the point just when the wire starts to be in contact and locked.

Given that the initial and final values of the curvatures and tortuosity are essentially the same from equations 6.3 – 6.5 (because the coil is locked), this implies that the internal moments which were defined using the constitutive relationship as described in chapter 3 are then given by

$$G_n = 0 \tag{6.6}$$

$$G_b = EI_b\left(\kappa_{b1} - \kappa_{b0}\right) = 0 \tag{6.7}$$

$$H = GJ\left(\tau_1 - \tau_0\right) = 0 \tag{6.8}$$

Using slender rod theory, the equilibrium equations presented earlier in equations 3.46 – 3.51 can now be employed. With expressions 6.3 – 6.8, equation 3.49 shows that the binormal shear force, N_b is equal to zero. Hence, the equilibrium equation reduces to the form shown below.

$$T\kappa_{b1} + X = 0 \tag{6.9}$$

The radial line loading component, X, corresponds to the resultant of the contact force, between the contacting surfaces of the interlocked profile, pointing towards the centreline of the helical spring axis. This contact force is denoted X_c to avoid confusion with the internal line loading force which corresponds to an internal pressure load. X_c can be defined in terms of the individual contact forces between the coils, thus this is very similar to the situation of contacting of the wire surfaces as described in Phillips and Costello (1973), except here, the wire profile is of approximately rectangular in nature. Figure 6.9 shown overleaf indicates that for any one coil cross-section, two adjacent coils contact it; hence two contact forces are experienced. From an understanding of the geometry of the helix, if a section is taken along plane **A-A**, then it can be seen that the individual coils sit along curves whose radius is defined by the angle of cut.

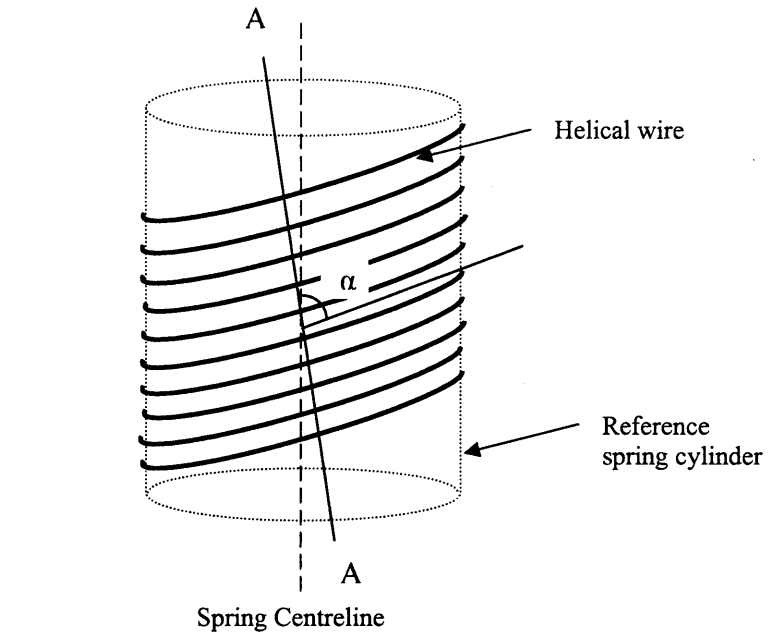

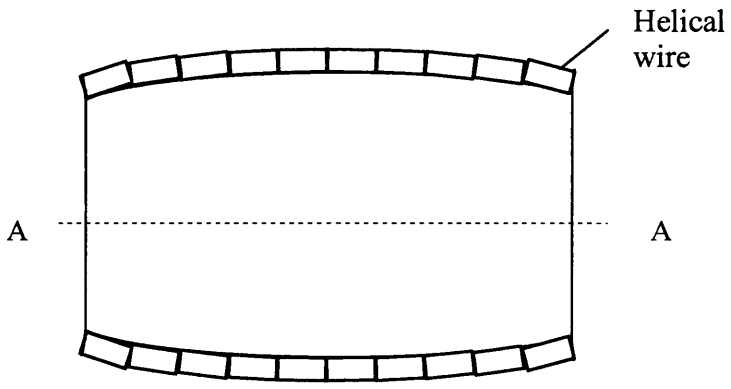

Note that the interlock features are not shown here

Figure 6.9 Observation of the contact force through cut section A-A

When observed through cut section **A-A**, the true cross-section of the wire under the contact loads can be observed. The cross-section of each coil can now be approximated by an elongated rectangular area contacting its adjacent coils. Additionally, a helical wire cross-section is located on the reference spring cylinder (see figure 6.9) with an angle γ to adjacent coil cross-sections. It can be seen that along this cut section **A-A**, the reference cylinder is now somewhat

elliptical in nature. However, the angle γ is small and the distance of the wire centreline to the spring centreline is still taken as the radius of the helical spring in order to derive the contact load angle to the resultant contact force towards the spring centreline, denoted here by λ. The derivation given by Phillips and Costello (1973) cannot be used in this scenario, in part because their analysis considered a number of helical wires wound concentrically together. Also, due to the fact that the helical angle considered is very large, observation of the cross-section through the cut section generates a very different view from the one shown in figure 6.9. The definition of the angle λ is illustrated in figure 6.10, where the contact point is at point A shown on the helical wire cross-section.

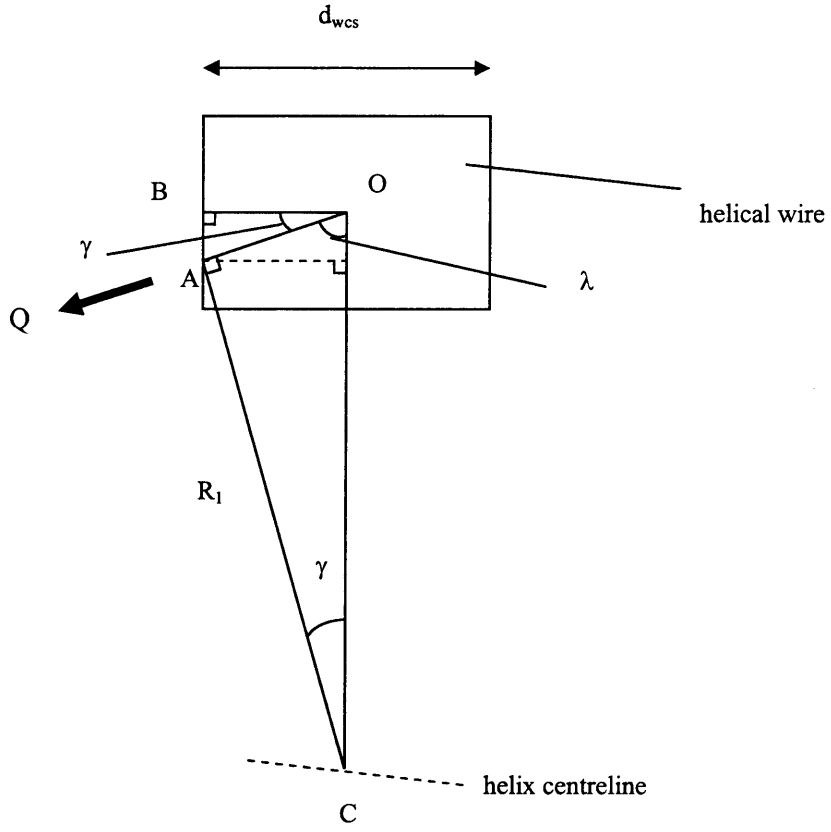

Figure 6.10 Definition of wire contact angle to centreline of helical coil from cut section A-A

The width of the profile from the cut section **A-A**, d_{wcs} is given by

$$d_{wcs} = \frac{d_w}{\cos\alpha_1} \tag{6.10}$$

where d_w = width of wire cross-section

α_1 = final helix angle

It is assumed that the dimensions of the helical cross-section are small compared to the coil diameter, hence the angle between the contact force and the surface of the reference cylinder, γ is given by

$$\sin\gamma = \frac{d_{wcs}}{2R_1} \tag{6.11}$$

where R_1 = final radius of helix

Substituting equation 6.10 into 6.11 gives

$$\sin\gamma = \frac{d_w}{2R_1\cos\alpha_1} \tag{6.12}$$

From figure 6.10, it can be observed that the angle γ and angle λ add up to $\pi/2$. Therefore the angle between the contact force and the resultant force towards the spring centreline, λ is given here as

$$\lambda = \frac{\pi}{2} - \left(\sin^{-1}\frac{d_w}{2R_1\cos\alpha_1}\right) \tag{6.13}$$

The line of action of the contact force is acting approximately towards to the centreline of the helical wire. Hence the resultant of this contact force between the contacting surfaces of the adjacent coils gives

$$X_c = -2Q\cos\lambda \tag{6.14}$$

where X_c = radial line loading

Q = contact force per unit length

As can be observed from figure 6.10, the resultant of this contact force in the axial direction of the helical spring cancels out because one side of the interlocked profile is pulling while the other is being pulled. As discussed in section 6.2, for an interlocked profile helical wire, it is expected to have a higher structural stiffness compared to a normal helical spring which has large degree of freedom of movement. This implies that a helical spring with an interlocked profile, such as the Omega wire can be made to withstand some axial load. In conventional flexible pipes, the tensile armour wires, which have large helical angles, take up most of the axial load of the pipe structure. If an interlocked profile pressure armour is used, the tensile armour wires could be constructed using a smaller cross-sectional wire area. Hence, the overall weight of the pipe structure could be reduced, while still retaining its axial load carrying capacity.

The axial load, F_A can now be expressed in terms of the component of its line loading in the axial direction of the pipe as the interlocked helical wire is now treated as a cylindrical tube. This is given by

$$F_A = 2\pi R_1 Q_L \cos\alpha_1 \tag{6.15}$$

where Q_L = helical line load in the axial direction of pipe

Further to this, the relationship of the helical line load in the axial direction of the pipe, Q_L to the actual contact force, Q is given by

$$Q_L = Q \sin \lambda \tag{6.16}$$

Therefore, the applied axial load can then be expressed in terms of the contact force, Q of the contacting surfaces and is given here by

$$F_A = 2\pi R_1 Q \cos \alpha_1 \sin \lambda \tag{6.17}$$

Furthermore, from equations 6.9, 6.14 and 6.17, the tension in the wire gives

$$T = \frac{F_A}{\pi \cos^3 \alpha_1 \tan \lambda} \tag{6.18}$$

Although the interlocked helical wire now behaves like a tube, this tension force still exists because of the possibility of some sliding contact between the wire surfaces.

The axial load carrying capacity of the interlocked helical coils is determined by the yield strength of the material. Once the yield strength is reached, then necking can occur at the thinnest portion of the interlocking profile. The stress at this part is given by the force normal to the surface area under load, which is approximated by

$$\sigma_p = \frac{Q \sin \lambda}{h_w} \tag{6.19}$$

Where σ_p = contact stress at thin width of protrusion

h_w = height of wire cross-section

and λ is defined in figure 6.10

6.3.2 Internal Pressure Loading Analysis

The behaviour of an interlocked helical spring subjected to internal pressure is based on the conclusion that the initial and final configuration of the helical spring remains the same, as given by equations 6.3 – 6.5. Furthermore, for consideration of a symmetric cross-section, that is a cross-section which does not twist with respect to the internal pressure (see section 4.2), the conditions 6.6 – 6.8 apply. Hence, from the set of equilibrium equations in 3.46 – 3.51, the solution reduces to the form shown below.

$$T\kappa_{b1} + X_R = 0 \tag{6.20}$$

where X_R = total line loading in radial direction

The total line loading, X_R, is made up of the internal pressure line loading, X, as well as the contact line loading, X_c given that the helical wires are fully in contact with their adjacent coils. The direction of the internal pressure is always pointing out from the spring centreline while the contact force is pointing in the opposite direction (see figure 6.10). Therefore, the response of an interlocked helical spring with a symmetric cross-section subjected to pressure is given by

$$P_X = \frac{T\kappa_{b1} - 2Q\cos\lambda}{d_w} \tag{6.21}$$

where P_X = internal pressure on helical wire

It can be observed from the solutions derived above, that an interlocked helical spring under internal pressure behaves in a similar manner to a cylindrical tube. Essentially, the tension in the wire is influenced by the applied internal pressure, just as would be the case for a thin walled cylindrical tube. However, localized stresses are generated in the case of an interlocked helical spring, at the interlocked contact sites and this makes the pressure armour more susceptible to failure than a solid of similar dimensions. The above analysis has ignored the

possibility of relative movement between the coils as suggested in section 6.2. As has been discussed, such movements even if minute, could impact upon the fretting fatigue behaviour of interlocked pressure armour.

For the case of non-symmetric cross-section helical wire, consideration has to be made for the possibility that rotation of the cross-section could occur. The curvatures and twist of an interlocked helical spring subjected to an internal pressure are given by the analysis undertaken in section 4.3.2.

$$\kappa_{n1}' = \kappa_{n0}' = \kappa_{b1} \sin\varphi \tag{6.22}$$

$$\kappa_{b1}' = \kappa_{b0}' = \kappa_{b1} \cos\varphi \tag{6.23}$$

$$\tau_1' = \tau_0' \tag{6.24}$$

where κ_{n0}', κ_{n1}' = initial and final normal curvatures of non-symmetric section

κ_{b0}', κ_{b1}' = initial and final binormal curvatures of non-symmetric section

τ_0', τ_1' = initial and final tortuosity of non-symmetric section

φ = angle of twist of cross-section

Assuming small wire strain after the loads are applied, the internal moments have the following form (extending the analysis from axial loading mode in section 6.3),

$$G_n = G_b = 0; H = GJ\frac{df}{ds} \tag{6.25}$$

where GJ = torsional rigidity

f = angle between cross-section principal axes to rod centreline principal normal

s = arc length

The set of equilibrium equations now reduces to the form as shown here.

$$-N_b\tau_1 + T\kappa_{b1}\cos\varphi + X = 0 \tag{6.26}$$

$$-T\kappa_{b1}\sin\varphi + N\tau_1 = 0 \tag{6.27}$$

$$-N\kappa_{b1}\cos\varphi + N_b\kappa_{b1}\sin\varphi = 0 \tag{6.28}$$

$$H\kappa_{b1}\cos\varphi - N_b = 0 \tag{6.29}$$

$$-H\kappa_{b1}\sin\varphi + N = 0 \tag{6.30}$$

Where - X = internal line load

N, N_b, T = resultant internal forces

G_n, G_b, H = resultant internal moments

Substituting the values in equation 6.24 into 6.26 – 6.30, inspection showed that equation 6.29 and 6.30 give rise to expression 6.28. Additionally, equation 6.27 expresses the tension in the wire in terms of the shear force in the helical wire in the normal direction. Therefore, to obtain the expression for an interlocked helical spring subjected to internal pressure, expression 6.26 was used. The internal pressure, P_X considering the effect of the contacting surfaces and twisting of cross-section of the wire is then given by

$$P_X = \frac{\kappa_{b1}\cos\varphi - \left(T - GJ\dfrac{df}{ds}\tau_1\right) - 2Q\cos\lambda}{d_w} \tag{6.31}$$

6.3.3 Combination of Axial and Internal Pressure Loading Analysis

From the analysis done above, the response of the interlocked helical structure to combined axial and internal pressure loading can be deduced. Using equations 6.9, 6.18 and 6.21, the response of the helical spring of symmetric section subjected to internal pressure, P_X with fixed axial load step for $F_A \neq 0$ is given by

$$P_X = \frac{F_A + 2\pi R_1 Q \cos\alpha_1 \sin\lambda}{\pi R_1 d_w \cos\alpha_1 \tan\lambda} \tag{6.32}$$

Similarly, for an interlocked helical wire with a symmetric section, the axial load, F_A with fixed internal pressure ($X \neq 0$) is given by

$$F_A = \pi R_1 \cos\alpha_1 \left(P_X d_w \tan\lambda - 2Q\sin\lambda\right) \tag{6.33}$$

Finally, for non symmetric cross-sections, the response of the interlocked helical wire to the combined loading modes can be deduced using equations 6.18 and 6.31. The response is given by the expression below for internal pressure, P_X with fixed axial load ($F_A \neq 0$),

$$P_X = \frac{\kappa_{b1}\cos\varphi\left(\dfrac{F_A}{\pi\cos^3\alpha_1\tan\lambda} - GJ\dfrac{df}{ds}\tau_1\right) + 2Q\cos\lambda}{d_w} \tag{6.34}$$

and rearranging expression 6.34 for an interlocked helical wire subjected to axial with fixed internal pressure ($X \neq 0$),

$$F_A = \left[\frac{\left(P_X d_w - 2Q\cos\lambda\right)}{\kappa_{b1}\cos\varphi} + GJ\frac{df}{ds}\tau_1\right]\pi\cos^3\alpha_1\tan\lambda \tag{6.35}$$

Where possible, the verification of the analytical solutions developed for the interlocked helical wire, in particular the Omega profile was performed using finite element analysis. Additionally, attempts to cut an interlocked Omega profile polystyrene spring were successful and are described in chapter 5. The finite element analysis on an interlocked spring subjected to axial load is described in the next section.

6.4 Verification by Finite Element and Discussion of Results

From the analysis performed in this chapter, it was found that the interlocked helical spring behaves much like a cylindrical tube when it is fully interlocked. This means that the helical coil overall will not change its length and its radius. Hence, the helical angle remains constant. When an axial or internal pressure is applied to the interlocked helical spring, the interlocked helical coil will not fail until the stress at the contacting surfaces of the profile exceeds the yield strength of the material. At this stage, necking of the thinnest part of the wire in the interlocked profile can occur given that the axial and/or internal pressure load now causes the helical wire to deform plastically.

In order to model the localized stresses, it was not appropriate to perform finite element analysis using a beam element model on a helical spring because beam elements are assumed to be slender rods. Additionally, using the beam element model to analyze the global response of an interlocked system would have been complicated by the need to link adjacent coils together. Thus an attempt was made to model the entire 3-dimensional solid helix, but it proved problematic to run and solve the model in ABAQUS. This was thus abandoned in favour of a simpler, but nevertheless valuable model consisting of vertical interlocked sections from a hypothetical Omega helix. The dimensions of the representative Omega profile modelled is shown in figure 6.11. The chosen representative helix radius was 152.4 mm, which corresponded to a typical flexible pipe configuration.

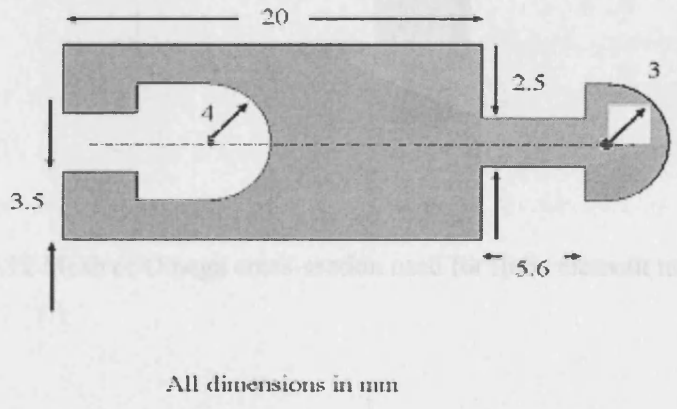

Figure 6.11 Dimensions of Omega cross-section used for finite element modelling

A total of four interlocked sections, each corresponding to a 5 degree turn of the helix, were chosen and the material employed was steel with a Young's modulus of 207 GPa and Poisson's ratio of 0.33. The end section was constrained from movement while a total axial load of 8400N was applied at the other end of the protrusion to cause the structure to yield at the thin width portion of the protrusion. This level was chosen with reference to the analytical solutions presented earlier as sufficient to cause yielding of parts of the Omega profile. The yield strength of the material was taken to be about 250 MPa for low carbon steel as given by Llewellyn (1992). Figure 6.12 shows the mesh of the helical sections modelled, with a higher mesh density chosen for the contacting parts of the central profiles.

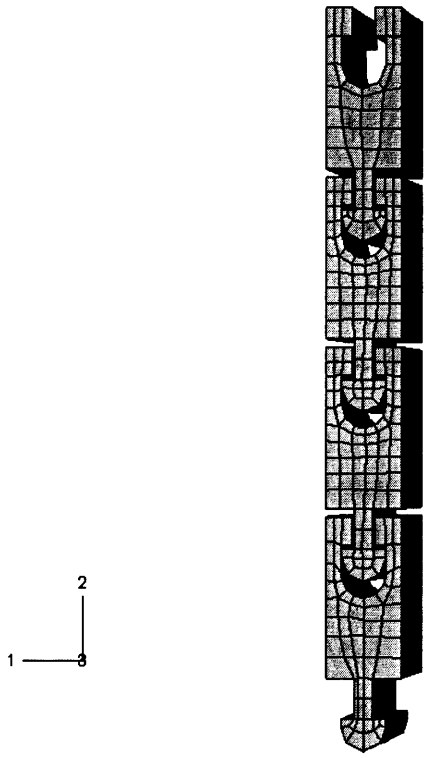

Figure 6.12 Mesh of Omega cross-section used for finite element modelling

It is important to note that each segment is curved in nature and also interlocks its neighbour along a plane inclined to the horizontal (as defined by the helix angle – calculated as 1.3 degrees. Figure 6.13 illustrates this geometry.

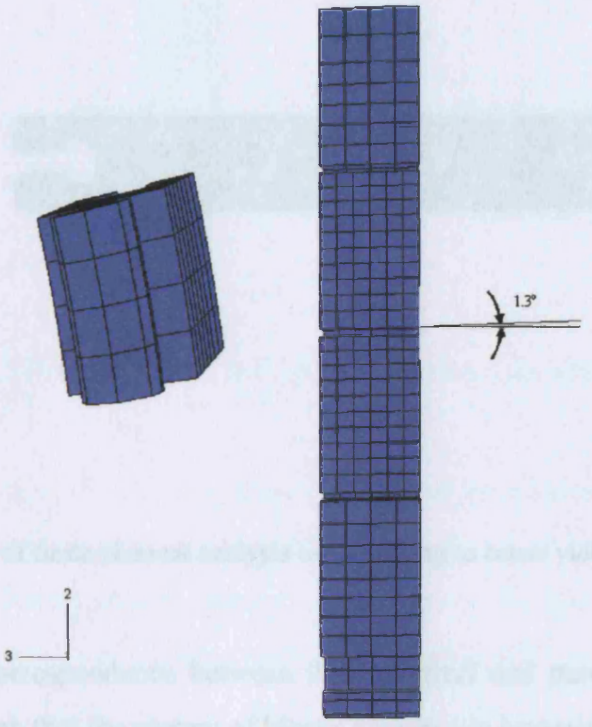

Figure 6.13 Omega profile helical segments

Figure 6.14 shows the result of the finite element analysis. The von Mises stress within the Omega profile was measured as 243 MPa. Von Mises stresses were utilized because these better represent the yield criterion in multiaxial stress systems. The stress calculated corresponded with that predicted using the analytical solution presented earlier, to within 3%. The small difference can be attributed to the fact that the axial load was applied at two node points rather than using a line loading, which cannot be done on solid sections in the finite element package utilized. The use of a higher mesh density could also have improved the accuracy of the result.

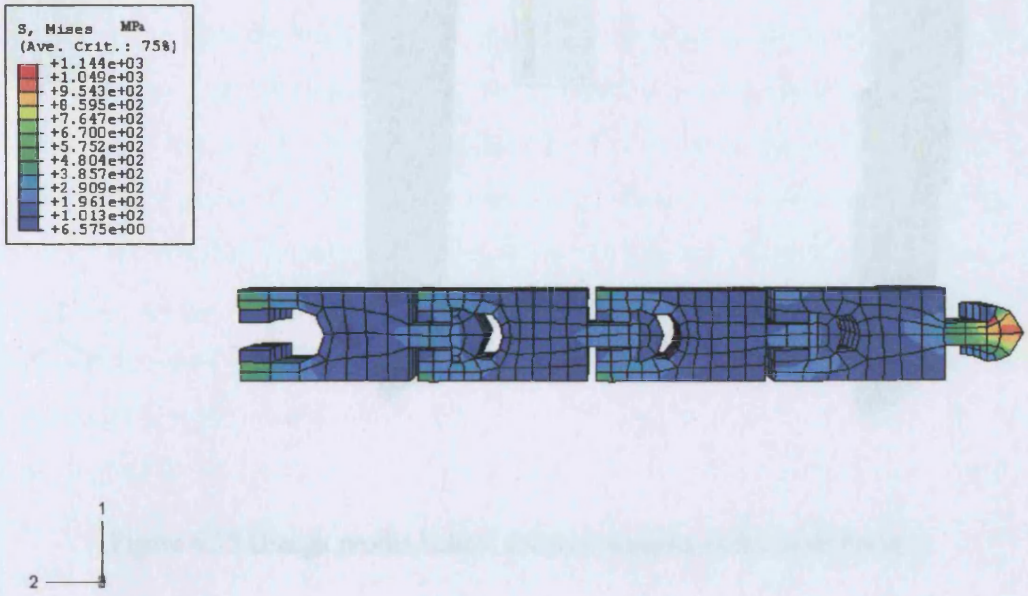

Figure 6.14 Result of finite element analysis axial loading to cause yielding at protrusion

The reasonable correspondence between the analytical and numerical models is not surprising given that the system of blocks chosen can essentially be reduced to a simple 2-dimensional model, given that the helical angle is small and the spring radius is large. However, the finite element model was also valuable in confirming the tendency of the sections to slip relative to one another. This can be seen in figure 6.15. As discussed in section 6.2, such movement, if it occurs would eventually stop as it becomes necessary to bend the coil in order to reduce its radius. However, even small micro-level movements could be sufficient to establish the conditions for fretting fatigue.

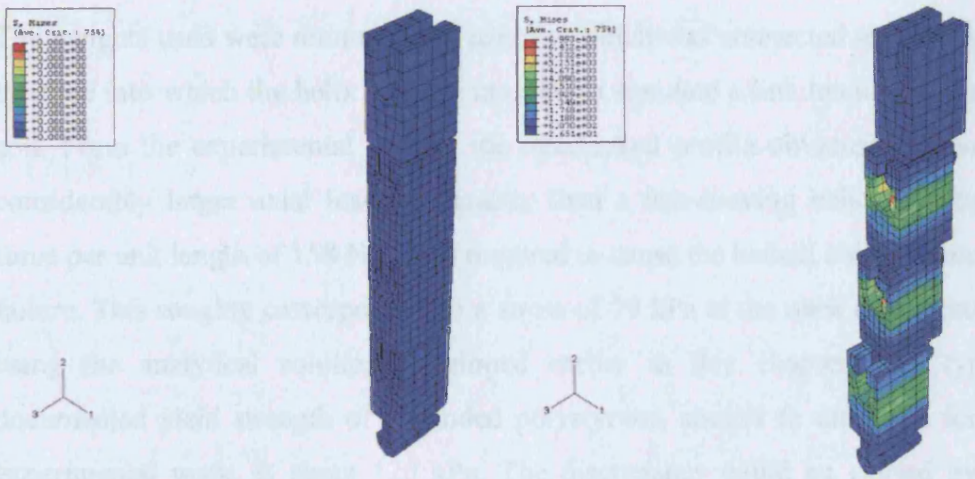

Figure 6.15 Omega profile helical sections slipping under axial loading

As an enhancement of the above analyses, the polystyrene lathe described earlier (chapter 5) was used to cut an Omega profiled helix. This was subjected to tensile testing to destruction in order to observe the behaviour. For this experiment, four Omega profiled continuous coils were cut. The resultant helix was mounted in the apparatus shown in figure 5.12 in the previous chapter, and loaded in tension using a set of weights. Both ends of the polystyrene helix were fixed from rotation. The dimensions in mm of the Omega cross-section that was cut is shown in figure 6.16. The dimensions chosen were a compromise between what could be, in practice, cut and what was necessary to model a hypothetical Omega profile.

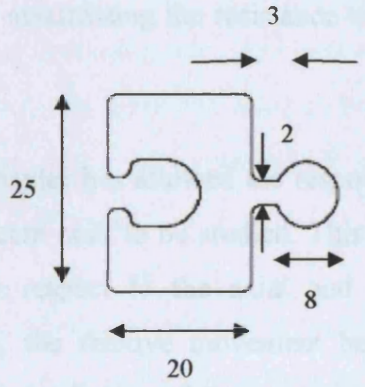

All dimensions in mm

Figure 6.16 Dimensions of Omega cross-section used for tensile testing

The weights used were mounted in a pannier, which was connected to the base of the tube into which the helix was cut in order to simulate a line loading along the coil. From the experimental testing, the interlocked profile obviously showed a considerably larger axial loading capacity than a free-moving helical spring. A force per unit length of 158 N/m was required to cause the helical coil to stretch to failure. This roughly corresponded to a stress of 79 kPa at the neck of the profile, using the analytical solution developed earlier in this chapter. The typical documented yield strength of expanded polystyrene, similar to one used for the experimental work, is about 120 kPa. The discrepancy could be caused by the Omega profile not being cut uniformly along the coil given that it had a small overall protrusion dimension. The 'neck' stress was assumed to be uniform along the helix although this may have not been the case experimentally.

It is also likely that stress concentrations present at the corner of the profile could have initiated failure earlier. Failure of the neck section was not accompanied by much plastic deformation. This is unlikely to be the case for Omega profiles formed from metallic materials, where plasticity would be expected as a prelude to failure. The fact that the failure occurred by fracture and not by the 'pull-out' of the profiles as a result of elastic or plastic deformation of the adjacent profile edges illustrates that interlocking profile designs can be optimized against a particular form of failure. Finite element appears to be the obvious choice for this process, given that the desire is to create a geometry that is both economic in material usage, whilst maximizing the resistance to either pull-out, plastic failure or fracture.

The analysis in this chapter has allowed the response of a helical wire, which is interlocked to its adjacent coil, to be studied. This has enabled the movement of the helical wire with respect to the axial and internal pressure load to be characterized. In turn, the relative movement between contacting surfaces, if present, can give rise to fretting fatigue mechanisms. This aspect is further discussed in the next chapter.

7 Fretting Fatigue and Design Recommendations

7.1 Introduction

As described previously, the pressure armour layer of a flexible pipe consists of a helical wire of a particular cross-sectional profile wound such that there is some overlap between adjacent coils. This overlap and the inherent flexibility of the pipe encourages relative movements between the contacting surfaces of adjacent coils when external loads are applied. As discussed in the literature review in chapter 2, the consideration of the structural integrity of the flexible pipe structure ignored the contact between the helical wire coils for simplicity of analysis (Oliveira et al, 1985; Goto et al, 1987). However, issues of the contacting surfaces become increasingly important when high pressure loads are experienced by the flexible pipe as would be the case if it was used in deep water regions. The internal pressure load, together with the possible relative movement between the coils in the same layer and the between the different layers (if multiple layers are used) of the flexible pipe could combine to cause premature failure of the pipe structure due to fretting fatigue. Fretting damage could thus be a possible failure mechanism operating in deep water flexible pipes, although no data exists in the literature to characterize whether it is a significant factor in determining overall lifetimes. This may not necessarily indicate that fretting fatigue is unimportant, but just that insufficient studies have been performed. Additionally, as deep water structures become more commonplace, such damage may well emerge, given the additional loads placed on the structure. Also, as will be seen below, with complex cross-sectional profiles of the fully interlocked type, rubbing contact will be a definite feature in this behaviour.

The work here considers issues of contact between the coiled wire of the pressure armour layer, with particular reference to the Omega profiled wire. Notably, the latter is fully interlocked into its adjacent coil and the contacting surfaces slide against each other when axial and internal load is applied. From an initial viewpoint, the protrusion of the Omega profile is likely to slide (axially) past the surfaces of the socket of its next turn. Continuous axial loading and unloading of

the pressure armour could thus give rise to fretting fatigue, where crack initiation occurs due to the relative microslip movements between the coils under oscillatory motion. It is assumed that when an Omega profiled coil is finally manufactured, the maximum relative movements between the coils will be restricted by the profile dimension to displacements of a few millimetres, or less. This level of movement is more than sufficient to generate conditions suitable for fretting, given that microslip movement on the contacting surfaces of the order of 25 to 100 micrometres are assumed. Additionally, the potential fretting fatigue process would be exacerbated by the fact that the contact surfaces will experience high normal contact forces in the form of the internal pressure from the fluid being conveyed. In addition to pure axial movement, this work has identified many more modes of relative displacement between adjacent coils, including radial and intercoil sliding mode. All or some of these could lead to fretting damage.

This chapter considers some of these modes of movement identified previously, together with the loading scenarios and attempts to utilize the literature on fretting fatigue to predict possible sites for the generation of cracks. The important parameters in understanding the likelihood of fretting damage include the contact pressure, the contacting sites and the relative level of sliding motion. Factors such as the geometry of the wire's cross-section, the level of axial loading and the internal pressure all impact upon the condition of fretting, and are thus considered in this chapter. Additionally, the issues of fretting fatigue generated in multiple pressure armour layer systems are also discussed here. Multiple pressure armour layers are employed in situations where very high internal pressure loads are experienced. Each helical coil is sheathed in another coil and therefore the possibility for intercoil contact can occur.

After the possible modes of relative movement have been considered, design recommendations are developed to help optimize future Omega profiles to reduce the potential fretting sites. In this way, it is hoped that the basic understanding of the mechanics of helical coils can be employed to better design pressure armour profiles to prolong their lifetime.

The next section presents the description of the underlying conditions for fretting in general, of contacting surfaces, moving on to the surfaces within a pressure system, with particular emphasis on a fully interlocked Omega profile scenario. Potential sites for fretting damage are identified and their implications discussed.

7.2 Fretting Fatigue Mechanisms

There are several parameters that are significant in identifying potential fretting failure in a pressure armour. These are namely, the contact pressures developed, slip amplitudes generated and the contact area present. A basic review of the mechanics of fretting fatigue in consideration of these parameters is presented here based on the works by Johnson (1985), Waterhouse (1992), Hills and Nowell (1994) and Szolwinski and Farris (1996). Where possible, this information on fretting is discussed in the context of a pressure armour. Additionally, brief consideration is made on the likely influence of fretting crack initiation and propagation stages on the overall lifetime of a pressure armour, using data from Nowell and Hills (1990), Szolwinski and Farris (1996), Fellows et al (1997) and Lindley (1997).

7.2.1 Contact Conditions in Pressure Armour

The stress distribution at contact points is highly influenced by the contact shape and the shape of the contacting components. In considering pressure armour of the Omega profile type, the protrusion part of the cross-section is in contact with the flat surfaces of the socket when the coil of the wire is interlocked. This is shown in figure 7.1. When an axial load is applied to the interlocked coil, or as discussed in section 6.3 when an internal pressure is applied to the helix, the protrusion can be displaced by a small amount tangentially (direction parallel to the flat surface of the socket) whilst under a contact pressure. Hence, the Omega profiled wire is akin to a cylinder-on-flat Hertzian contact commonly considered in fretting fatigue literature. Such a contact is usually described as non-conformal and

incomplete, that is having dissimilar contacting bodies and only a small area of the protrusion is assumed to be in contact with the surface of the socket.

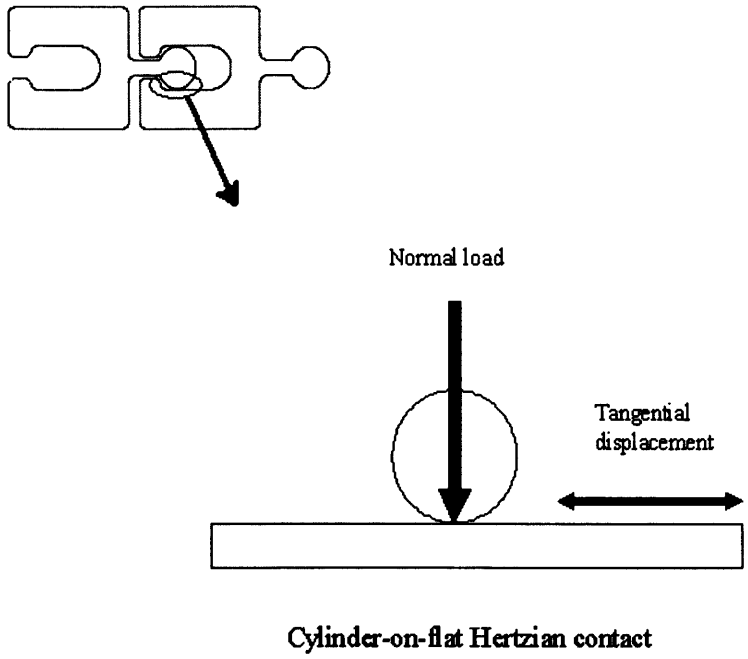

Figure 7.1 Contact geometry of the Omega profiled wire

Johnson (1985) provides a comprehensive review of the mechanics relevant to Hertzian contact and fretting fatigue. Considering the cylinder-on-flat plate above, in order to simplify the analysis of the local deformation of the contacting surfaces, assumptions such as the contact being in the form of an ellipse are made. Furthermore, the highly concentrated stresses on the contact surfaces are treated separately from the general distribution of the stress in the two components, which arise from the loading conditions as well as the body shapes. Therefore the contact area must be small compared to the dimensions of each component and the radius of curvature of their surfaces. The equations that result from these assumptions allow parameters such as the contact pressure (local stress) and contact size to be determined, which in turn can be used with real-world data to predict the susceptibility to fretting.

For the contact of two cylinders pressed together under normal load, P, and subsequently loaded by a tangential shear force, Q_f, the solution of the distribution of normal pressure, p was given by Mindlin (1949). If the radius of one of the

cylinders is assumed to be very large, and therefore approaching infinity, the solution can be used to define the contact of a cylinder on a flat (plane) surface.

The distribution of the Hertzian normal pressure, p(x) is presented in Hills and Nowell (1994) as

$$p(x) = -p_o\sqrt{1-\left(\frac{x}{a}\right)^2} \tag{7.1}$$

where p_0 = peak contact pressure

x = horizontal displacement point of the contact surface

a = contact half-width

The peak contact pressure is defined in Hills and Nowell (1994) as

$$p_o = \frac{2P}{\pi a} \tag{7.2}$$

and the contact half-width, a is given by

$$a = \left(\frac{4P}{\pi E' k}\right)^{\frac{1}{2}} \tag{7.3}$$

where E' is the equivalent Young's modulus and k is the relative curvature which is given respectively by

$$\frac{1}{E'} = \frac{1-\nu_1^2}{E_1} + \frac{1-\nu_2^2}{E_2} \tag{7.4}$$

$$k = \frac{1}{R_{c1}} + \frac{1}{R_{c2}} \tag{7.5}$$

where υ = Poisson's ratio

Here, E refers to Young's modulus and R_c is the contact radius the subscripts 1 and 2 refer to the two different contacting components respectively.

To understand how the pressure and contact area affect the fretting behaviour, it is necessary to determine the distribution of the stresses generated and the relationship between this and the relative movement of the contacting surfaces. Friction obviously plays an important part in altering the fretting behaviour. Following Amonton's law of sliding friction quoted in Hills and Nowell (1994),

$$|q| = \mu p(x) \tag{7.6}$$

where μ is the coefficient of friction and q is the 'shear traction' on the surface. The parameter q helps to define to the mode of movement at the sliding surfaces.

When subjected to a sliding load, surfaces can 'stick' or 'slip' apart. In most cases, a combination of stick and slip occurs across the contact zone. This mixed scenario is illustrated in figure 7.2 from which it can be seen that the shear traction differs depending on whether the stick or slip zones are considered. From Szolwinski and Farris (1996), the shear traction equates to

$$q(x) = q'(x) + q''(x) \tag{7.7}$$

where

$$q'(x) = \mu p_o \sqrt{1 - \left(\frac{x}{a}\right)^2} \qquad c_{sz} < |x| \le a \tag{7.8}$$

$$q''(x) = \mu p_o \frac{c_{sz}}{a} \sqrt{1 - \left(\frac{x}{c_{sz}}\right)^2} \qquad |x| \le a \tag{7.9}$$

The parameters 'c_{sz}' and 'a' define the extent of the zones within the overall contact area, where c_{sz} is the stick zone half-width.

The relationship of c_{sz}/a is defined by

$$\frac{c_{sz}}{a} = \left(1 - \frac{Q_f}{\mu P}\right) \tag{7.10}$$

Equation 7.9 presented in Szolwinski and Farris (1996) missed out the c_{sz}/a term and this is thought to be a typographical error. The surface traction distribution due to the applied normal load and the coordinate system used is illustrated in the diagram shown in figure 7.2 as provided by Szolwinski and Farris (1998).

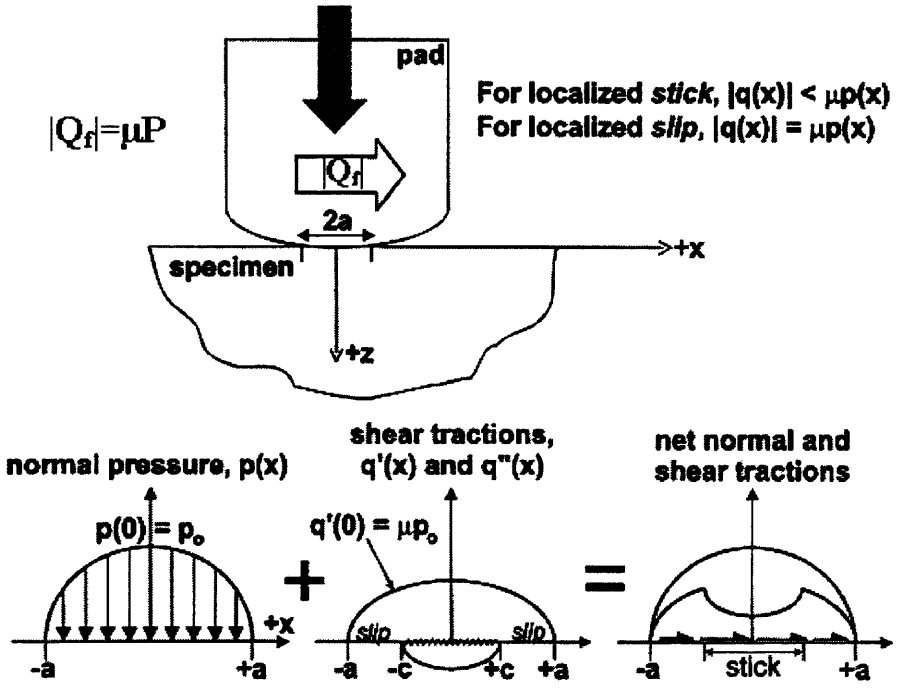

Figure 7.2 Fretting contact shear traction distribution and the coordinate system for normal pressure analysis (Szolwinski and Farris, 1998)

Here, the x and y axes taken are purely for fretting fatigue analysis and must not be confused with the axes used for global helical spring deformation analysis in the previous chapters. Additionally, the normal and shear forces are denoted by the capital letters 'P' and 'Q_f' here for the fretting analysis. ('P' has been used in previous chapters to denote applied internal pressure.)

Additionally, the components may be subjected to a bulk stress which displaces the contacting surfaces from their current position. This essentially happens when the components are subjected to some loading other than the normal contact load or the tangential force. Hence, there is a shift in the shear traction and the boundaries of the various zones, and this is then given by Hills and Nowell (1994) as

$$q''(x) = \mu p_o \frac{c_{sz}}{a}\sqrt{1-\left(\frac{x-e}{c_{sz}}\right)^2} \qquad |x-e| \le c_{sz} \tag{7.11}$$

where e = offset of centre of stick zone from centre of contact

Expression 7.11 reduces to the form of expression 7.9 when the bulk stress is not present. It must be noted, however, that the solution is only valid if the bulk stress is small compared to the tangential force, or else the edge of the stick zone will approach the edge of the overall contact area. Hills and Nowell (1994) give this range of bulk stress, σ_b as

$$\sigma_b \le 4\mu p_o\left(1-\sqrt{1-\frac{Q_f}{\mu P}}\right) \tag{7.12}$$

If the applied bulk stress is large, then reverse slip takes place, where the stick zone shifts towards the leading edge of the contact.

The fretting fatigue life is influenced by the slip amplitude parameter (a measure of the relative displacement of the contacting surfaces) as reported by Waterhouse (1992). As pointed out by Vingsbo and Soderberg (1988), the contact condition in fretting fatigue changes with the change in the slip amplitude. It was in their work that a series of fretting maps was proposed, based on the regimes that the contacting surfaces were in. These regimes can be classified into four categories and are summarized here.

Firstly, the stick regime, where the wear and oxidation of the material is small as no slip of the contacting points is observed. No crack formation is observed in this regime. The second regime, known as the mixed stick-slip regime, is where slip occurs at the surfaces of the contact. Wear and oxidation are small although in this region the fretting fatigue life can be severely be reduced because of extensive crack formation and growth. This is the most important state in fretting fatigue life analysis. In the gross slip region, slip occurs over the entire contact area and fretting wear is observed. Here severe surface damage is encountered although crack formation in this regime is limited. Lastly, in the reciprocating sliding regime, the wear rate becomes identical to the conditions of unidirectional sliding and is termed 'sliding wear'.

Vingsbo and Soderberg (1988) measured the tangential loading, Q_f parameter to the relative surface displacement, d_f for a complete fretting cycle to determine the different regimes of fretting contact. This is illustrated in figure 7.3. The changes in the dynamic tangential force, Q_f were compared to the fretting scars obtained from experiments of fretting on engineering alloys and hence the fretting regimes identified.

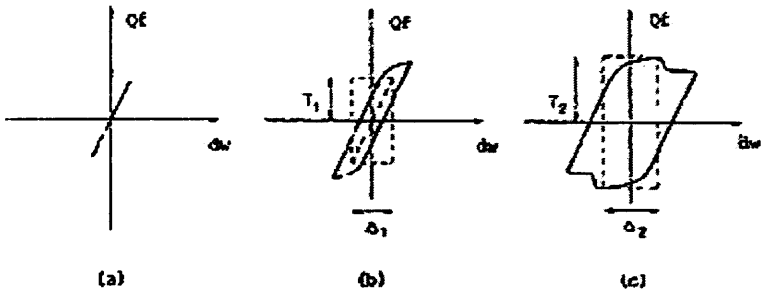

Characteristic examples of tangential force ,Qf versus displacement, d recordings for different contact conditions. Δ1 is the transition amplitude corresponding to incipient partial slip and T1, the corresponding tangential force. Δ2 is the transition amplitude corresponding to incipient gross slip and T2, the corresponding tangential force.
(a) stick zone (b) mixed stick-slip zone (c) gross slip

Figure 7.3 Tangential force, Q_f versus the relative contact displacement for different fretting contact regimes (adapted from Vingsbo and Soderberg, 1988)

They then produced fretting maps which correlated the various parameters that affect the fretting fatigue life of the contacting points. For example, the relationship between the wear and fretting fatigue life as a function of the slip amplitude is shown in figure 7.4 as re-presented by Lindley (1997). The fretting fatigue life decreases with increasing slip amplitude up to a certain threshold value and increases again as the slip amplitude increases. The wear is seen to increase rapidly under the gross slip regime. It can be seen, however, that the components should operate in the gross slip regime if the fatigue life is to be increased. This may be attributed to the fact that solid debris formed from the wear process can inhibit crack propagation. The wear rate then accelerates in the full sliding regime. It was pointed out by Hills and Nowell (1994) that the wear process can abrade the initial embryo cracks before they have a chance to grow.

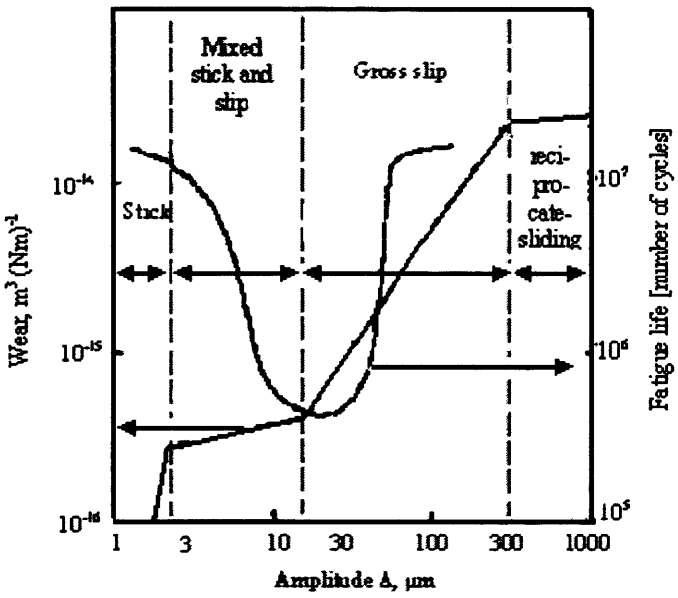

Figure 7.4 Example of Vingsbo and Soderberg (1988) fretting map for relationship between wear and fatigue life as function of slip amplitude (Lindley, 1997)

Furthermore, experiments on the fretting fatigue of structural steels were performed by Gao et al (1991) and the relationship of fretting fatigue life as a function of slip amplitude under different pressure loads was established. A similar trend to one from the Vingsbo and Soderberg fretting maps was obtained.

The types of steel studied were of the 2Cr13 composition, which has a low carbon content, and 35CrMo structural steel, which has medium carbon content. Results of fretting life as function of slip amplitude under normal pressure of 24.5 MPa and 49 MPa from experiments done by Gao et al (1991) for the different steels are shown in figure 7.5.

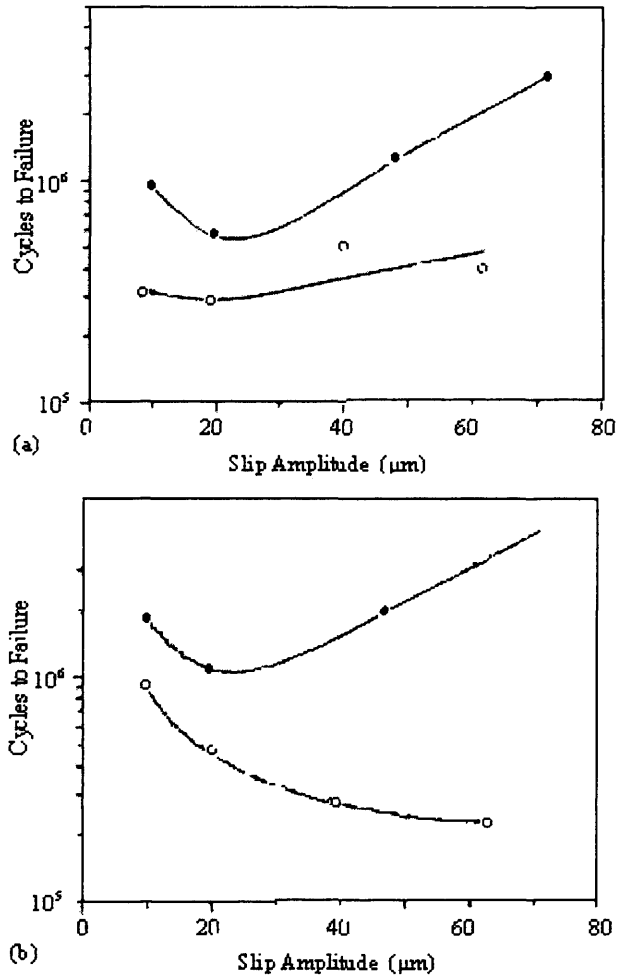

Diagrams (a) 2Cr13 specimen and (b) 35CrMo(AC) specimen
for contact pressures 24.5 MPa ●
49 MPa ○

Figure 7.5 Results of fretting life as function of slip amplitude for different steels and normal pressure (adapted from Gao et al, 1991)

Investigations into the effect of the slip amplitude and the normal load to fretting susceptibility of high strength steel were further studied by Nakazawa et al (1994).

The results of the fretting life as function of slip amplitude to the different normal loads from Nakazawa's work is shown in figure 7.6 for steel with 0.18% carbon content. These figures are applicable to the present work given that the pressure armour layer is likely to be manufactured from structural steel of low to medium carbon content depending on requirements of the oil field.

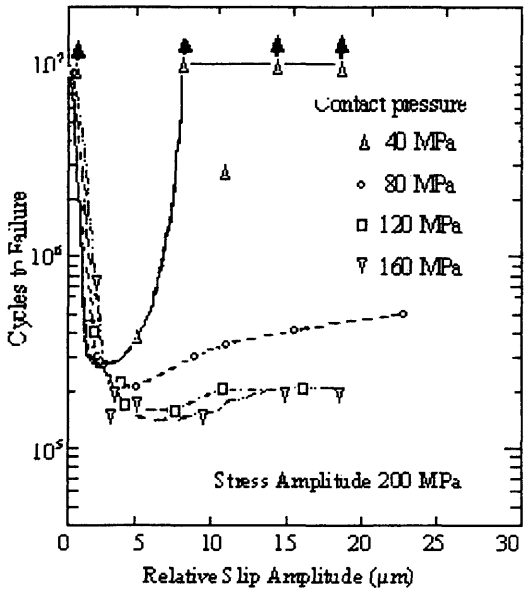

Figure 7.6 Results of fretting life as function of slip amplitude for various normal pressures (Nakazawa et al, 1994)

7.2.2 Crack Initiation and Propagation

The analytical solutions described earlier enable the sites of fretting in pressure armour to be identified and quantified for various parameters given the basic assumption that Hertzian contact occurs. The remaining work in this chapter focuses on the prediction of sites where fretting fatigue is likely to occur. Once fretting damage occurs, however, crack-like defects are created and these can propagate under the applied global loads by 'plain' fatigue mechanisms. It is therefore insufficient to simply determine the points of initiation, if no consideration is given to the subsequent crack propagation given that the lifetime of a structure such as pressure armour, is as important as the knowledge of where fretting will develop.

Fatigue fracture consists of a crack initiation and a propagation stage. In fretting fatigue, where two components in contact are subjected to bulk stress and normal loads, the fretting fatigue crack can be initiated in the early stages of the stress cycle and then propagated under plain fatigue mechanisms. It is obvious that fretting fatigue plays an important role in the initiation of the crack while plain fatigue is more important in the propagation stage. Hills and Nowell (1994) described the crack initiation process in fretting fatigue as a continuous process rather than a discrete process. This meant that the crack initiation phase took place over a period of time and involved accumulation of damage when loads were applied. Cracks were observed after a number of cycles but it was not possible to quantify when the damage from the applied loading due to fretting fatigue became a crack. As pointed out by Waterhouse (1992), the fretting fatigue crack initiation process is a complex interaction between physical factors such as the slip amplitude, normal pressures, mechanical factors such as morphology and the environmental factors which include temperature and presence of corrosive agents.

However, many researchers (Hills and Nowell, 1994; Szolwinski and Farris, 1996) have used the crack initiation damage parameter, $\sigma_T \tau_{ss} d_f$, where σ_T is the maximum tangential stress, which is the stress parallel to the contacting surfaces, τ_{ss} is the maximum traction during one cycle and d_f is the relative slip between the surfaces. This damage parameter was formulated by Ruiz et al in 1984 and presented in the works of Hills and Nowell (1994), Szolwinski and Farris (1996) and Lindley (1997). A crack was predicted to initiate at the point where the maximum value of the crack initiation damage parameter reaches a critical value as pointed out by Lindley (1997).

In fretting fatigue, the initiation phase of fatigue is quite short as mentioned by Hills and Nowell (1994) and most of a component's life is consumed by the propagation phase. The initiation phase occurs at a microscopic scale, while the propagation phase of crack life can be quantified using a fracture mechanics approach as used in plain fatigue once the crack size has grown to a few material grain sizes. The life of a crack can be divided to a number of stages. Hills and Nowell (1994) explained that the crack growth takes place by shear deformation in the localized slip band near the crack tip. This is the early stage of crack growth

when the threshold stress intensity factor is reached. Once the crack has grown to within a few diameters of the grain size, it moves into a region of fast growth rate, where the crack now grows due to the principal applied load being normal to the crack plane. Lastly, once the crack reaches the high stress intensity factor range region, the crack growth accelerates to fracture. The stress intensity factor, K_C is a measure of the fracture toughness of the material. Stress intensity factor has the general form as shown below.

$$K_C = Y_K \sigma_b \sqrt{\pi a_{crack}} \tag{7.13}$$

where Y_K = geometric factor of component

σ_b = bulk stress

a_{crack} = crack half-length

According to Hills and Nowell (1994), the stress intensity factor range is more useful in quantifying cyclic loading conditions and is given by

$$\Delta K_C = K_{C\max} - K_{C\min} \tag{7.14}$$

where K_{Cmax} = maximum value of stress intensity factor during loading cycle

K_{Cmin} = minimum value of stress intensity factor during loading cycle

The relationship between the crack growth rate, da_{crack}/dN and the stress intensity factor range, ΔK_C can be described by the well-known Paris law for metallic materials, whereby

$$\frac{da_{crack}}{dN} = C\left(\Delta K_C\right)^m \tag{7.15}$$

where C and m are constant that depends on the material and environment.

Crack propagation rate can be plotted against the stress ratio, S_R. This is defined in Hills and Nowell (1994) as

$$S_R = \frac{K_{C\min}}{K_{C\max}} \tag{7.16}$$

When fretting conditions are superimposed upon plain fatigue scenarios, the response of the component differs from that under pure plain fatigue conditions. Experiments to determine the extent of such effects in steel were performed by Endo and Goto (1976) and also by Sato and Fujii (1986). The effects of the stress ratios to fatigue life as a function of the crack growth length were established by Sato and Fujii (1986) and are shown in figure 7.7. It can be seen that for a given crack length, the crack was initiated earlier in the fretting specimens. However, when the data in figure 7.7 was used to work out the crack propagation rate, it was found that the crack propagation in fretting specimens was lower compared to the plain (normal) fatigue specimens. It was concluded by Sato and Fujii (1986) that the crack growth in fretting fatigue can be retarded because of crack closure experienced by the components unlike in plain fatigue, where the crack propagation rate increased monotonically with crack growth.

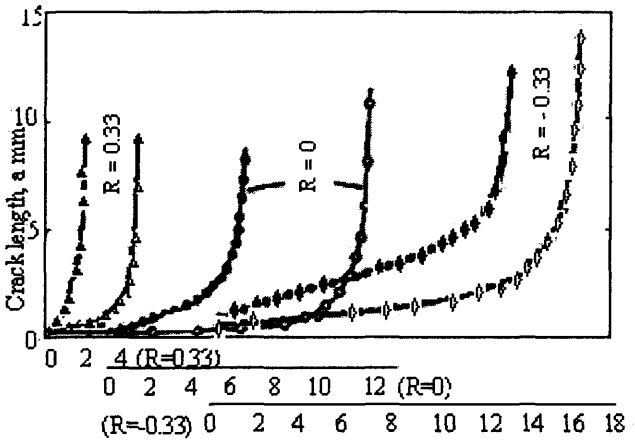

N-a relation for p = 80 MPa and R = 0.33, 0 and -0.33 of SUS304L steel (σ_a = 120 MPa)

▲ , ● , ◆ fretting fatigue Δ , ○ , ◇ normal fatigue

Figure 7.7 Results of fretting life as function of crack depth for various stress ratios (Sato and Fujii, 1986)

It should be noted that when in service, pressure armour is more likely to be subjected to a combination of both plain fatigue and fretting conditions, hence an understanding of how rubbing contact alters the plain fatigue behaviour is of significant importance.

7.2.3 Contact Condition in Multi-layered Armour

Returning to the original argument, the solution described earlier applies for the Hertzian contact condition, where the protrusion of the Omega profiled wire is contacting the surface of the socket in the adjacent turn. For the analysis of multiple layers of helical wire reinforcement, the assumption of a cylinder-on-flat surface is not applicable as the dimensions of the components are not small compared to the contact area. Hence, a new analytical solution for the stress at the contacting points is required. This was described in the work of Saevik and Berge (1995) for two layers of helical wire reinforcement in contact when loads were applied.

Saevik and Berge (1995) assumed that the contact area was circular, with radius of curvature taken as the contact line curvature of the contacting components. This is illustrated in figure 7.8. The fretting damage was observed from their experimental work to be on either side on the inner helical wire. Saevik and Berge (1995) explained that the curvature of the outer helical wire was larger than the curvature of the inner helical wire along their common contact line and thus the contact would be at some point on either side of the helical wire centreline.

The maximum contact stress, σ_c and the contact radius, R_c is given in Saevik and Berge (1995) by

$$\sigma_c = \frac{E}{2}\left(2p_o \frac{d_w^{\,2}}{h} \frac{\cos^2\alpha \cos 2\alpha}{\pi RE} \right)^{\frac{1}{2}} \tag{7.17}$$

$$R_c = \left(\frac{2R}{\cos^2\alpha}\right)^{\frac{1}{2}} \left(2p_o d_w{}^2 h \frac{\cos^2\alpha \cos 2\alpha}{\pi RE}\right)^{\frac{1}{4}} \tag{7.18}$$

where E = Young's modulus

R = radius of helical spring

α = helix angle

p_o = peak contact pressure

d_w = width of helical wire

h = thickness of helical layer

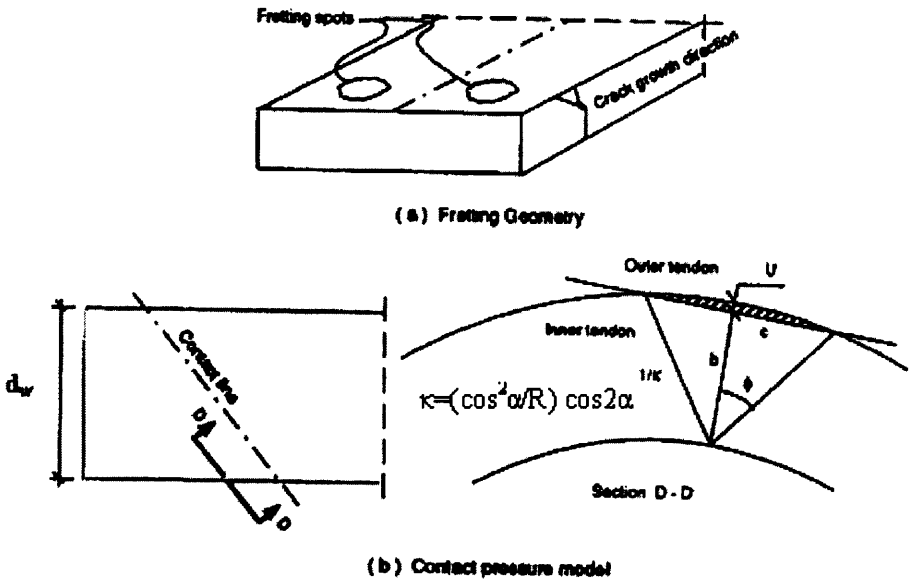

Figure 7.8 Fretting fatigue contact model for helical reinforcement layers (Saevik and Berge, 1995)

The literature on fretting is extremely comprehensive, but for the purposes of this study, it has been important only to define to conditions under which fretting can occur in the materials of interest. The following section presents several 'contact scenarios' that have been identified within an Omega profile type pressure armour layer, on the basis of the previously described work on mechanics of helices, which are strong candidates for sites of fretting damage. These sites are predicted based on the conditions of contact that are present in the mating surfaces of the pressure armour both before and after application of an applied axial and/or pressure load. Design recommendations are made to mitigate the potential effects

of fretting where possible, through optimization of the profile and/or other considerations based on the fretting review presented in section 7.2.

7.3 Potential Sites of Fretting and Design Recommendations

There are various configurations that the contacting surfaces of the pressure armour are in, at any given time. Initially, the geometry of the profile will determine the contact points, but when the helical wire is subjected to axial load and internal pressure, movements will occur and new contacts established. Some of these movements are due to the cross-sectional behaviour of the Omega profile while others involve the global movement of the helical structure. Here, the various configurations of the pressure armour are described and the potential sites of fretting due to the contacting surfaces are discussed. The deterrence of fretting fatigue is also discussed based on the optimization of the cross-section and/or the use of palliatives where such design changes could not be achieved.

Configuration 1 – Single Pressure Armour Layer under Various Loading Modes

It was shown from the previous analyses in chapters 3 and 4 on helical springs, that the coils move closer together under internal pressure and stretches further apart when under axial tension load. When the helical wire is interlocked into its adjacent coil, the movement of the helical spring is restricted as the coils are in contact and locked after some axial deflection of the pipe.

Considering a single layer of pressure armour, where the Omega profiled wire is wound into its adjacent coil, there is the possibility of contact between the protrusion and the surface of the socket, and relative sliding when it is subjected to axial and internal pressure loading. As a flexible pipe is constructed from various structural layers, the pressure armour is prevented from larger expansion due to the internal pressure and cylindrical wall of the subsequent layer. Hence, the Omega profiled wire is akin to a cylinder-on-flat contact configuration under normal load as shown in figure 7.9. It is assumed that the stress field on the

contact radii of both sides of the protrusion is independent of each other as the dimension of the protrusion is large compared to the contact radii. Additionally, axial loads can cause slip of the contacting surfaces and the fretting effect is very much governed by the coefficient of friction of the contacting components, and hence the relative displacement between the two contacting surfaces.

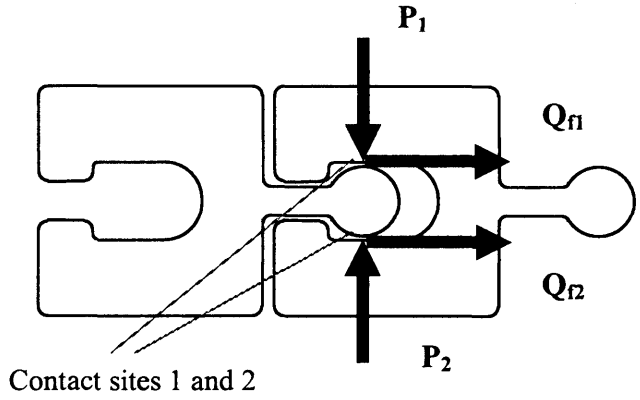

Figure 7.9 Protrusion – socket contact of the Omega profiled wire

There is a variation in the stress field on both points of contact of the Omega profile. Potentially, the effect of fretting at the contact surfaces at the bottom of the protrusion due to normal load P_2 is larger than the top portion of the protrusion because of the inherent internal pressure load acting at the bottom of the profile to push the cross-section in the upward direction.

- Behaviour under Axial Load

An interesting insight would be to observe whether contraction in the helical coil contributes to the potential fretting on contact site 1 in figure 7.9, which is the top side of the protrusion, due to axial loading. It was recalled in section 3.5 that as an axial load is applied to a helical structure, the radius of the helix reduces if the load is tensile and rises if it is compressive. To model this, the helical coil is fixed at one end while an axial load is applied at the other end. A radius contraction of the helical coils is expected when an axial tensile load, F_A is applied. This can be approximated akin to a deflection in a cantilever beam and is shown in figure 7.10.

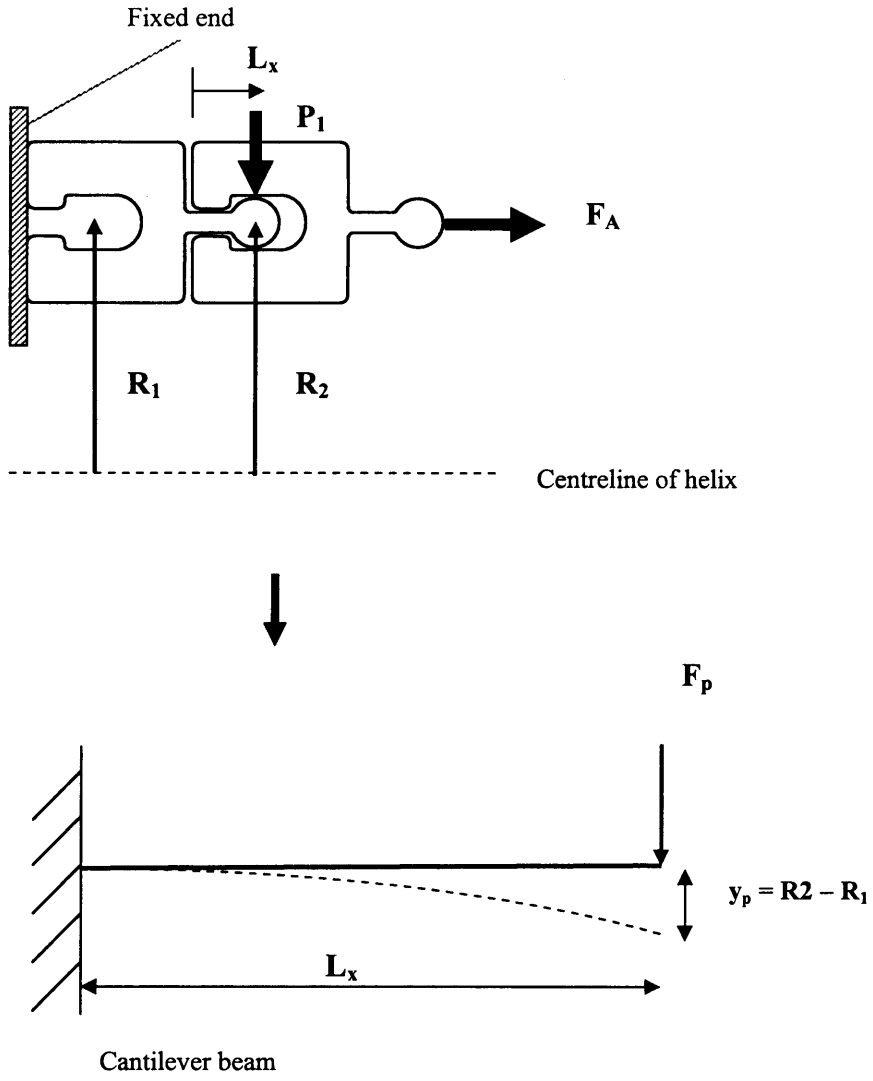

Figure 7.10 Pressure armour axial loading and cantilever beam analogy

Assuming that the contact point is at the end of the cantilever beam, the radius contraction, $R_1 - R_2$ is equivalent to the deflection of the cantilever beam experienced when a load is applied, shown in the figure as F_p. Hence, the contact load, F_p can be measured once the deflection is known. From the beam deflection equation for cantilever beam obtained in Timoshenko (1955), rearranging the equation to give the contact load, F_p in terms of the beam deflection, we obtain: -

$$F_p = \frac{3EIy_p}{L_x^3} \tag{7.19}$$

where y_p = deflection of cantilever beam

L_x = length of beam

In order to quantify this possible mode of contact, a parametric study was performed using equation 7.19 to observe the effects of changing the deflection of the beam (by changing the geometry of the helical spring) and the displacement length of the beam to the contact load. The dimension of the Omega profiled wire used was similar to that shown in figure 6.11 in the previous chapter. Table 7.1 shows some selected results of deflection of the helical spring for typical 76.2 – 152.4 mm (3 and 6 inches) radius flexible pipe and pitch length of 21 mm. The slip amplitude of the contact surfaces of the Omega profiled wire was also varied from 5 – 10 mm. This is the amount of 'slack' in the design of the profile, and provides the freedom of movement which is required to generate flexibility in the pipe. This is one of the variables that has to be optimized when a fully interlocked profile such as the Omega system is designed. Young's modulus of 207 GPa of a typical steel was chosen with section I = 8.33 x 10^{-10} m^4.

helix radius (mm)	76.2		76.2		152.4	
max. allowable slip amplitude (mm)	5		10		10	
helix extension(mm)	y_p (mm)	F_p (N)	y_p (mm)	F_p (N)	y_p (mm)	F_p (N)
2	0.014628	0.00151	0.014628	0.00076	0.007313	0.00038
4	0.030589	0.00316	0.030589	0.00158	0.015292	0.00079
6	0.047883	0.00495	0.047883	0.00248	0.023936	0.00124
8	0.066513	0.00688	0.066513	0.00344	0.033245	0.00172
10	0.086478	0.00895	0.086478	0.00447	0.043221	0.00224

Table 7.1 Comparison of contact load, helix radius and slip amplitude

From this simple analysis, it can easily be seen that as the helix is allowed to extend in length, the contact load rises as a consequence of a decrease in the helix radius. Also, the contact load appears to be larger for smaller diameter flexible pipes as the radius contraction due to axial loading is larger. An unexpected result is that as the slip amplitude increases, the contact load can be seen to reduce. This is because the maximum slip amplitude is obviously related to the length of the Omega protrusion. As this rises, the load generated by its deformation drops for a given value of deflection. It should be noted that the slip amplitude coincided with the reciprocating sliding regime of the Vingsbo and Soderberg (1988) fretting map as depicted in figure 7.4, where wear rate accelerates, and fretting is less of a problem.

Figure 7.11 shows the calculated contact load, F_p for applied helix deflection of a 6 inch radius helical spring with maximum slip amplitude of 10 mm. It can be seen that the contact load increases progressively with the helical spring deflection, up to a point where the Omega profile is fully locked, and then the contact load increases rapidly. It can be seen however, that an Omega profiled pressure armour subjected to axial loading will not generate a sufficiently large contact load to cause fretting at contact site 1 shown in figure 7.9. The high stresses, if incurred at this point are probably due to the internal pressure loading 'squeezing' the profile together.

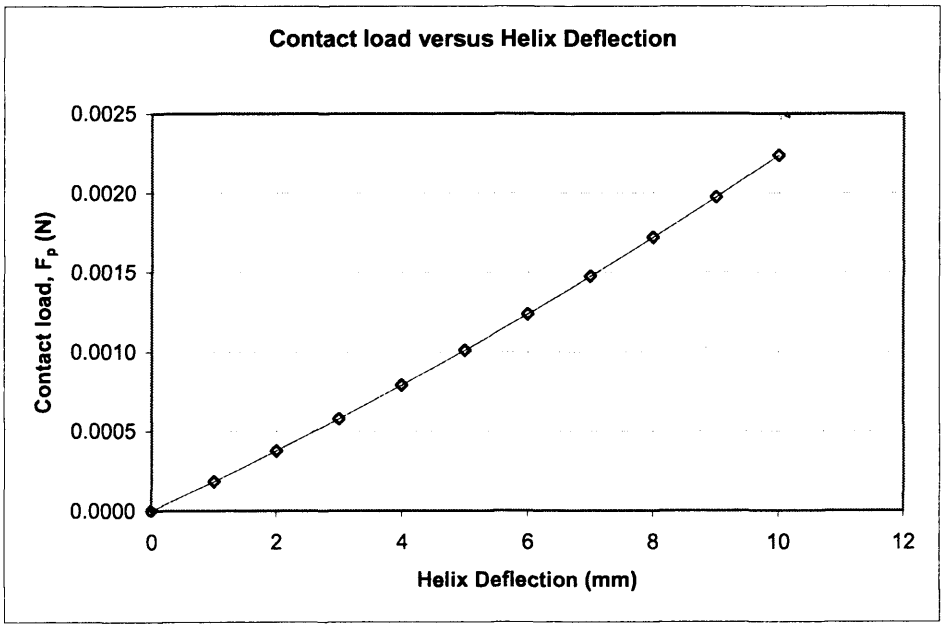

Figure 7.11 Contact load versus helix deflection for 6 inch helical spring

To minimize the effect of fretting, the contact width of the protrusion should be increased so that the total contact area is increased when subjected to internal pressure. This is observed through equation 7.1, where increasing contact width of the contacting surface reduces the peak contact pressure experienced, hence reducing the overall stress distribution at the contact areas. The potential for fretting crack formation depends on the slip amplitude regime that the contact is in, and other factors such as bulk stress as discussed in section 7.2. The use of lubricants is also encouraged to reduce the coefficient of friction and lower the effect of wear, although this might have an effect on the fretting behaviour.

- Behaviour under Internal Pressure

To understand the movement under internal pressure loads, the finite element approach was used as a tool to observe the stresses at the contact surfaces of the pressure armour profile and to perform the optimization of the cross-sectional shape to reduce the high stresses experienced at the contact points and hence susceptibility to fretting. Axisymmetric modelling of the pressure armour profile was performed to observe the variation in contact stresses to applied internal pressure loading. Although the axisymmetric models do not replicate the full helical spring, it is extremely useful in observing the stress distribution at the contacting points of the surfaces.

The omega profiled wire with dimensions as given in figure 6.11 in the previous chapter was used as a starting point to perform the stress analysis under internal pressure loading. A 20 MPa internal pressure was applied to the 152.4 mm (6 inch) pressure armour constructed from steel with Young's modulus of 207 GPa. Figure 7.12 shows the result of the stress distribution across cross-section for a few coils using a coarse mesh and the end pieces fixed from axial and radial movement.

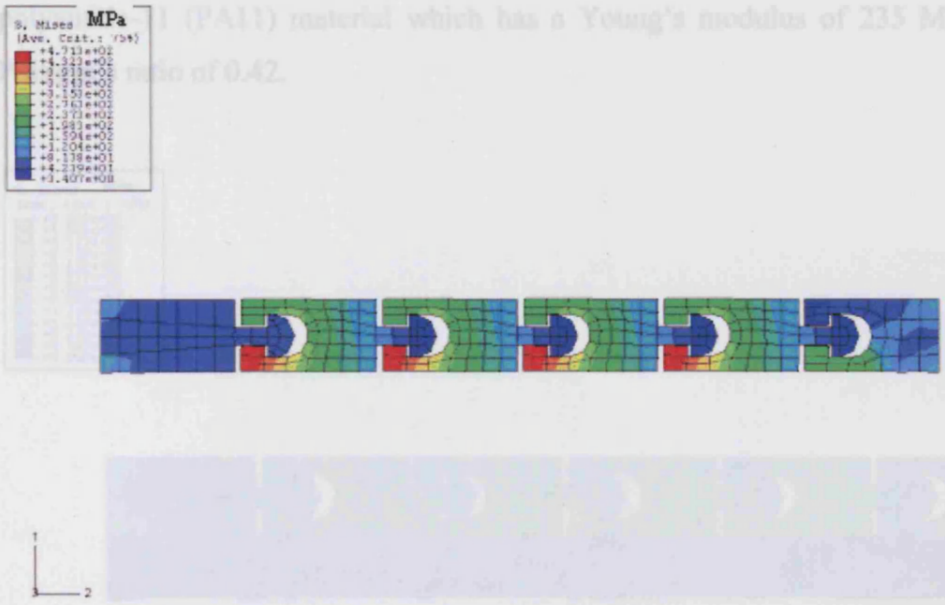

Figure 7.12 Axisymmetric model of Omega profile under 20 MPa internal pressure

The stress distribution of the coils towards the middle section is more uniform as the end profiles of the pressure armour are constrained from movement, and thus suffer from boundary condition effect. Hence, to obtain the true stress distribution, the middle section is considered. An internal pressure load could alter the contact points and loading in several ways. Firstly, if contacts are already established during manufacture, an applied pressure would raise the contact load especially if an external constraint exists. Also, if rotation of the cross-section of the helical wire occurs (see section 4.3), then new contacts can be established and loads altered. From the analysis, it can be observed that the base of the pressure armour experiences bending due to the high applied loads. This in turn causes the high stresses seen at the base and not at the contact sites as predicted from discussions above. The undesirable effect of bending the overall structural behaviour of the pressure armour can be removed when a polymer layer is added into the axisymmetric model. This is appropriate given that in the actual flexible pipe structure, the polymer fluid containment layer is beneath the pressure armour and the internal pressure exerted by the fluid conveyed is transferred directly to the pressure armour layer. An example of the axisymmetric layer which includes the polymer layer is shown in figure 7.13. The polymer layer is modelled using

polyamide-11 (PA11) material which has a Young's modulus of 235 MPa and Poisson's ratio of 0.42.

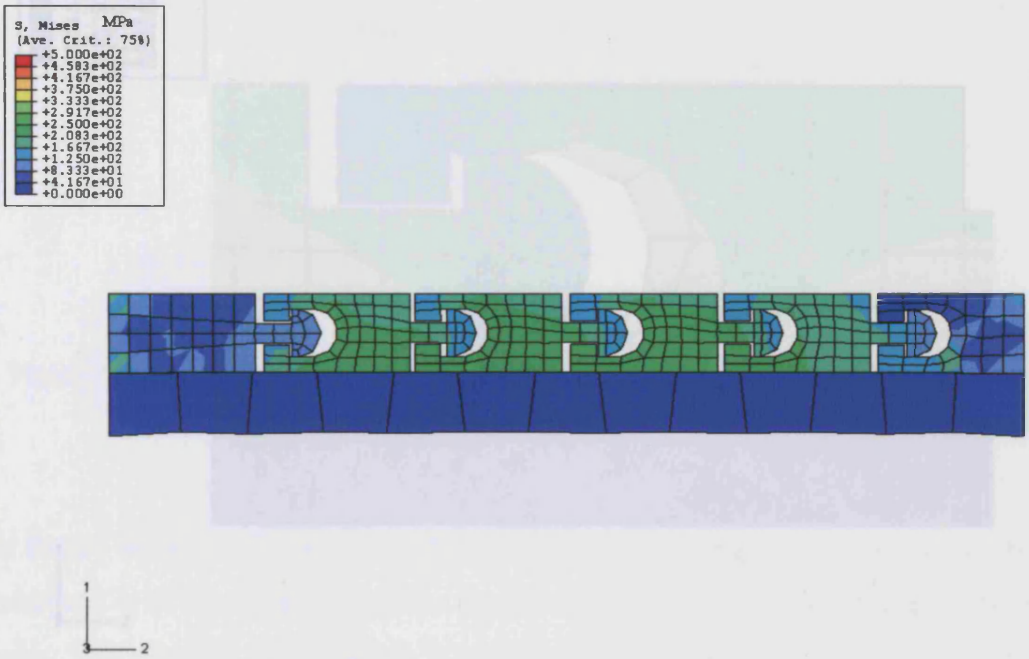

Figure 7.13 Axisymmetric model of Omega profile and polymer under 20 MPa internal pressure

It can be observed that the stress distribution is more uniform than previously, without the effects of bending being induced at the base of the Omega profile. The average stress across the profile is approximately 250 MPa. Closer inspection of the contact surfaces using higher mesh densities reveal that the contact stresses are high between the base and the protrusion, and is shown in figure 7.14. This was expected given that the internal pressure load acts to push out the base of the profile. It was found that the higher stress occurred at the base side of the contact, with the highest stress distribution measured at about 264 MPa.

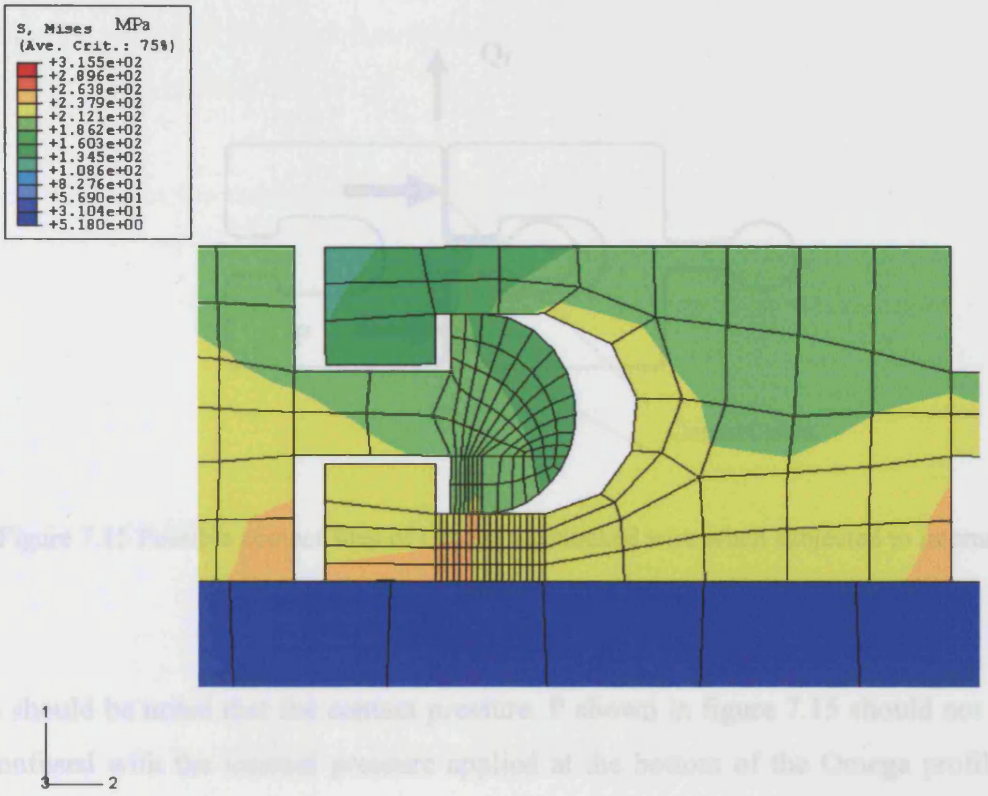

Figure 7.14 Close-up of contact between protrusion and socket of Omega profile under 20 MPa internal pressure

Additionally, when the internal pressure is large, such that it is enough to cause the coils to move so close to each other that it is now locked and prevented from more compressive movements, some surfaces of the Omega profiled wire are now in contact and can lead to fretting failure when microslip movements are present. The contact sites are depicted in figure 7.15. This movement is a direct consequence of the reduction in helix length as an internal pressure is applied, and was first analyzed in section 3.5.

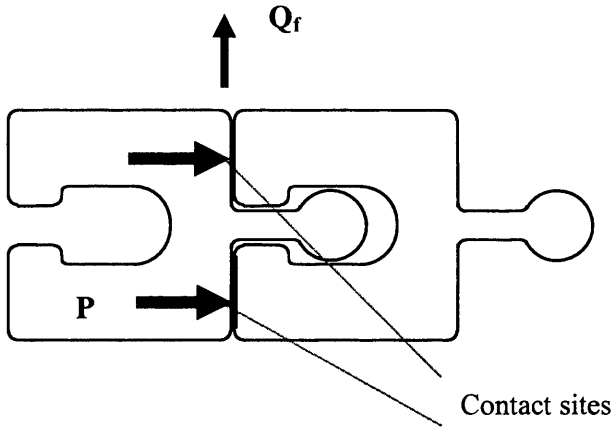

Figure 7.15 Possible contact sites of Omega interlocked wire when subjected to internal pressure

It should be noted that the contact pressure, P shown in figure 7.15 should not be confused with the internal pressure applied at the bottom of the Omega profiled wire. This potential contact site is in addition to the contact between the protrusion and the socket surface as depicted in figure 7.9 due to internal pressure pushing the contact surfaces together. From equation 7.1, it can be seen that high internal pressure causes the stress at the contact points to be large. As the internal pressure is the external parameter that defines the design of the flexible pipe pressure armour, the use of higher strength steels should be encouraged in place of low carbon steels. This is confirmed from various analyses such as the one shown in figure 7.5 as presented by Gao et al (1991), which confirms an increase in the service life of the component, for a given pressure, if a higher strength steel is used.

If palliatives are considered in order to mitigate either wear or fretting damage, it should be noted that it is difficult for liquid lubricants to be applied to the contacting surfaces due to their proximity. However, the use of molybdenum disulphide coatings or polymeric films (for example, polystyrene) on the contacting surfaces can be considered (as described in Zhou and Vincent (1999)) as part of the manufacturing process. The latter researchers reported, however, that there were concerns that these types of protective coatings were only valid in

the early stages of fretting because of the low bonding strength between the film and the metal surface.

Another palliative method considered here is to put a polymeric layer between each turn of the coil. In essence, another helical coil made of polymeric material in inserted between each turn of the Omega profiled wire as shown in figure 7.16. The coefficient of friction of polymer to steel is relatively very low compared to the coefficient of friction of steel to steel surface. One possible problem with this method might be the issue of polymeric extrusion due to the high temperatures and pressures experienced in service conditions.

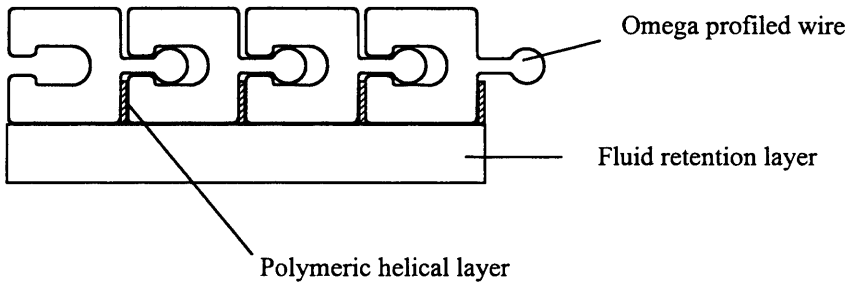

Figure 7.16 Polymeric protective layer between each turn of Omega profiled wire

As described earlier, an appropriately design Omega profiled wire when subjected to axial load can extend initially as a free helix, by the protrusions sliding along the surfaces of the socket. This process continues until each protrusion is locked and in contact with the wall of the socket. In this instance, there are additional contacting sites that can cause fretting damage. This is shown in figure 7.17, with the original fretting sites included.

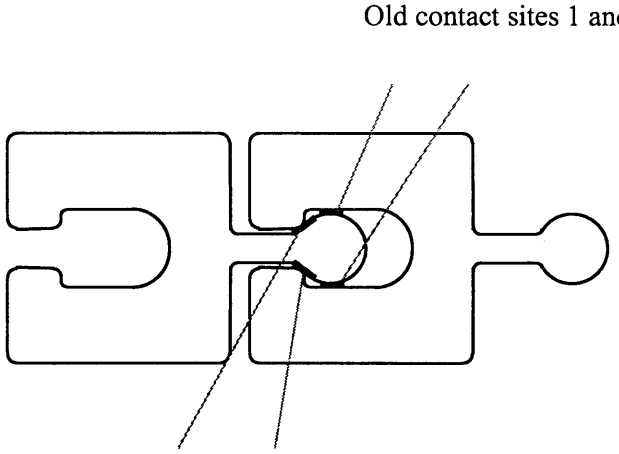

Figure 7.17 Contacting sites of fully locked Omega profiled wire under axial load

From here, it can be observed that the fretting damage is a competition between the contact surfaces of the protrusion at the wall and the flat surface of the socket. When optimizing the design of the cross-section, considerations should take into account whether contact at wall or surface is desired in terms of the applied load and also the dimensions of the protrusion and socket.

Configuration 2 – Rotation of Cross-section due to Non-symmetric Sections

One of the conclusions of the work presented here, is that when internal pressure is applied to a helical wire, rotation of the cross-section is possible if the profile is non-symmetric (refer to chapter 4 for further details on the analysis of rotation the cross-section under internal pressure). The Omega profiled wire used in a pressure armour is indeed non-symmetric in nature. When internal pressure is applied to the profile, the cross-section might therefore be expected to rotate about the wire section (although the profile may not rotate much due to proximity to being a rectangular section). The direction of rotation depends on the direction of the moment generated from the non-symmetric section. Figure 7.18 shows the rotation of the section under internal pressure. The protrusion is still in contact with the surface of the socket and could potentially lead to fretting failure due to

the high pressure experienced at the contact points as described in previous cases. Additionally, there is geometric contact at the surfaces of the profile when the coils are rotated.

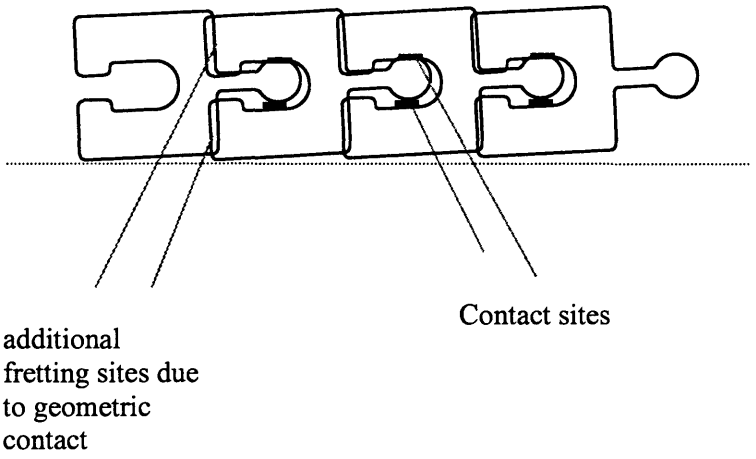

Figure 7.18 Contacting surfaces of rotated Omega wire cross-section under internal pressure

The sliding contact generated between the protrusion and the socket under applied pressure is similar to the other configurations mentioned above and therefore lubricants could be used to alter the fretting damage behaviour. For the geometric contact problem, however, the design of the Omega profile could be altered to avoid mating at the surfaces shown. Figure 7.19 shows a possible design of the profile to avoid such geometric contact. However, such a design would need to be further optimized to take into consideration other factors such as the effect of creep of the polymer sheath underneath the pressure armour layer.

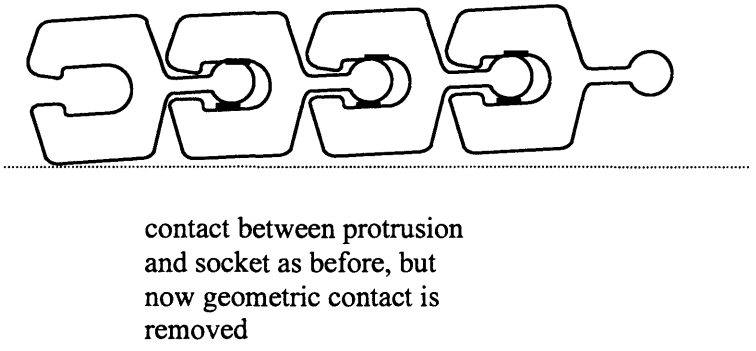

Figure 7.19 Example of changes to the design of Omega profiled wire

In addition to developing contact stress, the rotation of the cross-section under an applied pressure load could influence the stress distribution at the existing contact sites in the pressure armour profile. This would be more apparent in sections that have a greater propensity to rotate. For example, in the Z profiled wire, there is a tendency for the cross-section to twist as described in chapter 4, and this would increase the sliding and contact load between the contacting points. An example of the stress distribution of such a profile generated from axisymmetric modelling is shown in figure 7.20. The Z profiled wire chosen had a base length of about 15 mm with thickness of 10 mm and was assumed to be constructed from steel with a Young's modulus of 207 GPa and Poisson's ratio of 0.33.

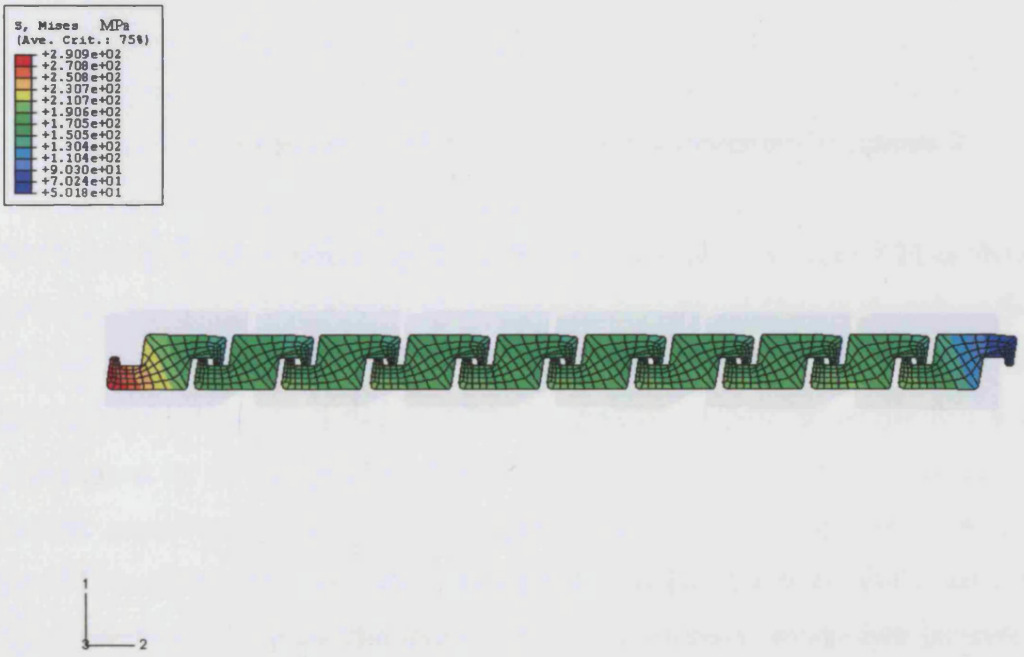

Figure 7.20 Axisymmetric model of Z profiled wire under 20 MPa internal pressure

The model indicates that the stress distribution in not uniform although the contact stresses due to the clockwise rotation of the Z profiles are quite small. It could be argued that since all the profiles rotate, the contact load may not necessarily increase although this would not be the case near the constrained ends. Additionally, it should be noted that the numerical values in this analysis should not be directly compared with the Omega profiled wire analysis since they have different cross-sectional areas.

The contact stresses are lower if the section becomes more symmetric, because the angle of twist of the cross-section becomes smaller. This is best illustrated through various axisymmetric models generated from the finite element analysis for the optimization of an Omega profiled wire. Figure 7.13 depicted earlier shows the original Omega profile wire under a 20 MPa internal pressure load. If the cross-sectional profile is shaped in such a way to encourage rotation, a higher stress gradient is expected together with higher contact stresses at contacting points. Figures 7.21 and 7.22 show some of these exaggerated 'less symmetric' Omega profiles to encourage rotation.

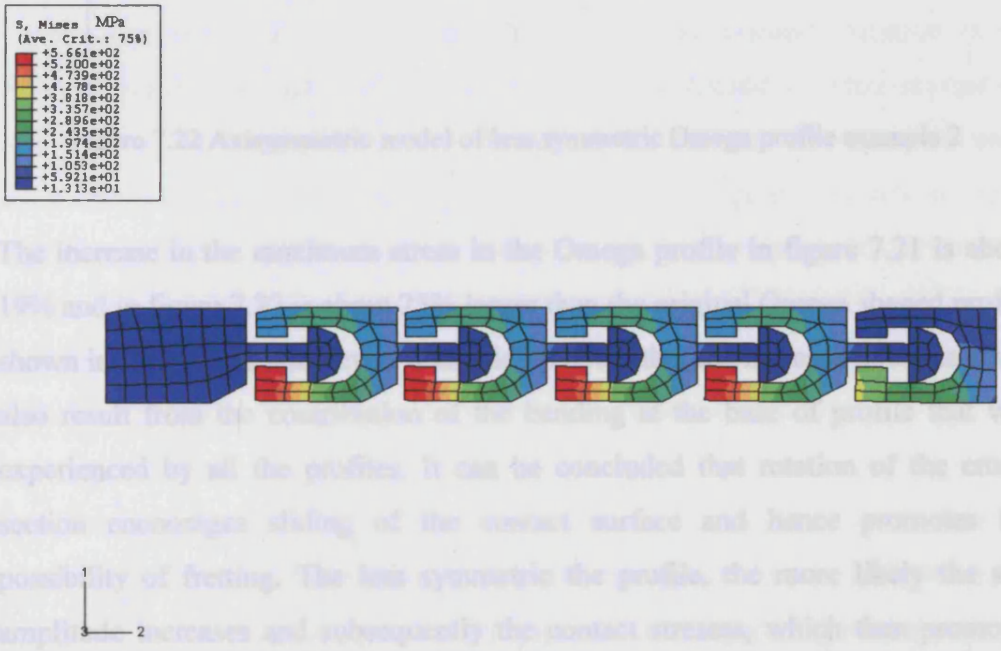

Figure 7.21 Axisymmetric model of less symmetric Omega profile example 1

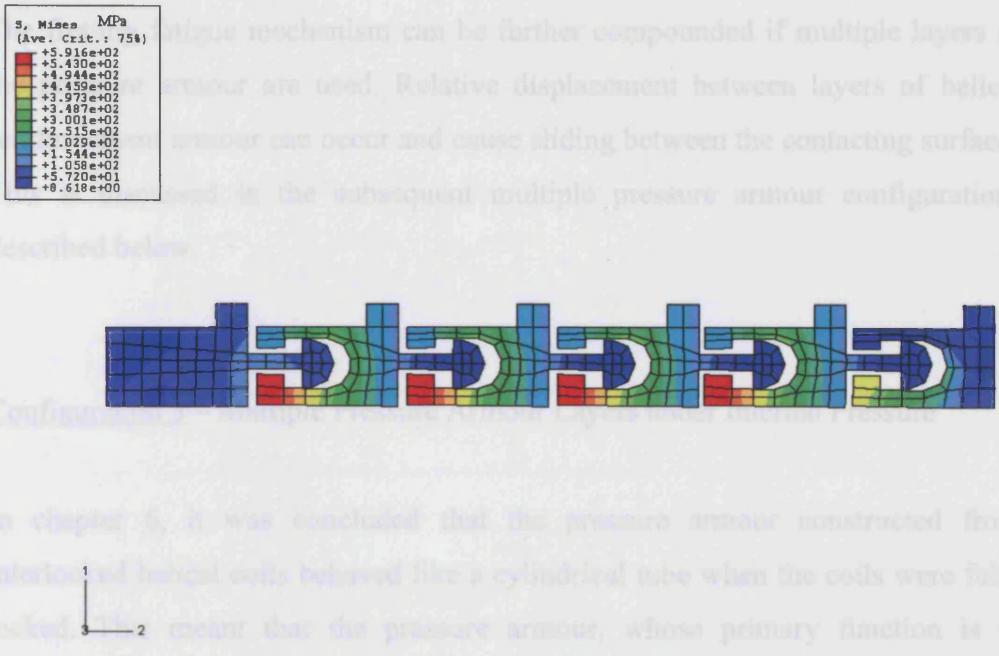

Figure 7.22 Axisymmetric model of less symmetric Omega profile example 2

The increase in the maximum stress in the Omega profile in figure 7.21 is about 19% and in figure 7.22 is about 25% larger than the original Omega shaped profile shown in figure 7.12. However, it should be noted that the increase in stress could also result from the contribution of the bending at the base of profile that was experienced by all the profiles. It can be concluded that rotation of the cross-section encourages sliding of the contact surface and hence promotes the possibility of fretting. The less symmetric the profile, the more likely the slip amplitude increases and subsequently the contact stresses, which then promotes fretting.

By reducing the slip amplitude of the contacting surfaces, the life of the structure is increased. This is evident from the work of Gao et al (1991), where contact pressures of 24.5 MPa on a low carbon steel gave rise to a material life of 10^6 cycles for a 10 μm slip amplitude. This compares to a decrease in the life if the slip amplitude was increased to 20 – 30 μm. Experimental data from the likes of Gao et al (1991) and Nakazawa et al (1994) served as a useful tool to analyze fretting life of the contacting components once the contact stresses were determined using the finite element analysis performed here.

The fretting fatigue mechanism can be further compounded if multiple layers of the pressure armour are used. Relative displacement between layers of helical reinforcement armour can occur and cause sliding between the contacting surfaces. This is discussed in the subsequent multiple pressure armour configurations described below.

Configuration 3 – Multiple Pressure Armour Layers under Internal Pressure

In chapter 6, it was concluded that the pressure armour constructed from interlocked helical coils behaved like a cylindrical tube when the coils were fully locked. This meant that the pressure armour, whose primary function is to withstand internal pressure loading, can be made to withstand a certain amount of axial loading. For example, it was deduced that the pressure armour of six inch radius with a thin protrusion height of 2.5 millimetres can be subjected to an axial load of magnitude of few hundred kilonewtons. This compares to the tensile armour layer of the same pipe which can withstand axial loads of few thousand kilonewtons. Hence, a pressure armour layer, if designed appropriately can be made to carry 10% – 30% of the load of the conventional tensile armour.

Therefore it is possible to construct multiple layers of helical wire reinforcement to withstand internal pressure loads and some axial loads. Figure 7.23 shows an example of the configuration of a flexible pipe with two layers of pressure armour. The American Petroleum Institute (API) document 17B (1998) quotes that a back-up pressure armour can be put in place and be used to withstand additional pressure seen in service environments. This type of configuration generally has a few advantages for the loading capacity of the flexible pipe structure. Firstly, the most obvious is that the amount of internal pressure that it can withstand is increased significantly and hence the ability to operate in higher pressure environments. Additionally, if multiple pressure armour layers are used, the size of the tensile armour wire cross-section can be reduced significantly as each pressure armour layer is able to withstand about 10 - 30% of the total load experienced by the flexible pipe, thereby reducing the weight of the structure. On the other hand, the total weight of the pressure armour layers is increased and

hence the design needs to be optimized, based on the requirements of the in-service conditions.

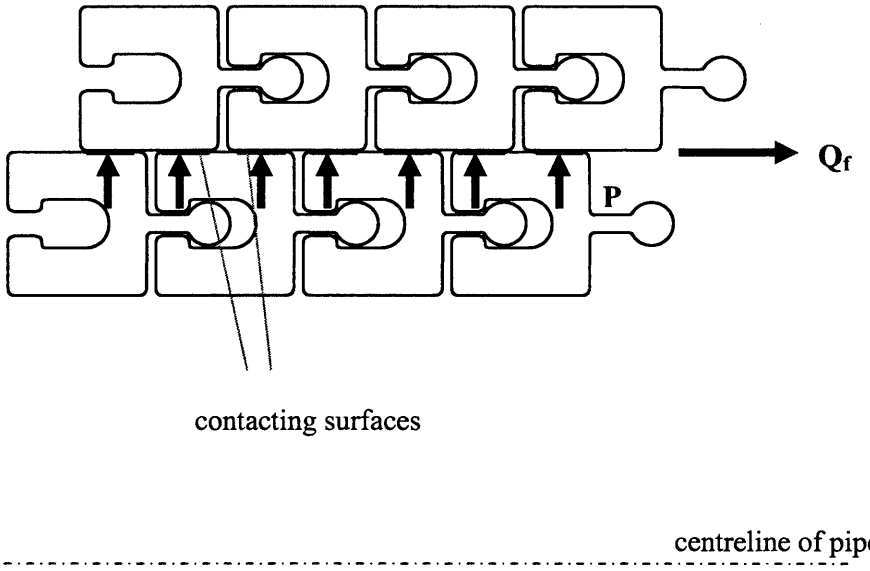

Figure 7.23 Configuration of pressure armour layers under internal pressure

The use of multiple pressure armour layers poses issues of contact of surfaces between the helical wires. High pressures experienced by the armour can cause the Omega profiled wire pressure armour layer to expand in radius and shorten in length. Potentially, these small deflections can cause the pressure armour layers to experience small amount of slip (mixed stick – slip and gross slip regime) against each other on the contacting surfaces together with the applied normal load as shown in figure 7.23. This could result in fretting fatigue due to the high contact pressures experienced by these layers.

Additionally, when the Omega profiled wire is locked-up between the protrusion and the socket, a bulk stress is present in the Omega profiled wire and therefore the pressure armour layer. It is possible for fretting cracks to initiate at the contacting surfaces shown and propagate inwards to the centre of the cross-section.

Palliative effects using lubricant were mentioned earlier as a possible solution to this contact problem. However, Burke and Witz (1999) concluded that lubricants

do not appear to affect the contact stresses in a statically loaded system. In fatigue experiments carried out by Saevik and Berge (1995) on flexible pipes with multiple tensile armour layers, the same conclusion was reached, whereby the lubricants did not appear to alleviate the contact problem between the armour layers.

An anti-friction tape layer is therefore highly encouraged to be placed in between the two pressure armour layers to prevent the inner surface of one layer to contact the outer surface of the other as shown in figure 7.24. It is not appropriate to place an additional polymer sheath in between the layers of pressure armour subjected to high contact pressures, unlike in the case of tensile armour layers. Although this polymer sheath could act as an anti-friction layer, its inherent material properties mean that it will creep through the gaps of the Omega profiled wire under the effects of high pressure and also the high temperature, seen in service conditions.

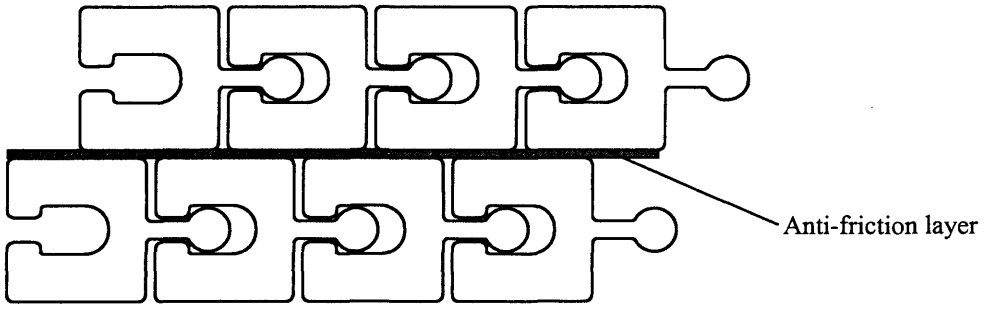

Figure 7.24 Anti-friction tape between the pressure armour layers

Configuration 4 – Multiple Pressure Armour Layers under Axial Load

In this configuration, the arrangement of the pressure armour layers used in the previous section is used, but an axial tension load is applied to the pressure armour. This is akin to axial load being applied to stretch two concentric helical springs wrapped around a core. As concluded from the analysis performed in section 3.5, when a helical coil is stretched axially, the radius of the helical structure contracts. When two helical springs of differing radius are stretched

together, there is the possibility that the coils of the outer spring will contact the coils of the inner spring. This is further illustrated using the graph shown in figure 7.25, which shows the response of two springs subjected to axial loading.

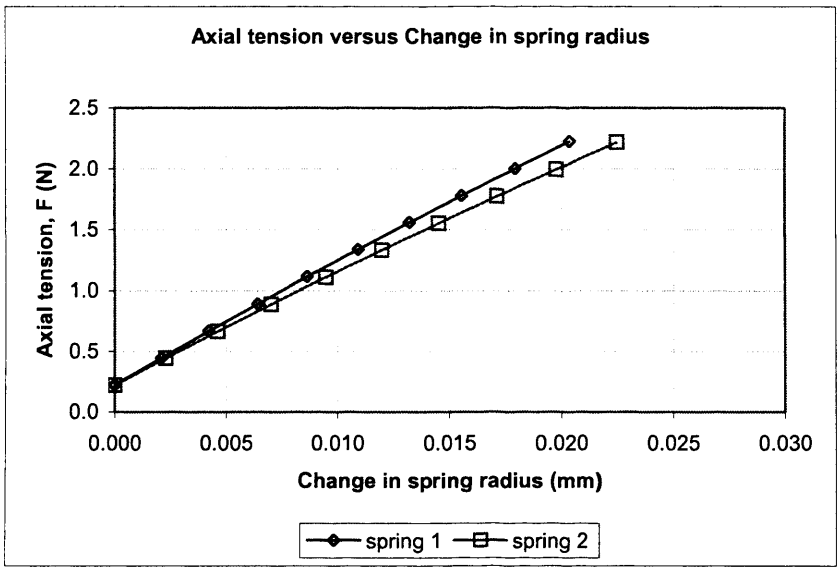

Figure 7.25 Axial tension – change in spring radius for two springs concentric to core

From the analysis, hypothetical helical springs of the same steel material were used. The inner spring (denoted by spring 1) has a spring diameter of 152.4 mm (6 inches). The height of the cross-sectional area was 6 mm and therefore the outer spring (denoted by spring 2) was constructed in such a way that it was positioned above the inner spring. When the same amount of axial load was applied to the two springs, it was observed that the contraction in radius of the outer helical spring was greater than the contraction in radius of the inner spring. This meant that the coils of the outer helical spring would come into contact with the surface of the inner helical spring. With increasing axial load, the contact force between the two layers must therefore increase. Thus, the pressure armour layers under axial load could be subjected to fretting damage.

This effect is exacerbated by the fact that the pressure armour is predominantly used to resist the internal pressure during the loading cycle. The sites of likely fretting damage are shown in figure 7.26. Sliding wear between the helical coils is

inevitable given that the pressure armour layers induce the condition for fretting when subjected to axial load.

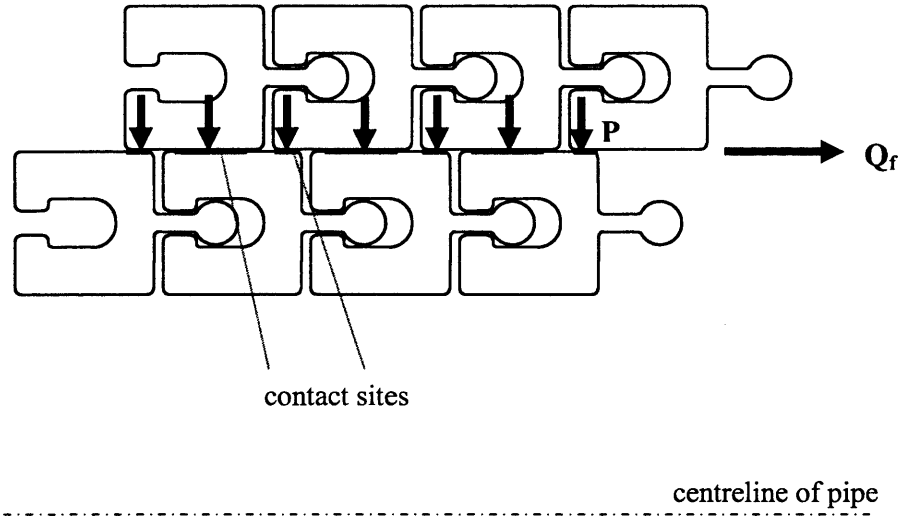

Figure 7.26 Configuration of pressure armour layers under axial load

In a similar manner to the case of pressure armour layers subjected to internal pressure, the fretting contact sites can be eliminated using an anti-friction tape layer placed in between the two contacting surfaces as shown in figure 7.24. As described by Saevik and Berge (1995), the contact geometry between two helical armour layers is not similar to that of Hertzian contact because the dimension of the contact is large compared to the overall structure of the pressure armour. Hence, to evaluate the maximum contact stress experienced for a given internal pressure load and helical spring geometry, the equations 7.17 and 7.18 in section 7.2 can be used.

Configuration 5 – Effect of Fixed Ends due to Pipe End Terminations

As discussed in chapter 6, when helical wires are fixed from movement at the end of a pipe using end terminations, discontinuity in the response of the helical coils to applied loads is obtained for coils near the terminations. The relative movement of the coils would be fairly symmetric from coil to coil in the middle portion of a

long pipe, but additional relative sliding of coils occurs for helical coils near the end because of the constraint placed on the movement. Because of this discontinuity, enhanced contact is likely to develop and hence fretting or sliding wear of the pipe will be encouraged. Indeed this aspect of fretting near the end terminations has been discussed in Ramsey (1991) and has also been observed experimentally by Saevik and Berge (1995). When designing the flexible pipe structure, the end termination portion should be taken into consideration as it may result in fretting fatigue failure even though other design aspects of the cross-section of the pressure armour might have been optimized. Additional palliative methods should be considered near the ends besides the use of lubricants.

The configurations shown describe the potential fretting contact sites for in-plane movements. This is partly due to the fact that the axial load and internal pressure only cause such movements, as described in the earlier chapters. When the flexible pipe structure is fixed from movement because of the end terminations, sliding of coils is not permitted. It should be noted that movements such as relative sliding of the helical coils are more likely to occur during twisting of the flexible pipe as well as bending loads. In addition to the fretting fatigue under in-plane movements, due to the effect of internal pressure and axial load, the structure will undergo out-of-plane movements when twisting and bending are considered. Consequently, the fretting problem is made even more complicated.

The design of the pressure armour to minimize the effect of fretting is therefore an interplay between optimising the contact pressure requirements, width of the Omega wire strip, number of layers of helical wire reinforcement, lubrication and design of cross-sections of the interlocked helical wire profile.

A fully interlocked wire such as the Omega profiled system has been shown (chapter 6) to withstand some axial loading in addition to its primary function of resisting internal pressure load. Therefore, this type of interlocking has an advantage compared to a partially interlocked wire (for example, Z profile), where the application of axial load could cause the unlocking of the profile (hence requiring extra axial load bearing components). From the analysis in this chapter, both the fully and partially interlocked wire could be subjected to fretting damage

given the pressure loading and the predicted contact between adjacent coils. However, since a fully interlocked profile is made to withstand some axial loading, it is equally possible that a cyclical tensile load could cause plain fatigue to occur in addition, or as an alternative, to fretting fatigue.

Cracks can initiate under fretting condition and grow to a length of few grain sizes before propagating to failure under plain fatigue condition if cyclical tangential stresses due to an axial load exist. Such loading could occur, for example due to internal pressure variations or movement of the flexible pipe either by sea currents or more likely wave/vessel motion. Stress concentrations in combination with the higher stresses generated in the thinnest section of the profile would create ideal conditions for plain fatigue initiation and propagation. The net result could be a significant reduction in the lifetime of the pressure armour layer although the helical wire is subjected to stresses below the yield strength. For a fully interlocked profile, therefore consideration has to be given to the fact that both fretting fatigue and plain fatigue interaction can be critical to the overall lifetime of the whole pipe structure. Cross-sectional designs of the fully interlocked profiles such as the Omega wire should take into account such damage parameters and look to increase the thickness of the thinnest section in order to reduce the likelihood of fracture due to plain fatigue crack formation.

The next chapter presents the conclusions from the investigation into the mechanics of pressure armour for flexible pipes and the future work to be undertaken in order to further the understanding on how pressure armour behaves when subjected to the combination of the various loading modes. A comprehensive study of the design of the Omega profiled wire is clearly necessary to ensure the structural integrity of the flexible pipe, and to minimize the potential for premature failure due to fretting fatigue.

8 Conclusions and Recommendations

8.1 Conclusions

The analyses performed in this work permitted the analytical solution of the pressure armour structure of a flexible pipe subjected to axial and internal pressure for various profile shapes. In particular, pressure armour profiles with interlocking features were investigated to establish its pressure and axial load carrying capacity. As the interlocked pressure armour profiles were intended for use in very high pressure environments, the loading modes investigated were important in optimization of the flexible pipe design as a whole, in terms of the load carrying capacity, weight, structural life and costs.

Given that a pressure armour is constructed from a helically wound wire, the configuration of the pressure armour structure was reduced to the form of a simple helical spring for analytical formulation using the slender rod theory presented by Love (1934). The use of the slender rod theory permitted the following analytical solutions to be established: -

1) The response of the helical wire structure under axial, internal pressure and the combined axial and internal pressure loading. Although a small wire strain was assumed in the analysis, the solution could be used to measure large helical spring deflections. In particular, the analytical solution of the helical spring subjected to the combination of axial and internal pressure loading is new, and an unexpected but salient feature, due to the combined loading was observed. The helical spring subjected to axial tension loads for fixed internal pressure step loads showed an increase in the spring stiffness. This implied that the helical spring could vary its spring stiffness when internal pressure was applied.

2) The analytical solutions included the responses of the helical spring for various cross-sectional profiles subjected to the loading modes as mentioned above. They fell into two categories, one which was symmetric

and the other, non-symmetric sections. The response of symmetric and non-symmetric cross-sections to internal pressure load differed significantly. For the non-symmetric cross-sections, the helical spring subjected to internal pressure could rotate about the helical wire centreline. The twisting of the cross-section of the pressure armour affected the pressure loading capacity significantly. An increase in the angle of twist of the wire cross-section indicated a decrease in the pressure load capacity. In this work, the twisting of the cross-section of the wire was factored into the analytical solution in order to account for the reduction in loading capacity. This twisting effect was not taken into account in the analytical solutions of flexible pipe structure by previous researchers. Although some numerical modelling was carried out by previous researchers to observe the twisting of the cross-section, this was based on an axisymmetric model, which meant that the cross-section was modelled as a series of rings rather than helical coils. It was shown in chapter 4 that the helical spring was not as rigid as a ring section, hence larger deflections of the spring were expected for the applied load. Since this was the case, the modelling using a series of rings resulted in measurements of twist of the cross-section which was much lower than a helical spring, hence overestimating the pressure loading capacity. It was also shown here that the response of the helical spring for non-symmetric cross-sections subjected to internal pressure was non-linear in contrast to linear responses obtained for symmetric cross-sections.

3) The analytical solution for an interlocked helical spring subjected to the various loading modes was also established. In such a configuration, the overlapping of the wire inevitably caused the surfaces to be in contact, and the contact loads between the contacting surfaces were also determined analytically. Particular reference was made for the pressure armour profile used, which was the Omega profiled wire devised in UCL. It was concluded that the interlocked Omega profiled pressure armour subjected to axial and internal pressure behaved like a cylindrical tube (albeit with a line of weakness) when it was fully locked and in contact with its adjacent coils. Hence, it can be seen that the pressure armour constructed from

interlocked Omega profiled wire could be used to resist some axial load in addition to its primary function of withstanding internal pressure. Such a feature is attractive, as it allows the tensile armour layers to be removed or scaled down depending on the in-service environments, which in turn is able to reduce the weight of the flexible pipe for deep-water applications.

4) Verification of the analytical solutions developed in this work was performed using numerical modelling. ABAQUS finite element analysis software was used, and both consistent and close agreement with analytical results were obtained. Furthermore, the physical deformation of helical springs was realized using a novel experimental setup. This included the design of a spring lathe to cut helical springs made from polystyrene. The spring lathe enabled the cutting of springs with various cross-sectional shapes such as rectangular and Z profiles for experimental measurements, which would otherwise have not been achieved using metallic helical springs. This is due to the fact that the cross-sectional shapes available commercially and the load required to cause significant deformation for measurement were not practical for verification work. Successful attempts to cut interlocked polystyrene springs were also achieved. This was possible because the polystyrene cross-section could be shaped using a hot wire cutter, thus alleviating the residual stresses that would be present if the wire was slotted into its adjacent coil. An interlocked profile made from metallic materials would have been slotted in together, consequently causing some plastic deformation even before being placed in-service. Simulation of an internal pressure load on the polystyrene spring was rather difficult as a pressure load acted on the inner surface of the open coil structure, rather than on a tube surface. A purposed built pulley test rig was assembled to apply radial forces at various points to a helical coil to replicate internal pressure loading. There were significant discrepancies in the results of this experimental work compared to those obtained analytically. This error was attributed to the fact that the radial loading applied caused the coils to expand non-uniformly in the radial direction. A possible solution to this problem is to

increase the number of points of applied load to obtain a more uniform radial expansion.

5) Issues of contact between mating surfaces from the use of interlocked pressure armour profiles were discussed. In this work, it was shown that the movements and applied loads on the helical spring encouraged conditions for fretting fatigue. Potential sites of initiation of fretting were identified based on the analysis done and design recommendations were made to overcome premature pressure armour fatigue failure.

8.2 Recommendations and Future Work

Some good design practice is summarized here based on the analysis carried out in this work. Ideally, the cross-sections of the pressure armour profile should have a symmetric section. This is to avoid twisting of the wire cross-section, which reduces the pressure load carrying capacity of the pipe and allow the creeping of the fluid retention polymer layer underneath. A pressure armour cross-section with a small base width is desired, to maximize the stiffness of the helical wire and to increase internal pressure loading capacity. However, this should be optimized with consideration to the overall increase in costs and weight of the flexible pipe. The use of full interlocked pressure armour profiles such as the Omega profiled wire should be encouraged given that it can withstand some of the axial loads resisted primarily by the tensile armours.

There are discontinuities in the behaviour of the helical coils near to the end terminations. Further design considerations have to be taken at the terminations to account for the relative slip of the coils, which can promote fretting mechanism. From the analysis carried out in chapter 7, when optimizing the Omega profiled wire for the various loading modes, considerations have to be given to the potential fretting damage due to the contacting surfaces. Ideally, the design of the profile should eliminate unnecessary geometric contact. However, this is not always possible and hence the use of lubricants or other protective methods such as material coating should be considered.

In summary, the following conclusions can be derived from the analyses performed with respect to the generic pressure armour designs: -

- The depth of the profile (radial direction of pipe) should be larger than the width (axial direction of pipe) to achieve larger pressure load capacity. Conversely, a larger cross-sectional width has higher axial stiffness (see page 152).

- The cross-sections should be as symmetric as possible to avoid twisting under pressure loading. Twisting can bring adjacent sections, which were previously non-contacting, into close contact. Point loading can thus be generated and hence the possibility of fretting damage is present. Non-symmetric sections also exhibit a non-uniform distribution and can support stress concentrations.

- The axial load carrying capacity obviously depends on the thickness of the slender part of the cross-section in fully interlocked systems. Plain fatigue in these areas can be encouraged if high stresses and/or stress concentrations are designed in and fretting may thus be an incidental consideration.

- Where contact between the surfaces exists, the contact width should be increased to reduce the overall stress around the contact area, and hence reduce the possibility of fretting damage.

- A compromise between the amount of freedom of axial movement of the cross-sections allowed and the resulting gap between adjacent coils has to be attained in order to increase the likelihood that the contact zones work in the sliding regime rather than the mixed stick-slip regime to reduce the onset of fretting (see page 228). However, large gaps could increase the risk of polymer extrusion through the profile and hence loss of pressure integrity and fluid containment ability. Smaller gaps have the added disadvantage of reducing overall pipe flexibility.

- Lubrication is a plausible method to reduce fretting crack initiation. However, considerations have to be given to the fact that although the coefficient of friction is being reduced, the slip amplitude will increase as a result and this can cause sliding wear. Ironically, it may be that sliding wear is more preferable to fretting damage, highlighting the many compromises that interlocking profile design will demand.

In addition to the above, it should be noted that there are further issues relating to the design which have not been discussed in this work, but which are relevant to future design methodology. Chief among these are the methods used to manufacture a fully interlocked profile. For example, it is clear that generating an interlock would require plastic deformation of the socket part of each coil. It is unlikely that pure elastic deformation would be sufficient to generate a reliable interlock given the high stiffness of metals used in pressure armour. Residual stresses would thus be present in the structure in zones which are clearly subjected to high loads and stress concentration. Such stresses could enhance crack propagation rates and hence reduce lifetimes.

As mentioned earlier, the interlocked pressure armour behaved very much like a cylindrical tube, albeit with a line of weakness when subjected to axial and internal pressure load. This is because a pressure armour still consisted of a helically wound wire. However, when a pressure armour is twisted about the pipe centreline, relative slip of the helical coils can occur. This can affect the pressure loading capacity and/or cause potential fatigue failure due to fretting. This aspect should be investigated further.

Additionally, in a flexible pipe, the bending load is an important loading mode in service conditions. The overbending of a flexible pipe can cause the pressure armour to collapse under applied loads and the possibility of unlocking of the interlocked pressure armour profile. Furthermore, the pipe structure undergoes tensile stresses on one side of the coil while the other side is under compressive stresses when bent. As such, the contact between the Omega profiled wire contacting surfaces is even more complex given that one side of the pressure armour experiences higher stresses than the other side. The bending of a flexible

pipe structure can also cause reciprocating sliding in the interlocked helical coils because of relative slip between the contacting surfaces of the coils. This can result in the sliding wear of the pressure armour layer, and reduces the pressure loading capacity and service life of the pipe.

Therefore, there is a need to quantify twisting about a pipe centreline and the bending characteristics of a flexible pipe in conjunction with the response of the pressure armour to the various loading modes that was established here. Furthermore, flexible pipes in service conditions are subjected to various combinations of dynamic loading, hence the interaction is more complex than the static case analysed here. Further work should therefore be performed to simulate the actual deformations experienced. On the experimental front, which has implications on the production of the interlocked pressure armour profiles, further investigation should be carried out to enhance the manufacturing process of Omega profiled wire made from metallic material in order to eliminate residual stresses induced and potential sliding of contacting surfaces due to slotting of the profile.

References

Ancker C J and Goodier J N, 1958 Pitch and Curvature Corrections for Helical Springs, Journal of Applied Mechanics, Vol. 25 **No. 4**, 466 – 470

API Document 17B, 1998 Recommended Practice for Flexible Pipe, American Petroleum Institute

Berge S, Engseth A, Fylling I, Larsen C M, Leira B J, Nygaard I and Olufsen A, 1992 Handbook of Design and Operation of Flexible Pipes, FPS2000, SINTEF, Trondheim, Norway

Blanco J A and Costello G A, 1974 Cylindrical Constraint of Helical Springs, Journal of Applied Mechanics, Vol. 41 **No. 4**, 1138 -1140

Blouin F and Cardou A, 1989 A Study of Helically Reinforced Cylinders Under Axially Symmetric Loads and Application to Strand Mathematical Modelling, International Journal of Solids and Structures, Vol. 25 **No. 2**, 189 – 200

Burke R N and Witz J A, 1999 Fretting Fatigue of Flexible Pipe Pressure Armour, Marinflex

Chen B, Kalman M, Lewicki P and Zhang Y, 1995 Analytical and Finite Element Modelling of Nonbonded Flexible Pipe Structures, Marinflex 95, Proceedings of the Second European Conference on Flexible Pipes, Umbilicals and Marine Cables, London

Chironis N P, 1961 Spring Design and Application, McGraw-Hill Book Co., 169 – 173

Costello G A, 1990 Theory of Wire Ropes, Springer Verlag

Costello G A and Phillips J W, 1976 Effective Modulus of Twisted Wire Cables, Journal of the Engineering Mechanics Division, Vol. 102 **No. 1**, 171 – 181

Custodio A B and Vaz M A, 2002 A Nonlinear Formulation for the Axisymmetric Response of Umbilical Cables and Flexible Pipes, Applied Ocean Research, Vol. 24, 21 – 29

Endo K and Goto H, 1976 Initiation and Propagation of Fretting Fatigue Cracks, Wear, Vol. 38, 311 – 324

Feld G, 1992 Static and Cyclic Mechanical Behaviour of Hellically-wound Subsea Power Cables, Ph.D thesis, Faculty of Engineering, Heriot-Watt University

Fellows L J, Nowell D and Hills D A, 1997 On the Initiation of Fretting Fatigue Cracks, Wear, Vol. 205, 120 – 129

Feret J J and Bournazel C L, 1987 Calculation of Stresses and Slip in Structural Layers of Unbonded Flexible Pipe, Journal of Offshore Mechanics and Artic Engineering, Vol. 109, 263 - 269

Gao H, Gu H and Zhou H, 1991 Effect of Slip Amplitude on Fretting Fatigue, Wear, Vol. 148, 15 – 23

Goss G L, Hoeppner D W, 1974 Normal Load Effects in Fretting Fatigue of Titanium and Aluminium Alloys, Wear, Vol. 27, 153 – 159

Goto Y, Okamoto T, Araki M and Fuku T, 1987 Analytical Study of the Mechanical Strength of Flexible Pipes, Journal of Offshore Mechanics and Arctic Engineering, Vol. 109, 249 - 253

Hamilton G M and Goodman L E, 1966 The Stress Field Created by a Circular Sliding Contact, Journal of Applied Mechanics, 371 – 376

Hibbitt, Karlsson and Sorensen, 2004 ABAQUS 6.4 User Manual

Hills D A and Nowell D, 1994 Mechanics of Fretting Fatigue

Hills DA, Nowell D and O'Connor J J, 1988 On the Mechanics of Fretting Fatigue, Wear, Vol. 125, 129 – 146

Hruska F H, 1951 Calculation of Stresses in Wire Ropes, Wire and Wire Products, Vol. 26, 766 – 767, 799 – 801

Hruska F H, 1952 Radial Forces in Wire Ropes, Wire and Wire Products, Vol. 27, 459 – 463

Hruska F H, 1953 Tangential Forces in Wire Ropes, Wire and Wire Products, Vol. 28, 455 – 460

Johnson K L, 1985 Contact Mechanics, Cambridge University Press

Jolicoeur C and Cardou A, 1991 A Numerical Comparison of Current Mathematical Models of Twisted Wire Cables under Axisymmetric Loads, Journal of Energy Resources Technology Vol. 113, 241 – 249

Knapp R H, 1979 Derivation of a New Stiffness Matrix for Helically Armoured Cables Considering Tension and Torsion, International Journal for Numerical Methods in Engineering, Vol. 14, 515 – 529

Knapp R H, 1988 Structural Modelling of Undersea Power Cables, Proceedings of the Seventh International Conference on Offshore and Arctic Engineering, 497 – 506

Kreyszig E, 1999 Advanced Engineering Mathematics, 8th Edition, John Wiley & Sons Inc

Lanteigne J, 1985 Theoretical Estimation of the Response of Helically Armoured Cables to Tension, Torsion and Bending, Journal of Applied Mechanics, Vol. 52, 423 – 432

LeClair R A and Costello G A, 1986 Axial Bending and Torsional Loading of a Strand with Friction, Proceedings of Fifth International Conference on Offshore Mechanics and Arctic Engineering, 550 – 555

Lin Y and Pisano A P, 1988 The Differential Geometry of the General helix as Applied to Mechanical Springs, Journal of Applied Mechanics, Vol. 55 **No. 4**, 831 – 836

Lindley T C, 1997 Fretting Fatigue in Engineering Alloys, International Journal of Fatigue, Vol. 19 Supp. **No. 1**, S39 – S49

Liu Z, Neville A and Reuben R L, 2001 A Numerical Calculation of the Contact Area and Pressure of Real Surfaces in Sliding Wear, Journal of Tribology, Vol. 123, 27 – 35

Love A E H, 1934 A Treatise on the Mathematical Theory of Elasticity, Fourth Edition, Cambridge University Press, Chapter 18 and 19

Machida S and Durelli A J, 1973 Response of a Strand to Axial and Torsional Displacements, Journal of Mechanical Engineering Science, Vol. 15 **No. 4**, 241 – 251

McIver D B, 1995 A Method of Modelling the Detailed Component and Overall Structure Behaviour of Flexible Pipe Sections, Engineering Structures, Vol.17 **No. 4**, 254 – 266

McNamara J F and Harte A M, 1989 Three Dimensional Analytical Simulation of Flexible Pipe Wall Structure, Proceedings of the Eighth International Conference on Offshore Mechanics and Arctic Engineering, The Hague, 477 – 482

Mindlin R D, 1949 Compliance of Elastic bodies in Contact, Journal of Applied Mechanics, Vol. 16, 259 – 268

Moobola R, Hills D A and Nowell D, 1998 Designing against Fretting Fatigue: Crack Self-arrest, Journal of Strain Analysis, Vol. 33 **No.1**, 17 – 25

Nakazawa K, Maruyama N and Hanawa T, 2003 Effect of Contact Pressure on Fretting Fatigue of Austenitic Stainless Steel, Tribology International, Vol. 36, 79 – 85

Nakazawa K ,Sumita M and Maruyama N, 1994 Effect of Relative Slip Amplitude on Fretting Fatigue of High Strength Steel, Fatigue and Fracture of Engineering Materials and Structures, Vol. 17 No.7 751 – 759

Nowell D and Hills D A, 1990 Crack Initiation Criteria in Fretting Fatigue, Wear, Vol. 136, 329 – 343

Oliviera J G de, Goto Y and Okamoto T, 1985 Theoretical and Methodological Approaches to Flexible Pipe Design and Application, OTC 5021, 517 – 526

Pascoe K J, 1978 An Introduction to the Properties of Engineering Materials, Van Nostrand Reinhold Co.

Patel M H, Witz J A and Tan Z, 1993 A Flexible Riser Design Manual, Bentham Press

Phillips J W and Costello G A, 1973 Contact Stresses in Twisted Wire Cables, Journal of the Engineering Mechanics Division, Proceeding of the American Society of Civil Engineers, Vol. 99, 331 – 341

Phillips J W and Costello G A, 1979 General Axial response of Stranded Wire Helical Springs, Journal of Non-Linear Mechanics, Vol. 14 **No. 4**, 247 - 257

Ramos Jr R, Pesce C P and Martins C A, 2000 A Comparative Analysis Between Analytical and FE-Based Models for Flexible Pipes Subjected to Axisymmetric Loads, Proceeding of the Tenth International Offshore and Polar Engineering Conference, Seattle USA, 80 – 88

Ramsey H, 1988 A Theory of Thin Rods with Application to Helical Constituent Wires in Cables, International Journal of Mechanical Sciences, Vol. 30 **No. 8**, 559 – 570

Ramsey H, 1990 Analysis of Interwire Friction in Multilayered Cables under Uniform Extension and Twisting, International Journal of Mechanical Sciences, Vol. 32 **No. 8**, 709 – 716

Ramsey H, 1991 Localized Effect of Clamp or Socket End Connections on Helical Wires in Multilayered Cables, International Journal of Solids and Structures, Vol. 28 **No. 6**, 779 – 790

Raoof M, 1991 Methods of Analyzing Large Spiral Strands, Journal of Strain Analysis for Engineering Design, Vol. 26 **No. 3**, 165 – 174

Raoof M and Hobbs R E, 1988 Analysis of Multilayered Structural Strands, Journal of Engineering Mechanics, Vol. 114 **No. 7**, 1166 – 1182

Reiner M, 1960 Deformation, Strain and Flow: An Elementary Introduction to Rheology, Chapter 4

Saevik S and Berge S, 1995 Fatigue Testing and Theoretical Studies of Two 4in Flexible Pipes, Engineering Structures, Vol. 17 **No. 4**, 276 – 292

Sato K and Fujii H, 1986 Crack Propagation Behaviour in Fretting Fatigue, Wear, Vol. 107, 245 – 262

Smith J O and Liu C K, 1953 Stresses Due to Tangential and Normal Loads on an Elastic Solid with Application to Some Contact Stress Problems, Journal of Applied Mechanics, Vol. 21, 157 – 166

Szolwinski M P and Farris T N, 1996 Mechanics of Fretting Fatigue Crack Formation, Wear, Vol. 198, 93 – 107

Szolwinski M P and Farris T N, 1998 Observation, Analysis and Prediction of Fretting Fatigue in 2024 - T351 Aluminum Alloy, Wear, Vol. 221, 24 – 36

Tan Z, 1992 On the Mechanics of Flexible Pipes, Umbilicals and Marine Cables, Ph.D thesis, Department of Mechanical Engineering, University College London, University of London

Thomson K W and Tait P G, 1889 Treatise on Natural Philosophy, Cambridge University Press

Timoshenko S, 1955 Strength of Materials, Part 1

Timoshenko S, 1956 Strength of Materials, Part 2

Timoshenko S P and Goodier J N, 1970 Theory of Elasticity

Velinsky S A, Anderson G L and Costello G A, 1984 Wire Ropes with Complex Cross Sections, Journal of Engineering Mechanics, Vol. 110 **No. 3**, 380 – 391

Vingsbo O and Soderberg S, 1988 On Fretting Maps, Wear, Vol.126, 131 – 147

Wahl A M, 1963 Mechanical Springs, McGraw-Hill Book Co.

Waterhouse R B, 1992 Fretting Fatigue, International Materials Reviews, Vol. 37 **No. 2**, 77 - 97

Wittrick W H, 1966 On Elastic Wave Propagation in Helical Springs, International Journal of Mechanical Science, Vol. 8, 25 – 47

Witz J A, 1996 A Case Study in the Cross-section Analysis of Flexible Risers, Marine Structures, Vol.9, 885 – 904

Witz J A and Burke R N, 1999 Helically Wound Reinforcing Components for Flexible Tubular Conduits, GB Patent No. 2336886

Witz J A and Tan Z, 1992 On the Axial Torsional Structural Behaviour of Flexible Pipes, Umbilicals and Marine Cables, Marine Structures **No. 5**, 205 – 227

Young W C, 1989 Roark's Formula for Stress and Strain, McGraw-Hill

Zhou Z R and Vincent L, 1999 Lubrication in Fretting – A Review, Wear, Vol. 225 – 229, 962 – 967

Appendix A

Supplementary Derivation for Helical Wire Analysis

Energy method

Derivation for wire axial strain: -

$$\varepsilon_{aw}+1=\frac{\sin\alpha}{p}l_1$$

$$\varepsilon_{aw}+1=\frac{\sin\alpha}{p}\left[\left(p+\Delta p\right)^2+\left(2\pi R_1+R\phi\right)^2\right]^{\frac{1}{2}}$$

$$\left(\varepsilon_{aw}+1\right)^2=\frac{\sin^2\alpha}{p^2}\left[\left(p+\Delta p\right)^2+\left(2\pi R_1+R\phi\right)^2\right]$$

$$=\frac{\sin^2\alpha}{p^2}\left[\left(p+\Delta p\right)^2+\left(2\pi R+2\pi\Delta R+R\phi\right)^2\right]$$

$$=\sin^2\alpha\left[\left(1+\frac{\Delta p}{p}\right)^2+\left(\frac{2\pi R}{p}+\frac{2\pi\Delta R}{p}+\frac{R\phi}{p}\right)^2\right]$$

$$=\sin^2\alpha\left[\left(1+\frac{\Delta p}{p}\right)^2+\left(\frac{1}{\tan\alpha}+\frac{2\pi\Delta R}{p}+\frac{R\phi}{p}\right)^2\right]$$

$$=\sin^2\alpha\left[\left(1+\frac{\Delta p}{p}\right)^2+\left(\frac{1}{\tan\alpha}+\frac{\Delta R}{R\tan\alpha}+\frac{R\phi}{p}\right)^2\right]$$

$$=\sin^2\alpha\left[\left(1+\frac{\Delta p}{p}\right)^2+\left(\frac{1}{\tan\alpha}\left(1+\frac{\Delta R}{R}\right)+\frac{R\phi}{p}\right)^2\right]$$

$$=\sin^2\alpha\left[\left(1+\frac{\Delta p}{p}\right)^2+\left(\frac{1}{\tan\alpha}\left(1+\varepsilon_r\right)+\frac{R\phi}{p}\right)^2\right] \qquad \text{(A.1)}$$

The wire axial strain is linearized by ignoring all second order strain values, hence

$$1+2\varepsilon_{aw}=\sin^2\alpha+\cos^2\alpha+2\sin^2\alpha\left(\frac{\Delta p}{p}\right)+2\sin\alpha\cos\alpha\left(1+\varepsilon_r\right)R\left(\frac{\phi}{p}\right)$$

$$\varepsilon_{aw}=\sin^2\alpha\left(\frac{\Delta p}{p}\right)+R\left(1+\varepsilon_r\right)\sin\alpha\cos\alpha\left(\frac{\phi}{p}\right)$$

$$=\sin^2\alpha\left(\frac{\Delta p}{p}\right)+R_1\sin\alpha\cos\alpha\left(\frac{\phi}{p}\right) \qquad \text{(A.2)}$$

Thus, the variation in internal strain energy is given by

$$\delta U_i=E\iiint_{dv}\varepsilon_{aw}\,\delta\varepsilon_{aw}dv$$

$$=\iiint_{dv}\left[\sin^2\alpha\left(\frac{\Delta p}{p}\right)+R_1\sin\alpha\cos\alpha\left(\frac{\phi}{p}\right)\right]\sin^2\alpha\,\delta\left(\frac{\Delta p}{p}\right)\frac{\rho d\rho d\varphi dz}{\sin\alpha}$$

$$=E\iiint_{dv}\left[\sin^3\alpha\left(\frac{\Delta p}{p}\right)+R_1\sin^2\alpha\cos\alpha\left(\frac{\phi}{p}\right)\right]\delta\left(\frac{\Delta p}{p}\right)\rho d\rho d\varphi dz$$

$$=E\iint\left[\sin^3\alpha\left(\frac{\Delta p}{p}\right)+R_1\sin^2\alpha\cos\alpha\left(\frac{\phi}{p}\right)\right]\delta\left(\frac{\Delta p}{p}\right)\left[\frac{\rho^2}{2}\right]_0^r d\varphi dz$$

$$=E\int\left[\sin^3\alpha\left(\frac{\Delta p}{p}\right)+R_1\sin^2\alpha\cos\alpha\left(\frac{\phi}{p}\right)\right]\delta\left(\frac{\Delta p}{p}\right)\frac{r^2}{2}\left[\varphi\right]_0^{2\pi}dz$$

$$=E\left[\sin^3\alpha\left(\frac{\Delta p}{p}\right)+R_1\sin^2\alpha\cos\alpha\left(\frac{\phi}{p}\right)\right]\delta\left(\frac{\Delta p}{p}\right)\pi r^2\left[z\right]_0^p$$

$$= AE\left[\sin^3\alpha\left(\frac{\Delta p}{p}\right)+R_1\sin^2\alpha\cos\alpha\left(\frac{\phi}{p}\right)\right]\delta\left(\frac{\Delta p}{p}\right)p$$

$$= AE\left[\sin^3\alpha\left(\Delta p\right)+R_1\sin^2\alpha\cos\alpha\left(\phi\right)\right]\delta\left(\frac{\Delta p}{p}\right) \qquad \text{(A.3)}$$

Slender rod theory

Derivation of the internal line load and axial load in terms of the binormal shear force of wire: -

$$-N_b\tau_1+T\kappa_{b1}+X=0$$

$$-N_b\tau_1+\frac{F_A-N_b\cos\alpha_1}{\sin\alpha_1}\kappa_{b1}+X=0$$

$$-X=\left(\frac{F_A}{\sin\alpha_1}-\frac{N_b}{\tan\alpha_1}\right)\kappa_{b1}-N_b\tau_1$$

$$=\frac{F_A}{\sin\alpha_1}\frac{\cos^2\alpha_1}{R_1}-\left(N_b\frac{\sin\alpha_1\cos\alpha_1}{R_1}+N_b\frac{\cos\alpha_1\cos^2\alpha_1}{R_1\sin\alpha_1}\right)$$

$$=-N_b\left(\frac{\cos\alpha_1\left(\sin^2\alpha_1+\cos^2\alpha_1\right)}{R_1\sin\alpha_1}\right)+\frac{F_A\cos\alpha_1}{R_1\tan\alpha_1}$$

$$=\frac{-N_b\cos\alpha_1}{R_1\sin\alpha_1}+\frac{F_A\cos\alpha_1}{R_1\tan\alpha_1}$$

$$=\frac{F_A\cos\alpha_1-N_b}{R_1\tan\alpha_1} \qquad \text{(A.4)}$$

Appendix B

Computer Program Listing for Helical Coil

- Program for element listing of a helical coil

```
#include <iostream.h>
#include <fstream.h>
#include <math.h>
#include <iomanip.h>

int main()
{
        ofstream output_file("elementlisting.txt");

        float n , x , y;
        for (int i = 1; i<=40; i++)          //1 pitch + 2 nodes on each end

        {
                n = 0+i;          //number for listing of result

                x = 0+i;          //node 1
                y = 1+i;          //node 2

                output_file << setw(5) << n <<",    " << setw(5) << x << ",    "
                                        << setw(5) << y << endl;

        }
}
```

- Program for generating nodes of a helical coil

```
#include <iostream.h>
#include <fstream.h>
#include <math.h>
#include<iomanip.h>

int main()
{
        ofstream output_file("coord_result.txt");

        int degree = 0;
        float n , x , y , z , t;
        for (int i = 1; i<=37; i++)          //37 for 1 helix turn

        {
                t = degree*3.141592654/180;

                n = 2+i;            //number for listing of result

                // define parametric expressions

                x = 152.4*cos(t);                   //6" radius
                y = 152.4*sin(t);                   //6" radius
                z = 20*t;

                output_file << setw(10) << setprecision(0) << n <<", "
                                        << setiosflags(ios::fixed) << setw(10)
                                        << setprecision(2)
                                        << x << ",  "
                                        << setw(10) << y << ",  " << setw(10) << z << endl;


                degree += 10;               // for every 10 degrees turn
        }
}
```

Appendix C

Supplementary Results for Circular Cross-section

- Results for Axial Loading (Large Deformation)

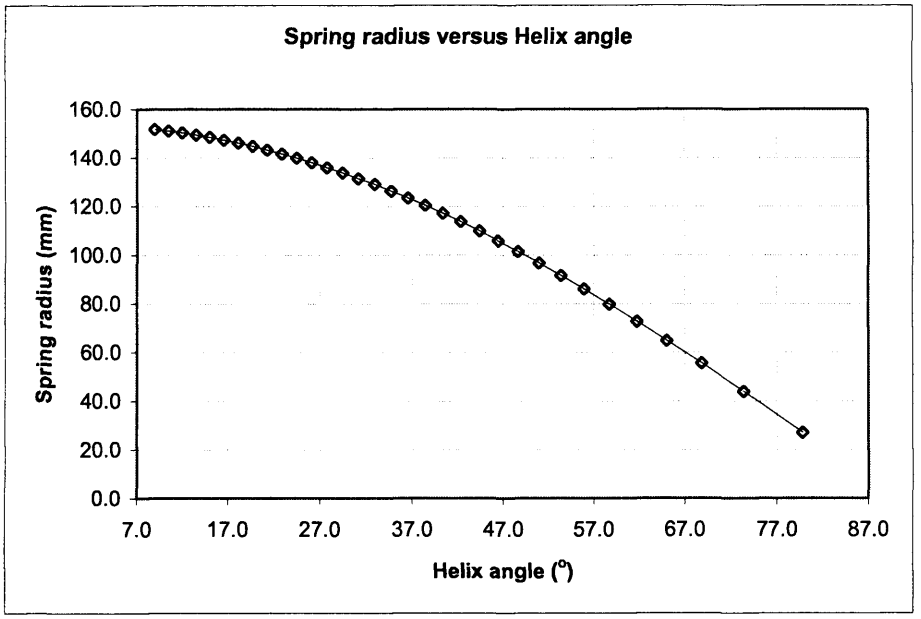

Figure C.1a Spring radius versus helix angle for large deformation

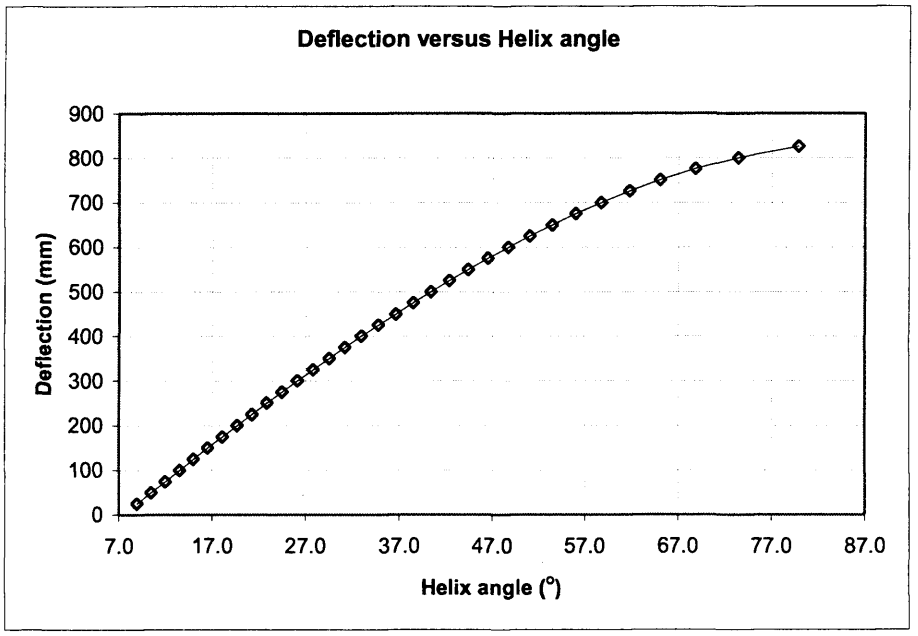

Figure C.1b Deflection versus helix angle for large deformation

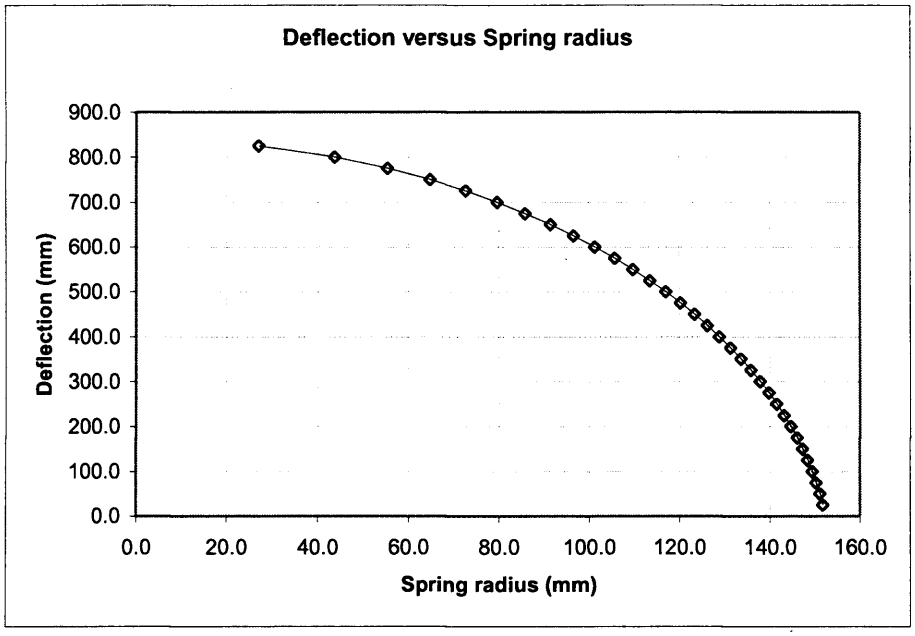

Figure C.1c Deflection versus spring radius for large deformation

- Results for Axial Tension (Small Deformation)

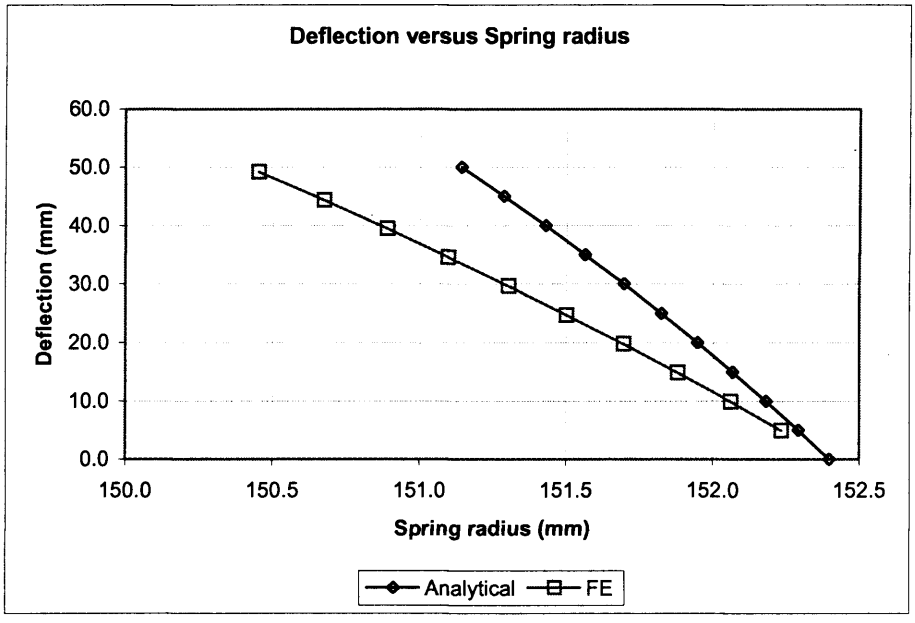

Figure C.2a Deflection versus spring radius for analytical and finite element

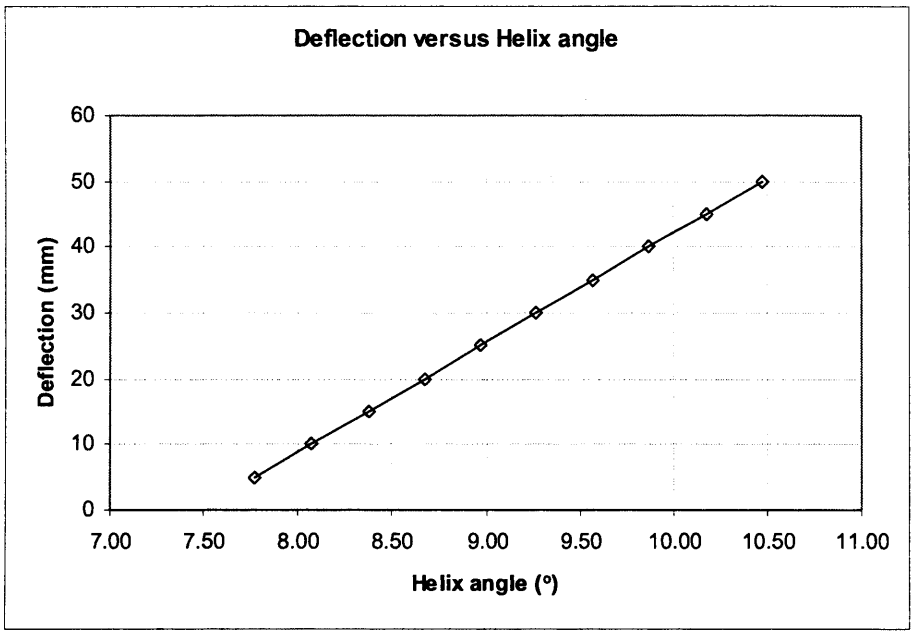

Figure C.2b Deflection versus helix angle for analytical solution

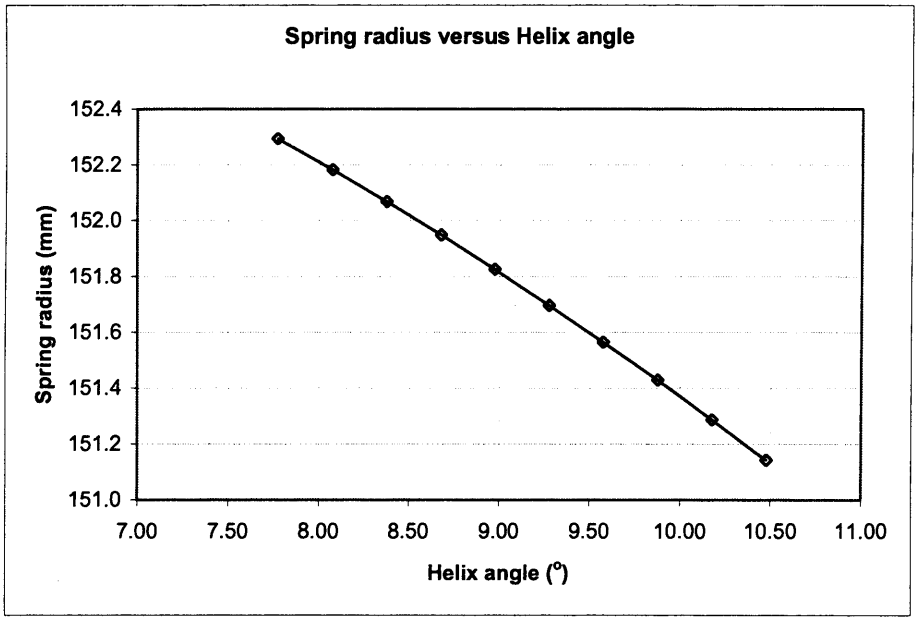

Figure C.2c Spring radius versus helix angle for analytical solution

- *Results for Axial Compression (Small Deformation)*

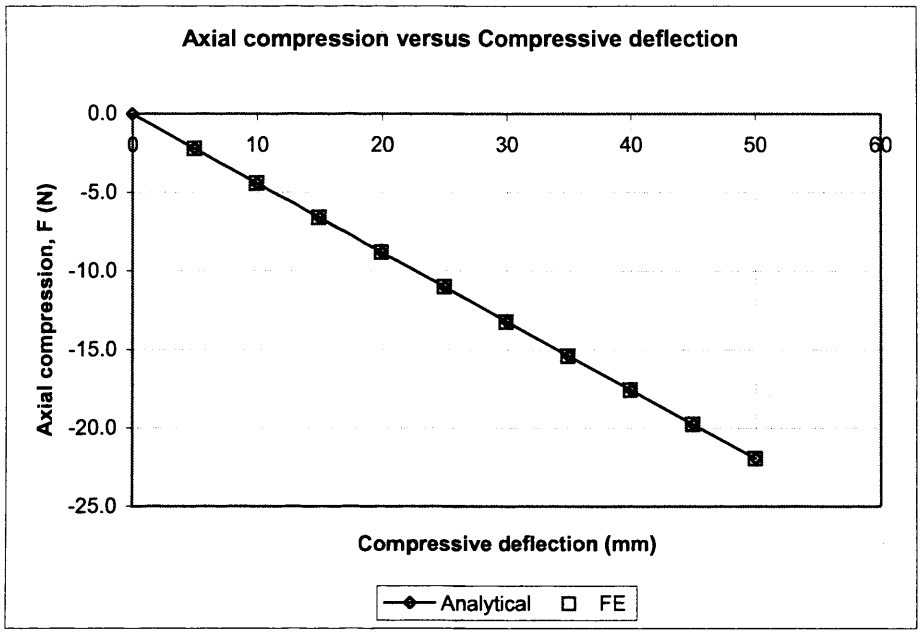

Figure C.3a Axial compression versus deflection for analytical and finite element

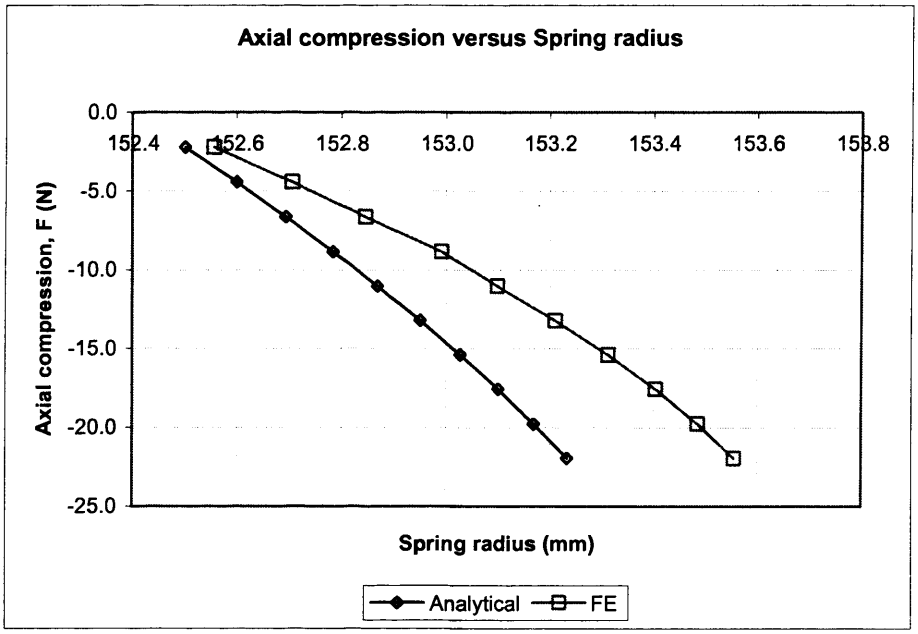

Figure C.3b Axial compression versus spring radius for analytical and finite element

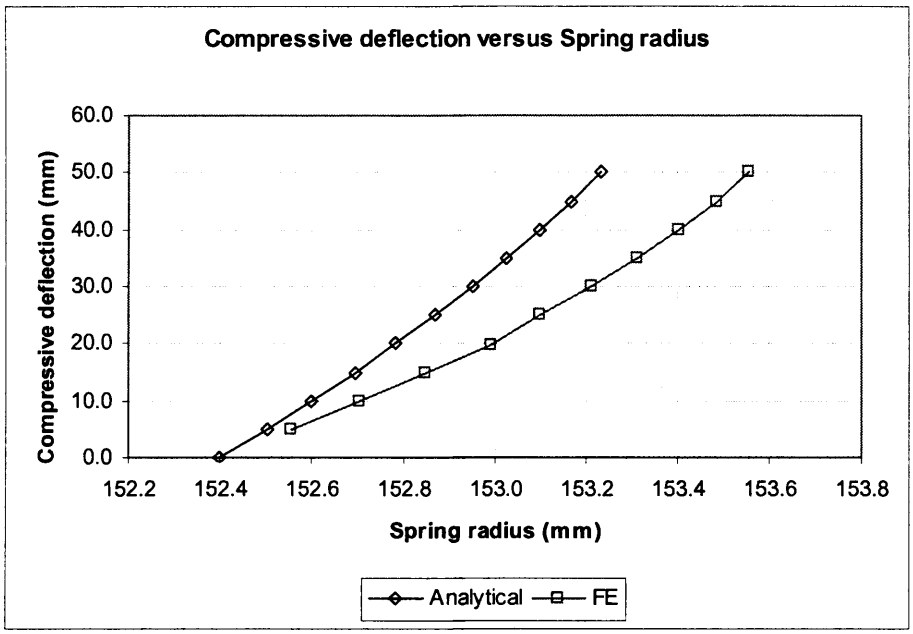

Figure C.3c Compressive deflection versus spring radius for analytical and finite element

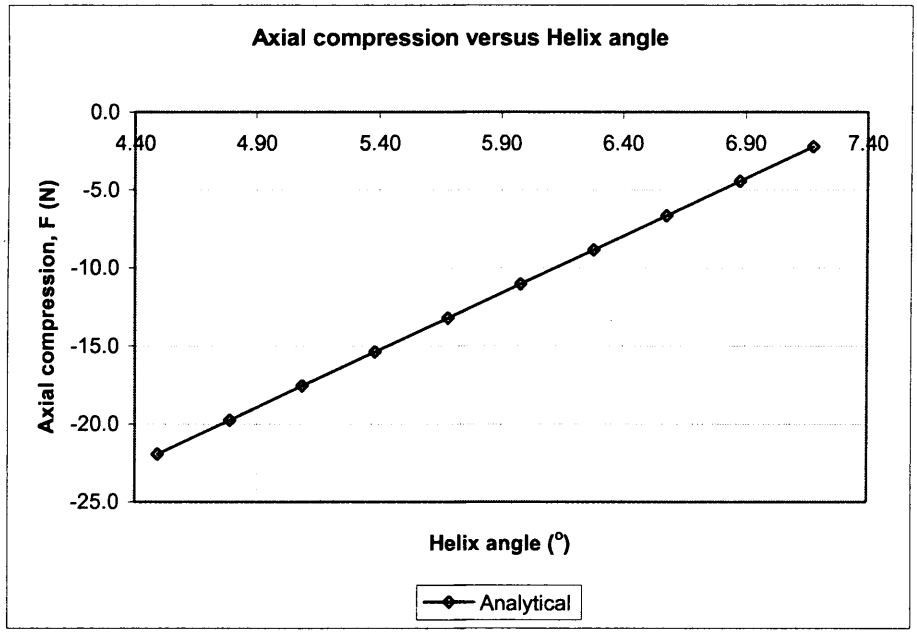

Figure C.3d Axial compression versus helix angle for analytical solution

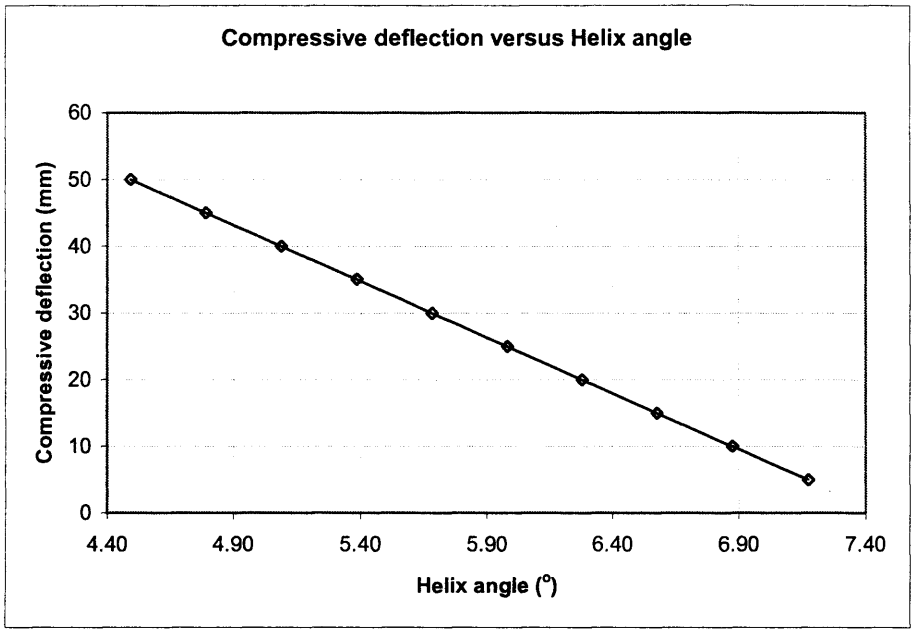

Figure C.3e Compressive deflection versus helix angle for analytical solution

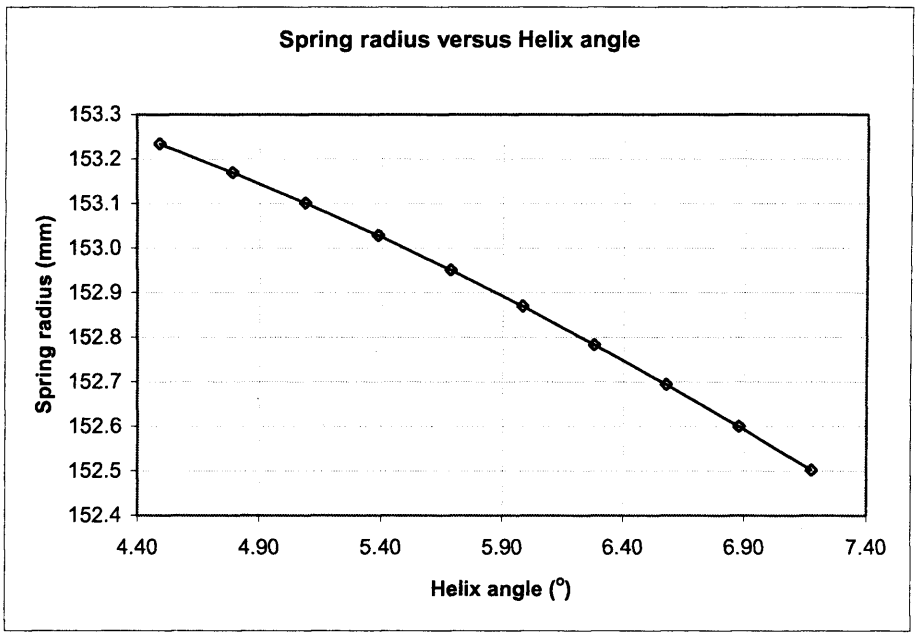

Figure C.3f Expansion of radius versus helix angle for analytical solution

- Results for Combined Axial Tension and Internal Pressure Loading

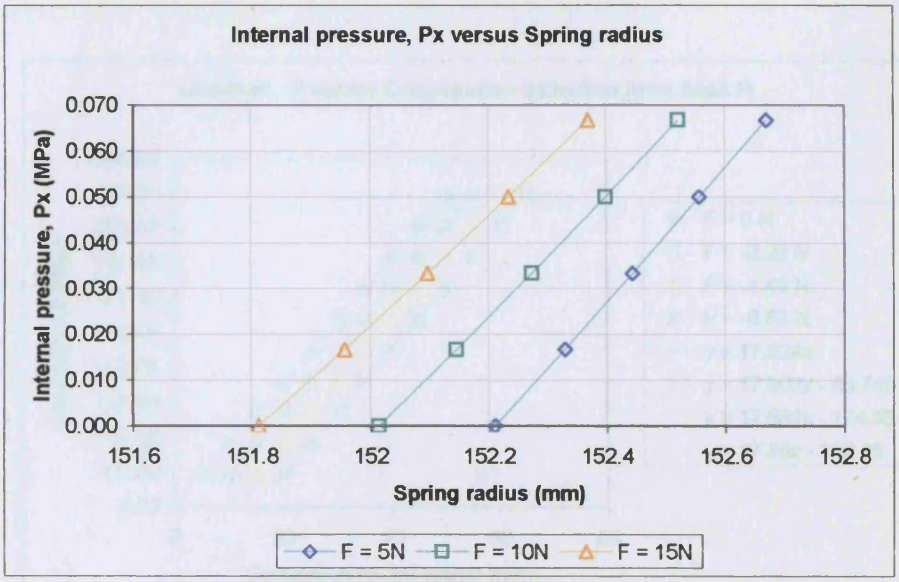

Figure C.4 Internal pressure versus spring radius for fixed axial tension step values

- Results for Combined Axial Compression and Internal Pressure Loading

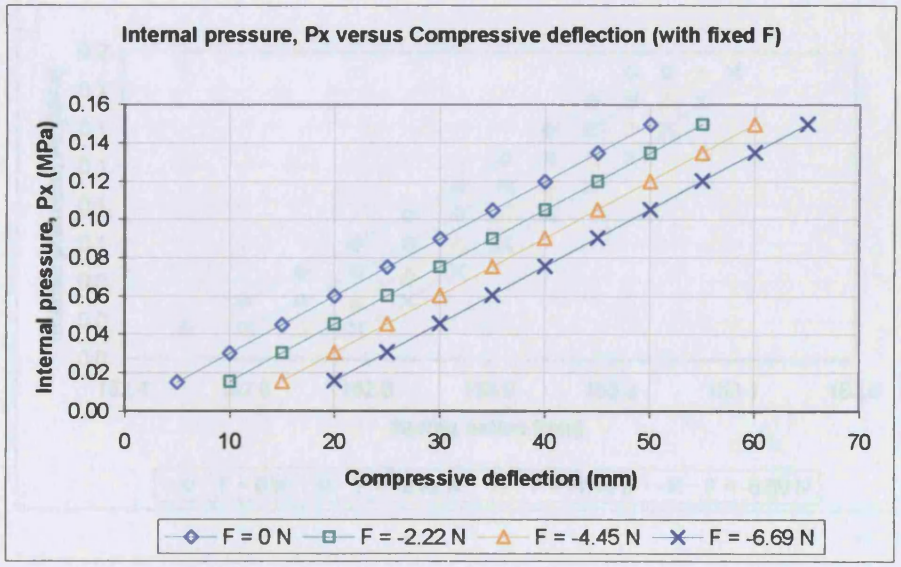

Figure C.5a Internal pressure versus deflection for fixed axial compression step values

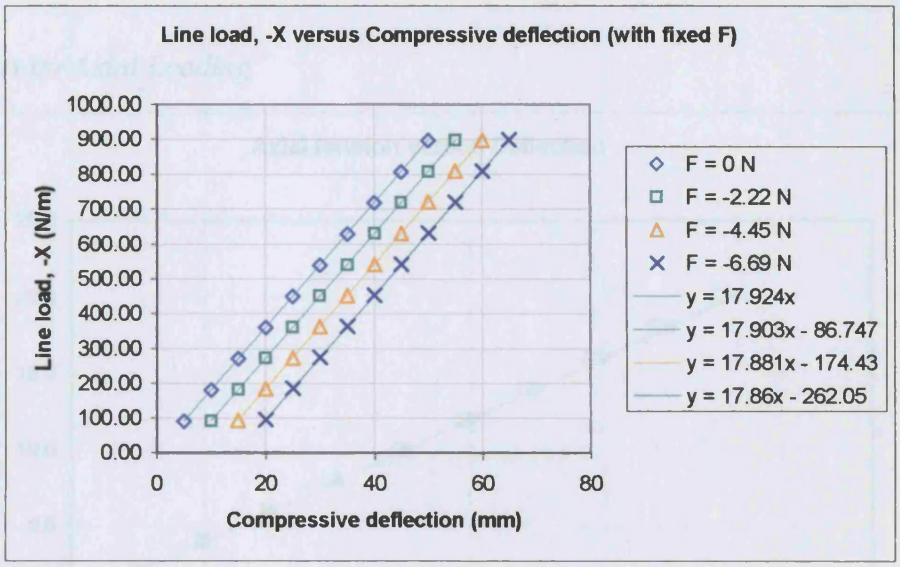

Figure C.5b Internal line load versus deflection for fixed axial compression step values

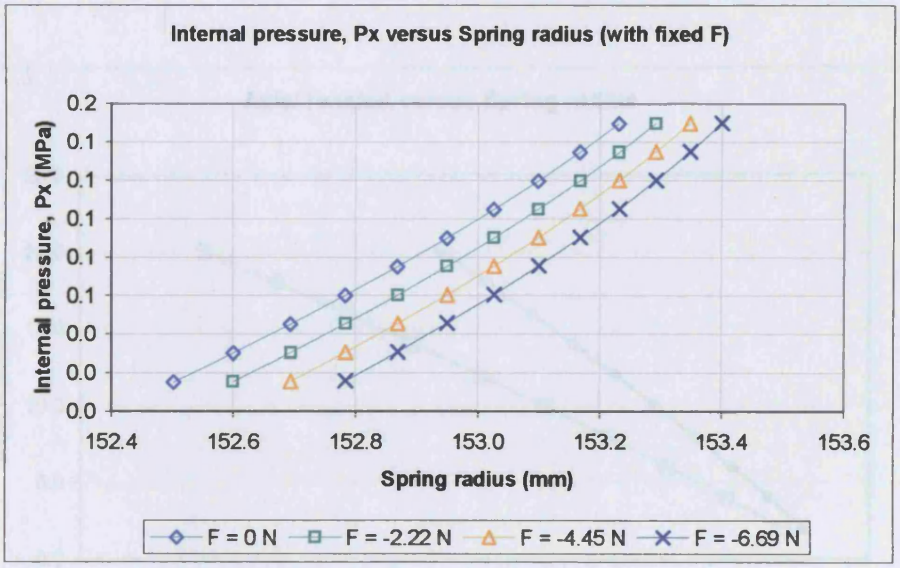

Figure C.5c Internal pressure versus spring radius for fixed axial compression step values

Appendix D

Supplementary Results for Non-circular Cross-sections

- Results for Axial Loading

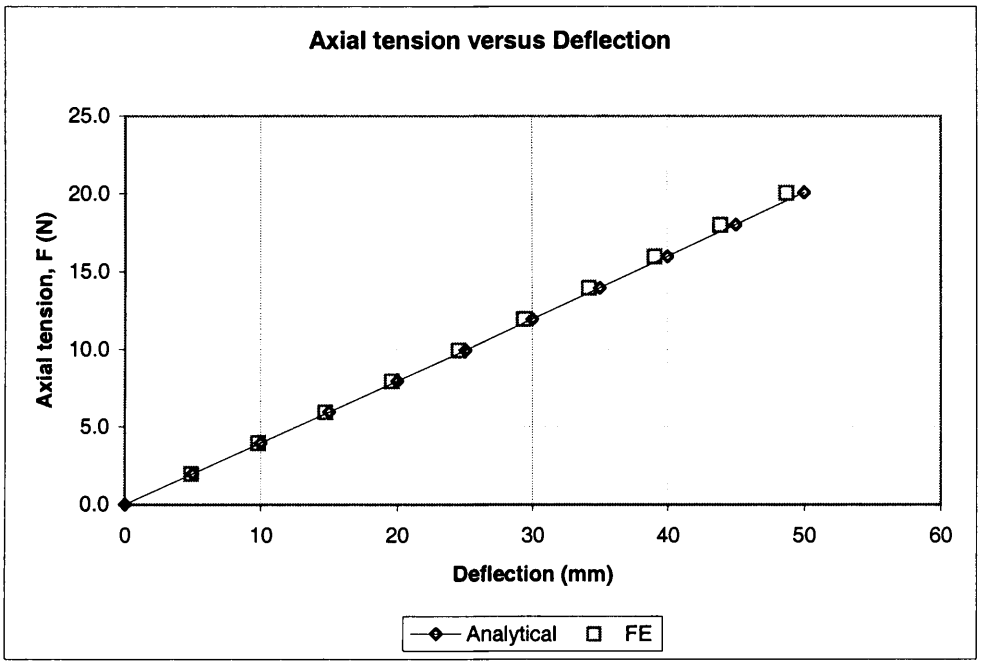

Figure D.1a Axial load - deflection for analytical and finite element for square section

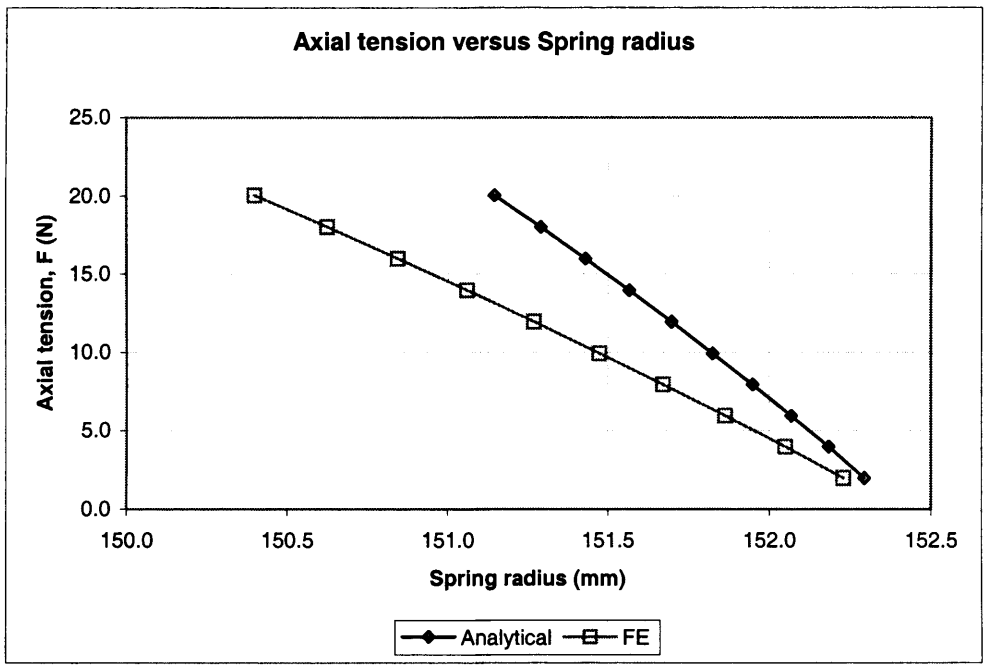

Figure D.1b Axial load – spring radius for analytical and finite element for square section

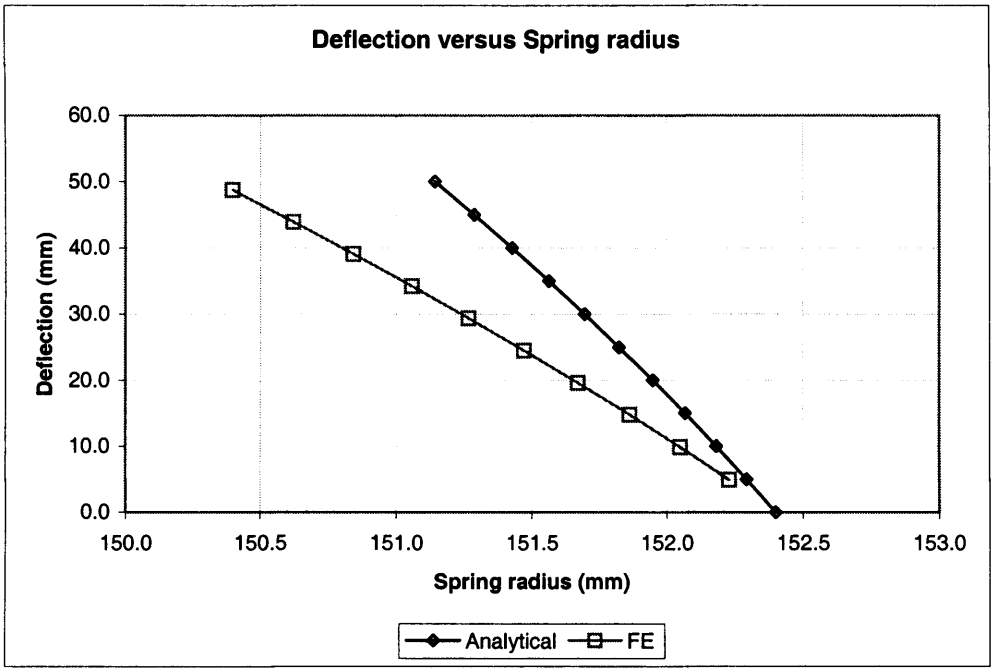

Figure D.1c Deflection – spring radius for analytical and finite element for square section

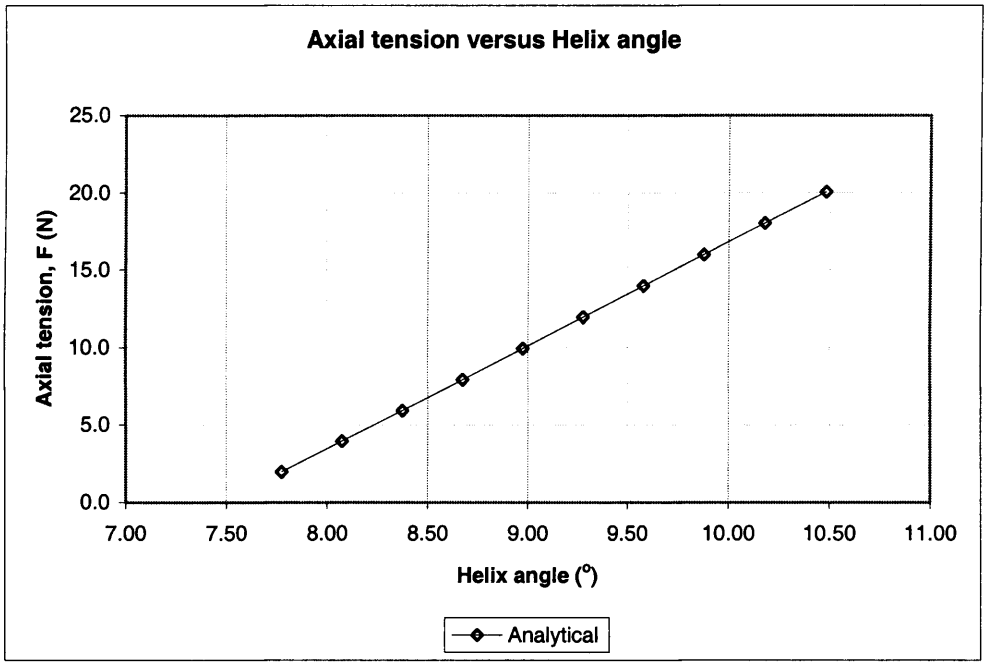

Figure D.1d Axial load – helix angle for analytical solution for square section

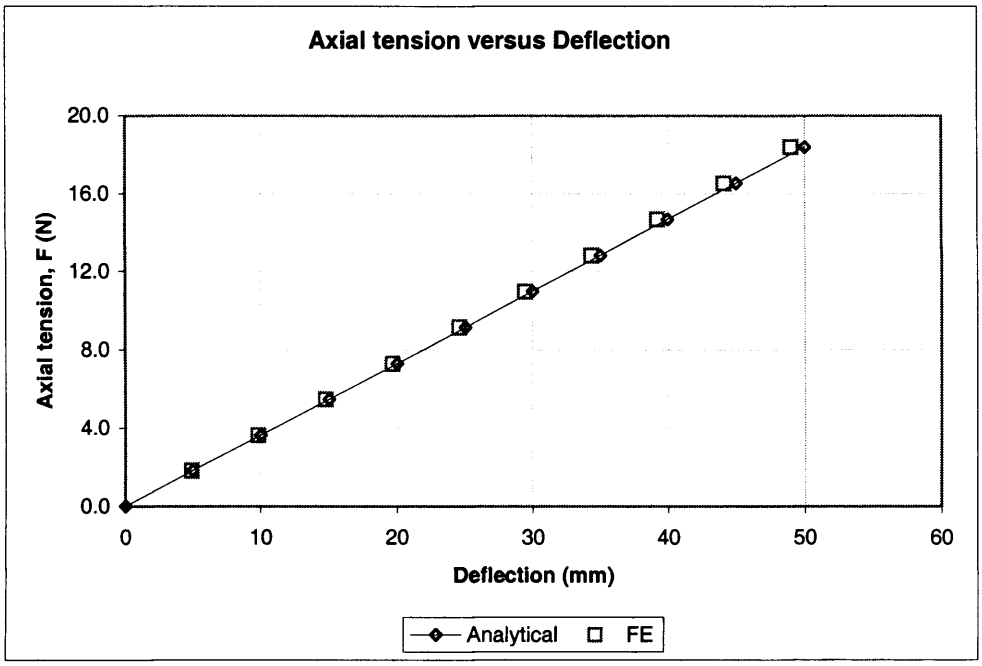

Figure D.2a Axial load - deflection for analytical and finite element for rectangular section (6.5mm x 4.3499mm)

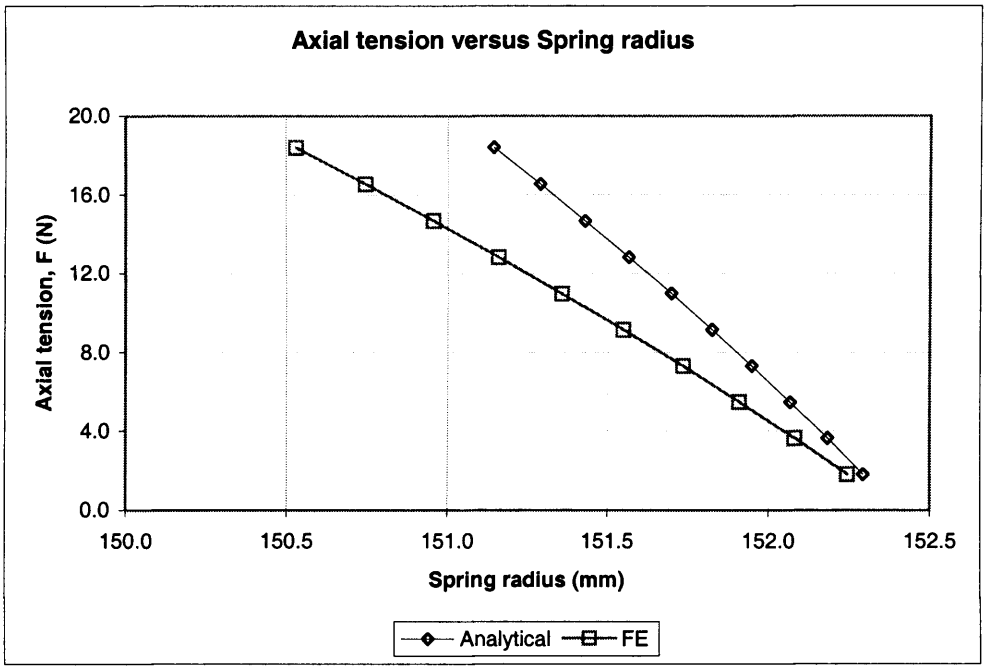

Figure D.2b Axial load – spring radius for analytical and finite element for rectangular section (6.5 x 4.3499)

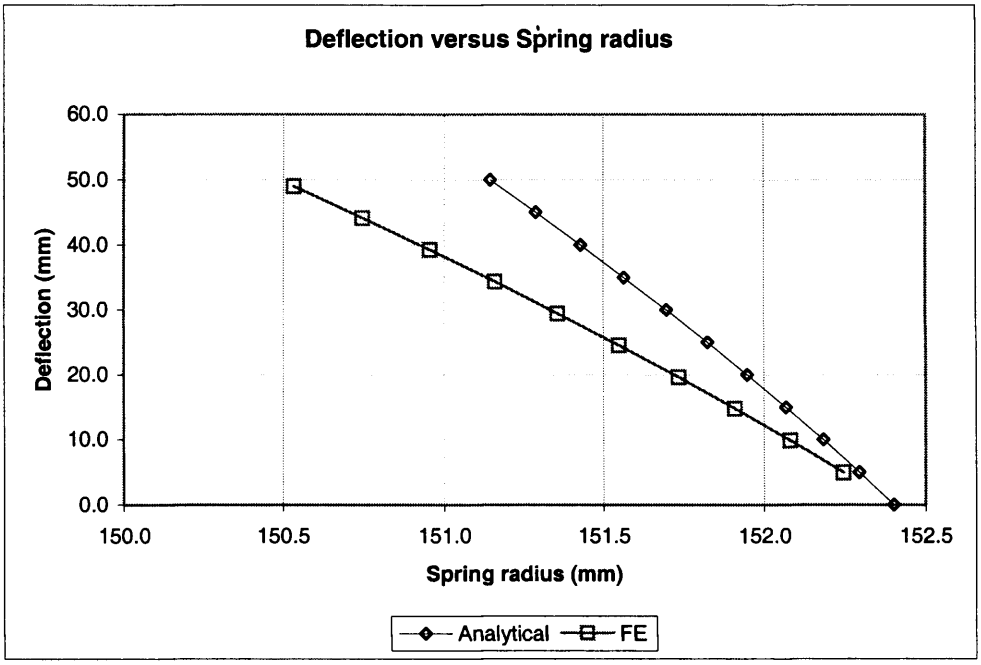

Figure D.2c Deflection – spring radius for analytical and finite element for rectangular section (6.5mm x 4.3499mm)

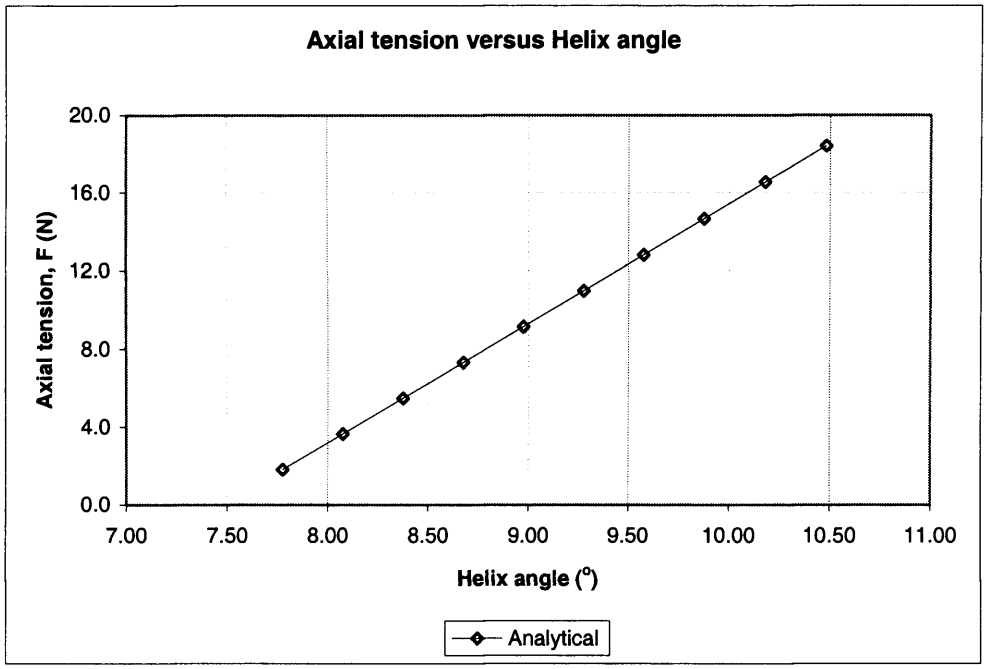

Figure D.2d Axial load – helix angle for analytical solution for rectangular section (6.5mm x 4.3499mm)

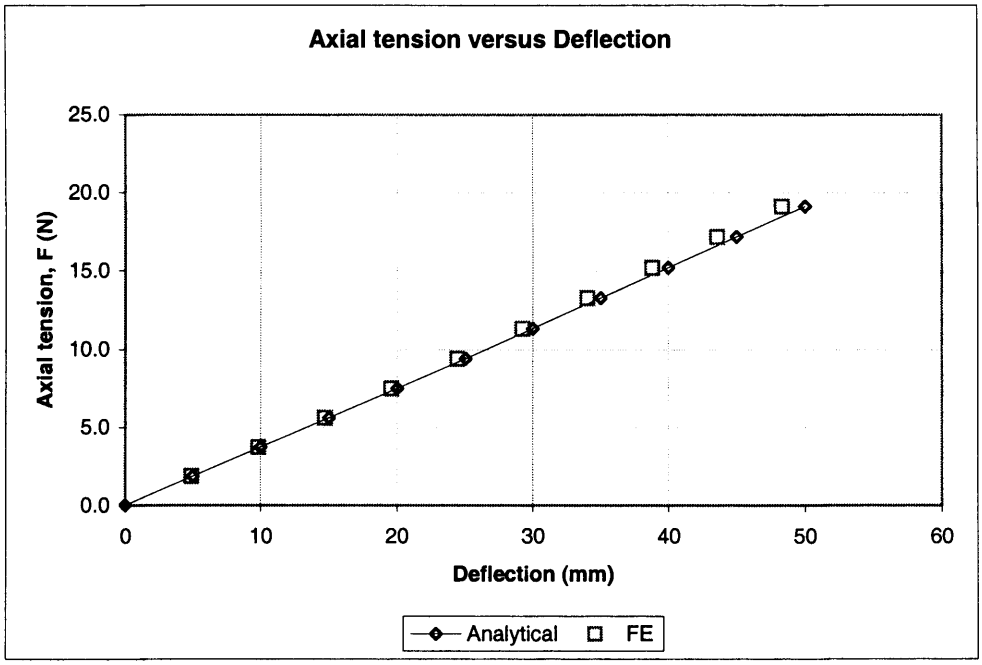

Figure D.3a Axial load - deflection for analytical and finite element for rectangular section (4.3499mm x 6.5mm)

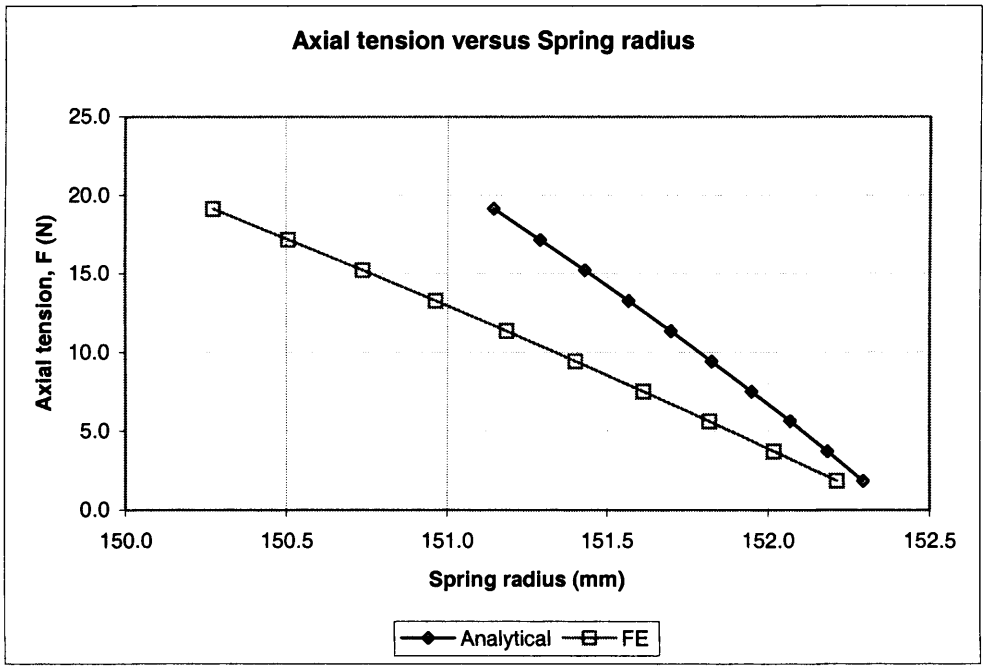

Figure D.3b Axial load – spring radius for analytical and finite element for rectangular section (4.3499mm x 6.5mm)

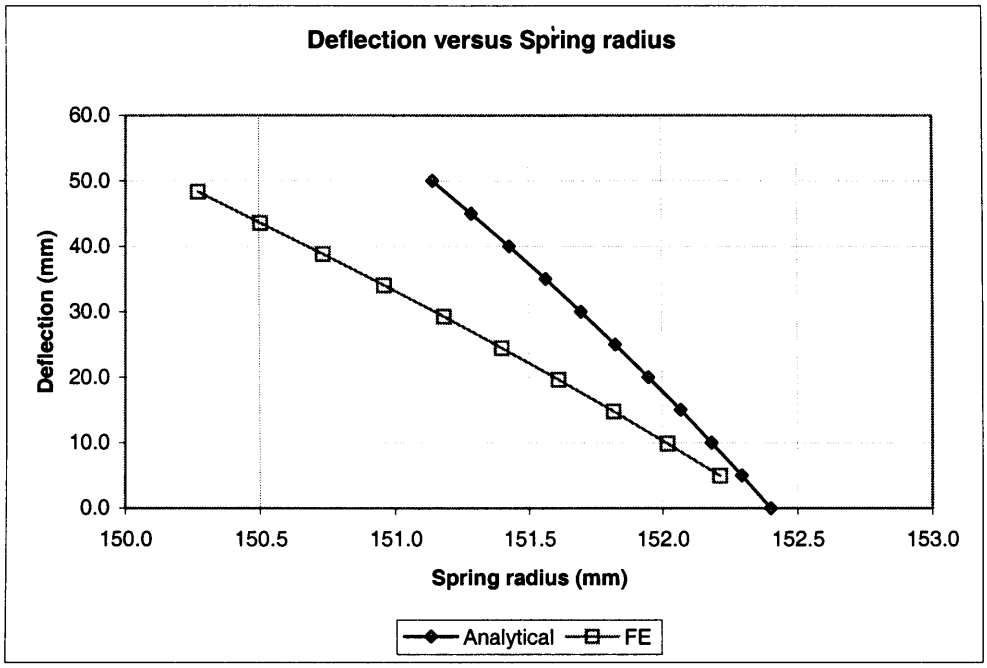

Figure D.3c Deflection – spring radius for analytical and finite element for rectangular section (4.3499mm x 6.5mm)

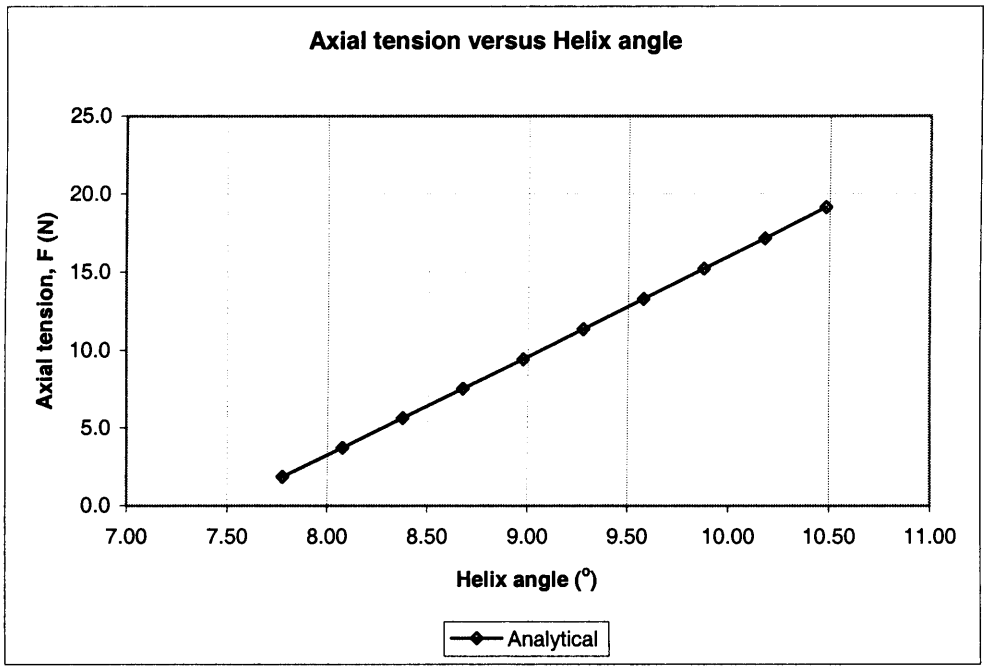

Figure D.3d Axial load – helix angle for analytical solution for rectangular section (4.3499mm x 6.5mm)

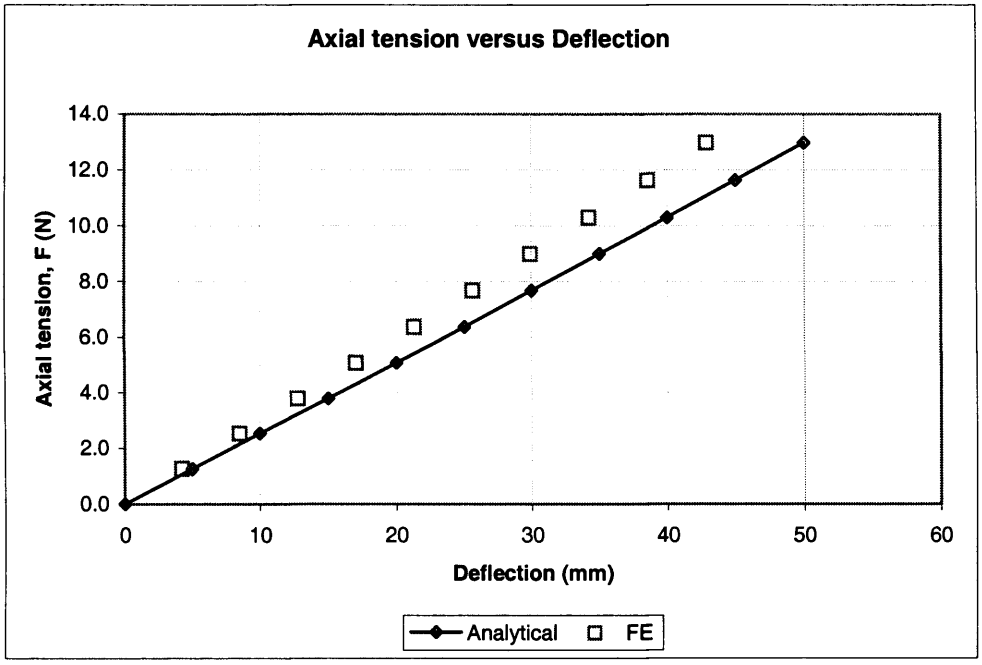

Figure D.4a Axial load - deflection for analytical and finite element for L-section

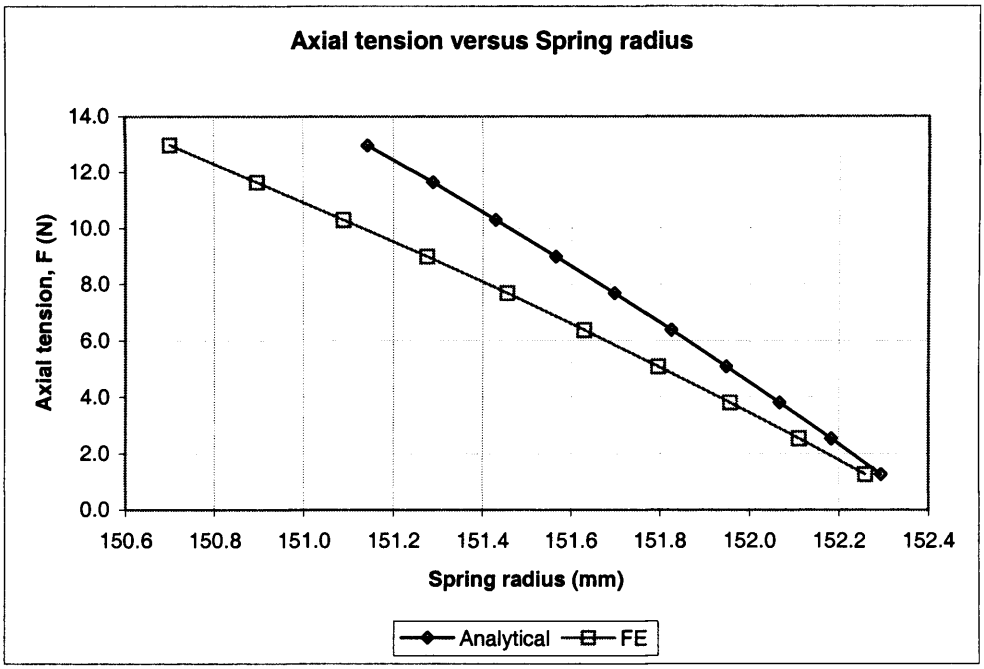

Figure D.4b Axial load – spring radius for analytical and finite element for L-section

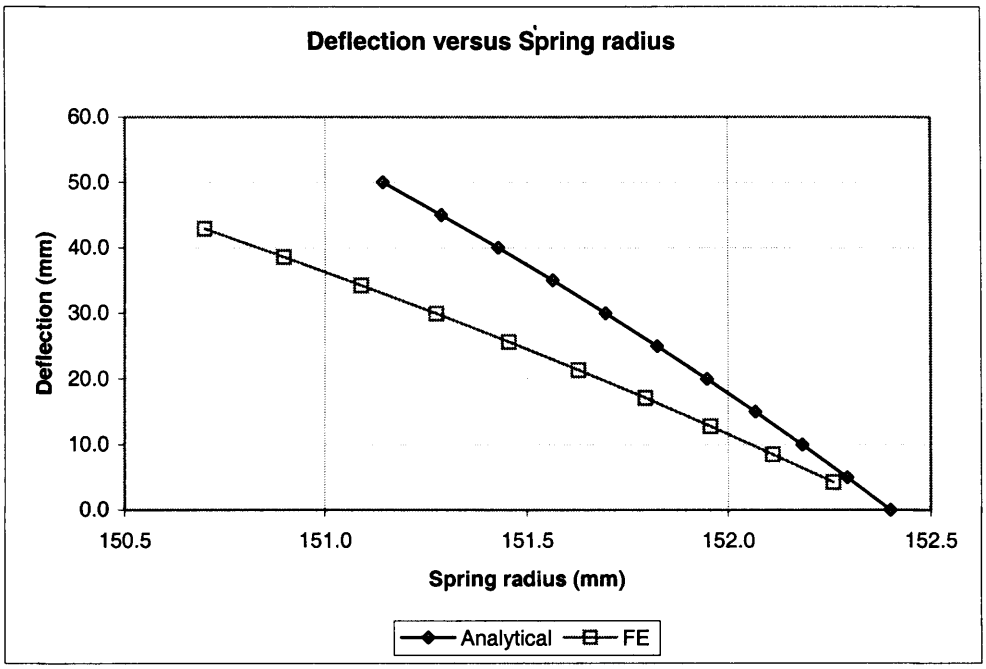

Figure D.4c Deflection – spring radius for analytical and finite element for L-section

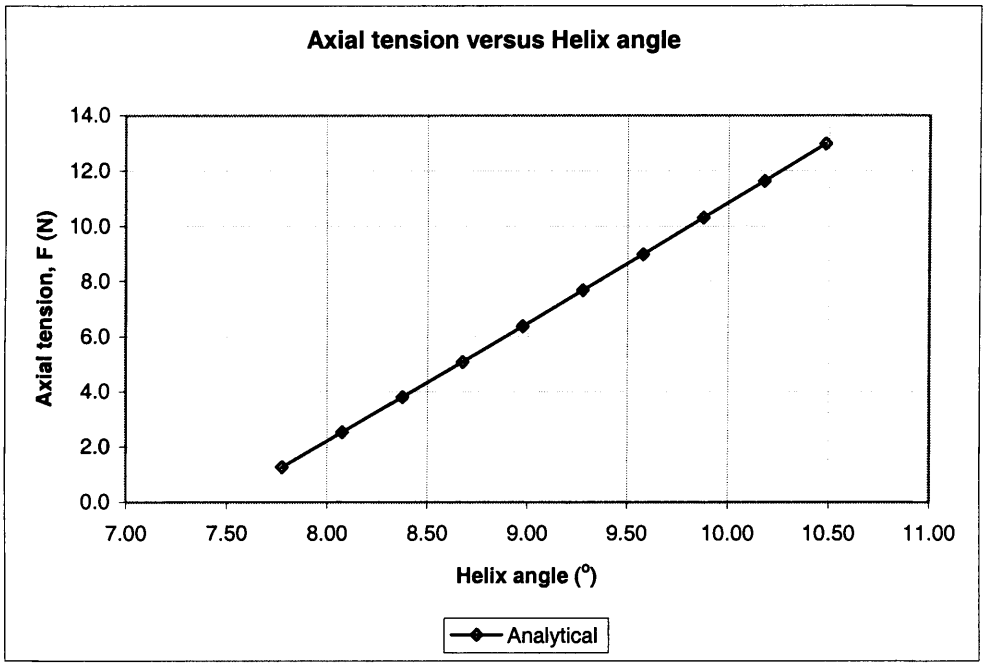

Figure D.4d Axial load – helix angle for analytical solution for L-section

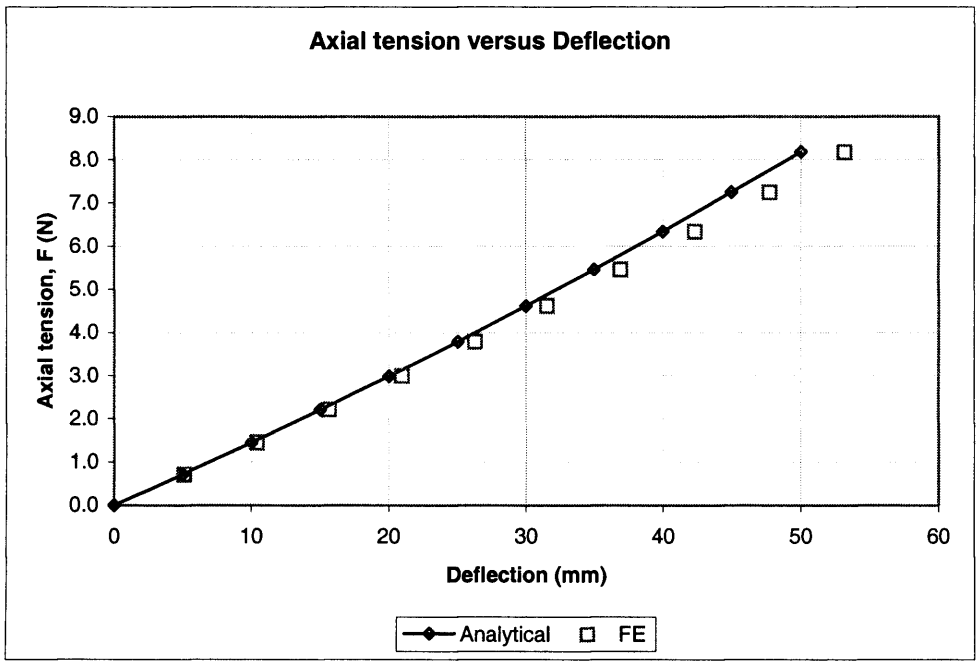

Figure D.5a Axial load - deflection for analytical and finite element for Z-section

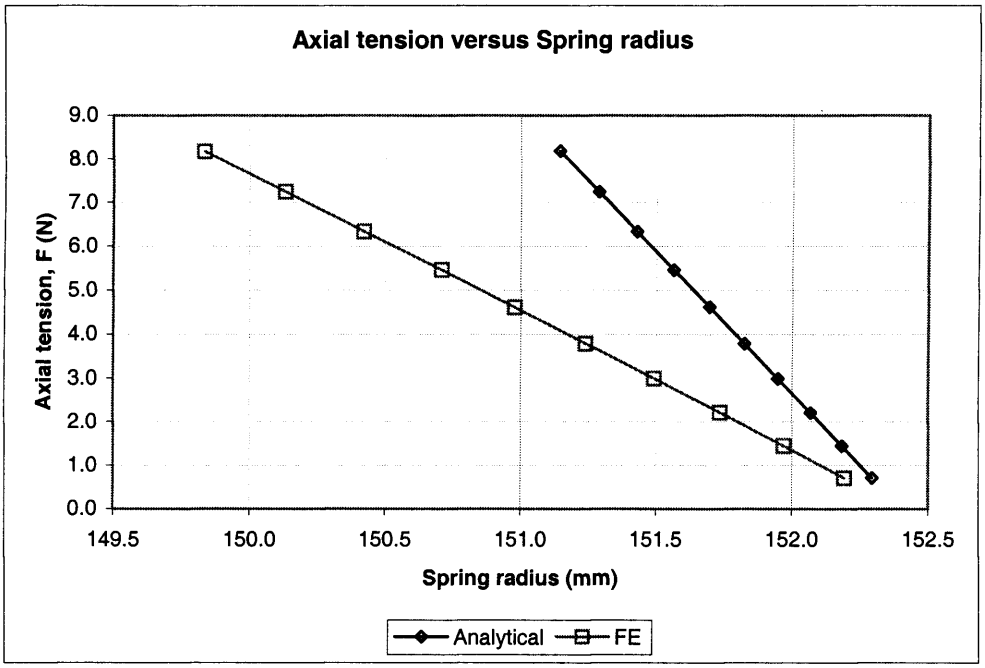

Figure D.5b Axial load – spring radius for analytical and finite element for Z-section

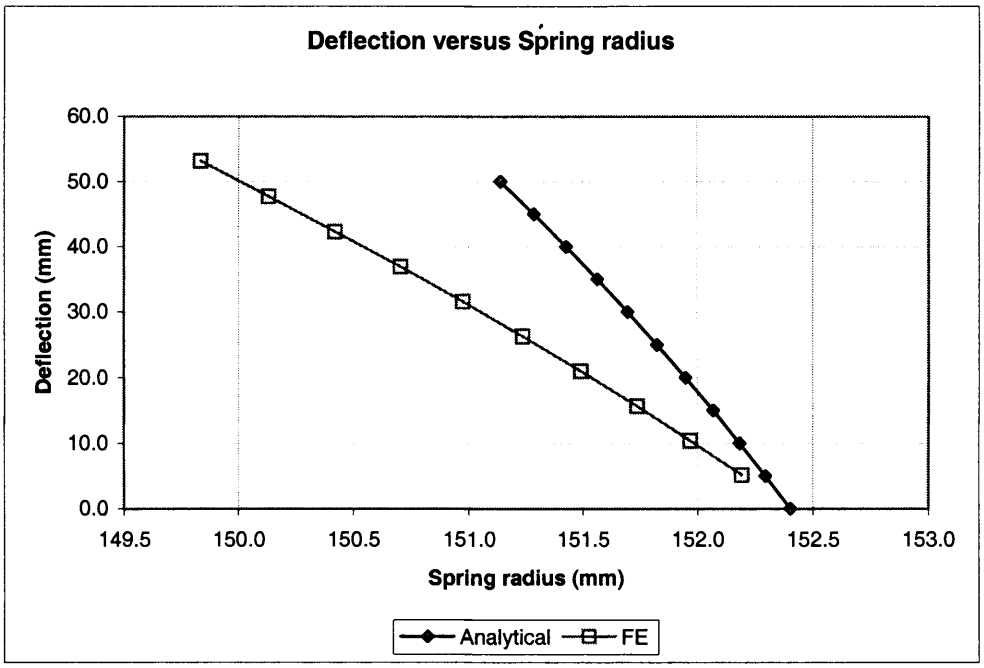

Figure D.5c Deflection – spring radius for analytical and finite element for Z-section

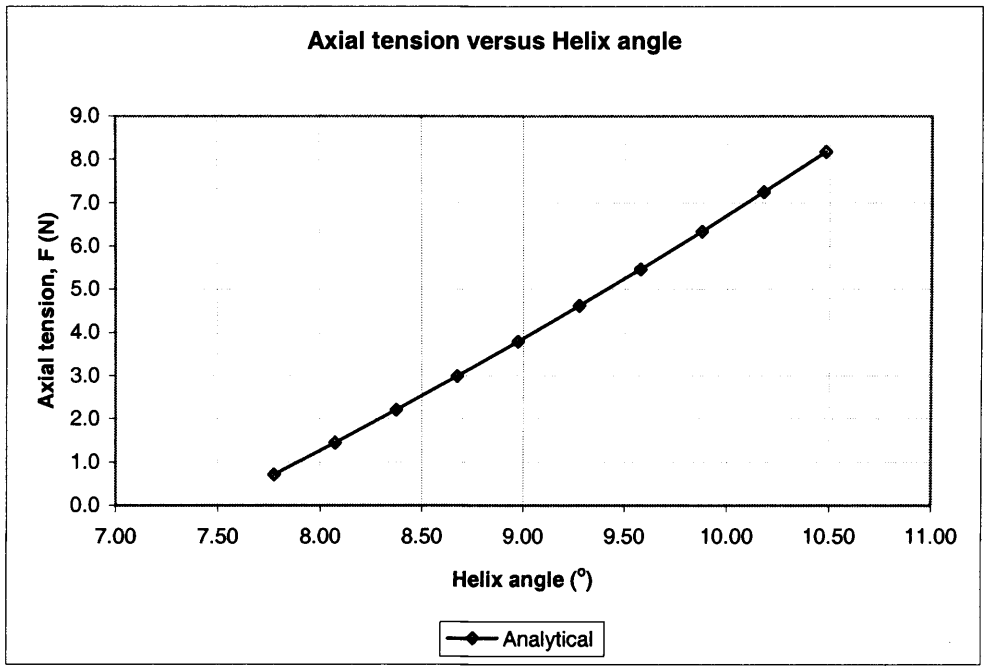

Figure D5d Axial load – helix angle for analytical solution for Z-section

- *Results for Internal Pressure Loading*

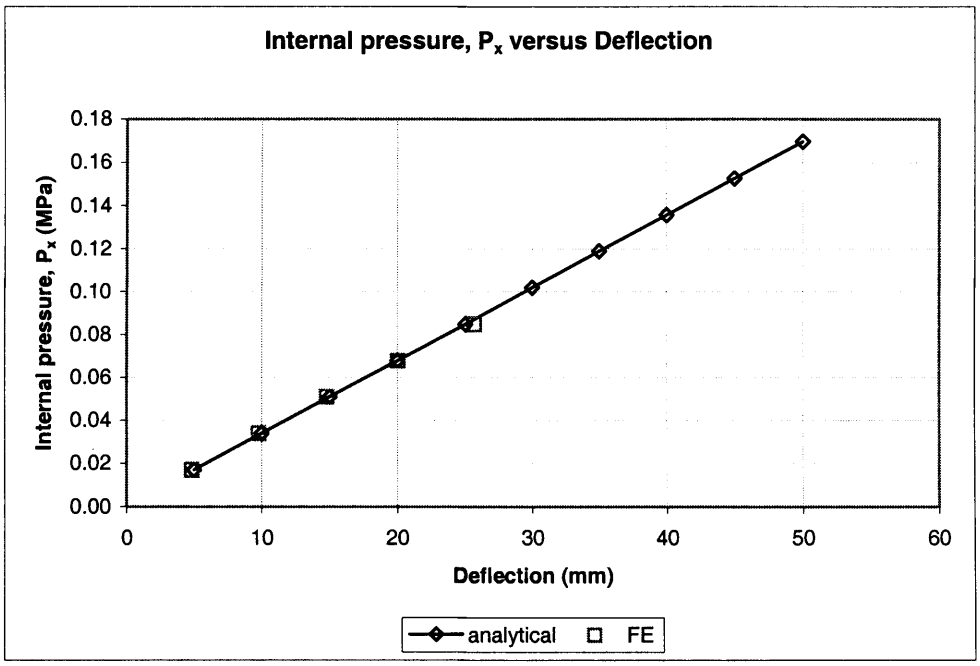

Figure D.6a Internal pressure - deflection for analytical and finite element for square section

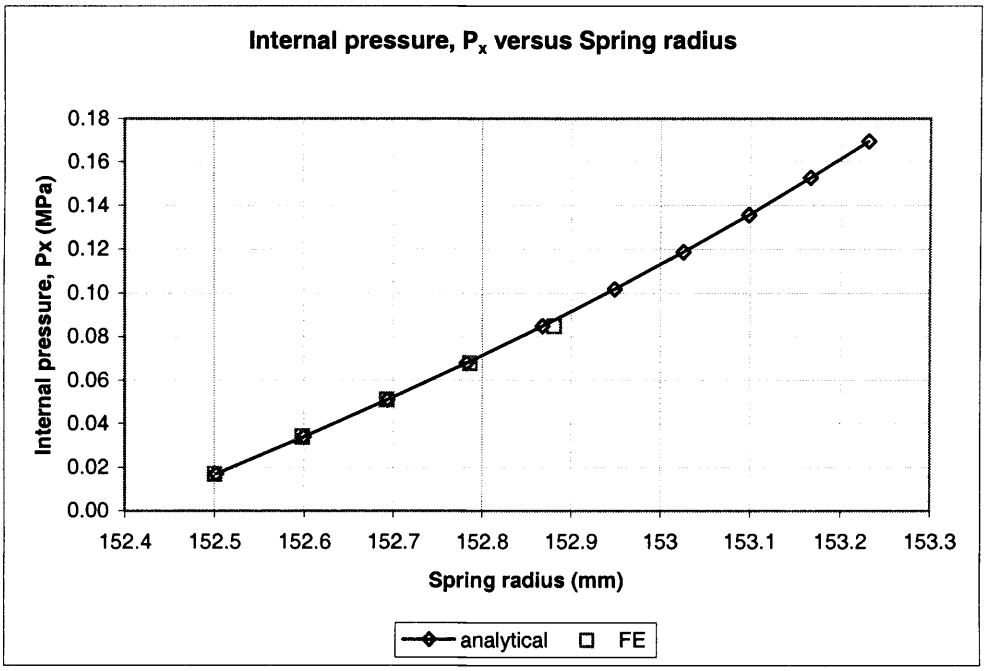

Figure D.6b Internal pressure – spring radius for analytical and finite element for square section

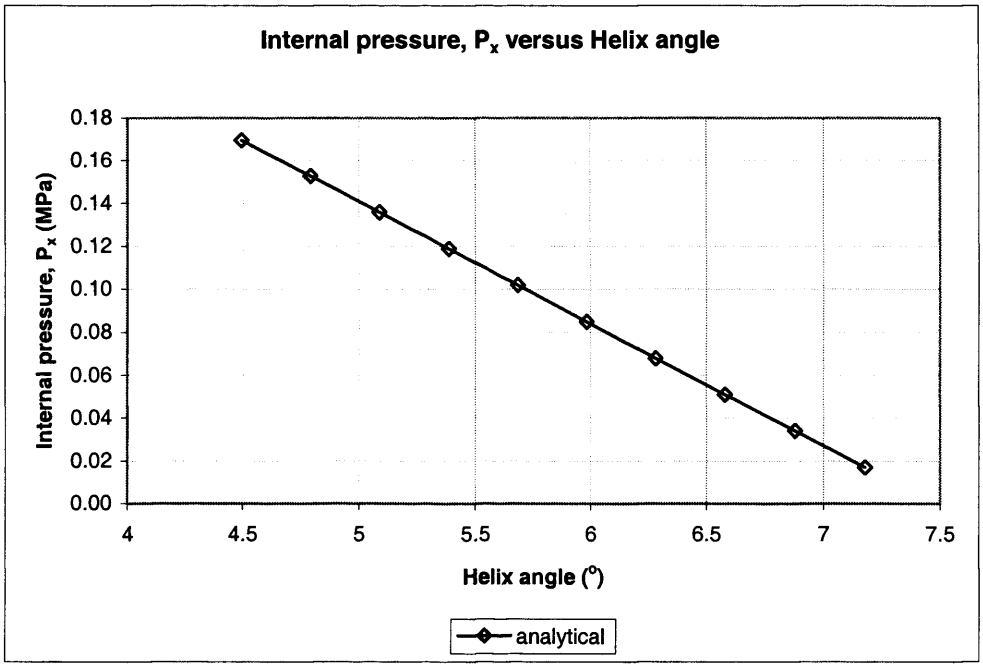

Figure D.6c Internal pressure – helix angle for analytical solution for square section

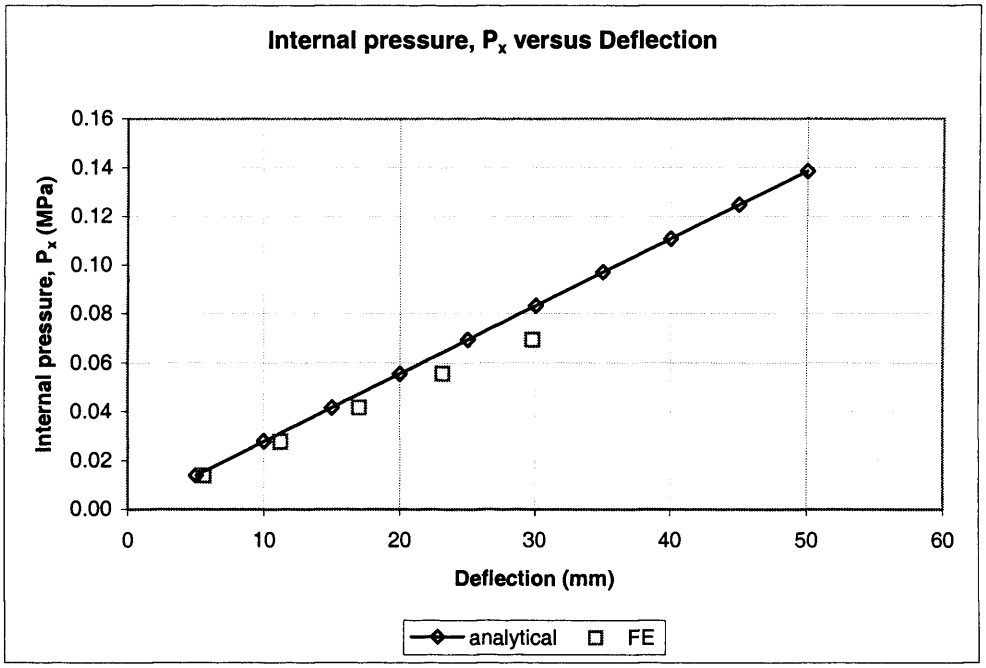

Figure D.7a Internal pressure - deflection for analytical and finite element for rectangular section (6.5mm x 4.3499mm)

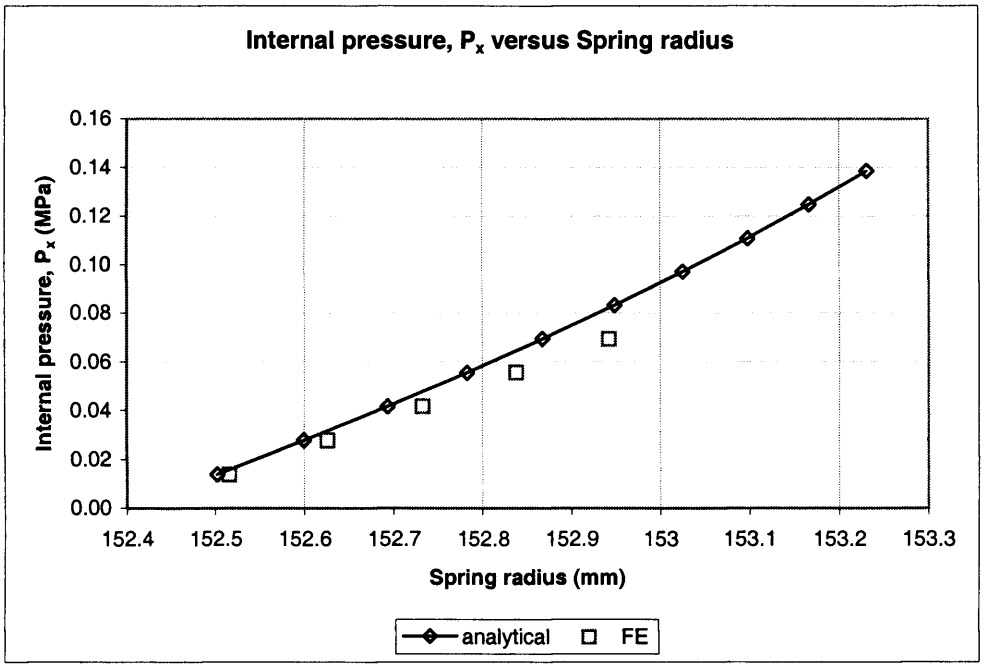

Figure D.7b Internal pressure – spring radius for analytical and finite element for rectangular section (6.5mm x 4.3499mm)

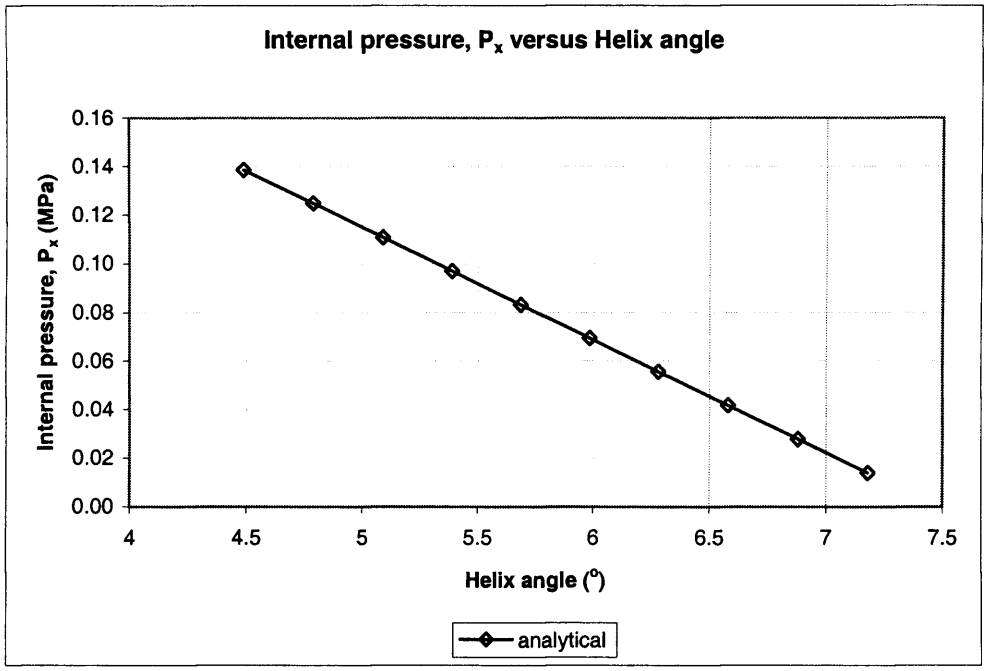

Figure D.7c Internal pressure – helix angle for analytical solution for rectangular section (6.5mm x 4.3499mm)

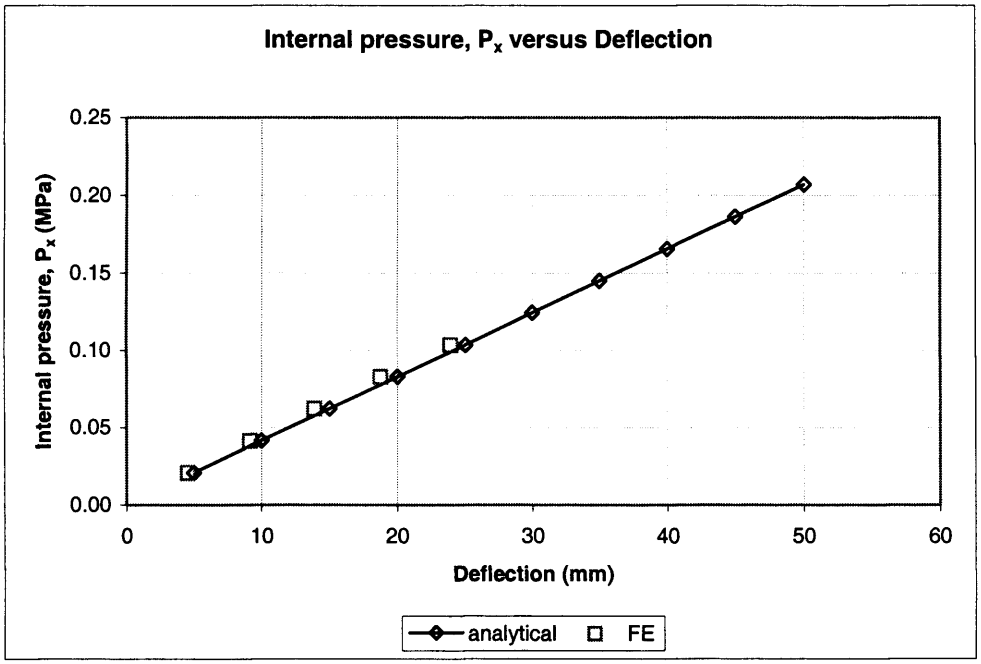

Figure D.8a Internal pressure - deflection for analytical and finite element for rectangular section (4.3499mm x 6.5mm)

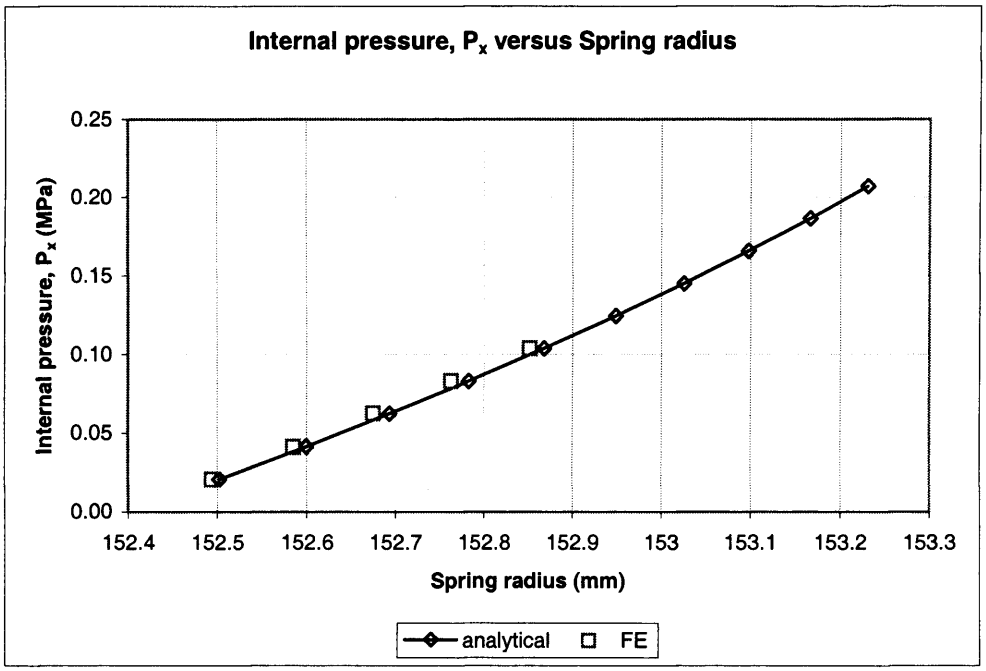

Figure D.8b Internal pressure – spring radius for analytical and finite element for rectangular section (4.3499mm x 6.5mm)

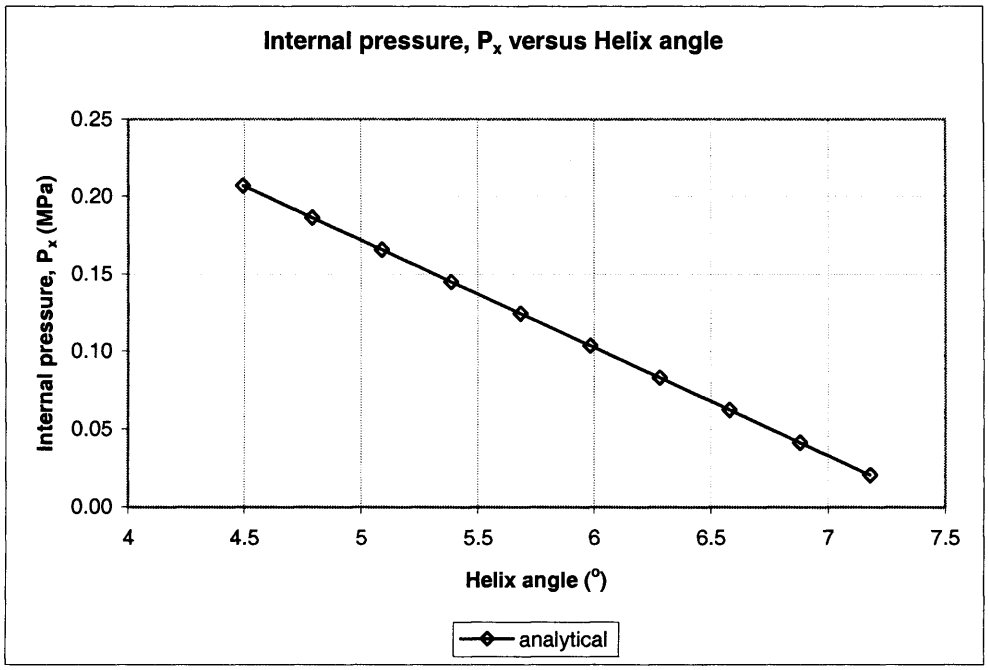

Figure D.8c Internal pressure – helix angle for analytical solution for rectangular section (4.3499mm x 6.5mm)

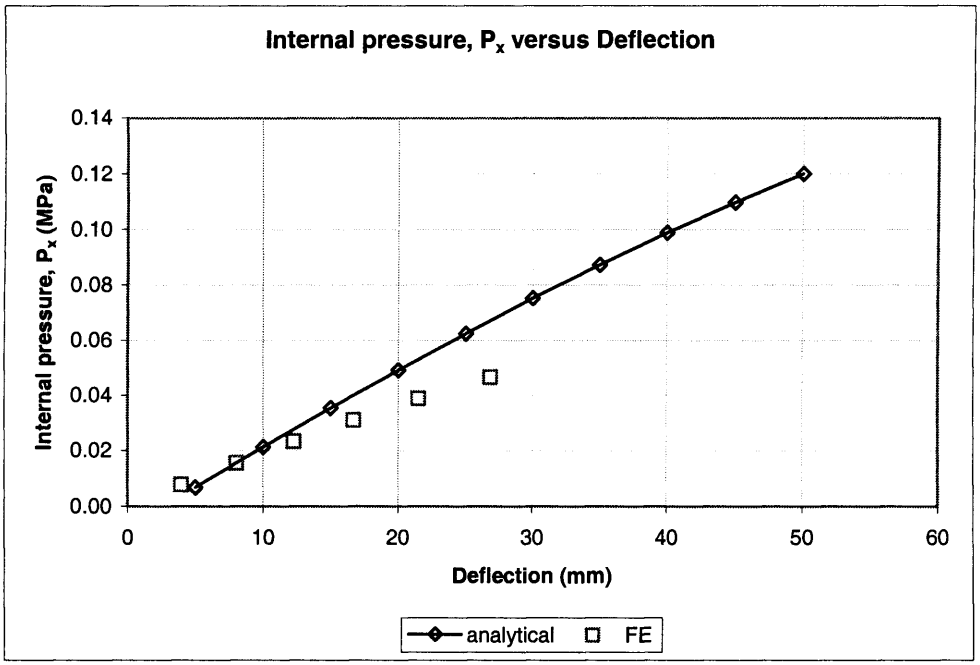

Figure D.9a Internal pressure - deflection for analytical and finite element for L-section

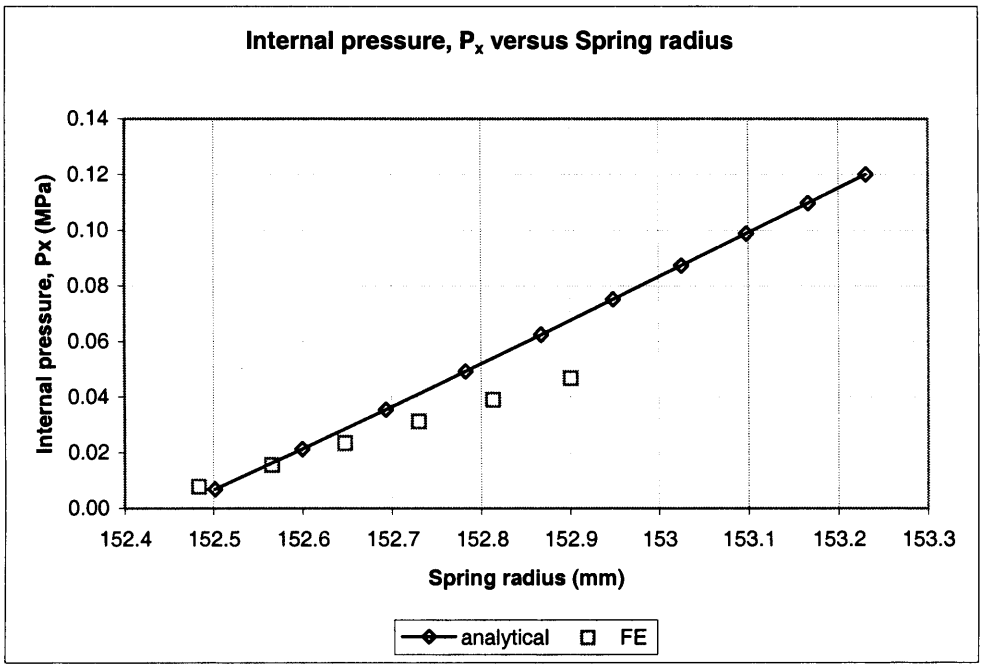

Figure D.9b Internal pressure – spring radius for analytical and finite element for L-section

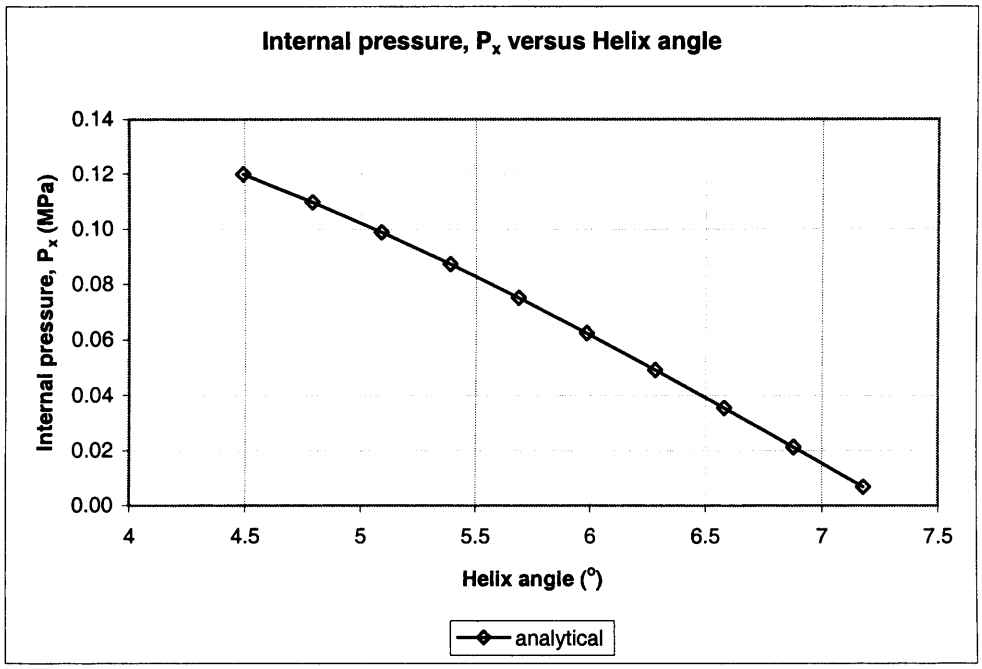

Figure D.9c Internal pressure – helix angle for analytical solution for L-section

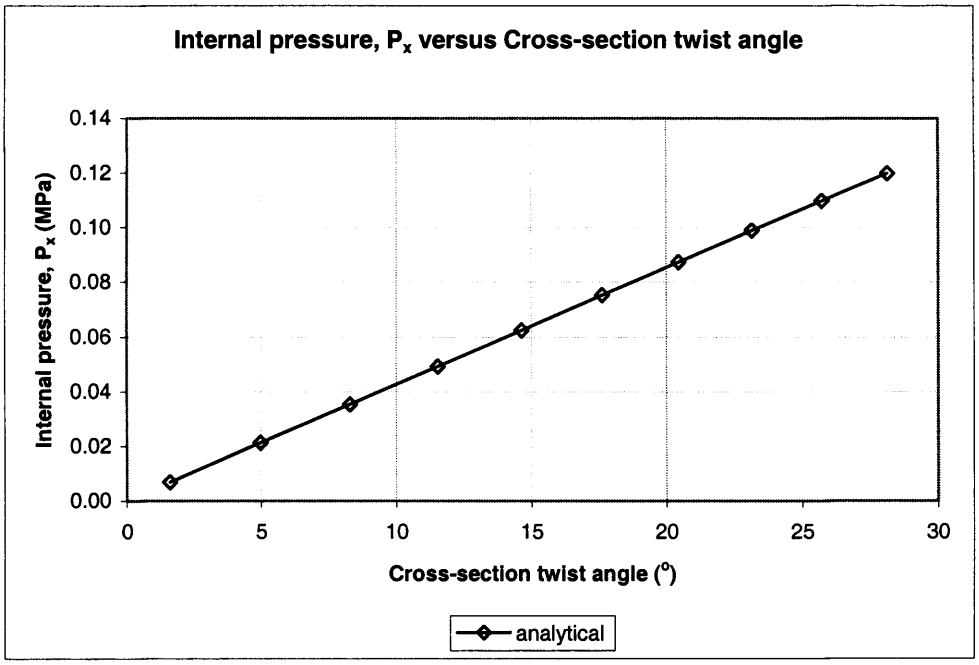

Figure D.9d Internal pressure – cross-section twist angle for analytical solution for L-section

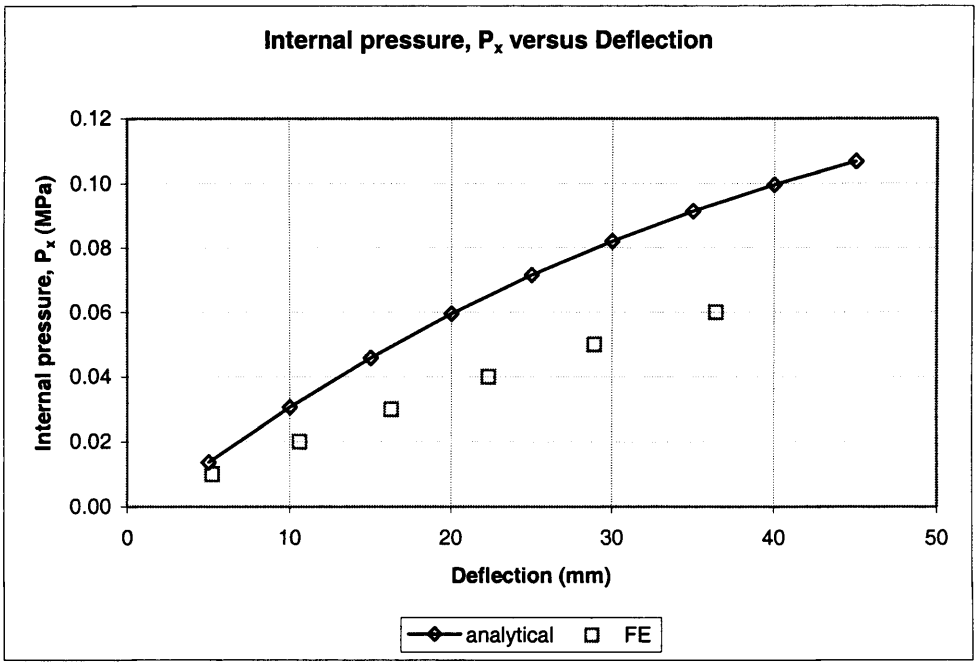

Figure D.10a Internal pressure - deflection for analytical and finite element for Z-section

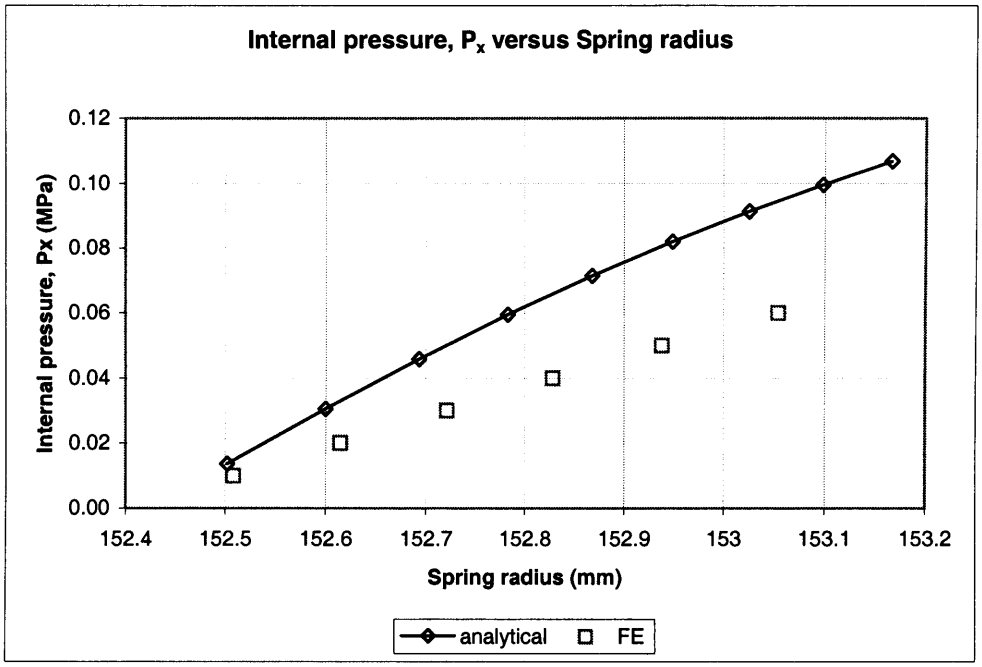

Figure D.10b Internal pressure – spring radius for analytical and finite element for Z-section

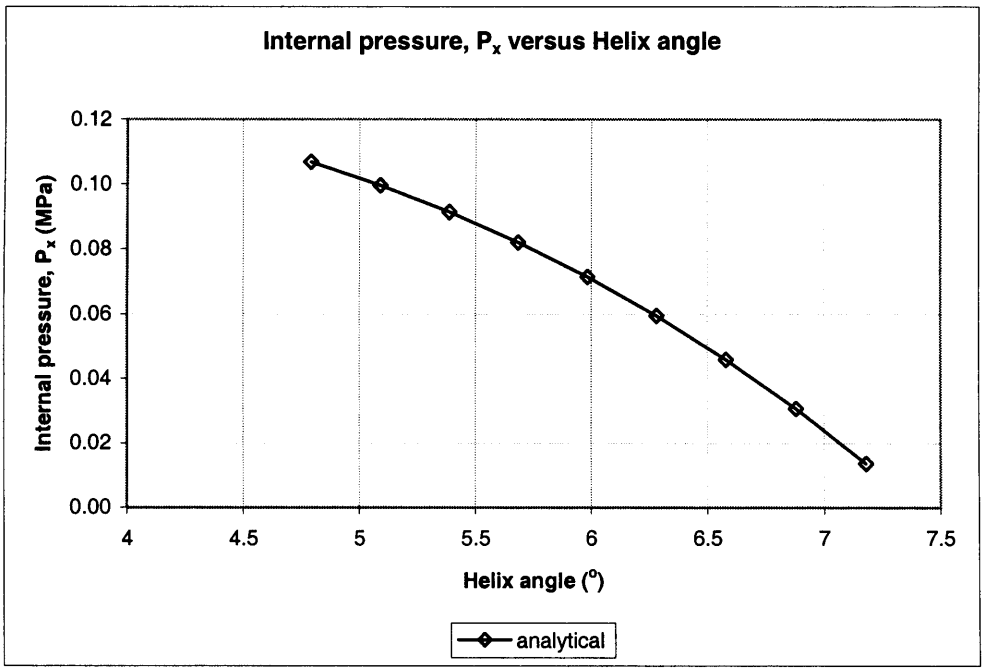

Figure D.10c Internal pressure – helix angle for analytical solution for Z-section

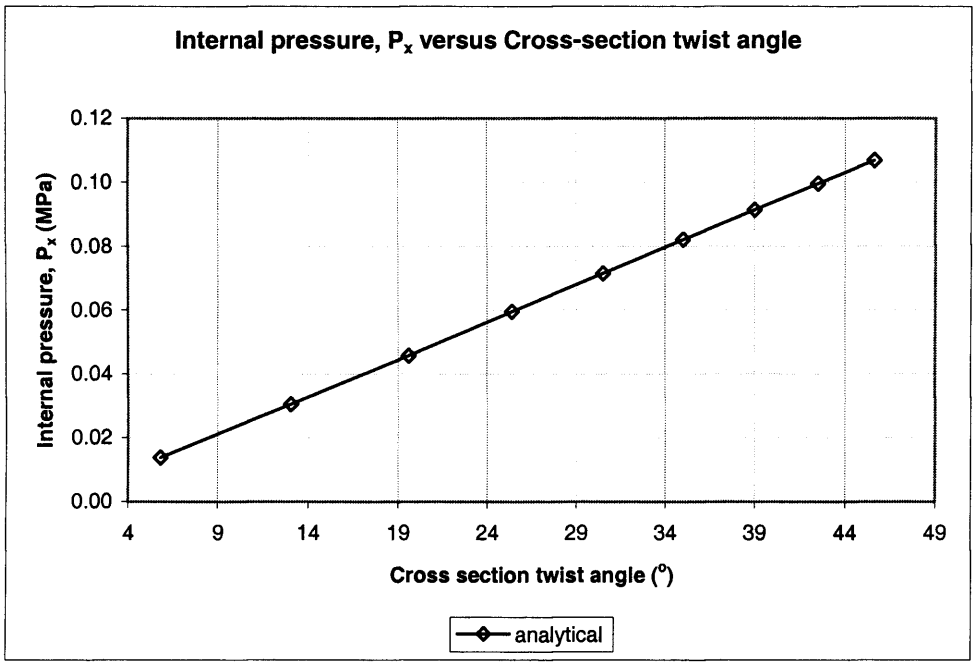

Figure D.10d Internal pressure – cross-section twist angle for analytical solution for Z-section

Appendix E

Supplementary Experimental Results for Various Cross-sections

- Results for Axial Loading

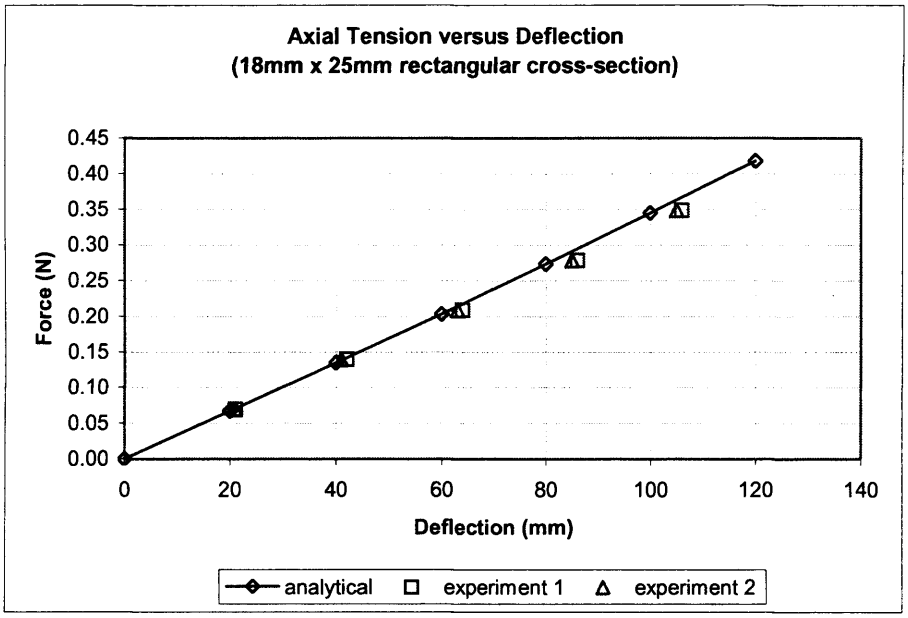

Figure E.1a Axial load – deflection for rectangular cross-section (18mm x 25mm) experimental result

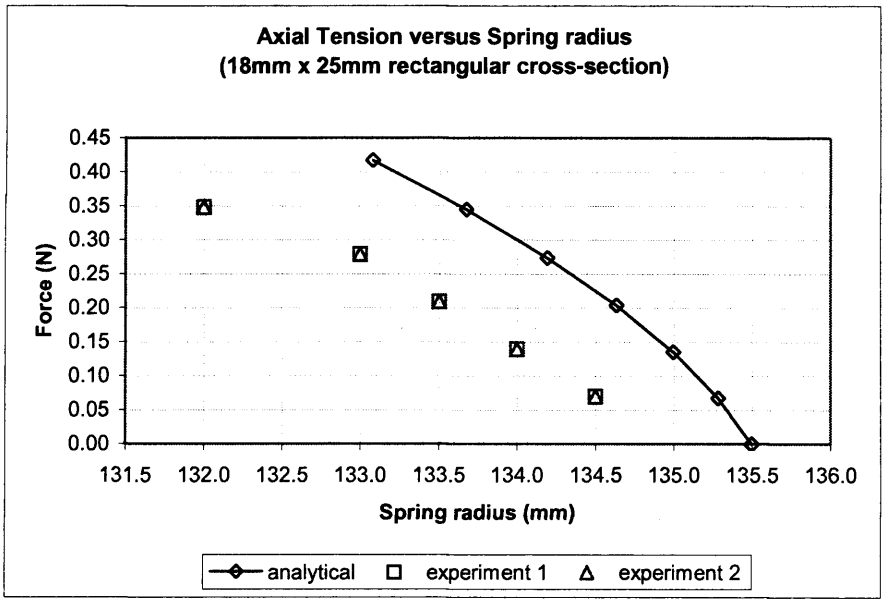

Figure E.1b Axial load – spring radius for rectangular cross-section (18mm x 25mm) experimental result

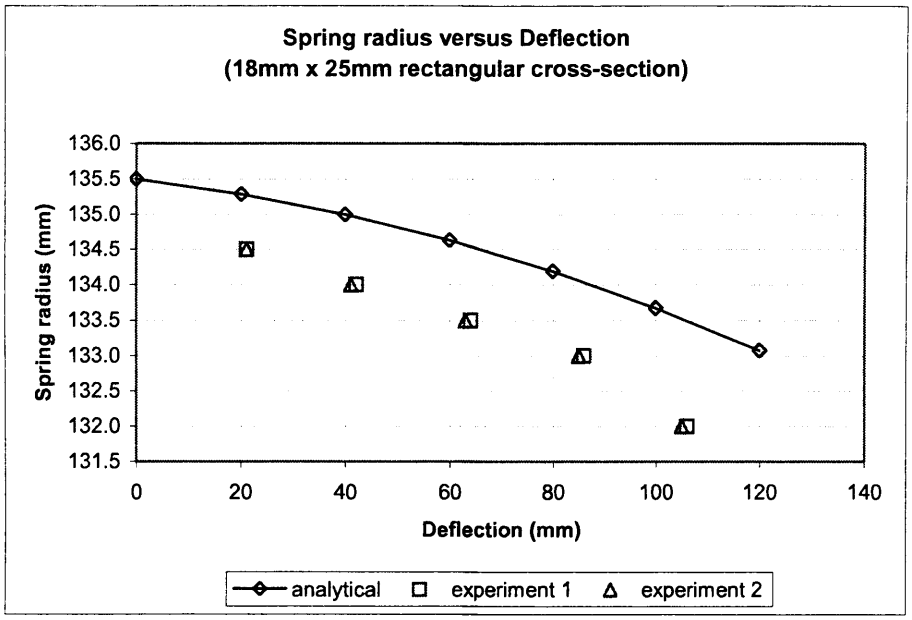

Figure E.1c Spring radius – deflection for rectangular cross-section (18mm x 25mm) experimental result

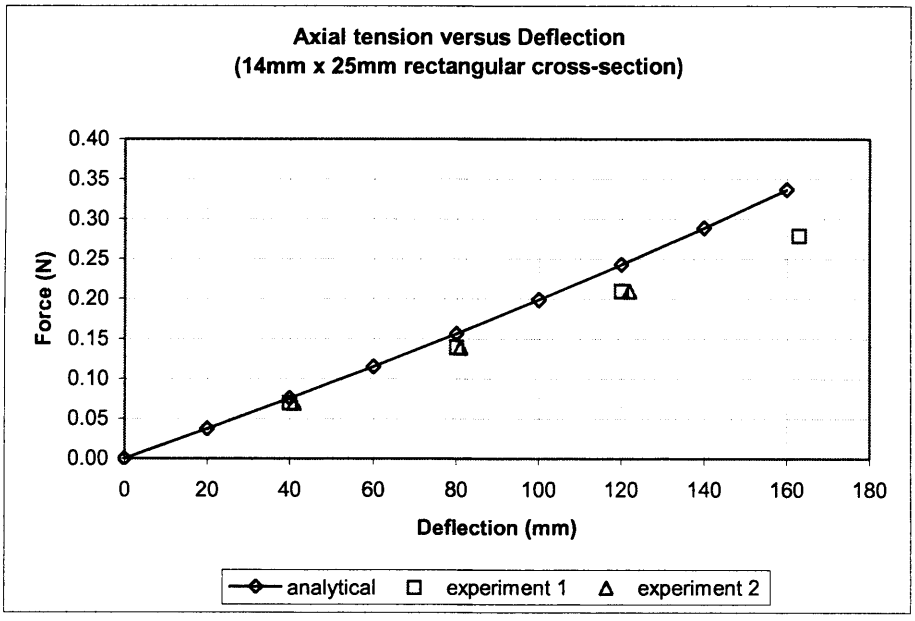

Figure E.2a Axial load – deflection for rectangular cross-section (14mm x 25mm) experimental result

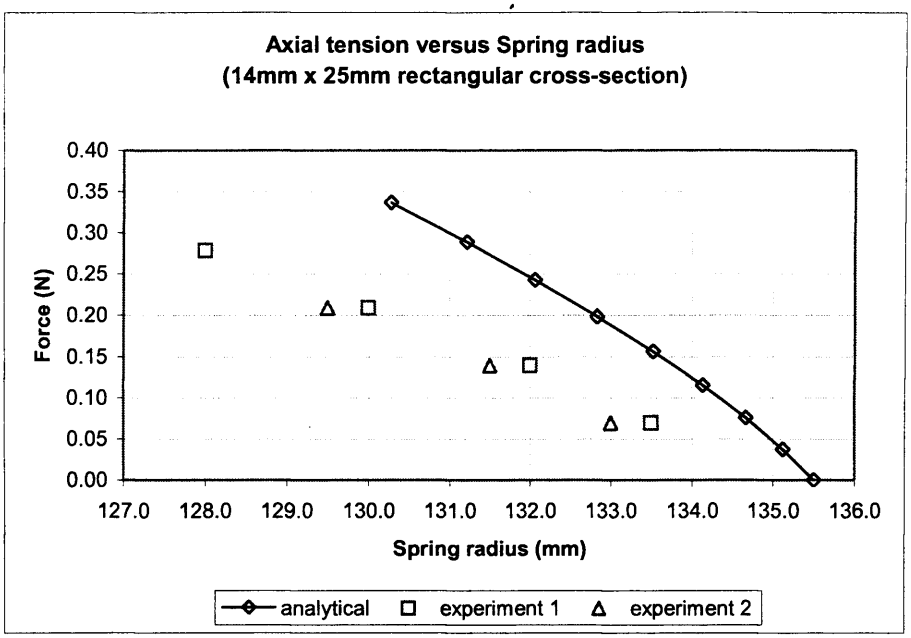

Figure E.2b Axial load – spring radius for rectangular cross-section (14mm x 25mm) experimental result

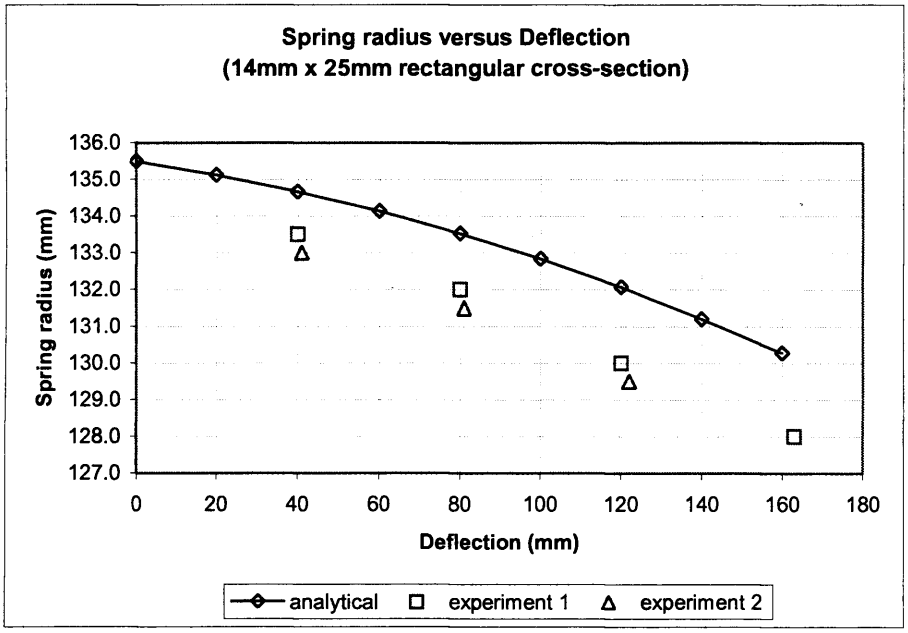

Figure E.2c Spring radius – deflection for rectangular cross-section (14mm x 25mm) experimental result

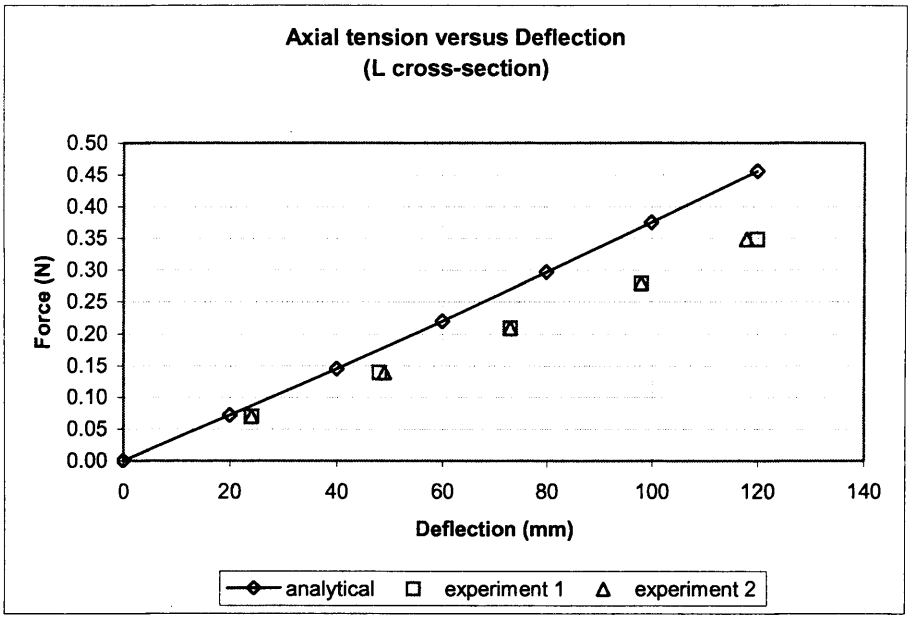

Figure E.3a Axial load – deflection for L cross-section experimental result

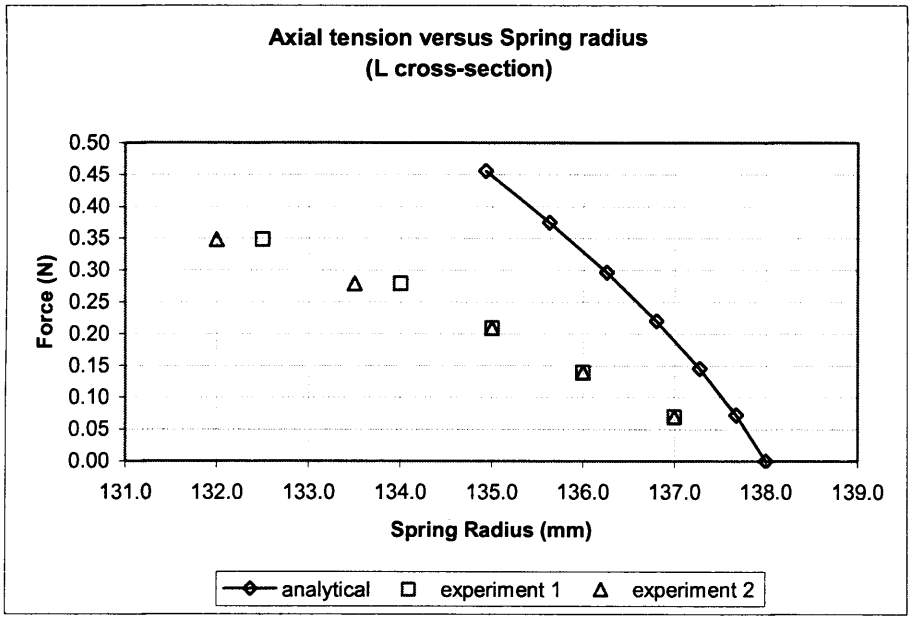

Figure E.3b Axial load – spring radius for L cross-section experimental result

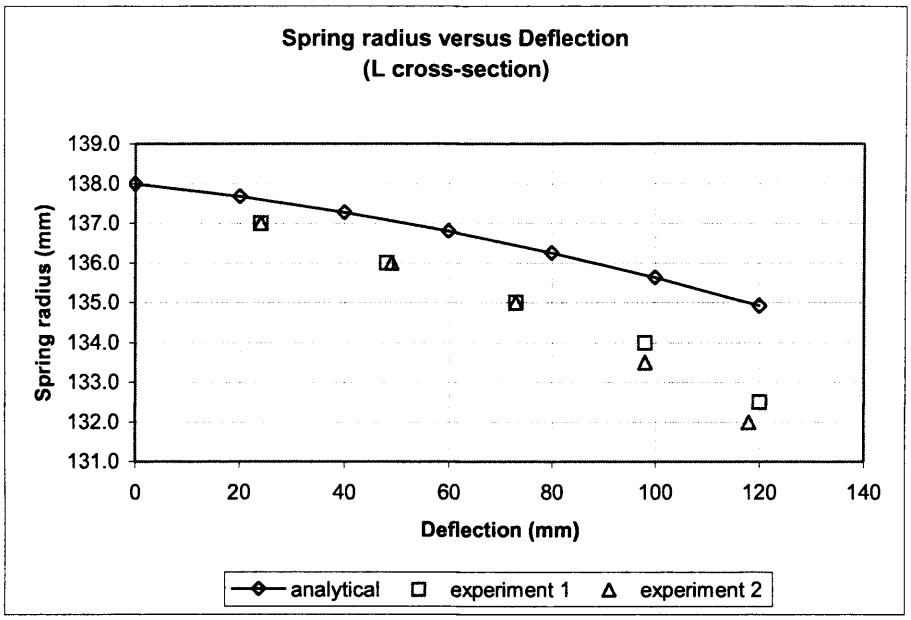

Figure E.3c Spring radius – deflection for L cross-section experimental result

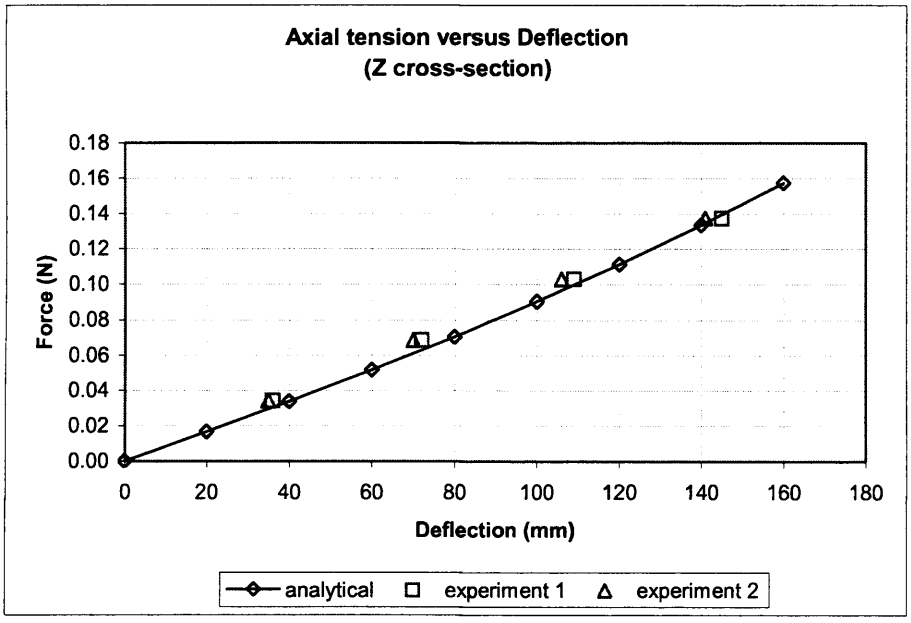

Figure E.4a Axial load – deflection for Z cross-section experimental result

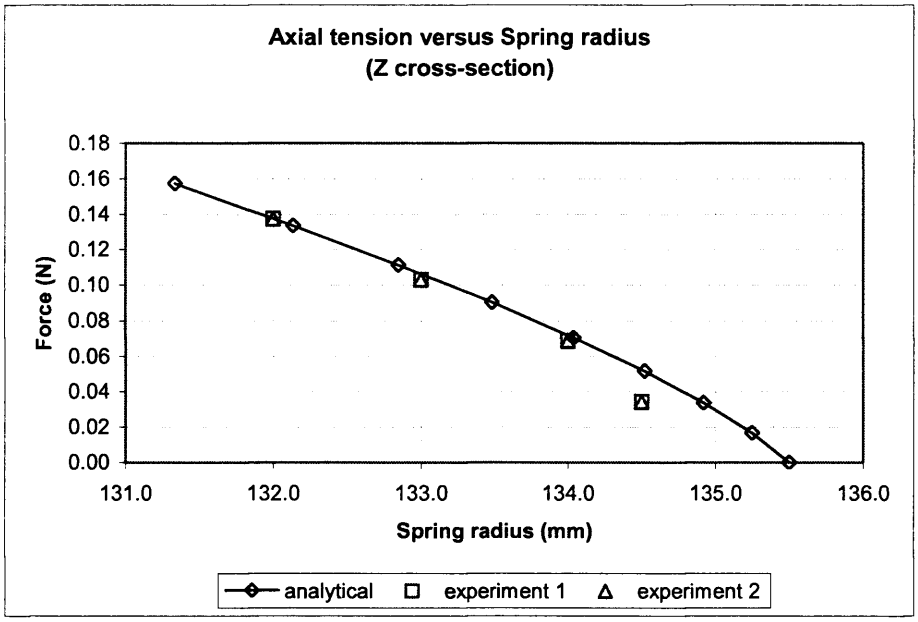

Figure E.4b Axial load – spring radius for Z cross-section experimental result

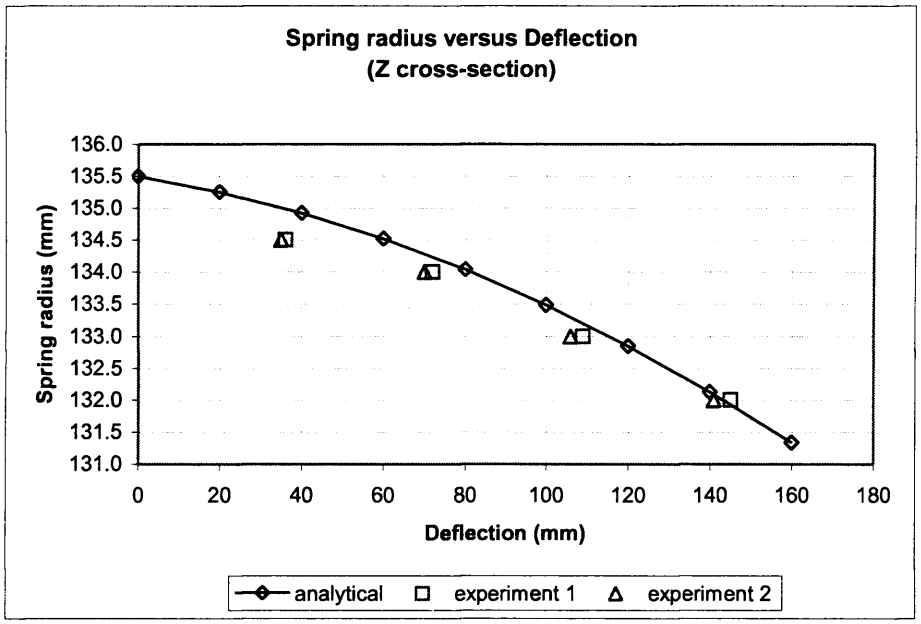

Figure E.4c Spring radius – deflection for Z cross-section experimental result

- Results for Internal Pressure Loading

Note that internal pressure loading results were plotted only for the experimental data obtained.

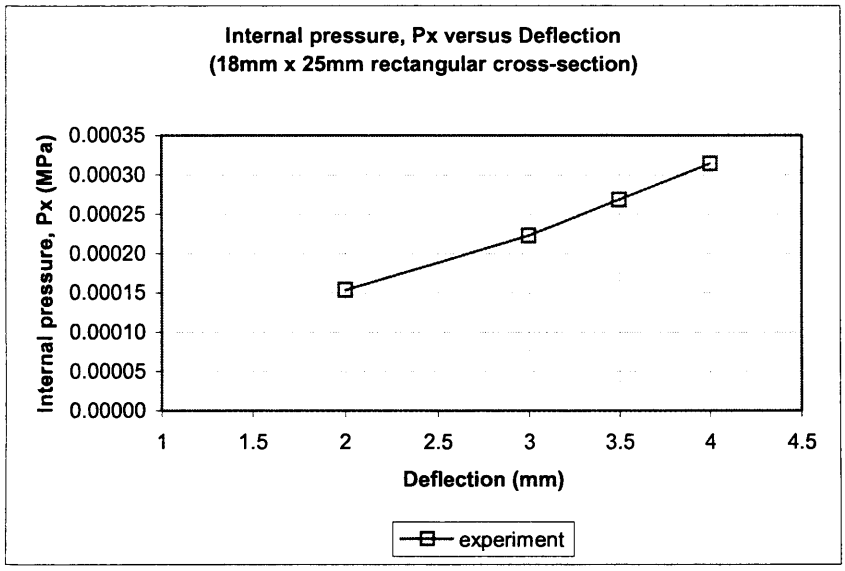

Figure E.5a Internal pressure – deflection for rectangular cross-section (18mm x 25mm) experimental result

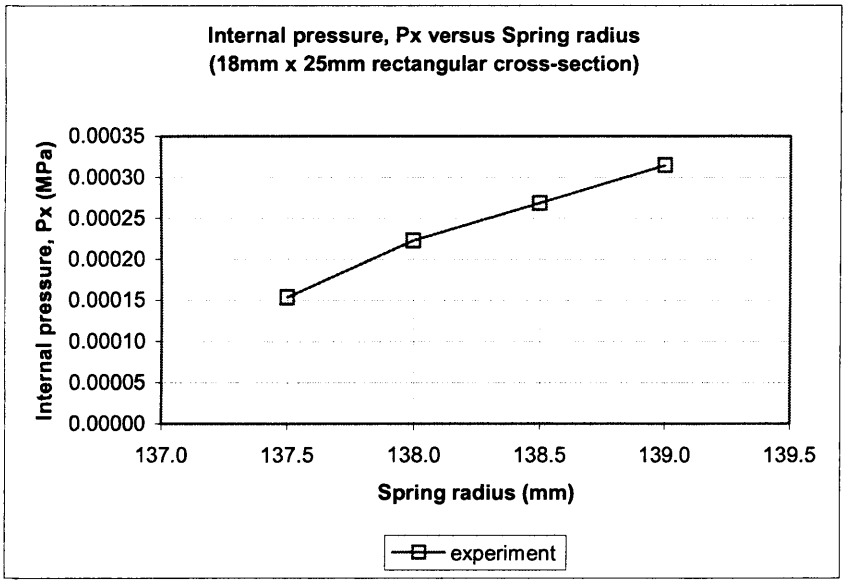

Figure E.5b Internal pressure – spring radius for rectangular cross-section (18mm x 25mm) experimental result

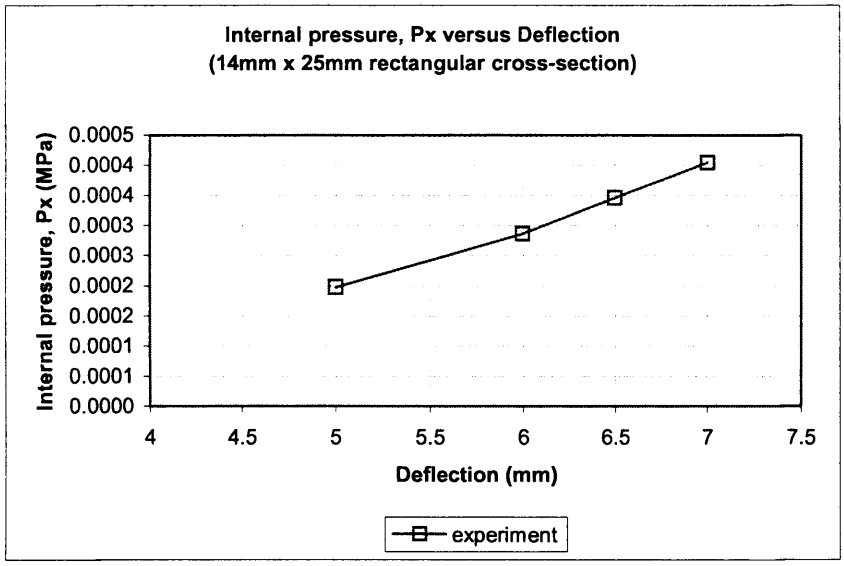

Figure E.6a Internal pressure – deflection for rectangular cross-section (14mm x 25mm) experimental result

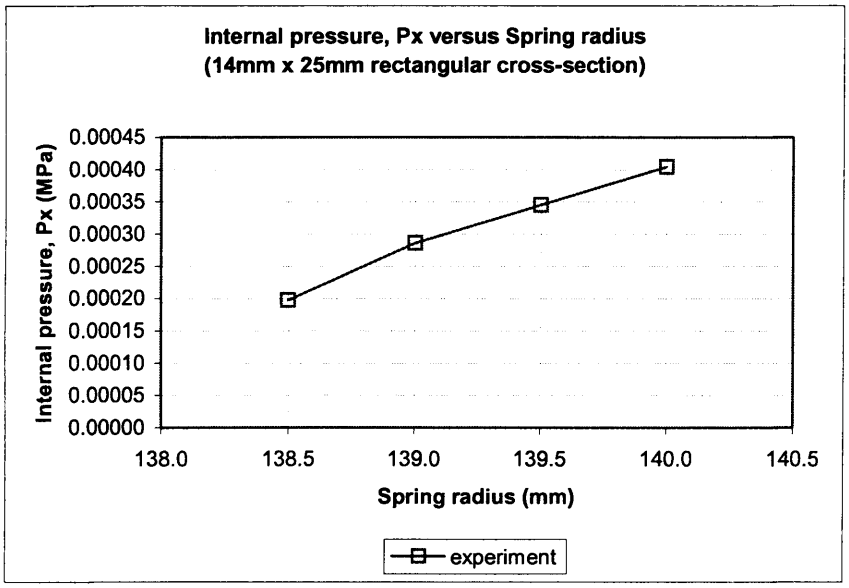

Figure E.6b Internal pressure – spring radius for rectangular cross-section (14mm x 25mm) experimental result

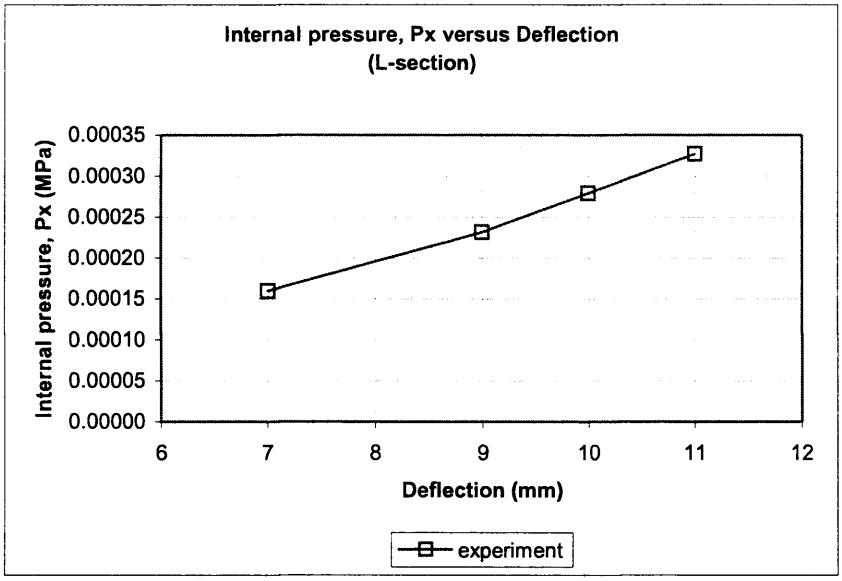

Figure E.7a Internal pressure – deflection for L cross-section experimental result

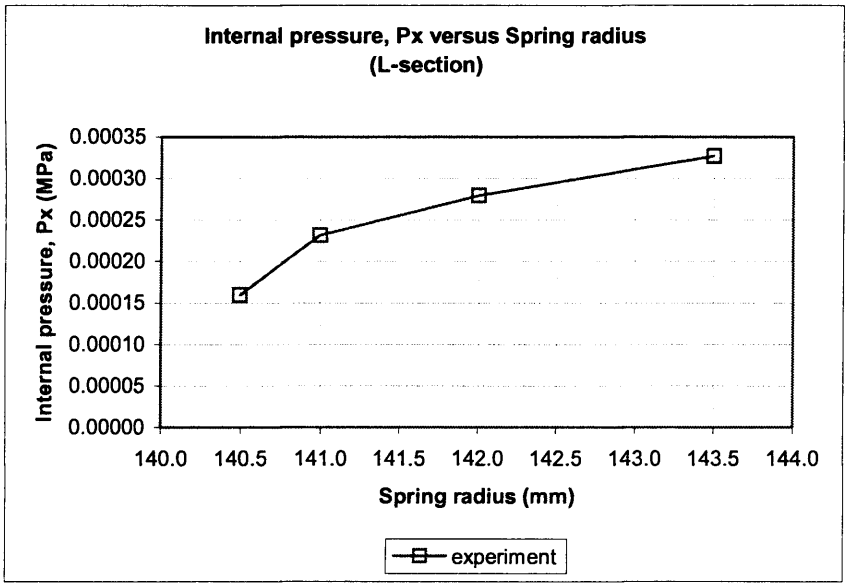

Figure E.7b Internal pressure – spring radius for L cross-section experimental result

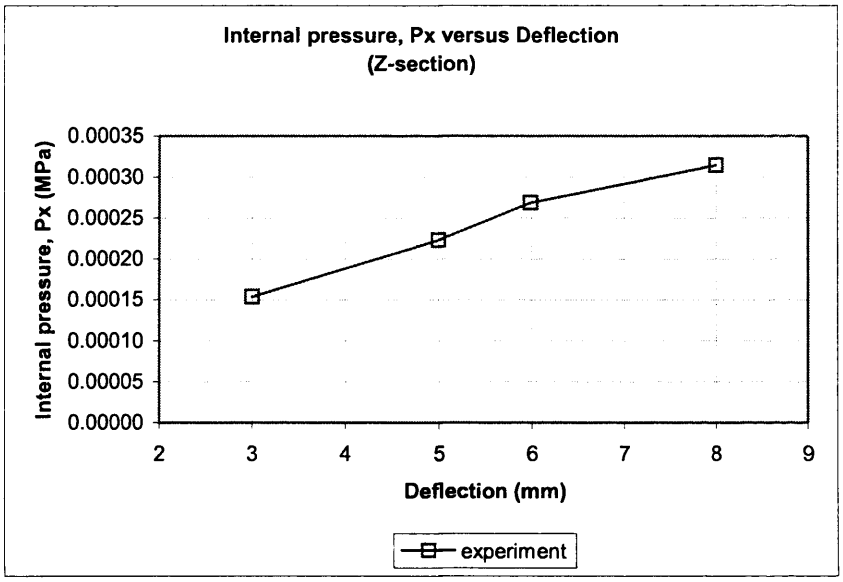

Figure E.8a Internal pressure – deflection for Z cross-section experimental result

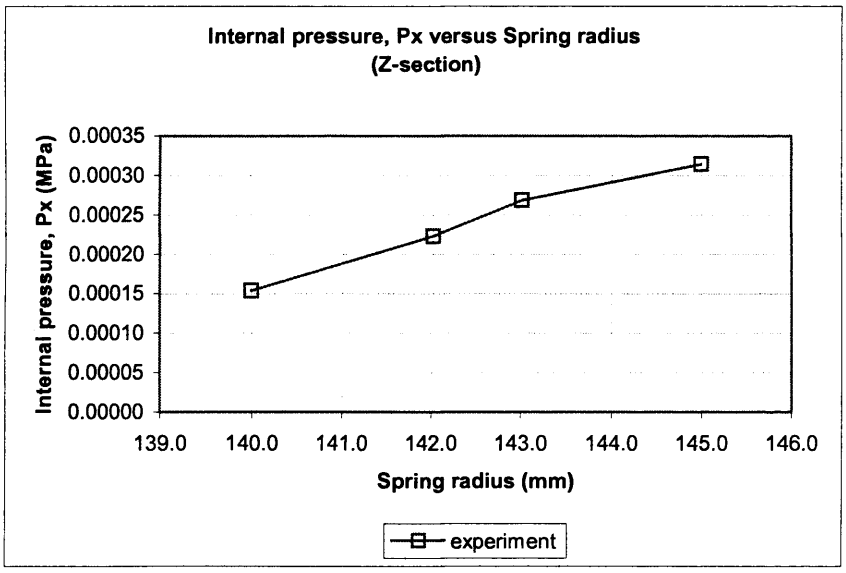

Figure E.8b Internal pressure – spring radius for Z cross-section experimental result

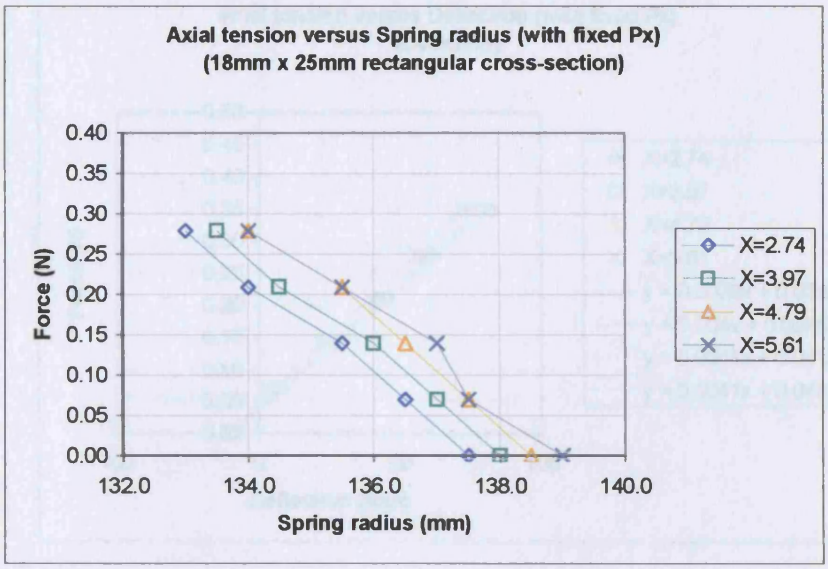

Figure E.9 Axial tension – spring radius for fixed internal pressure step values (experimental result for rectangular section (18mm x 25 mm))

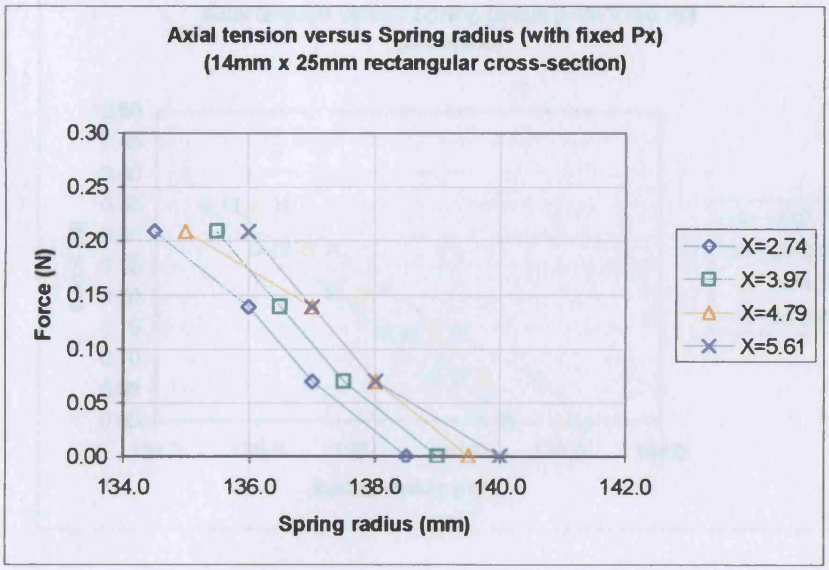

Figure E.10 Axial tension – spring radius for fixed internal pressure step values (experimental result for rectangular section (14mm x 25 mm))

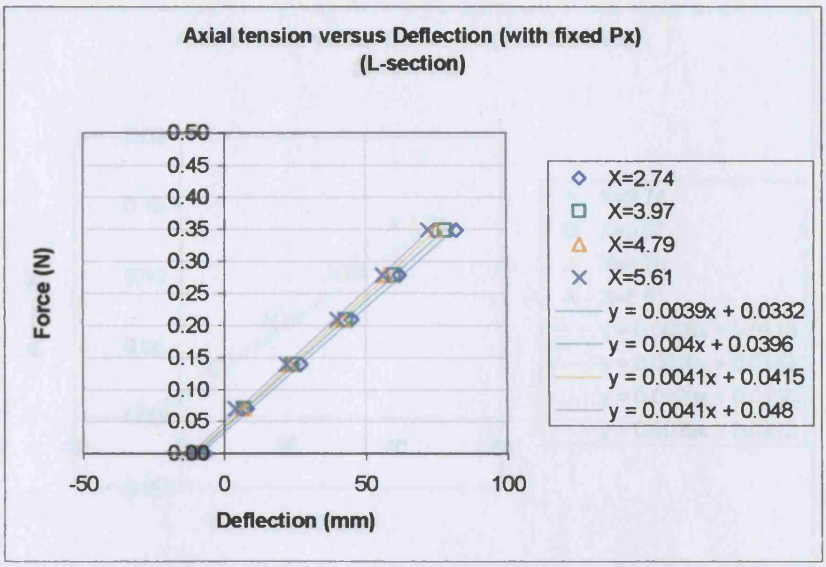

Figure E.11a Axial tension - deflection for fixed internal pressure step values (experimental result for L section)

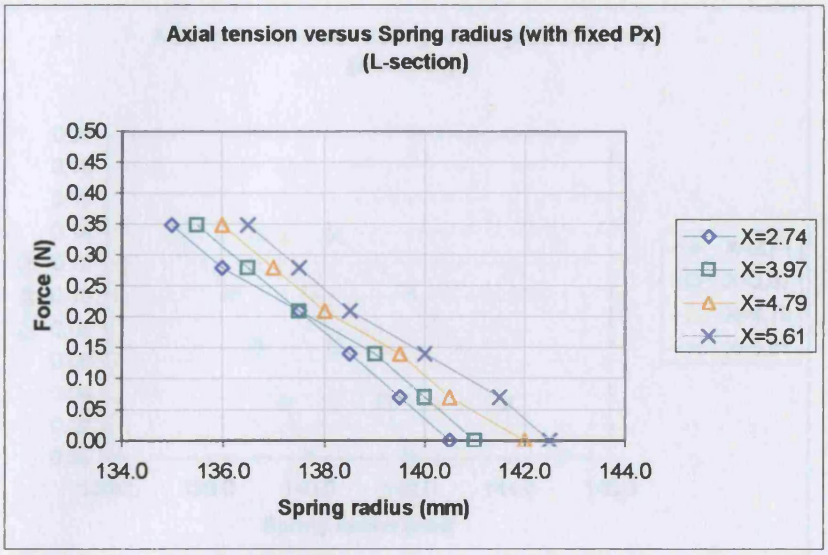

Figure E.11b Axial tension – spring radius for fixed internal pressure step values (experimental result for L section)

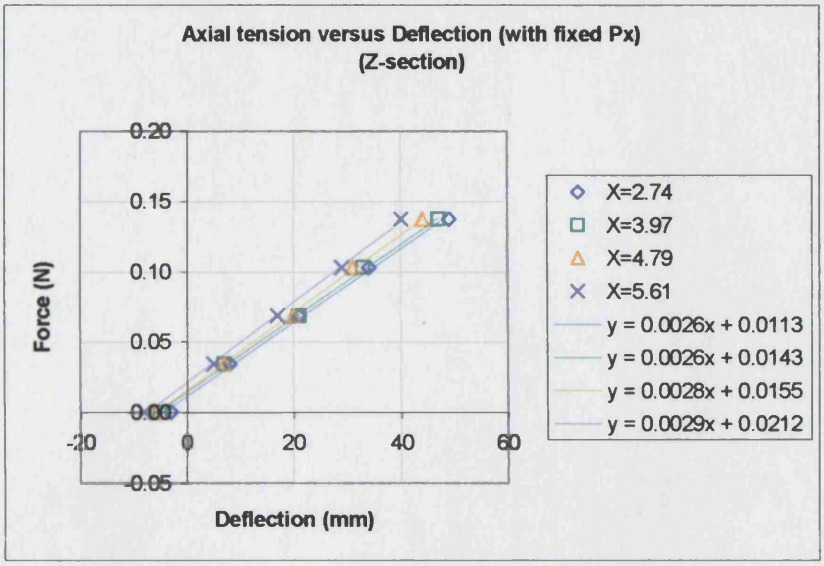

Figure E.12a Axial tension - deflection for fixed internal pressure step values (experimental result for Z section)

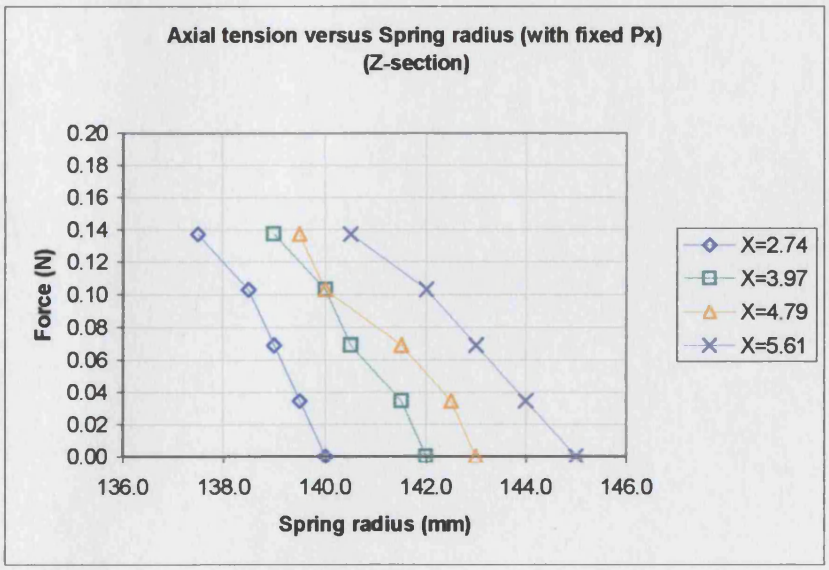

Figure E.12b Axial tension – spring radius for fixed internal pressure step values (experimental result for Z section)